

**MODAL IDENTIFICATION OF LINEAR TIME PERIODIC
SYSTEMS WITH APPLICATIONS TO CONTINUOUS-SCAN
LASER DOPPLER VIBROMETRY**

by

Shifei Yang

A dissertation submitted in partial fulfillment of the requirements for the degree of

DOCTOR OF PHILOSOPHY

(Engineering Mechanics)

at the

UNIVERSITY OF WISCONSIN-MADISON

2013

Date of final oral examination: 08/26/2013

The dissertation is approved by the following members of the Final Oral Committee:

Matthew S. Allen,	Associate Professor, Engineering Physics
-------------------	--

Daniel E. Kammer,	Professor, Engineering Physics
-------------------	--------------------------------

Michael E. Plesha,	Professor, Engineering Physics
--------------------	--------------------------------

Roderic S. Lakes,	Professor, Engineering Physics
-------------------	--------------------------------

Roxann L. Engelstad,	Professor, Mechanical Engineering
----------------------	-----------------------------------

© Copyright by Shifei Yang 2013

All rights reserved

Abstract

Many structures have to be modeled as Linear Time Periodic (LTP) systems to better characterize their time varying behavior, e.g., rotorcraft and wind turbines. However, current system identification methods are mostly limited to Linear Time Invariant (LTI) systems. This work develops several frequency domain identification algorithms for LTP systems. These algorithms are completely analogous to the algorithms for LTI systems, and they are capable of extracting the modal parameters of LTP systems under any type of input, using the well-established identification routines for LTI systems. The theory is based on the harmonic transfer function concept [Wereley, PhD Thesis 1991]. Whereas a transfer function relates the output of an LTI system to the input at the same frequency, a harmonic transfer function relates the output of an LTP system at a collection of frequencies to the input at the same collection, each separated by the fundamental frequency of the periodic system. In addition, in many cases it might be difficult or even impossible to directly measure the input. Therefore, the power spectrum in output-only modal analysis of LTI systems is also extended to LTP systems, introducing the harmonic power spectrum where the input is not measured but is assumed to be uniformly distributed random noise. Later, a simplified output-only algorithm is developed by lifting the positive harmonic correlation function, which is analogous to the impulse response of LTP systems. The lifting approach groups the responses at the same time instant in a period. As a consequence, the lifted spectra contain only one peak for each mode, therefore they are far easier to interpret and can be readily curve-fitted with virtually any modal parameter identification routine.

The proposed modal identification algorithms were combined with a novel technique, Continuous-Scan Laser Doppler Vibrometry (CSLDV). In CSLDV, the laser beam is redirected

by a pair of mirrors to continuously sweep over a structure while measuring, capturing spatially detailed dynamic information in the same amount of time that is required by conventional methods to capture a single point. When the laser spot moves in a closed and periodic pattern on an LTI structure, the acquired velocity signal appears to be from an LTP system. Therefore, the proposed identification algorithms can be used to extract modal parameters of the underlying LTI structure from CSLDV measurements.

In order to validate these algorithms, the harmonic transfer function was used to identify the operational shape of a cantilever beam under sinusoidal excitation. Important issues in modal testing using CSLDV were discussed, including the speckle noise and uncertainty in the reconstructed operational shape. The harmonic transfer function was also used to simultaneously measure the translational and rotational velocities of a small region by scanning a small circle around the point of interest. With the input-output relationship defined by the harmonic transfer function, the circular-scan can be easily combined with the conventional point-by-point scanning LDV, acquiring 3-D velocities at each point in a measurement grid in the same amount of time that is required for obtaining only the translational velocity. The harmonic power spectrum and lifting approach were used to extract the first few modes of a parked wind turbine measured with CSLDV. Simulations on a free-free beam indicated that these two output-only algorithms provided equivalent results, but the identification using the lifting approach was far simpler. Then, the harmonic power spectrum was used to study the dynamics of an operating turbine instrumented with accelerometers. A periodic mode in the edgewise direction was captured, which proves the applicability of the proposed modal identification algorithms in the analysis of general LTP systems.

Acknowledgements

I am highly indebted to my advisor Dr. Matt S. Allen for his invaluable advice and encouragement during my PhD study. I learned a great deal from him as his student; not only his attitudes towards science but also his great personality. He sets a great example for me to work and communicate with my students for when I pursue a career in academia.

I am also grateful for the help from my colleagues along the way: Dr. Mike Sracic, Dr. Sonny Nimityongskul, Robert Kuether, Brandon Deaner, and David Ehrhardt. They helped me adapt to the life and study in a different country than where I grew up. I was lucky enough to work in an office where I could meet so many bright and fun colleagues.

Finally, thanks to my family for their support throughout my study. Thanks to my wife for her sacrifices to our little family and the baby. This dissertation is also dedicated to my grandfather. He raised me and taught me to read and write with the hope that I wouldn't have to work on the farm my family has lived on for generations. Now I have accomplished his will. Being at the other side of the planet, I couldn't travel to his funeral but he will be always with me.

Abbreviations and Nomenclature

Abbreviations

AMI	Algorithm of Modal Isolation
CSLDV	Continuous-scan Laser Doppler Vibrometry
DOF	Degree-of-freedom
FFT	Fast Fourier Transform
LTI	Linear Time Invariant
LTP	Linear Time Periodic

Nomenclature

a, b, c	scalar constants
d	displacement vector
f	nonlinear equation of motion function
h	nonlinear output equation of motion function
i, j, k, l, m	scalar integers
n, p, q, r, s	scalar integers
q	modal participation factor
t	time variable
$u(t)$	input vector
$u_0(t)$	initial input vector
$x(t)$	state vector
$x_0(t)$	initial state vector
$y(t)$	output vector

y_i	i^{th} sample in periodic response
x, y, z	directions in space
$\mathbf{A}_{r,l}$	residue matrix
$A(t)$	system matrix
$B(t)$	control or input matrix
$C(t)$	output matrix
C_d	damping matrix
$D(t)$	direct input matrix
\mathbf{D}	diagonal matrix of Fourier coefficients of input matrix
\mathbf{E}_r	constant matrix
$F(t)$	external force
$\mathbf{G}(\omega)$	harmonic transfer function
$H(\omega)$	transfer function
I	identity matrix
$K(t)$	stiffness matrix
L	constant matrix in Floquet theory
L_r	r^{th} row vector of the inverse of the diagonalizer
$M(t)$	mass matrix
N	constant integer
N_A	number of point per period
N_c	number of period
$P(t)$	diagonalizer of the system matrix A

Q	constant matrix in Floquet theory
R	matrix to diagonalize L matrix in Floquet theory; radius of circle
$R[n]$	harmonic correlation function
S_n	amplitude of n^{th} Fourier coefficient
$S_{\mathbf{Y}\mathbf{Y}}(\omega)$	power spectrum of modulated output
$S_{\mathbf{Y}\mathbf{Y}}(\omega)$	power spectrum of output
$S_{\mathbf{U}\mathbf{U}}(\omega)$	power spectrum of modulated input
$S_{\mathbf{U}\mathbf{U}}(\omega)$	power spectrum of input
T	transformation matrix from Fourier coefficients to polynomial coefficients
T_A	fundamental period
T_s	sampling period
$\mathbf{U}(\omega)$	exponentially modulated periodic input
$U_n(\omega)$	spectrum of a specific modulated input
$V(t)$	acquire velocity using laser Doppler vibrometer
V_n	amplitude of n^{th} order polynomial
V_z	velocity along laser direction
$\mathbf{W}(\omega)$	power spectrum of the net force
$X(t)$	fundamental matrix of state space model
\mathbf{X}_r	matrix of Fourier coefficient vector
$\mathbf{Y}(\omega)$	exponentially modulated periodic output
$Y_n(\omega)$	spectrum of a specific modulated output
$Y(\omega)$	output spectrum of time invariant system
Z	vibration amplitude along laser direction

\tilde{u}	perturbation input vector
$\tilde{x}(t)$	perturbation state vector
y_m^L	m^{th} sample of the lifted output vector
$\bar{\mathbf{B}}_{r,n}$	left mode vector of periodic system
$\bar{B}_{r,n}$	n^{th} Fourier coefficient in the left mode vector
$\bar{\mathbf{C}}_{r,n}$	right mode vector of periodic system
$\bar{C}_{r,n}$	n^{th} Fourier coefficient in the right mode vector
$\hat{\mathbf{C}}(t)$	second half of output matrix
$H_{\text{YY}}^+(\omega)$	positive harmonic power spectrum
$\bar{P}(t)$	periodic matrix
$R^+[n]$	harmonic correlation function
$R_m^+[k]$	lifted harmonic correlation function at m th point in a period
$\{S\}$	vector of Fourier coefficient
$\{V\}$	vector of polynomial coefficient
\mathbf{Res}_r	residue of lifted spectra
α_n	phase angle of n^{th} order polynomial
β	mirror phase lag
γ	phase angle
λ_r	r^{th} eigenvalues

ζ_r	rth damping ratio
ψ_r	r^{th} left eigenvalues
ϕ_r	mode vector
τ	constant time variable
ω	circular frequency variable
ω_A	periodic orbit frequency
ω_r	r^{th} natural frequency
Λ	diagonal matrix of (Floquet) eigenvalues
$\hat{\Lambda}$	diagonal matrix of (Floquet) eigenvalues
$\Phi(t, t_0)$	state transition matrix
$\Psi(t)$	matrix of eigenvectors
Θ_A	amplitude of rotation in along the principle axis
Θ_B	amplitude of rotation in along the principle axis

Contents

Abstract.....	i
Acknowledgements	iii
Abbreviations and Nomenclature.....	iv
Contents	ix
1 Introduction.....	1
1.1 Review of System Theory	1
1.2 Review of Linear Time Periodic System Identification	3
1.3 Continuous-scan Laser Doppler Vibrometer	6
1.4 Modal Testing with Continuous-Scan Laser Doppler Vibrometry	9
1.4.1 Polynomial Approach.....	10
1.4.2 Lifting Approach	12
1.5 Linear Time Periodic Model of CSLDV	13
1.6 Summary of the Dissertation	16
2 Linear Time Periodic System Theory	20
2.1 Introduction	20
2.2 Floquet Theory	22
2.3 Harmonic Transfer Function	24
2.4 Harmonic Power Spectrum.....	29
2.5 Positive Harmonic Power Spectrum.....	32
2.6 Lifting the Positive Harmonic Correlation Function.....	34
2.7 Post Processing.....	36
2.7.1 Singular Value Decomposition	37

2.7.2	Weighted Average Method	38
2.8	Summary of Output-only Identification Algorithms	38
2.9	Summary.....	42
3	Experimental Modal Analysis using the Harmonic Transfer Function	45
3.1	Introduction	45
3.2	Experimental Setup.....	47
3.3	Speckle Noise in CSLDV	49
3.4	Experimental Results.....	52
3.4.1	Point-by-point Scanning LDV	52
3.4.2	Continuous-scan Laser Doppler Vibrometry	53
3.5	Uncertainty in Reconstructed Operational Shape.....	60
3.6	Summary.....	64
4	Measuring Translational and Rotational Velocities using CSLDV	66
4.1	Introduction	66
4.2	Measuring Rotational Velocities using CSLDV	68
4.3	Speckle Noise in Circular-scan.....	72
4.4	Deflection Mode Shapes.....	80
4.5	Rotational Velocity and Local Slope.....	83
4.6	Summary.....	90
5	Output-only Modal Analysis using CSLDV	92
5.1	Introduction	92
5.2	CSLDV Measurements from a Free-free Beam	93
5.3	Effect of Scan Frequency	103

5.4	Application to Wind Turbine.....	108
5.5	Summary.....	114
6	Lifting Approach on Output-only Modal Analysis.....	116
6.1	Introduction	116
6.2	Comparison of Output-only Algorithms on a Simulated Beam	117
6.3	Application to Wind Turbine using Remote Sensing Vibrometer	124
6.4	Summary.....	133
7	Output-only Modal Analysis of Rotating Wind Turbine using Harmonic Power Spectrum.....	135
7.1	Introduction	135
7.2	Experimental Setup.....	137
7.3	Output-only Modal Analysis of Parked Turbine	140
7.4	Output-only Modal Analysis of Operational Turbine	145
7.4.1	Analysis of a Single Point	145
7.4.2	Discussion	151
7.4.3	Analysis of Multiple Blades.....	153
7.5	Summary.....	157
8	Conclusion	159
9	Future work.....	163
	References.....	165
	Appendix 1: List of Publications	171
	Appendix 2: Matlab Examples – A Simulated Free-free Beam.....	172

1 Introduction

This chapter reviews previous efforts on linear time periodic system identification prior to the dissertation. Then, continuous-scan laser Doppler vibrometry and existing signal processing techniques are introduced. Finally, this chapter summarizes the key contributions of the dissertation.

1.1 Review of System Theory

Most physical structures are time varying and nonlinear. The dynamics of these structures may be described with a first order differential equation,

$$\dot{x}(t) = f(x(t), u(t), t) \quad (1)$$

where $x(t)$ is the internal state and $u(t)$ is the input force. f is a differentiable function that describes the internal state's time rate of change, $\dot{x}(t)$. Often in practice, only some or a combination of the states $x(t)$ is measured, and the output $y(t)$ is,

$$y(t) = h(x(t), u(t), t) \quad (2)$$

The function h is also differentiable.

The behavior of a nonlinear system can be extremely complicated, yet some nonlinear systems can be linearized in small regions near equilibria [1]. For example, let $(x_0(t), u_0(t))$ be an equilibrium of the system, and let $(\tilde{x}(t), \tilde{u}(t))$ be small deviations from the equilibrium (i.e., $\tilde{x}(t) = x(t) - x_0(t)$ and $\tilde{u}(t) = u(t) - u_0(t)$), Eq. (1) and Eq. (2) can be approximated with Taylor series expansions about the equilibrium. After truncating to only the linear terms (first order partial derivative), the differential equations become,

$$\begin{aligned}
\dot{\tilde{x}}(t) &= \left[\partial \mathbf{f}_i / \partial x_j \right] \Big|_{(x_0(t), u_0(t))} \tilde{x}(t) + \left[\partial \mathbf{f}_i / \partial u_j \right] \Big|_{(x_0(t), u_0(t))} \tilde{u}(t) \\
y(t) &= \left[\partial \mathbf{h}_i / \partial x_j \right] \Big|_{(x_0(t), u_0(t))} \tilde{x}(t) + \left[\partial \mathbf{h}_i / \partial u_j \right] \Big|_{(x_0(t), u_0(t))} \tilde{u}(t)
\end{aligned} \tag{3}$$

$\left[\partial \mathbf{f}_i / \partial x_j \right] \Big|_{(x_0(t), u_0(t))}$ means that the component in the i^{th} -row and j^{th} -column of this matrix is the first partial derivative of the i^{th} component of \mathbf{f} with respect to the j^{th} component of $x(t)$, evaluated at the equilibrium $(x_0(t), u_0(t))$. Eq. (3) is the linear state space model that describes the local properties of the original nonlinear system in a small region near the equilibrium.

Perhaps the most general form of the linear state space model is defined as,

$$\begin{aligned}
\dot{x}(t) &= A(t)x(t) + B(t)u(t) \\
y(t) &= C(t)x(t) + D(t)u(t)
\end{aligned} \tag{4}$$

where $A(t)$ is the system matrix, $B(t)$ is the control matrix, $C(t)$ is the output matrix, and $D(t)$ is the direct input matrix. All of these matrices vary with time for a general linear time varying system. For example, the full analytical model of a wind turbine is time varying when accounting for large deformations, orientation of rotors in a gravitational field, etc.

The most commonly used case of linear system theory is the Linear Time Invariant (LTI) system where the coefficient matrices are constant. A parked wind turbine with small deformation is usually modeled as an LTI system. The response is independent of the time the input is applied, and can be easily obtained via a Laplace transformation of Eq. (4) given the known coefficient matrices. When the turbine is rotating (still small deformation), the coefficient matrices are periodic with period T_A (e.g., $A(t+T_A) = A(t)$), the system is called Linear Time Periodic (LTP). The dynamics of an LTP system can be analyzed using Floquet Theory [2-4], which essentially converts the periodic system matrix $A(t)$ to a time invariant matrix via coordinate transformation. Thus the new state space model has the mathematical

form of an LTI system, and can be studied using the well-established LTI techniques. The periodic response can be obtained by converting the solution of the new LTI model to the original coordinates.

1.2 Review of Linear Time Periodic System Identification

Finite element analysis is extensively used in the modeling of linear and nonlinear structures. The method can correctly represent the dynamics of most simple structures, but may not be sufficiently accurate for complex structures with many sub-components due to the modeling errors in the interfacial contacts and in approximating complicated geometry, etc. On the other hand, large structures such as wind turbines have to be carefully designed because different resonances may occur and break the structure. Hence, accurate and valid numerical models are necessary in the design process. System identification builds the dynamical models of structures from experimental data, providing direct links between real life systems and their computational models. Therefore, system identification has always been an essential part of model updating, structure health monitoring, damage detection, and many other applications.

Numerous algorithms have been developed for the parameter identification of LTI systems, for example, the Ibrahim time domain method [5], stochastic subspace identification [6] and eigensystem realization algorithm [7]. Many of these algorithms may be described by a polynomial model, whose response is represented with polynomials of either a complex augment s (Laplace transform) or z (z -transform) [8]. An in-depth review of existing identification algorithms for LTI systems in both the time and frequency domains can be found in [9].

However, many systems have to be modeled as linear time periodic to better characterize their time varying behavior, e.g., rotorcraft [10] and wind turbines [11-14]. In addition, a wide

class of nonlinear systems can be linearized along a periodic orbit as linear time periodic systems, e.g., human gait systems [15-18]. Figure 1 illustrates the difference between an LTI system and an LTP system in the response to a single frequency input. The response of an LTI system is at the same input frequency but with a different amplitude and phase. In contrast, the response of an LTP system is more complicated; it can contain the same input frequency component as well as its infinite number of harmonics separated by the fundamental frequency ω_A (i.e., $\omega_A = 2\pi / T$), each having a different amplitude and phase. As a result, conventional modal identification routines developed for LTI systems cannot be directly applied to the identification of LTP systems.

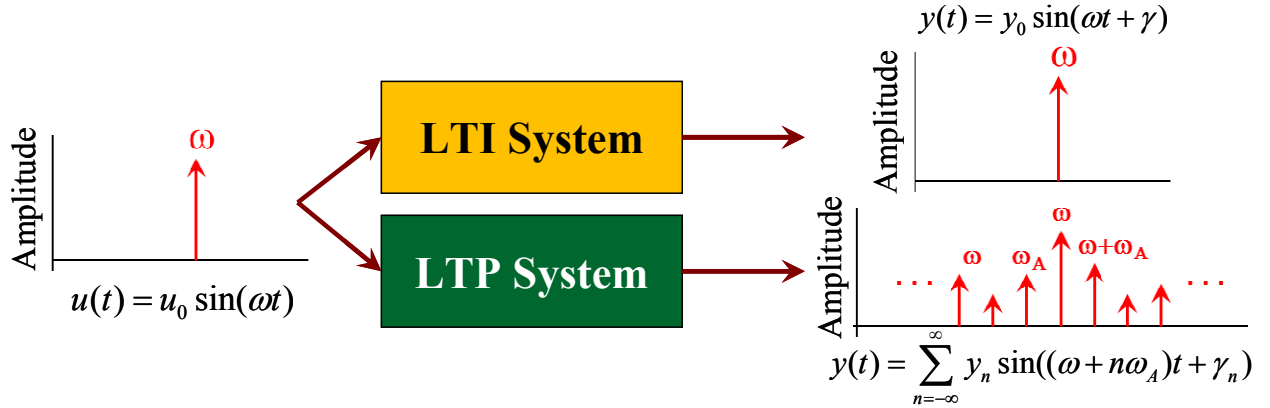


Figure 1 System response to a single frequency input

So far, the research on identification of LTP systems is still rather limited. Several time domain algorithms have been developed with the primary concerns on control and stability analysis [19-22]. The subspace identification methods [19, 21, 23] rely on the realization of a periodic state space model, whose system matrices are decomposed from the overdetermined Hankel matrices of system input and output. The linear fractional transformation method [24] treats an LTP system as an LTI system with additional time periodic feedback. The system matrices are then obtained by minimizing the output error using optimization techniques such as

least squares. However, both of the algorithms are computationally expensive and are only capable of studying simplified models with a few degrees of freedom. Sinha et al. [25] proposed a Lyapunov-Floquet transformation that eliminates the periodic terms in the system equation using Floquet eigenvectors as the basis. Hansen et al. [14, 26] used the Lyapunov-Floquet transformation to analyze the dynamics of operating wind turbines with isotropic and anisotropic rotors. Unfortunately, so far the Lyapunov-Floquet transformation is only an analytical tool for simulated models and cannot be applied to the experimental identification of general LTP systems.

Time domain methods are sensitive to noise because averaging of multiple tests is not applicable. This dissertation focuses on the frequency domain methods. Allen recently suggested two frequency domain approaches based on Floquet Theory [2], namely, the Fourier series expansion method and the lifting approach [27]. In the Fourier series expansion method, the state transition matrix is expressed in the form of a Fourier series, of which the coefficients are obtained from the harmonics belonging to each mode in the output. The other approach applies a lifting transformation that essentially resamples the full periodic response signal. Then the responses at the same time instant in each period of the periodic response are grouped together to create a larger set of signals. The key contribution of both methods is that the resulting mathematical form of the measured signal is equivalent to that for an LTI system. Consequently, any standard parameter extraction technique for LTI systems can be used to identify a model of the LTP system. Unfortunately, these two approaches apply only to the free response of an LTP system.

Most system identification methods for LTI systems make use of transfer function estimation. Wereley et al. extended the concept of a transfer function to LTP systems [28, 29].

They introduced the exponentially modulated periodic signal that consists of an infinite number of harmonics, each separated by the fundamental frequency of the LTP system. Revisiting Figure 1, a single frequency input at ω to an LTP system causes an output at a cluster of frequencies $\omega \pm n\omega_A$, and an input at 2ω also produces an output at the same comb (although the center frequency is different). Therefore, an exponentially modulated periodic input at $\omega \pm n\omega_A$ to the LTP system will cause a modulated output at the same frequency comb but with each harmonic having a different magnitude and phase. Thus a harmonic transfer function that is completely analogous to the frequency response function of LTI systems can be established. Hwang et. al used this harmonic transfer function to identify system parameters of a simulated helicopter rotor under controlled input [30, 31] in order to study the control of individual blades. Their efforts build the foundation of this work. In the dissertation, LTP identification theory is extended to the modal analysis of real life structures under either controlled or unmeasured random input. The proposed algorithms are combined with a novel Continuous-scan Laser Doppler Vibrometry (CSLDV) technique to acquire modal parameters of a structure tens or even hundreds of times faster than conventional modal testing techniques.

1.3 Continuous-scan Laser Doppler Vibrometer

A Laser Doppler Vibrometer (LDV) is a non-contact sensor that detects Doppler frequency shift in a beam of laser light and converts it to the velocity component of a target along the direction of the incident laser [32]. The LDV provides the same precision as traditional transducers such as accelerometers, but its non-contact nature offers significant advantages when measuring targets that are difficult to access (e.g., wind turbine blades high on the tower [33]), challenging to attach a physical transducer to (e.g., liquid flow [34]), or sensitive

to mass loading (e.g., MEMS devices [35]). The primary source of uncertainty in LDV measurements is the laser speckle noise, which has been studied extensively in the past 30 years [36-39]. Laser speckle is formed as coherent laser light scatters from a rough surface, which causes the backscattered laser to have randomly distributed intensity and phase. A portion of the backscattered laser is collected and interfered at the photo detector to obtain the surface velocity along the direction of the incident laser. The speckle noise level is affected by many factors, including surface roughness, standoff distance, and incident angle. A comprehensive study on laser speckle noise can be found in [40].

In scanning Laser Doppler Vibrometry, the laser is redirected by a pair of orthogonal mirrors from one point to another to measure the responses at these points. This is more efficient than physically moving the vibrometer, though additional artifacts may be introduced due to the mirror configuration [41]. Continuous-scan laser Doppler vibrometry is a technique built on scanning LDV; the hardware is essentially the same except that the mirrors are driven with time varying signals (e.g., sinusoidal), so the laser spot sweeps continuously over the target while recording the responses along the laser path. This approach can greatly accelerate modal testing, providing spatially detailed dynamic information about a structure at tens or even hundreds of points in the time that is required to measure a single point using scanning LDV.

Two continuous-scan mechanisms were built in this dissertation, both using a Polytec[®] PSV-400 scanning vibrometer unless otherwise specified. The first continuous-scan system uses the internal mirrors in the PSV-400 by connecting them to a function generator. The data acquisition is performed using the Polytec software. The laser speckle noise of this continuous-scan mechanism is relatively low because the internal mirrors are well configured. However, the internal mirrors are designed for point-by-point scan, so their performance under continuous-

scan were not known. In addition, they could be extremely expensive to repair if broken. As an alternative, an external mirror system was designed for the cases where higher scan frequencies and longer testing durations are necessary. The external mirror system consists of two galvanometer scanners each under closed-loop control; each scanner has a position detector that measures the instantaneous rotational angle, allowing precise and accurate control of the laser position. These position signals are recorded to determine the laser path, whereas only the mirror driving signals are available from the internal mirror system. Naturally, since a galvanometer scanner is a mechanical system, there are limits on how fast the mirror can be moved to different angles. The maximum scan frequency ever tried with this external mirror system was 300Hz. Beyond this frequency the nonlinearity between the input voltage and the output mirror angle prevails, and the accuracy of CSLDV measurements may be affected.

The continuous-scan system with internal mirrors is essentially the same as the original PSV-400 system except with an additional function generator that controls the mirrors (one can even use the built-in function generator in the PSV-400). The continuous-scan system using external mirrors is shown in Figure 2, where the CSLDV was employed to measure the vibration of a three-bladed fan by scanning a cloverleaf pattern over the blades [42]. The control and data acquisition system was built using National Instrument PXI, which is modular and configurable with a range of boards; an NI-PXI-6733 board and a BNC-2120 connector were used to drive the external mirror system; an NI-PXI-4472 data acquisition board with 8 analog input channels was used to record the measured signals. A LabVIEW program was developed to integrate the features including the function generator, data acquisition, and signal processing. The program is also capable of performing CSLDV when the fan is rotating, tracking and scanning the blades simultaneously, using the signal from an encoder mounted on the motor [42].

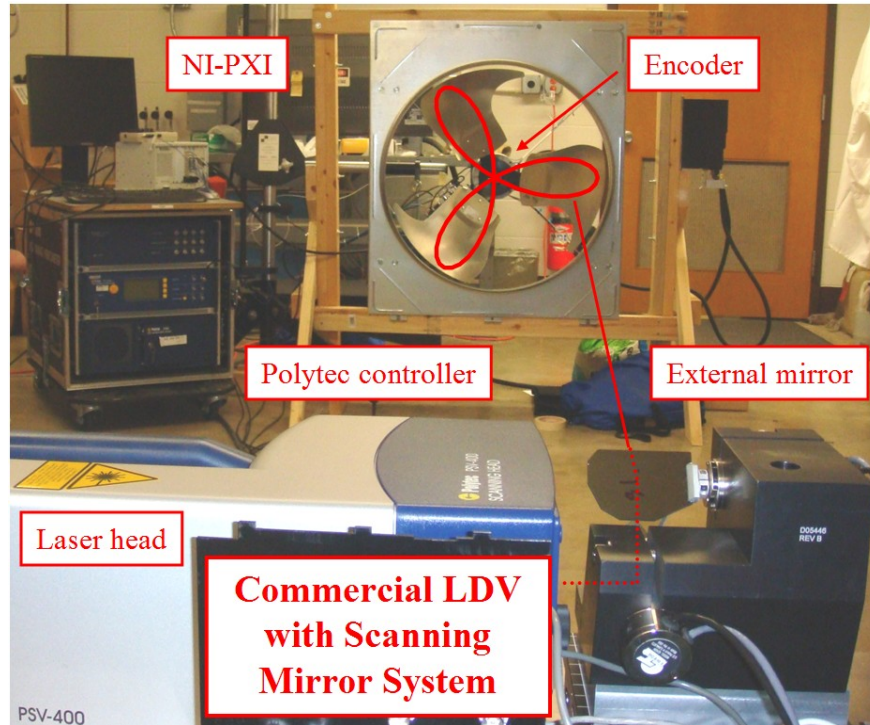


Figure 2 Photograph of the CSLDV system with external mirror system

1.4 Modal Testing with Continuous-Scan Laser Doppler Vibrometry

CSLDV is capable of acquiring greatly increased spatial dynamic information of a structure within limited testing time, which could lead to insights into the dynamics of the structure that may be helpful in force reconstruction, structural health monitoring, and model correlation and updating. However, processing measurements from CSLDV is more challenging than processing measurements from conventional transducers because the measuring laser is continuously moving. Various algorithms have been devised to determine the mode shapes along the laser scan path. Sriram et al. appear to have been the first to publish regarding CSLDV in the early 1990's [43, 44], but most of the advancements in this area proceeded from the research group at Imperial College in London (Stanbridge, Ewins, Martarelli and Di Maio) during the following decade. They coined the name "CSLDV" and developed a polynomial

approach that extracts 1-D and 2-D operating deflection shapes from CSLDV measurements under sinusoidal excitation[45], impact excitation [46, 47], and periodic random excitation [48]. Other notable contributions include the work by Vanlanduit et al. [49, 50], who presented a CSLDV method that uses multi-sine (periodic broadband) excitation.

1.4.1 Polynomial Approach

The idea behind the polynomial approach is rather straightforward. The response along the laser path can be approximated with a polynomial function of the laser position x . Since the response of an LTI structure to a sinusoidal excitation will be at the same frequency but with a different amplitude and phase, the acquired velocity at any time instant can be expressed as,

$$V(t) = \sum_{n=0}^{\infty} V_n x^n \cos(\omega t + \alpha_n) \quad (5)$$

Here ω is the excitation frequency applied to the structure. V_n is the amplitude of the n^{th} order polynomial, and α_n is the phase. It is convenient to assume the laser scans a line pattern $x = \cos(\omega_A t + \beta)$, where ω_A is the laser scan frequency and β is the initial mirror phase angle. Substituting the laser position x into the measured velocity in Eq. (5), and simplifying the expression using trigonometric functions, one obtains,

$$\begin{aligned} V(t) &= \sum_{n=0}^{\infty} V_n \cos^n(\omega_A t + \beta) \cos(\omega t + \alpha_n) \\ &= \sum_{n=-\infty}^{\infty} S_n \cos((\omega + n\omega_A)t + \alpha_n + n\beta) \end{aligned} \quad (6)$$

Hence, the acquired velocity signal from CSLDV contains the frequency components at the excitation frequency ω and also its infinite number of harmonics $\omega + n\omega_A$. The amplitudes and phases at these frequencies can be easily extracted using the frequency response analysis

[51]. The polynomial coefficient V_n can then be obtained via a linear transformation from the Fourier coefficient S_n , $\{V\} = [T]\{S\}$, where $\{S\}$ is the one-sided Fourier coefficient vector that contains the absolute value of S_n for $n = 0 \dots \infty$. The sign of the n^{th} element in $\{S\}$ is determined by the phase angle of S_n . Note that one must include a correction of the mirror initial angle $n\beta$ (see Eq. (5)). Ewins et al. showed in [47] that the transformation matrix T for a 10^{th} order polynomial can be expressed as,

$$T = \begin{bmatrix} 1 & 0 & -2 & 0 & 2 & 0 & -2 & 0 & 2 & 0 & -2 \\ 0 & 2 & 0 & -6 & 0 & 10 & 0 & -14 & 0 & 18 & 0 \\ 0 & 0 & 4 & 0 & -16 & 0 & 36 & 0 & -64 & 0 & 100 \\ 0 & 0 & 0 & 8 & 0 & -40 & 0 & 112 & 0 & -240 & 0 \\ 0 & 0 & 0 & 0 & 16 & 0 & -96 & 0 & 320 & 0 & 800 \\ 0 & 0 & 0 & 0 & 0 & 32 & 0 & -224 & 0 & 864 & 0 \\ 0 & 0 & 0 & 0 & 0 & 0 & 64 & 0 & -512 & 0 & 2240 \\ 0 & 0 & 0 & 0 & 0 & 0 & 0 & 128 & 0 & -1152 & 0 \\ 0 & 0 & 0 & 0 & 0 & 0 & 0 & 0 & 256 & 0 & -2560 \\ 0 & 0 & 0 & 0 & 0 & 0 & 0 & 0 & 0 & 512 & 0 \\ 0 & 0 & 0 & 0 & 0 & 0 & 0 & 0 & 0 & 0 & 1024 \end{bmatrix} \quad (7)$$

After the polynomial coefficients are obtained, the operational mode along the laser path can be reconstructed using Eq. (5). Other scan patterns, such as the Lissajous curve or uniform-rate rectangular pattern, are discussed in detail in [46].

The polynomial approach is intuitive and easy to apply. One can even obtain spatial derivatives of the operational shape with respect to the laser path, e.g., the slope and curvature of the operational shape, directly from the polynomial coefficients. However, the transformation from the Fourier coefficients S_n to the polynomial coefficients V_n may amplify the noise in the Fourier coefficients because of the large numbers in the T matrix. In addition, this approach was initially designed to detect the operational deflection shapes, therefore special treatment is necessary if the mass-normalized mode shapes are of interest [52].

1.4.2 Lifting Approach

Allen et al. explored the use of high scan frequencies together with impact excitation in CSLDV. The lifting approach allows conventional modal analysis routines in the analysis of CSLDV measurements [53]. This method was later extended to obtain mass-normalized real and complex mode shapes of a free-free beam under impact excitation [54].

The lifting approach was initially devised to identify modal parameters of LTP systems [27]. When the fundamental period of a periodic response is known, one can perform an analysis based on the lifting. The periodic response is resampled to generate an integer number of samples per cycle, which are grouped into a larger set of signals. Assuming a periodic system of period T_A is being sampled with a step size of T_s , the response will be sampled N_A times per period (i.e. $N_A = T_A / T_s$). Let y_m denote the m^{th} sample in each period, the responses at the m^{th} sample in N_c periods could be grouped together to create a response vector y_m^L ,

$$y_m^L = [y_m, y_{m+N_A}, \dots, y_{m+N_c N_A}]^T \quad (8)$$

Here $m = 1 \dots N_A$. So, there is a constant time delay mT_s between the lifted response vector y_1^L at the first sample and the response vector y_m^L at the m^{th} sample in each period. Eq. (8) also shows clearly how subsequent responses in y_m^L are spaced by a time increment equal to the system period T_A . Therefore, it is important to realize that the lifting procedure changes the effective bandwidth of the lifted response to $(0, \omega_A/2)$ due to the sampling theorem, which aliases a mode that occurs at any frequency higher than $\omega_A/2$. For example, let ω_r be the frequency of a mode, if ω_r is greater than $\omega_A/2$, then this frequency will be aliased according to the following equation [55],

$$\omega_r^{\text{aliased}} = |\omega_r - n\omega_A| \quad (9)$$

Here n is an integer that makes the aliased frequency $\omega_r^{\text{aliased}}$ smaller than $\omega_A/2$.

The effect of aliasing is significant. The free response of an LTP system contains a linear superposition of all modes contributing to the response, and these modes may overlap with each other after being aliased. Fortunately, one often has control over the frequency of the periodic system (e.g., the scan frequency of CSLDV) so the aliasing can be avoided by choosing a frequency ω_A such that the effective bandwidth $\omega_A/2$ is sufficiently high. The advantage of the lifting approach is that all sideband harmonics in a periodic response will be collapsed into a single frequency line below $\omega_A/2$, so there is only one peak for each mode after lifting. The lifted response is directly analogous to the free response of a linear time invariant system, and one can use standard LTI routines to identify a parametric model for the LTP system.

All of the above CSLDV algorithms are valid only for the case where the input is either zero (free response), or it follows a specific form and is carefully controlled (e.g., sinusoidal). In practice one cannot always apply an input in one of these forms, but unmeasured random input forces may be present. For example, wind turbines are difficult to adequately excite due to their large size and mass, yet the wind provides a convenient broadband source of ambient excitation. This dissertation combines the proposed frequency domain identification algorithms for LTP systems with CSLDV, extracting modal parameters of LTI structures under any type of input.

1.5 Linear Time Periodic Model of CSLDV

An N degree of freedom (DOF) linear time invariant structure has the equation of motion as,

$$M\ddot{d} + C_d\dot{d} + Kd = F(t) \quad (10)$$

Here M is the mass matrix, C_d is the damping matrix and K is the stiffness matrix; they are all constant. $F(t)$ is the input force. If the system is underdamped, the eigenvalues λ_r and their corresponding mode vectors φ_r can be obtained by solving the eigenvalue problem $(\lambda_r^2 M + \lambda_r C_d + K)\varphi_r = 0$. The mode shape matrix $\Psi = [\varphi_1 \cdots \varphi_N]$ contains N linearly independent mode vectors in its columns. $\hat{\Lambda}$ is a diagonal matrix of the eigenvalues, $\lambda_r = -\zeta_r \omega_r + j\omega_r \sqrt{1 - \zeta_r^2}$, in terms of the r^{th} natural frequency ω_r and damping ratio ζ_r of the structure described in Eq. (10)

The classic equation of motion can be modeled using state space model by defining the internal state $x = \{d, \dot{d}\}^T [1]$,

$$\begin{aligned} \dot{x} &= Ax + Bu \\ y &= Cx + Du \end{aligned} \quad (11)$$

A is the $2N \times 2N$ system matrix of the state space model, B is the input matrix, and u is the input applied to each DOF, each defined as

$$A = \begin{bmatrix} \mathbf{0} & \mathbf{I} \\ -M^{-1}K & -M^{-1}C_d \end{bmatrix}, \quad B = \begin{bmatrix} \mathbf{0} & \mathbf{0} \\ \mathbf{0} & M^{-1} \end{bmatrix}, \quad u = \begin{Bmatrix} \mathbf{0} \\ F(t) \end{Bmatrix} \quad (12)$$

When a laser Doppler vibrometer is employed to measure this N -DOF time invariant system, the laser can be thought of as sweeping through these DOFs sequentially. The output matrix C can be taken as a row vector of zeros with a one entry at the location where the laser is measuring. For example, if the laser is being pointed at the k^{th} DOF, then,

$$C[k] = \left[\underbrace{0 \ \cdots \ 0}_N \middle| \underbrace{0 \ \cdots \ 0 \ \overset{k}{1} \ 0 \ 0 \ \cdots \ 0}_N \right]_{1 \times 2N} \quad (13)$$

Assuming the laser scans on a real structure along a closed periodic pattern, e.g., a line or circular path, at frequency ω_A , the output matrix becomes periodic, $C(t) = C(t + T_A)$, where $T_A = 2\pi / \omega_A$ is called the fundamental period. The direct input matrix D equals zero because the laser only picks up velocity.

One can diagonalize the state space model in Eq. (11) by defining $x = Pq$, where P is the diagonalizer or the eigenvector matrix of the state matrix A ,

$$P = \begin{bmatrix} \Psi & \Psi^* \\ \Psi \hat{\Lambda} & \Psi^* \hat{\Lambda}^* \end{bmatrix} \quad (14)$$

and q is the modal participation vector. Ψ and $\hat{\Lambda}$ are the eigenvectors and eigenvalues obtained from the classic equation of motion in Eq. (10). The notation $()^*$ represents the complex conjugate.

Substituting $x = Pq$ into Eq. (17) and pre-multiplying the first equation by P^{-1} , noting that D equals zero, the following uncoupled equations are obtained,

$$\begin{aligned} \dot{q} &= \Lambda q + P^{-1} B u \\ y &= C(t) P q \end{aligned} \quad (15)$$

Λ is a complex diagonal matrix of eigenvalues, i.e., $\Lambda = \text{diag}(\hat{\Lambda}, \hat{\Lambda}^*)$. Note that $C(t)$ is periodic because the measurement point is continuously moving, $C(t)P$ is a periodic row vector of complex mode shapes,

$$C(t)P = \left[\hat{C}(t)\varphi_1\lambda_1 \quad \cdots \quad \hat{C}(t)\varphi_N\lambda_N \quad \hat{C}(t)\varphi_1^*\lambda_1^* \quad \cdots \quad \hat{C}(t)\varphi_N^*\lambda_N^* \right] \quad (16)$$

For simplification, here $\hat{C}(t)$ refers to a $1 \times N$ vector comprising the second half of the vector C in Eq. (13) because only the velocity is recorded by the laser.

Eq. (15) in conjunction with Eq. (16) reveals that an LTI structure measured with CSLDV using a periodic scan pattern could be modeled as an LTP system. The r^{th} observed mode shape $\hat{C}(t)\phi_r$ appears to be time periodic only because the position of the measurement point is periodic. Therefore, the proposed linear time periodic system identification algorithms can be applied to CSLDV to extract modal parameters including the natural frequencies, damping ratios and mode shapes of the underlying LTI structure.

1.6 Summary of the Dissertation

This dissertation introduces a complete set of frequency domain linear time periodic system identification algorithms that can be applied to the modal analysis of LTP systems under either controlled or unmeasured random excitation. The proposed algorithms include the harmonic transfer function, the harmonic power spectrum, the positive harmonic power spectrum, and a lifting approach using the positive harmonic correction function. Each of these algorithms has its equivalent concept in the identification of LTI systems, allowing conventional well-established modal analysis routines to be used directly in the parameter estimation of LTP systems. The proposed identification algorithms are combined with the novel continuous-scan laser Doppler vibrometry, which forms an LTP system when measuring the response of an LTI structure with closed periodic scan pattern. In CSLDV, the laser spot sweeps continuously over the structure while measuring, capturing spatially detailed dynamic information in the same amount of time that is required by conventional methods to capture a single point. However, existing signal processing techniques for CSLDV apply only to the cases where the input is

either zero or it follows a specific form. With the proposed LTP system identification algorithms, CSLDV could be used to acquire the natural frequencies, damping ratios and mode shapes of LTI structures under any type of input.

Figure 3 summarizes the framework of this dissertation. The abbreviation under each block indicates the journal and year that the work was (or will be) published.

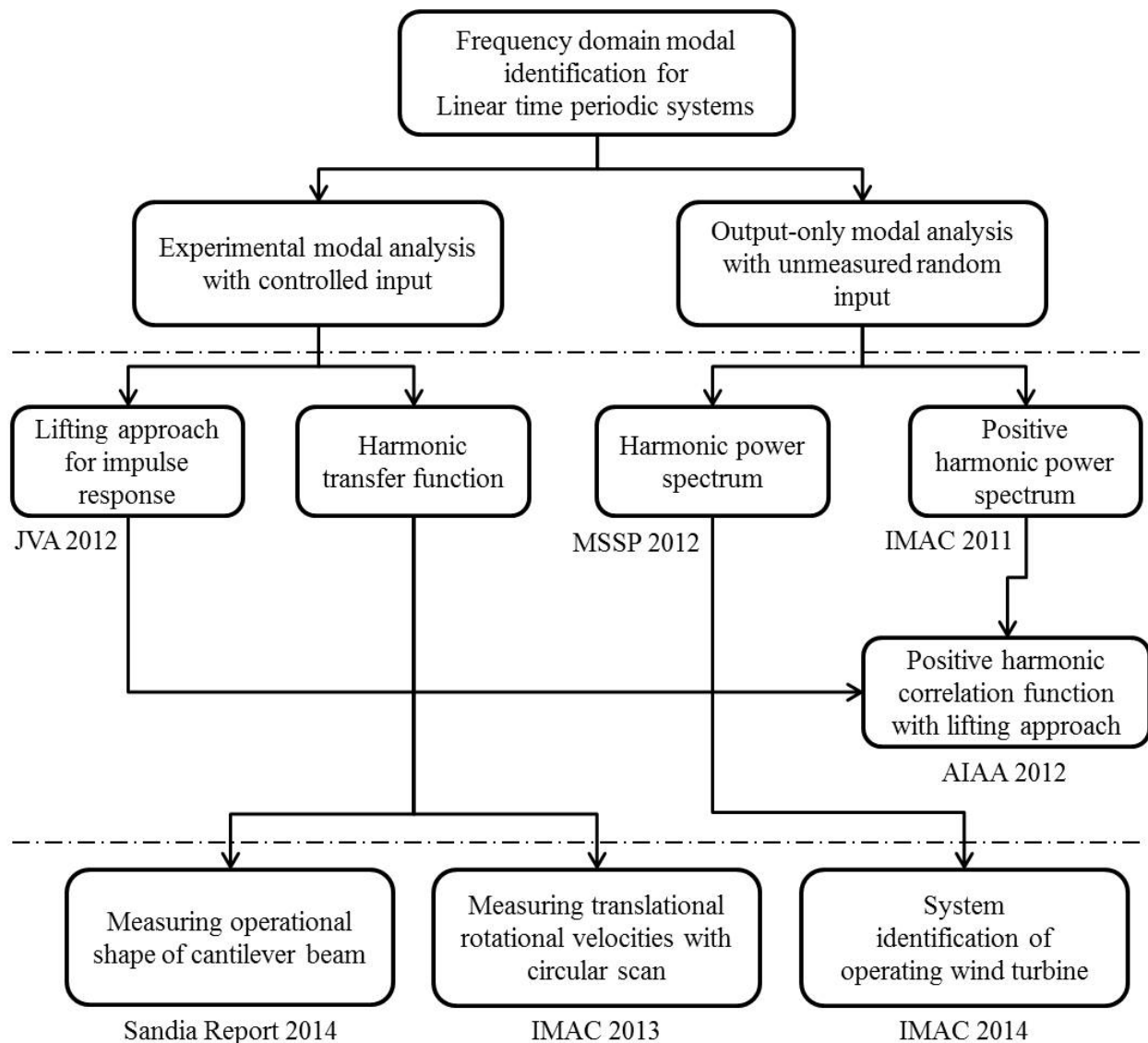


Figure 3 Content of the dissertation

The proposed LTP system identification algorithms are divided into two categories, experimental modal analysis with controlled input (e.g., sinusoidal and swept-sine), and output-only modal analysis where the input is unmeasured but uniformly distributed random noise. In experimental modal analysis, an improvement on the lifting approach was devised to obtain the mass-normalized real and complex mode shapes of a free-free beam under impulse excitation. This work was published in [54] but not included in this dissertation since the nature of the lifting approach is different from the proposed frequency domain algorithms based on the harmonic transfer function. The harmonic transfer function was then combined with CSLDV to measure the operational shape of a cantilever beam under sinusoidal excitation. The acquired mode shape was compared with those from the lifting approach and the polynomial approach, and the uncertainty of the acquired mode shape using the harmonic transfer function was discussed. This work was part of the research conducted for Sandia National laboratory to study the potential of applying CSLDV in force reconstruction. The harmonic transfer function was also used to simultaneously measure the translational and rotational velocities of a downhill ski under free-free boundary conditions with a circular-scan pattern. The speckle noise in circular-scan was discussed and compared with that in the conventional point measurement. The slope of the measured deflection shape was computed from the acquired rotational velocities, building the foundation for deriving a more accurate curvature shape used in damage detection [56].

In output-only modal analysis, the harmonic power spectrum was combined with CSLDV to identify the first few modes of a parked wind turbine. One key consideration, the choice of the scan frequency, was discussed. This work was published in [57]. Though the algorithm using the harmonic power spectrum was effective, the identification procedure was somewhat labor intensive because each mode appears at several harmonics, each having to be fitted to

obtain an accurate estimate of the mode shape. A lifting approach was then combined with the positive harmonic correlation function to simplify the identification. A new long range remote sensing vibrometer from Polytec was tested for the first time [58]. Finally, the harmonic power spectrum was used to identify the periodic mode of an operational wind turbine instrumented with accelerometers on each blade. The wind turbine is a general LTP system. The results were discussed and compared with those one would obtain using other approaches, which showed the great advantage of using the harmonic power spectrum to analyze real LTP systems. This work will be published in [59].

2 Linear Time Periodic System Theory

This chapter establishes the proposed linear time periodic system identification theory, including the harmonic transfer function, the harmonic power spectrum, the positive harmonic power spectrum, and a lifting approach that acts on the positive harmonic correlation function. Signal processing techniques are introduced as well to extract the best estimate of the Fourier coefficient vector.

2.1 Introduction

Revisiting the state space model of a linear time varying system introduced in Section 1.1,

$$\begin{aligned}\dot{x}(t) &= A(t)x(t) + B(t)u(t) \\ y(t) &= C(t)x(t) + D(t)u(t)\end{aligned}\tag{17}$$

$A(t)$ is the system matrix, $B(t)$ is the control matrix, $C(t)$ is the output matrix, and $D(t)$ is direct input matrix. It is convenient to assume that the physical structure described by the state space model in Eq. (17) is a single-input single-output system that has N degrees of freedom. In this case, $A(t)$ is a $2N \times 2N$ matrix, $B(t)$ is a $2N \times 1$ vector, $C(t)$ is a $1 \times 2N$ row vector, and $D(t)$ is a scalar function. All of these matrices vary with time for a general linear time varying system, and a unique solution of the output $y(t)$ exists for any initial state and input pair $(x_0(t), u_0(t))$. Note that the theory developed based on the single-input single-output assumption can be easily extended to a single-input multiple-output or multiple-input multiple-output system, as will be shown in the output-only modal analysis of an operational turbine in Chapter 7.

Suppose the state vectors $x_r(t)$ ($r = 1 \dots 2N$) are $2N$ linearly independent solutions of $\dot{x}(t) = A(t)x(t)$. Then, the state transition matrix $\Phi(t, t_0)$ relates the system state at any time t to the initial state at t_0 by,

$$x(t) = \Phi(t, t_0)x(t_0) \quad (18)$$

$X(t) = [x_1(t) \ x_2(t) \ \dots \ x_{2N}(t)]$ is called the fundamental matrix, which is nonsingular at any instant t because $x_r(t)$ are linearly independent. Then the state transition matrix can be expressed with the fundamental matrix as,

$$\Phi(t, t_0) = X(t)X(t_0)^{-1} \quad (19)$$

According to Eq. (19), it can be shown that the state transition matrix has the following properties,

$$\begin{aligned} 1. & \Phi(t, t) = I \\ 2. & \Phi(t, t_0)^{-1} = \Phi(t_0, t) \\ 3. & \Phi(t, t_0) = \Phi(t, t_1)\Phi(t_1, t_0) \\ 4. & \dot{\Phi}(t, t_0) = A(t)\Phi(t, t_0) \end{aligned} \quad (20)$$

The solution of the internal state $x(t)$ in the state space model is [1],

$$x(t) = \Phi(t, t_0)x(t_0) + \int_{t_0}^t \Phi(t, \tau)B(\tau)u(\tau)d\tau \quad (21)$$

The expression for state transition matrix in Eq. (19) and its properties in Eq. (20) can be used to verify that Eq. (21) is a valid solution of $\dot{x}(t) = A(t)x(t) + B(t)u(t)$. Thus, the general solution for the output $y(t)$ of a linear time varying system can be written in terms of the state transition matrix as,

$$y(t) = C(t)\Phi(t, t_0)x(t_0) + C(t)\int_{t_0}^t \Phi(t, \tau)B(\tau)u(\tau)d\tau + D(t)u(t) \quad (22)$$

More details about how to derive this general solution can be found in [1]. In this dissertation, the general solution in Eq. (22) and Floquet theory are used to derive most of the algorithms that are used to identify linear time periodic systems.

2.2 Floquet Theory

The state transition matrix $\Phi(t, t_0)$ is the key to obtaining the general solution of a linear system. When the system is linear time invariant, i.e., $A(t)$ and other coefficient matrices are constant, the state transition matrix is $e^{A \times (t-t_0)}$, since $d(e^{A \times (t-t_0)})/dt = Ae^{A \times (t-t_0)}$. This form for the state transition matrix can be further decomposed as,

$$\Phi(t, t_0) = e^{A(t-t_0)} = Pe^{\Lambda(t-t_0)}P^{-1} \quad (23)$$

where P is the matrix of eigenvectors of system matrix A , and Λ is a diagonal matrix of eigenvalues. The general solution is then obtained by substituting Eq. (23) into Eq. (22). However, this expression for the state transition matrix is no longer valid when $A(t)$ is time varying because $d(e^{A(t) \times (t-t_0)})/dt \neq Ae^{A(t) \times (t-t_0)}$. In fact, it is usually challenging or even impossible to find a closed form expression for $\Phi(t, t_0)$ unless the system matrix $A(t)$ has a certain form.

When the coefficient matrices in the state space model are time periodic, i.e., $A(t + T_A) = A(t)$, where $T_A = 2\pi / \omega_A$ is the fundamental period, the system is referred to as linear time periodic. The dynamics of a periodic system can be studied using Floquet theory [2-4, 60],

which defines a coordinate change that transforms the LTP system to an LTI system. As a result, Eq. (23) can be used to compute the state transition matrix of the transformed LTI system.

The fundamental matrix $X(t)$ satisfies $\dot{X}(t) = A(t)X(t)$ at any time instant t , and since the system matrix $A(t)$ of an LTP system is periodic, one has

$$\dot{X}(t+T_A) = A(t+T_A)X(t+T_A) = A(t)X(t+T_A) \quad (24)$$

According to the definition, $X(t+T_A)$ is also a fundamental matrix of $A(t)$. Therefore, both $X(t+T_A)$ and $X(t)$ consist of $2N$ linearly independent solutions of $\dot{x}(t) = A(t)x(t)$, and there exists a nonsingular constant $2N \times 2N$ matrix Q that converts $X(t)$ to $X(t+T_A)$, i.e. $X(t+T_A) = X(t)Q$. Furthermore, for any nonsingular matrix Q , there exists a complex matrix L of the same dimension that satisfies $Q = e^{LT_A}$, where T_A is the fundamental period of the LTP system. If the $2N \times 2N$ matrix $\bar{P}(t)$ is defined as,

$$\bar{P}(t) = X(t)e^{-Lt} \quad (25)$$

then $\bar{P}(t)$ is a periodic matrix. Indeed,

$$\begin{aligned} \bar{P}(t+T_A) &= X(t+T_A)e^{-L(t+T_A)} = X(t)Qe^{-LT_A}e^{-Lt} \\ &= X(t)QQ^{-1}e^{-Lt} = X(t)e^{-Lt} = \bar{P}(t) \end{aligned} \quad (26)$$

Thus the state transition matrix in Eq. (19) becomes,

$$\begin{aligned} \Phi(t, t_0) &= X(t)X(t_0)^{-1} = \bar{P}(t)e^{Lt}(\bar{P}(t_0)e^{Lt_0})^{-1} \\ &= \bar{P}(t)e^{L(t-t_0)}\bar{P}(t_0)^{-1} \end{aligned} \quad (27)$$

The eigenvalues of L are called the Floquet exponents [3, 4]. If all Floquet exponents are non-zero and non-repeated, i.e., L is nonsingular, then there exists a nonsingular matrix R that

diagonalizes L with $L = R\Lambda R^{-1}$, where Λ is a $2N \times 2N$ diagonal matrix of the Floquet exponents.

Then, the state transition matrix in Eq. (27) becomes,

$$\begin{aligned}\Phi(t, t_0) &= \bar{P}(t) e^{R\Lambda R^{-1}(t-t_0)} \bar{P}(t_0)^{-1} \\ &= \bar{P}(t) R e^{\Lambda(t-t_0)} R^{-1} \bar{P}(t_0)^{-1} . \\ &= P(t) e^{\Lambda(t-t_0)} P(t_0)^{-1}\end{aligned}\tag{28}$$

where $P(t) = \bar{P}(t)R$ is a $2N \times 2N$ matrix of time periodic eigenvectors for the LTP system ($\bar{P}(t)$ is time periodic). Since Λ is the diagonal matrix of Floquet exponents, the state transition matrix can be further decomposed into the following modal summation form,

$$\Phi(t, t_0) = \sum_{r=1}^{2N} \psi_r(t) L_r(t_0) e^{\lambda_r(t-t_0)}\tag{29}$$

where $\psi_r(t)$ is the r^{th} column of $P(t)$, and $L_r(t)$ is the r^{th} row of $P^{-1}(t)$. λ_r is the r^{th} Floquet exponent that is analogous to the r^{th} eigenvalue of an LTI system. The r^{th} Floquet exponent can be written in terms of the damping ratio ζ_r and natural frequency ω_r as $\lambda_r = -\zeta_r \omega_r + j \omega_r \sqrt{1 - \zeta_r^2}$ for an underdamped mode.

2.3 Harmonic Transfer Function

As explained in Figure 1, when an LTP system is excited by a single frequency input it will respond at the same frequency and possibly at an infinite number of harmonics of that frequency, each separated by the fundamental frequency ω_A . This idea was utilized by Wereley, who then extended the concept of the transfer function for LTI systems to LTP systems by defining the exponentially modulated periodic signal [61]. In the time domain, the exponentially modulated periodic input $u(t)$ and output $y(t)$ are described as,

$$u(t) = \sum_{n=-\infty}^{\infty} U_n e^{j(\omega+n\omega_A)t}, \quad y(t) = \sum_{n=-\infty}^{\infty} Y_n e^{j(\omega+n\omega_A)t} \quad (30)$$

where,

$$U_n = \int u(t) e^{-j(\omega+n\omega_A)t} dt, \quad Y_n = \int y(t) e^{-j(\omega+n\omega_A)t} dt \quad (31)$$

are the n^{th} modulated periodic signals in frequency domain. The equations show how the exponentially modulated periodic signals contain the frequency component at the excitation frequency and also its infinite number of harmonics separated by $n\omega_A$. Therefore, an exponentially modulated input to an LTP system causes an exponentially modulated output at the same collection of frequencies. Using this fact, the harmonic transfer function for LTP systems can be developed, and it is completely analogous to the commonly known transfer function for LTI systems.

The derivation of the harmonic transfer function makes use of the general solution in Eq. (22) and the Floquet theory in Section 2.2. Substituting the expression for the state transition matrix of an LTP system in Eq. (29) into Eq. (22), the general solution $y(t)$ becomes,

$$\begin{aligned} y(t) = & \sum_{r=1}^{2N} C(t) \psi_r(t) e^{\lambda_r t} L_r(t_0) x(t_0) e^{-\lambda_r t_0} \\ & + \sum_{r=1}^{2N} C(t) \psi_r(t) e^{\lambda_r t} \int_{t_0}^t L_r(\tau) B(\tau) u(\tau) e^{-\lambda_r \tau} d\tau + D(t) u(t) \end{aligned} \quad (32)$$

Since $\psi_r(t)$ is the r^{th} time periodic eigenvectors in $P(t)$, it is convenient to represent it with a Fourier series expansion, and similarly for $L_r(t)$. As is often the case in LTI systems, $C(t)$ may simply be a matrix of ones and zeros indicating which of the states are being measured. In any event, the Fourier series representations are,

$$C(t) \psi_r(t) = \sum_{n=-\infty}^{\infty} \bar{C}_{r,n} e^{jn\omega_A t} \quad (33)$$

$$L_r(t)B(t) = \sum_{n=-\infty}^{\infty} \bar{B}_{r,n} e^{jn\omega_A t} \quad (34)$$

where $\bar{C}_{r,n}$ is the n^{th} Fourier coefficient of the r^{th} observed mode $C(t)\psi_r(t)$, and similarly for $L_r(t)B(t)$. The periodic direct input matrix $D(t)$, if not zero, can be approximated with a Fourier series expansion as well,

$$D(t) = \sum_{n=-\infty}^{\infty} \bar{D}_n e^{jn\omega_A t} \quad (35)$$

Submitting the above equations into Eq. (32), the general solution becomes,

$$\begin{aligned} y(t) = & \sum_{r=1}^{2N} \sum_{s=-\infty}^{\infty} \bar{C}_{r,s} e^{(\lambda_r + js\omega_A)t} L_r(t_0) x(t_0) e^{-\lambda_r t_0} \\ & + \sum_{r=1}^{2N} \sum_{s=-\infty}^{\infty} \bar{C}_{r,s} e^{(\lambda_r + js\omega_A)t} \int_{t_0}^t \sum_{m=-\infty}^{\infty} \bar{B}_{r,m} e^{(-\lambda_r + jm\omega_A)\tau} u(\tau) d\tau + \sum_{s=-\infty}^{\infty} \bar{D}_s e^{js\omega_A t} u(t) \end{aligned} \quad (36)$$

The harmonic transfer function can be derived by substituting the exponentially modulated signals in Eq. (30) into Eq. (36),

$$\begin{aligned} \sum_{n=-\infty}^{\infty} Y_n e^{j(\omega + n\omega_A)t} = & \sum_{r=1}^{2N} \sum_{s=-\infty}^{\infty} \bar{C}_{r,s} e^{(\lambda_r + js\omega_A)t} L_r^T(t_0) x(t_0) e^{-\lambda_r t_0} \\ & + \sum_{r=1}^{2N} \sum_{s=-\infty}^{\infty} \bar{C}_{r,s} e^{(\lambda_r + js\omega_A)t} \sum_{m=-\infty}^{\infty} \sum_{n=-\infty}^{\infty} \int_{t_0}^t \bar{B}_{r,m} U_n e^{(j\omega - \lambda_r + j(m+n)\omega_A)\tau} d\tau \\ & + \sum_{n=-\infty}^{\infty} \sum_{s=-\infty}^{\infty} \bar{D}_s U_n e^{j(\omega + (n+s)\omega_A)t} \end{aligned} \quad (37)$$

Similar to the transfer function of an LTI system, only the steady state response is considered in the harmonic transfer function. The initial condition $x(t_0)$ can be chosen appropriately such that the first term in Eq. (37) is cancelled with the constant at t_0 from the integration. After much algebra and organization, Eq. (37) becomes,

$$\begin{aligned}
\sum_{n=-\infty}^{\infty} Y_n e^{j(\omega+n\omega_A)t} &= \sum_{r=1}^{2N} \sum_{n=-\infty}^{\infty} \sum_{s=-\infty}^{\infty} \sum_{m=-\infty}^{\infty} \frac{\bar{C}_{r,s} \bar{B}_{r,m}}{j\omega - \lambda_r + j(m+n)\omega_A} U_n e^{j(\omega+(n+s+m)\omega_A)t} \\
&+ \sum_{n=-\infty}^{\infty} \sum_{s=-\infty}^{\infty} \bar{D}_s U_n e^{j(\omega+(n+s)\omega_A)t}
\end{aligned} \tag{38}$$

The harmonic balance approach can be used to match the terms at the same frequency in the exponent of $e^{(i\omega+in\omega_A)t}$. Assuming $l = m+n$, then Eq. (38) becomes,

$$Y_n = \sum_{r=1}^{2N} \sum_{m=-\infty}^{\infty} \sum_{l=-\infty}^{\infty} \frac{\bar{C}_{r,n-l} \bar{B}_{r,l-m}}{i\omega - (\lambda_r - j l \omega_A)} U_m + \sum_{m=-\infty}^{\infty} \bar{D}_{n-m} U_m, \quad n \in (-\infty, \infty) \tag{39}$$

Defining the exponentially modulated periodic signals in frequency domain as follows,

$$\begin{aligned}
\mathbf{Y}(\omega) &= [\cdots \ Y_{-1}(\omega)^T \ Y_0(\omega)^T \ Y_1(\omega)^T \ \cdots]^T \\
\mathbf{U}(\omega) &= [\cdots \ U_{-1}(\omega)^T \ U_0(\omega)^T \ U_1(\omega)^T \ \cdots]^T
\end{aligned} \tag{40}$$

a harmonic transfer function can then be established in terms of the modal parameters of the state transition matrix,

$$\mathbf{Y}(\omega) = \mathbf{G}(\omega) \mathbf{U}(\omega) \tag{41}$$

where,

$$\begin{aligned}
\mathbf{G}(\omega) &= \sum_{r=1}^{2N} \sum_{l=-\infty}^{\infty} \frac{\bar{\mathbf{C}}_{r,l} \bar{\mathbf{B}}_{r,l}}{i\omega - (\lambda_r - i l \omega_A)} + \mathbf{D} \\
\bar{\mathbf{C}}_{r,l} &= [\cdots \ \bar{C}_{r,-1-l} \ \bar{C}_{r,-l} \ \bar{C}_{r,1-l} \ \cdots]^T \\
\bar{\mathbf{B}}_{r,l} &= [\cdots \ \bar{B}_{r,l+1} \ \bar{B}_{r,l} \ \bar{B}_{r,l-1} \ \cdots]
\end{aligned} \tag{42}$$

Here the n^{th} term in the vector $\bar{\mathbf{C}}_{r,l}$ is $\bar{C}_{r,n-l}$, which is the $(n-l)^{\text{th}}$ Fourier coefficient of $C(t)\psi_r(t)$.

Hence, mode vectors $\bar{\mathbf{C}}_{r,l}$ acquired at different peaks describe the same shape but the elements are shifted in position in each vector. For example, supposing the mode vector at frequency λ_r

is $\bar{\mathbf{C}}_{r,0} = [0 \ a \ b \ c \ 0]^T$, the mode vector at $\lambda_r + \omega_A$ should be $\bar{\mathbf{C}}_{r,-1} = [a \ b \ c \ 0 \ 0]^T$

multiplied with an unknown constant, and the mode vector at $\lambda_r - \omega_A$ should be proportional to $\bar{\mathbf{C}}_{r,l} = [0 \ 0 \ a \ b \ c]^T$. Similarly, $\bar{B}_{r,l-m}$ is the $(l-m)^{\text{th}}$ Fourier coefficient of $L_r(t)^T B(t)$. \mathbf{D} is a 2-D infinite matrix of the Fourier coefficients of $D(t)$. Since in most cases the direct input matrix is zero, \mathbf{D} is neglected for the remainder of this dissertation, but the extension of these derivations to nonzero $D(t)$ is straightforward.

The expression of the harmonic transfer function in Eq. (42) has the same mathematical form as the expression for the frequency response function of an LTI system in terms of its modal parameters,

$$H(\omega) = \sum_{r=1}^{2N} \frac{\varphi_r \varphi_{r,dp}}{i\omega - \lambda_r} \quad (43)$$

where φ_r is the r^{th} mode shape, $\varphi_{r,dp}$ is the amplitude at the driving point, and λ_r is the r^{th} eigenvector. Thus, the same algorithms for the modal analysis of LTI systems can be used to identify modal parameters of an LTP system, and the same intuition that is used to interpret frequency response functions can also be used to interpret the harmonic transfer function. However, there are a few differences that must be noted in signal processing:

- A linear time periodic system theoretically has an infinite number of peaks for each mode. Each peak occurs near the imaginary part of the Floquet exponent λ_r plus some integer multiple of the fundamental frequency ω_A . If the observed mode shapes $C(t)\psi_r(t)$ are constant in time, $\bar{\mathbf{C}}_{r,l}$ and $\bar{\mathbf{B}}_{r,l}$ contain only one nonzero term, i.e., $\bar{C}_{r,0}$ and $\bar{B}_{r,0}$. Then, Eq. (42) reduces to the familiar relationship for a linear time invariant system.

- The mode vectors of an LTI system describe the spatial pattern of deformation of a mode.

For an LTP system, the vectors $\bar{\mathbf{C}}_{r,l}$ consist of the Fourier coefficients that describe the time periodic spatial deformation pattern.

The harmonic transfer function will be explored further in Chapter 3 and Chapter 4, where the concept is combined with CSLDV to identify LTI structures.

2.4 Harmonic Power Spectrum

The harmonic transfer function that describes the input-output relationship is an essential part of the modal identification of LTP systems, but in many cases it is difficult or even impossible to directly measure the input, e.g., a wind turbine under wind excitation. Hence it is necessary to develop an output-only algorithm for LTP systems that uses only the output signal. This section derives the harmonic power spectrum that is completely analogous to the power spectrum of LTI systems.

The auto power spectrum of the exponentially modulated periodic signals in Eq. (40) are found in the conventional manner as in the LTI case,

$$S_{\mathbf{Y}\mathbf{Y}}(\omega) = \mathbf{E}(\mathbf{Y}(\omega)\mathbf{Y}(\omega)^H) \quad (44)$$

where $\mathbf{E}()$ is the expectation, and $()^H$ denotes the Hermitian. When the direct input matrix $D(t)$ equals zero, the harmonic power spectrum can be written in the following form in terms of the modes of the LTP system,

$$S_{\mathbf{Y}\mathbf{Y}}(\omega) = \sum_{r=1}^{2N} \sum_{l=-\infty}^{\infty} \sum_{s=1}^{2N} \sum_{k=-\infty}^{\infty} \frac{\bar{\mathbf{C}}_{r,l} \mathbf{W}(\omega)_{r,s,l,k} \bar{\mathbf{C}}_{s,k}^H}{[\mathbf{i}\omega - (\lambda_r - \mathbf{i}l\omega_A)][\mathbf{i}\omega - (\lambda_s - \mathbf{i}k\omega_A)]^H} \quad (45)$$

$$\mathbf{W}(\omega)_{r,s,l,k} = \bar{\mathbf{B}}_{r,l} S_{\mathbf{U}\mathbf{U}}(\omega) \bar{\mathbf{B}}_{s,k}^H$$

$\mathbf{W}(\omega)_{r,s,l,k}$ is a function of the input spectrum and the input matrix of the system. The dominant terms in the summation above are those for which $i\omega - (\lambda_r - il\omega_A)$ and $i\omega - (\lambda_s - ik\omega_A)$ are both minimum at the same frequency. If the sidebands for mode r do not overlap with those for mode s , then the largest terms occur when $r = s$ and $l = k$, and the expression becomes,

$$S_{\mathbf{Y}\mathbf{Y}}(\omega) \approx \sum_{r=1}^{2N} \sum_{l=-\infty}^{\infty} \frac{\bar{\mathbf{C}}_{r,l} \mathbf{W}(\omega)_{r,l} \bar{\mathbf{C}}_{r,l}^H}{[i\omega - (\lambda_r - il\omega_A)][i\omega - (\lambda_r - il\omega_A)]^H} \quad (46)$$

So the harmonic power spectrum tends to peak near the system's eigenvalues (Floquet multipliers) plus some integer multiple of the fundamental frequency. Here $\mathbf{W}(\omega)_{r,l}$ is related to the auto spectrum of modulated input signal. Specifically, if the control matrix $B(t)$ is constant (i.e., excitation location does not change), then $B_{r,n} = 0$ for $n \neq 0$. $\bar{\mathbf{B}}_{r,l}$ becomes an infinite row vector with all zeros but a non-zero constant $B_{r,0}$, and $\mathbf{W}(\omega)_{r,l}$ can be simplified as,

$$\begin{aligned} \mathbf{W}(\omega)_{r,l} &= \bar{\mathbf{B}}_{r,l} S_{\mathbf{U}\mathbf{U}}(\omega) \bar{\mathbf{B}}_{r,l}^H \\ &= B_{r,0} S_{\mathbf{U}\mathbf{U}}(\omega)_{0,0} B_{r,0}^H \\ &= B_{r,0} S_{\mathbf{U}\mathbf{U}}^{\text{LTI}}(\omega) B_{r,0}^H \end{aligned} \quad (47)$$

$S_{\mathbf{U}\mathbf{U}}(\omega)$ is the auto spectrum of the exponentially modulated input, and $S_{\mathbf{U}\mathbf{U}}^{\text{LTI}}(\omega)$ is the auto spectrum of the input $u(t)$ in the LTI case. So, the exponentially modulated input simplifies to the familiar LTI case when the excitation doesn't change location. In output-only modal analysis of LTI systems, the input is assumed to be uncorrelated random white noise. The same assumption is made for LTP systems. According to Eq. (47), $\mathbf{W}(\omega)_{r,l}$ is proportional to the input auto spectrum $S_{\mathbf{U}\mathbf{U}}^{\text{LTI}}(\omega)$, and independent of the harmonic order l . Therefore, for the work established in this dissertation, $\mathbf{W}(\omega)_{r,l}$ is treated as $\mathbf{W}(\omega)_r$.

Equation (46) shows that the auto spectrum of an exponentially modulated periodic output can be approximated by a sum of modal contributions. The harmonic power spectrum has the same form as the power spectrum of an LTI system,

$$S_{YY}(\omega) = E(Y(\omega)Y(\omega)^H) = \sum_{r=1}^N \frac{\varphi_r S_{UU}^{LTI}(\omega) \varphi_r^H}{[j\omega - \lambda_r][j\omega - \lambda_r]^H} \quad (48)$$

This function produces a peak in the spectrum when the excitation frequency ω is near the natural frequency $|\lambda_r|$, and the peak can be curve-fitted to identify the natural frequencies, damping ratios and mode shapes of the system. Note that the fitting process is a bit different for LTP systems; one needs to fit a peak to each harmonic of each mode in the harmonic power spectrum.

Similar to the LTI case, Eq. (46) can be further decomposed into a convenient form by partial fraction expansion. The expansion results in terms that resonate at both the stable poles $(\lambda_r - jl\omega_A)$, $(\lambda_r - jl\omega_A)^*$, which have negative real parts, and unstable poles $-(\lambda_r - jl\omega_A)$, $-(\lambda_r - jl\omega_A)^*$, which have positive real parts,

$$S_{YY}(\omega) \approx \sum_{r=1}^N \sum_{l=-\infty}^{\infty} \left[\frac{\mathbf{A}_{r,l}}{[j\omega - (\lambda_r - jl\omega_A)]} + \frac{\mathbf{A}_{r,l}^*}{[j\omega - (\lambda_r - jl\omega_A)^*]} + \frac{\mathbf{A}_{r,l}^*}{[-j\omega - (\lambda_r - jl\omega_A)]} + \frac{\mathbf{A}_{r,l}}{[-j\omega - (\lambda_r - jl\omega_A)^*]} \right] \quad (49)$$

The residue matrix at the l^{th} harmonic of the r^{th} mode is defined as,

$$\mathbf{A}_{r,l} = \frac{\bar{\mathbf{C}}_{r,l} \mathbf{W}(\omega) \bar{\mathbf{C}}_{r,l}^H}{\zeta_r \omega_r} \quad (50)$$

Hence, one can extract the Fourier coefficients $\bar{\mathbf{C}}_{r,l}$ of the r^{th} time periodic mode by fitting the harmonic power spectrum in Eq. (49) to a standard modal model with both stable and unstable poles at each peak. However, multiple estimates of $\bar{\mathbf{C}}_{r,l}$ can be obtained because each

mode presents at a comb of frequencies $\omega_r - l\omega_A$, and each $\bar{\mathbf{C}}_{r,l}$ can differ by a complex scalar, as explained in Section 2.3. Care must be taken since these mode vectors are generally not of equal quality. At some frequencies the modes are strong and stand out above the noise, while at others the modes might be barely visible or contaminated by neighboring modes. Two post processing techniques are developed to obtain the optimal estimate of the mode vector from multiple estimates of $\bar{\mathbf{C}}_{r,l}$, as will be introduced in Section 2.7.

The harmonic power spectrum was combined with CSLDV to measure a parked wind turbine in Chapter 5. In Chapter 7, the method was used to analyze the periodic response of an operating wind turbine that had to be modeled as an LTP system.

2.5 *Positive Harmonic Power Spectrum*

The harmonic power spectrum in Eq. (49) includes each of the system poles twice: One set having stable poles $(\lambda_r - j\omega_A)$, $(\lambda_r - j\omega_A)^*$ with negative real parts, and the other set having unstable poles $-(\lambda_r - j\omega_A)$, $-(\lambda_r - j\omega_A)^*$ with positive real parts. Most modal identification routines are developed for the frequency response function which contains only the stable poles. Therefore, one must use a curve-fitting routine that is specialized to output-only modal analysis. In output-only modal analysis of LTI systems, a positive power spectrum was proposed to eliminate the unstable poles [62]. The positive power spectrum is equivalent to a free response function, so conventional modal identification routines can be applied to extract modal parameters. This concept was recently extended to LTP systems, defining the positive harmonic power spectrum, which was used to process measurements of a simulated wind turbine [63].

The lifting approach proposed in this work uses the positive harmonic correlation function, which is the inverse FFT of the positive harmonic power spectrum. The harmonic

power spectrum in Eq. (49) is converted to the time domain using the inverse FFT, resulting in a harmonic correlation function that has the following form,

$$R[n] = \sum_{r=1}^N \sum_{l=-\infty}^{\infty} \mathbf{A}_{r,l} e^{(\lambda_r - j l \omega_A) n T_s} + \mathbf{A}_{r,l}^* e^{(\lambda_r - j l \omega_A)^* n T_s} + \mathbf{A}_{r,l}^* e^{-(\lambda_r - j l \omega_A)(n - N_s) T_s} + \mathbf{A}_{r,l} e^{-(\lambda_r - j l \omega_A)^* (n - N_s) T_s}, \quad 0 \leq n < 2N_s \quad (51)$$

where T_s is the sampling period, and N_s is the number of samples in the acquired time history. Figure 4 shows an example of the harmonic correlation function. The first two terms in Eq. (51) contain the stable poles with negative real parts in the exponents. When n is small (the n^{th} sample), the first two terms dominate the response, and the harmonic correlation function takes on the form of a decaying function (Figure 4 when the time is smaller than 6.4s). As n increases, the first two terms are damped out while the last two terms with positive real parts become dominant, and the system appears to be unstable (Figure 4 when the time is larger than 6.4s).

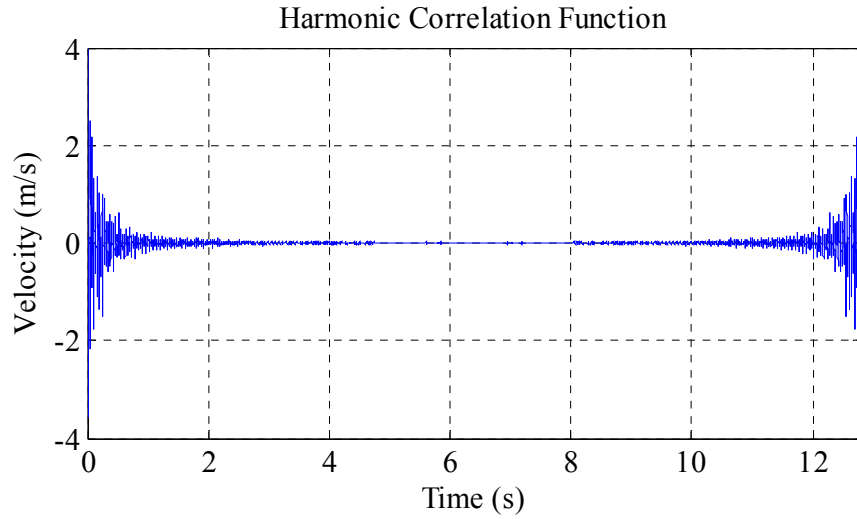


Figure 4 Harmonic correlation function computed from the harmonic power spectrum

When a two-sided inverse FFT is used to compute the harmonic correlation function, the signal after 6.4s in Figure 4 will be shifted to the negative time axis. A rectangular window can

be applied to delete this negative part, leaving only the positive part of the harmonic correlation function that contains only the stable poles,

$$R^+[n] = \sum_{r=1}^N \sum_{l=-\infty}^{\infty} \mathbf{A}_{r,l} e^{(\lambda_r - j l \omega_A) n T_s} + \mathbf{A}_{r,l}^* e^{(\lambda_r - j l \omega_A)^* n T_s}, \quad 0 \leq n < N_s \quad (52)$$

The positive harmonic correlation function is analogous to an impulse response that can be measured in an impact test, and the positive harmonic power spectrum is the FFT of the positive harmonic correlation function [63],

$$H_{yy}^+(\omega) \approx \sum_{r=1}^N \sum_{l=-\infty}^{\infty} \frac{\mathbf{A}_{r,l}}{[j\omega - (\lambda_r - j l \omega_A)]} + \frac{\mathbf{A}_{r,l}^*}{[j\omega - (\lambda_r - j l \omega_A)^*]} \quad (53)$$

This expression contains only the stable poles that can be easily fitted using any standard routine. In [63], the positive harmonic power spectrum was used to identify the modal parameters of a simulated wind turbine. This part is not included in the dissertation.

The positive harmonic power spectrum of the periodic system still has many peaks for each mode, making the identification procedure labor intensive. Fortunately, the positive harmonic correlation is analogous to the free response of a periodic system, so it can be lifted to simplify parameter estimation. This approach will be derived in the next section.

2.6 *Lifting the Positive Harmonic Correlation Function*

Assuming there are exactly N_A samples in each fundamental period of an LTP system, these samples can be viewed as N_A pseudo sensors uniformly distributed in each period [64]. The responses at the m^{th} pseudo sensor are acquired at time instants $mT_s + kT_A$, where T_s is the sampling interval, T_A is the period, and $T_A = N_A T_s$. Substituting $mT_s + kT_A$ for nT_s in the positive harmonic correlation function in Eq. (52), and considering $e^{(\lambda_r - j l \omega_A) k T_A} = e^{\lambda_r k T_A}$ because $\omega_A T_A = 2\pi$, the responses at the m^{th} pseudo sensor can be written as,

$$R_m^+[k] \approx \sum_{r=1}^N \sum_{l=-\infty}^{\infty} \mathbf{A}_{r,l} e^{(\lambda_r - j l \omega_A) m T_s} e^{\lambda_r k T_A} + \mathbf{A}_{r,l}^* e^{(\lambda_r - j l \omega_A)^* m T_s} e^{\lambda_r^* k T_A} \quad (54)$$

$e^{(\lambda_r - j l \omega_A) m T_s}$ is a constant for the m^{th} sensor, therefore Eq. (54) can be transferred to the frequency domain as,

$$\begin{aligned} \mathbf{R}_m^+(\omega) &= \sum_{r=1}^N \frac{\mathbf{Res}_{r,m}}{j\omega - \lambda_r} + \frac{\mathbf{Res}_{r,m}^*}{j\omega - \lambda_r^*} \\ \mathbf{Res}_{r,m} &= \sum_{l=-\infty}^{\infty} \mathbf{A}_{r,l} e^{(\lambda_r - j l \omega_A) m T_s} \end{aligned} \quad (55)$$

The above expression has the same mathematical form as a frequency response function that is measured at the m^{th} point. Therefore, after applying the lifting approach, a complicated expression of the harmonic power spectrum (Eq. (46)) boils down to a much more familiar form of the transfer function (Eq. (55)). It has a single resonance at $\omega_r \approx \text{Imag}(\lambda_r)$ for each mode. Since the resampling causes the eigenvalues $\lambda_r - j l \omega_A$ to collapse into a single frequency in $0 < \omega < 0.5\omega_A$, the unaliased natural frequency ω_r can be found by adding the correct integer multiple of ω_A to ω , where the lifted spectrum has the maximum amplitude [53, 65].

A least squares approach can be used to recover the mode vectors $\bar{\mathbf{C}}_{r,l}$ from the identified residue at each resonance. Supposing $n = -p \dots p$ is used to modulate the periodic output signal, and supposing the significant harmonics of the r^{th} mode are present at $l = -q \dots q$ in the harmonic power spectrum, one should select $p > q$ to include all significant harmonics when constructing the periodic mode shape. $\mathbf{Res}_{r,m}$ becomes a column vector of $(2p+1)$ elements that is the sum of terms in each sideband as $\sum_{l=-q}^q \mathbf{A}_{r,l} e^{(\lambda_r - j l \omega_A) m T_s}$. There are N_A measurement locations in each period, so the residue matrix for the r^{th} mode becomes,

$$\mathbf{Res}_r = \left[\sum_{l=-q}^q \mathbf{A}_{r,l} \quad \sum_{l=-q}^q \mathbf{A}_{r,l} e^{(\lambda_r - jl\omega_A)T_s} \quad \dots \quad \sum_{l=-q}^q \mathbf{A}_{r,l} e^{(\lambda_r - jl\omega_A)(N_A-1)T_s} \right] \quad (56)$$

$(2p+1) \times N_A$ $(2p+1) \times N_A$

Inserting the expression of $\mathbf{A}_{r,l}$ in Eq. (50) into Eq. (56),

$$\mathbf{Res}_r = \left[\overline{\mathbf{C}}_{r,-q} \frac{\mathbf{W}(\omega)_r C_{r,-q}^*}{\zeta_r \omega_r} \quad \dots \quad \overline{\mathbf{C}}_{r,q} \frac{\mathbf{W}(\omega)_r C_{r,q}^*}{\zeta_r \omega_r} \right] \begin{matrix} \mathbf{X}_r \\ \mathbf{E}_r \end{matrix} \begin{bmatrix} 1 & e^{(\lambda_r + jq\omega_A)T_s} & \dots & e^{(\lambda_r + jq\omega_A)N_A T_s} \\ \vdots & \vdots & \vdots & \vdots \\ 1 & e^{(\lambda_r - jq\omega_A)T_s} & \dots & e^{(\lambda_r - jq\omega_A)N_A T_s} \end{bmatrix} \quad (57)$$

$(2p+1) \times N_A$ $(2p+1) \times (2q+1)$ $(2q+1) \times N_A$

where $\mathbf{W}(\omega)_r C_{r,-q}^* / (\zeta_r \omega_r)$ is an unknown complex scalar. Equation (13) can be solved in a least squares sense,

$$\mathbf{X}_r = \mathbf{Res}_r \mathbf{E}_r^H (\mathbf{E}_r \mathbf{E}_r^H)^{-1} \quad (58)$$

These Fourier coefficient vectors, e.g., $\overline{\mathbf{C}}_{r,-q}$ and $\overline{\mathbf{C}}_{r,q}$, in \mathbf{X}_r describe the same r^{th} mode shape but have the terms shifted in position, as explained in Section 2.3. After shifting each column in \mathbf{X}_r to the correct position, singular value decomposition or weighted average approach can be used to extract the Fourier coefficient vector $\overline{\mathbf{C}}_r$, as discussed in the following section.

The lifting approach will be used to simplify the output-only modal analysis of a parked wind turbine measured with CSLDV in Chapter 6.

2.7 Post Processing

Multiple harmonics of the same mode appear in the measured response of an LTP system. In this section, two post processing techniques are developed to obtain the optimal estimate of the mode vector from these multiple estimates. Once the optimal estimate has been found, one can reconstruct the time periodic mode shapes of the system using Eq. (33).

2.7.1 Singular Value Decomposition

In singular value decomposition, various vectors corresponding to the r^{th} mode are arranged in a matrix. Each of these vectors was identified at a different peak in the harmonic power spectrum as follows,

$$\bar{\mathbf{C}}_r = [\cdots \quad \bar{\mathbf{C}}_{r,1} \quad \bar{\mathbf{C}}_{r,0} \quad \bar{\mathbf{C}}_{r,-1} \quad \cdots] \quad (59)$$

These vectors contain the same Fourier coefficients, but in different rows within each vector. This is remedied by shifting each vector so that the same Fourier coefficients occur on each row when forming the matrix $\bar{\mathbf{C}}_r$ above, and an example of $\bar{\mathbf{C}}_r$ is given later in Chapter 5. Some rows at the top and bottom of each vector will have to be deleted in this process since not all of the vectors $\bar{\mathbf{C}}_{r,l}$ will contain estimates of all of the same Fourier coefficients. If the measurements were noise-free, then each vector $\bar{\mathbf{C}}_{r,l}$ would be identical except for a complex scale factor, so the rank of $\bar{\mathbf{C}}_r$ should be one. In practice, where noise is blended in measurements, singular value decomposition can be used to compute a rank-one representation of $\bar{\mathbf{C}}_r$, and then the mode vector can be taken as the first vector in the rank-one matrix. Specifically, if $n = -p \dots p$ is used to modulate the periodic input signal, and if $(2q+1)$ estimates of $\bar{\mathbf{C}}_{r,l}$ are obtained from $(2q+1)$ different peaks in the harmonic power spectrum, then the $(2p+1) \times (2q+1)$ matrix $\bar{\mathbf{C}}_r$ can be decomposed as,

$$\bar{\mathbf{C}}_r = \mathbf{U} \mathbf{\Sigma} \mathbf{V}^H \quad (60)$$

where \mathbf{U} and \mathbf{V} are orthogonal matrices containing the left and right singular vectors of $\bar{\mathbf{C}}_r$. $\mathbf{\Sigma}$ is a diagonal matrix containing the corresponding singular values on the diagonal. The optimal estimate of the r^{th} mode vector $\bar{\mathbf{C}}_r^{\text{SVD}}$ is the first column in \mathbf{U} .

2.7.2 Weighted Average Method

An alternative to singular value decomposition is to compute a weighted average of the mode vectors $\bar{\mathbf{C}}_{r,l}$. The method first normalizes each vector by its largest element $a_{r,l} = \max(|\bar{\mathbf{C}}_{r,l}|)$ as,

$$\bar{\mathbf{C}}_{r,l}^{\text{Norm}} = \bar{\mathbf{C}}_{r,l} / a_{r,l} \quad (61)$$

Then the phase difference was addressed by rotating the vector to the phase of a reference vector.

Using the vector at $l = n$ as the reference, then,

$$\bar{\mathbf{C}}_{r,l}^{\text{NP}} = \bar{\mathbf{C}}_{r,l}^{\text{Norm}} \exp(j \cdot \text{angle}((\bar{\mathbf{C}}_{r,n}^{\text{Norm}})^H \bar{\mathbf{C}}_{r,l}^{\text{Norm}})) \quad (62)$$

where the angle of Hermitian inner product $(\bar{\mathbf{C}}_{r,n}^{\text{Norm}})^H \bar{\mathbf{C}}_{r,l}^{\text{Norm}}$ is a least squares estimate of the phase difference between $\bar{\mathbf{C}}_{r,l}^{\text{Norm}}$ and the reference vector $\bar{\mathbf{C}}_{r,n}^{\text{Norm}}$. If $(2q+1)$ estimates of $\bar{\mathbf{C}}_{r,l}$ are obtained from $(2q+1)$ different peaks in the harmonic power spectrum, the weighted average can be computed using,

$$\bar{\mathbf{C}}_r^{\text{AVG}} = \sum_{l=-q}^q \bar{\mathbf{C}}_{r,l}^{\text{NP}} a_{r,l} / \sum_{l=-q}^q a_{r,l} \quad (63)$$

It is clear that the vectors that are dominant in the response, and presumably less susceptible to noise, will be more strongly weighted using this approach.

2.8 Summary of Output-only Identification Algorithms

Three output-only identification algorithms for LTP systems were proposed in this chapter. The harmonic power spectrum is the foundation for output-only modal analysis of LTP systems. It allows conventional modal analysis routines of LTI systems to be used in the parameter estimation of LTP systems. However, the harmonic power spectrum contains both

stable and unstable poles, and requires special identification routines to extract modes from the measurements. The positive harmonic power spectrum eliminates the unstable poles in the harmonic power spectrum by keeping only the positive part of the harmonic correlation function. Unfortunately, the positive harmonic power spectrum still has multiple peaks for each mode, and hence requires extensive user input in the identification. The positive harmonic correlation function is analogous to the impulse response of an LTP system. Thus, positive harmonic correlation functions can be lifted to create a larger set of signals that appears to be from an LTI system. Therefore, the lifting approach can greatly simplify the output-only modal analysis of LTP systems.

For this dissertation, the previously derived modal identification algorithms for LTP systems will be applied to the CSLDV measurements. Figure 5 outlines the signal processing procedure of the output-only modal analysis algorithms for CSLDV. The signal processing steps involved are summarized as follows. Note that these steps also apply to a general linear time periodic system.

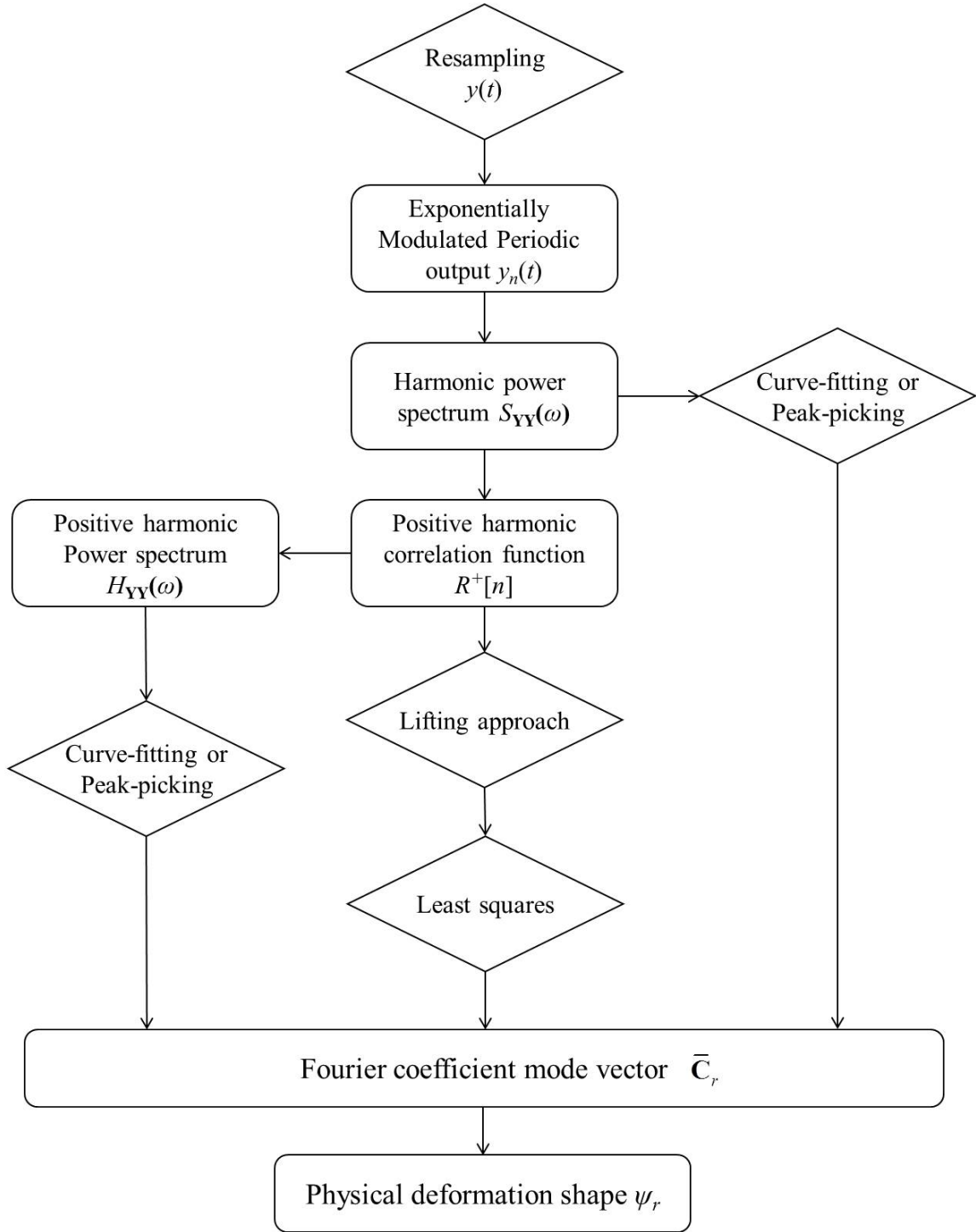


Figure 5 Output-only modal analysis algorithms using CSLDV

1. Record the response $y(t)$ of a time invariant structure to white noise random excitation using CSLDV and a periodic scan pattern.

2. Fit the mirror output signal with a multi sine to find a highly accurate estimate of the scan frequency.
3. Resample the response $y(t)$ such that there are precisely N_A samples per scan period.
4. Create modulated copies of the response $y(t)$ using $y_n(t) = y(t)e^{jn\omega_A t}$ for $n=-p \dots p$.
5. Split the modulated output signals into sub-blocks with overlap between neighboring blocks. The time record in each sub-block is windowed and zero-padded to twice its original length
6. Compute the primary column of the linear harmonic power spectrum as $S_{\mathbf{Y}\mathbf{Y}}(\omega)_{n,0} = E\left(\mathbf{Y}(\omega)Y_0(\omega)^H\right)$, where $E()$ denotes the expected value over all sub-blocks.
7. For the algorithm based on the harmonic power spectrum [57], use peak-picking or output-only curve-fitting routines to identify the Fourier coefficient vector $\bar{\mathbf{C}}_{r,l}$ from all of the harmonics peaks for each mode. Then skip to step 14.
8. Take the inverse FFT of the harmonic power spectrum to obtain the harmonic correlation function, $R[n]$.
9. Use a rectangular window to retain only the positive part of the harmonic correlation function, $R^+[n]$.
10. For the algorithm based on the positive harmonic power spectrum [63], take the FFT of the positive harmonic correlation function to obtain $H_{\mathbf{Y}\mathbf{Y}}^+(\omega)$ and use peak-picking or standard curve-fitting routines to identify the Fourier coefficient vector $\bar{\mathbf{C}}_{r,l}$. Then skip to step 14.
11. Lift the positive harmonic correlation function $R^+[n]$ by grouping the responses at the same

location along the laser path. Take the FFT to obtain the lifted spectra $\mathbf{R}_m^+(\omega)$ at all N_A locations.

12. Treat the lifted spectra at N_A points as the responses of a single-input multiple-output system. Identify the natural frequencies and the residue matrix using peak-picking or standard curve-fitting routines.
13. Form a least squares problem according to Eq. (56) to obtain the \mathbf{X}_r matrix of Fourier coefficient vectors.
14. Align each column of the identified matrix of Fourier coefficient vectors, use singular value decomposition or weighted average to find the best estimate of the Fourier coefficient vector $\bar{\mathbf{C}}_r$ from all harmonics.
15. Reconstruct the r^{th} time periodic mode shape $C(t)\psi_r$ using Eq. (33). The physical deformation shape of the underlying time invariant structure is obtained by plotting $C(t)\psi_r$ versus the laser path.

2.9 Summary

Table 1 lists the proposed frequency domain modal analysis algorithms for LTP systems. These algorithms are completely analogous to the algorithms for LTI systems, and they are capable of extracting the modal parameters of LTP systems under any type of input, using the well-established identification routines for LTI systems. The modal identification theory is based on the harmonic transfer function concept [66]. Whereas a transfer function of LTI systems relates the output to the input at the same frequency, a harmonic transfer function of LTP systems relates the output at a collection of frequencies to the input at the same collection,

each separated by the fundamental frequency of the periodic system. The power spectrum in output-only modal analysis of LTI systems is also extended to LTP systems, introducing the harmonic power spectrum where the input is not measured but is assumed to be uniformly distributed random noise. The positive correlation function is analogous to the impulse response of an LTI system. This concept is extended to LTP systems as well. The positive harmonic correlation function of LTP systems is lifted to simplify the output-only modal analysis of LTP systems. The lifted spectra contain only one peak for each mode, therefore they are far easier to interpret and can be readily curve-fitted with virtually any modal parameter identification routine. The positive harmonic power spectrum is analogous to the positive power spectrum of LTI systems. It contains only stable poles of an LTP system and was used in [63] to identify the periodic modes of a simulated wind turbine. This work is not reported in this dissertation.

Table 1 Comparison of modal identification algorithms for LTI and LTP systems

Identification algorithms	Linear time invariant	Linear time periodic
Input and output	$Y(\omega) = [y_0]$ $U(\omega) = [u_0]$	$\mathbf{Y}(\omega) = [\cdots \ y_{-1} \ y_0 \ y_1 \ \cdots]^T$ $\mathbf{U}(\omega) = [\cdots \ u_{-1} \ u_0 \ u_1 \ \cdots]^T$
Transfer function	$Y(\omega) = H(\omega)U(\omega)$ $H(\omega) = \sum_{r=1}^N \frac{\varphi_r \varphi_r^H}{i\omega - \lambda_r}$	$\mathbf{Y}(\omega) = \mathbf{G}(\omega)\mathbf{U}(\omega)$ $\mathbf{G}(\omega) = \sum_{r=1}^N \sum_{l=-\infty}^{\infty} \frac{\bar{\mathbf{C}}_{r,l} \bar{\mathbf{B}}_{r,l}}{i\omega - (\lambda_r - il\omega_A)}$
Power spectrum	$S_{YY}(\omega) = \sum_{r=1}^N \frac{\varphi_r (\varphi_r^H S_{UU}(\omega) \varphi_r) \varphi_r^H}{[j\omega - \lambda_r][j\omega - \lambda_r]^H}$	$S_{\mathbf{Y}\mathbf{Y}}(\omega) = \sum_{r=1}^N \sum_{l=-\infty}^{\infty} \frac{\bar{\mathbf{C}}_{r,l} (\bar{\mathbf{B}}_{r,l} S_{\mathbf{U}\mathbf{U}}(\omega) \bar{\mathbf{B}}_{r,l}^H) \bar{\mathbf{C}}_{r,l}^H}{[i\omega - (\lambda_r - il\omega_A)][i\omega - (\lambda_r - il\omega_A)]^H}$
Positive correlation function	$R^+[n] = \sum_{r=1}^N \mathbf{A}_r e^{\lambda_r n T_s} + \mathbf{A}_r^* e^{\lambda_r^* n T_s}$	$R^+[n] = \sum_{r=1}^N \sum_{l=-\infty}^{\infty} \mathbf{A}_{r,l} e^{(\lambda_r - jl\omega_A) n T_s} + \mathbf{A}_{r,l}^* e^{(\lambda_r^* - jl\omega_A^*) n T_s}$
Positive power spectrum	$H_{YY}^+(\omega) = \sum_{r=1}^{N/2} \sum_{l=-\infty}^{\infty} \frac{\mathbf{A}_{r,l}}{j\omega - \lambda_r} + \frac{\mathbf{A}_{r,l}^*}{j\omega - \lambda_r^*}$	$H_{\mathbf{Y}\mathbf{Y}}^+(\omega) = \sum_{r=1}^{N/2} \sum_{l=-\infty}^{\infty} \frac{\mathbf{A}_{r,l}}{[j\omega - (\lambda_r - jl\omega_A)]} + \frac{\mathbf{A}_{r,l}^*}{[j\omega - (\lambda_r^* - jl\omega_A^*)]}$

There are also two notable differences between the proposed modal identification algorithms for LTP systems and their counterparts for LTI systems. First, an LTP system theoretically has an infinite number of peaks for each mode, each separated by the fundamental frequency. The mode vectors at all these peaks have to be identified to obtain the best estimate of the mode vector. Second, the mode vector of an LTP system no longer describes the spatial pattern of deformation of a mode. Instead, the vector consists of the Fourier coefficients that describe the time periodic spatial deformation pattern. Once these differences have been addressed, one can use the well-established modal identification routines for LTI systems to identify the modal parameters of LTP systems. In the following chapters, the proposed algorithms will be used to identify modal parameters of LTI structures measured with CSLDV.

3 Experimental Modal Analysis using the Harmonic Transfer

Function

In this Chapter, the harmonic transfer function is used to identify the operational shape from the CSLDV measurements of a cantilever beam under sinusoidal excitation. The result is compared with those identified from the same data using the polynomial approach and the lifting approach. The noise and uncertainty in the reconstructed operational shape are discussed.

3.1 Introduction

The work presented in this chapter is part of the research conducted for Sandia National Laboratories with primary interest in the application of CSLDV in force reconstruction. The description of dynamic forces is essential in the design and optimization of mechanical structures. However, sometimes it is difficult or even impossible to directly measure the input forces, e.g., the forcing function to a space shuttle during the rollout [67]. On the other hand, dynamic responses can be easily measured using conventional transducers such as strain gauges and accelerometers. Force reconstruction is a process in which experimentally measured dynamic responses are used to infer the applied forces that produce these responses. An in-depth review of existing force reconstruction techniques can be found in [68]. These techniques usually require spatially detailed mode shapes of the structure, in order to improve the ill-condition when inverting the frequency response function matrix. However, acquiring detailed mode shapes is prohibitively expensive and time consuming with conventional transducers.

CSLDV is capable of providing spatially detailed vibration information of a structure in the same amount of time as is required to measure the response at a single point. Therefore,

CSLDV has great potential in force reconstruction where detailed mode shapes are preferred. In addition, CSLDV has few requirements on the storage size and surface treatment compared to other full-field measurement techniques such as digital image correlation [69, 70]. Digital image correlation employs a high speed camera to capture the displacement between consecutive frames at hundreds of points simultaneously. Therefore, the spatial and temporal resolution of the identified shape is determined by the number of pictures the computer memory can cache. On the other hand, CSLDV is capable of scanning at up to 300Hz from hundreds of meters away with a sampling rate up to 10MHz. The spatial and temporal resolution is almost unlimited. However, the accuracy of the mode shape is determined by the speckle noise level in the acquired velocity signal, more specifically, the number of harmonics that stand above the noise floor.

In this chapter, CSLDV is used to measure a cantilever beam with a point support in the center. Then, the harmonic transfer function is used to identify the operational shape under sinusoidal excitation. The result is compared with those identified from the same data using the polynomial approach [46] and the lifting approach [54]. The noise and uncertainty in the reconstructed operational shape are discussed as well. The rest of this chapter is organized as follows: Section 3.2 introduces the experimental setup; Section 3.3 discusses the noise level in the measured signal from CSLDV. In Section 3.4, the beam is measured with conventional scanning LDV and CSLDV, and acquired mode shapes from the different methods are compared with each other. In Section 3.5, the uncertainty of the reconstructed mode shape is discussed. Section 3.6 summarizes this chapter.

3.2 *Experimental Setup*

Figure 6 shows the experimental setup of the cantilever beam. The laser scans all but a few millimeters from both ends of the beam (Figure 6a). The aluminum beam ($30.5\text{cm} \times 2.5\text{cm} \times 0.32\text{cm}$) was clamped to a fixture using C-clamps. The clamped portion was approximately 3.8cm. A fine adjustment ball screw was installed at 11.5cm from the beam root to provide a point support (Figure 6c). The beam was excited at the other end, where a load cell was mounted to record the input force (Figure 6d). The input force oscillated from -8N to 6N, and the yield limit of the beam is 50N. Note that this input force is the maximum load that can be applied while keeping the point contact during the whole test. Later, a load spreader ($5\text{cm} \times 2.5\text{cm} \times 0.32\text{cm}$) was mounted between the ball screw and the beam (Figure 6d). The load spreader was installed to verify whether CSLDV can capture the operational shape change due to the change of the boundary condition.

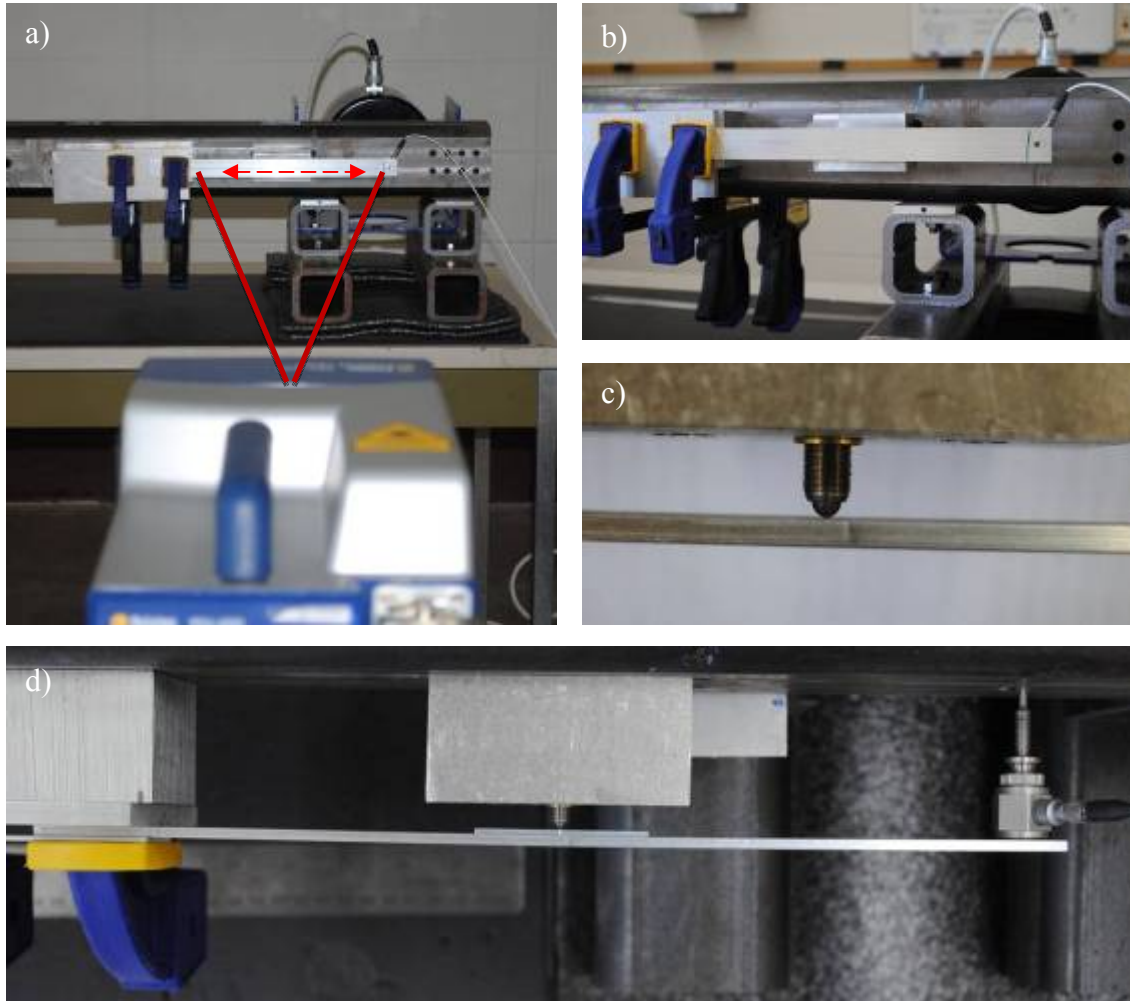


Figure 6 Experimental setup of the aluminum beam

The laser head stood 1.5m from the beam. This distance was chosen from the Polytec PSV-400 manual which specifies optimal standoff distances ($n \times 204\text{mm} + 99\text{mm}$) that have the best signal to noise ratio. In continuous-scan, the laser scanned a 24cm line from the root to the tip, so the mirror angle is about 10 degrees at a 1.5m standoff distance. The laser scanned at 3Hz on the beam surface directly with a sampling rate of 5120Hz. The VD-08 digital decoder was used to record the response, and for consistency the sensitivity was kept at 20mm/s/V in all tests. This sensitivity ensures that when the beam is excited with a -8N to 6N forcing signal, the

maximum voltage of the laser signal is at about 60% of the full range (-10V to 10V) in order to achieve the best accuracy.

3.3 *Speckle Noise in CSLDV*

When a coherent laser scatters from an optically rough surface, only a small portion of the backscattered light is collected by the photo detector. Laser speckle is formed when the backscattered light, with random deviation in phase and amplitude, interferes on the detector. As a primary source of uncertainty in CSLDV measurements, the speckle noise level is affected by many parameters. For example, the speckle noise increases with laser scan frequency (or sweeping speed). A higher laser sampling rate provides temporally denser velocity information but also includes more speckles in the measured response. This section studies the noise level when the laser scans on the stationary aluminum beam in order to find appropriate settings for the following tests. The laser sampling rate was 5120Hz, which is sufficient to measure a 20Hz operational shape in the following tests while limiting high frequency speckle noise.

Figure 7 shows the measured velocity signals when the laser was pointed at a stationary point at the tip of the beam. Different sensitivity settings of the VD-08 decoder were tested. Since the beam was kept stationary, the measured laser signals in Figure 7 are considered to be pure noise. Ideally, the acquired velocities are zero if the measurements were noise free. However, the laser signal varies randomly with time in addition to a bias error that may be incurred by the digital decoder. The bias error increases from 0.1mm/s to 1.7mm/s as the sensitivity increases from 1mm/s/V to 50mm/s/V. In the rest of this chapter, the laser sensitivity is set to 20mm/s/V (bias error 0.7mm/s), which ensures that the maximum vibration amplitude is

about 50%~60% of the full range when the beam is excited with a -8N to 6N sinusoidal force at 20Hz.

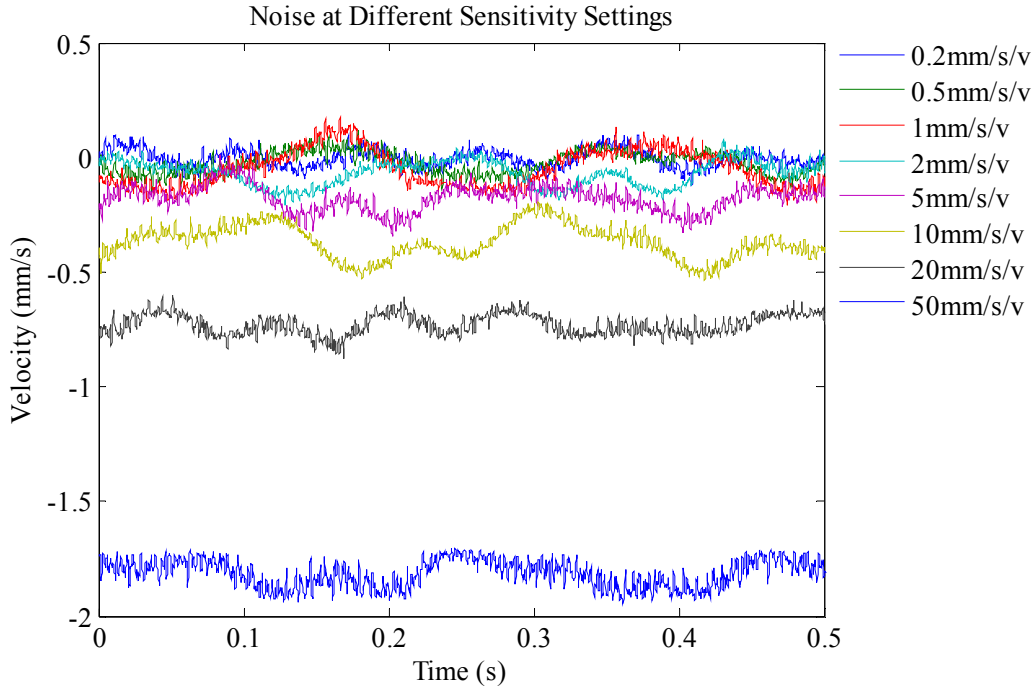


Figure 7 Noise signal with different sensitivity settings

Noise levels were evaluated when the laser was continuously scanning on the bare aluminum surface and on retro-reflective tape respectively. Figure 8 shows the arithmetic mean and standard deviation of the noise when the laser scans at different rates. The scan frequency ranged from 0 to 100Hz stepped by 5Hz, and the test duration was 102.4s. For a scan frequency higher than 100Hz, the internal mirror system becomes highly nonlinear, so the recorded laser position is no longer reliable. The speckle noise and deviation increase almost linearly with the scan frequency on both surfaces, which is similar to the observation in [71]. When the laser is not scanning, (0Hz), the noise level on each surface is around 0.7mm/s, which is the bias error at the sensitivity of 20mm/s/V (Figure 7). When the laser scans at 3Hz, the noise level on retro-reflective tape increases to 1.015mm/s and the standard deviation is 0.746mm/s. Note that the

maximum vibration amplitude when the beam is excited at 20Hz is about 170mm/s, so the noise level is only about 0.6%. The noise level on the beam surface is slightly larger (1.065mm/s with a standard deviation of 0.806mm/s). The difference in noise level on the two surfaces also increases with the scan frequency. This is reasonable since the retro-reflective tape is coated with small glass beads that reflect most of incident laser back to the laser source. Hence, the noise level and standard deviation are smaller than those when scanning directly on the bare beam surface, which scatters the incident laser in all directions. Since the noise level is similar on both surfaces when the laser scans at 3Hz, the following tests are performed on the beam surface directly without the retro-reflective tape.

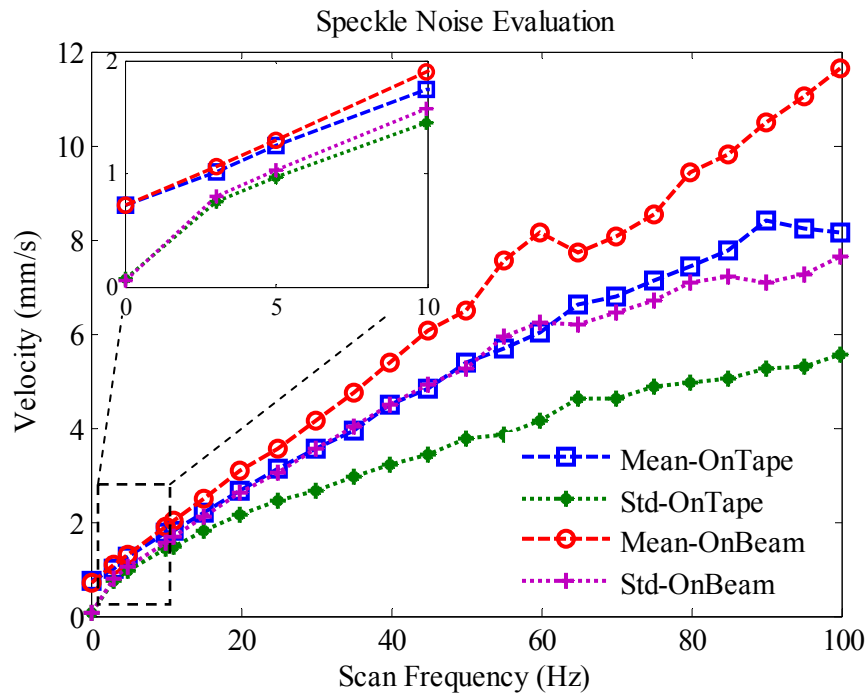


Figure 8 Noise level and standard deviation at different scan frequencies

3.4 *Experimental Results*

3.4.1 Point-by-point Scanning LDV

Prior to the continuous-scan test, a conventional point-by-point test was performed to measure the operational shape of the beam at 20Hz. The Fast-scan feather in the Polytec system was used. 59 evenly distributed points along the beam were measured, with three measurements at each point and 8s for each measurement, for a total duration of 24 minutes. Figure 9 shows the acquired operational shape of the beam with and without the load spreader. The operational shape is normalized with the input force to compare with the operational shapes acquired using CLSDV. The operational shape appears at the imaginary part of the transfer function since the velocity, not the displacement or acceleration, is measured. A small real part appears as well, which is incurred by the laser speckle noise. The amplitude of the operational shape is slightly smaller with the load spreader installed between the beam and ball screw. This is reasonable because the load spreader provides additional damping to the beam and suppresses the response. The maximum change of operational shape happens at the beam tip and is less than 4%, which is computed with respect to the maximum amplitude of the beam when point-supported.

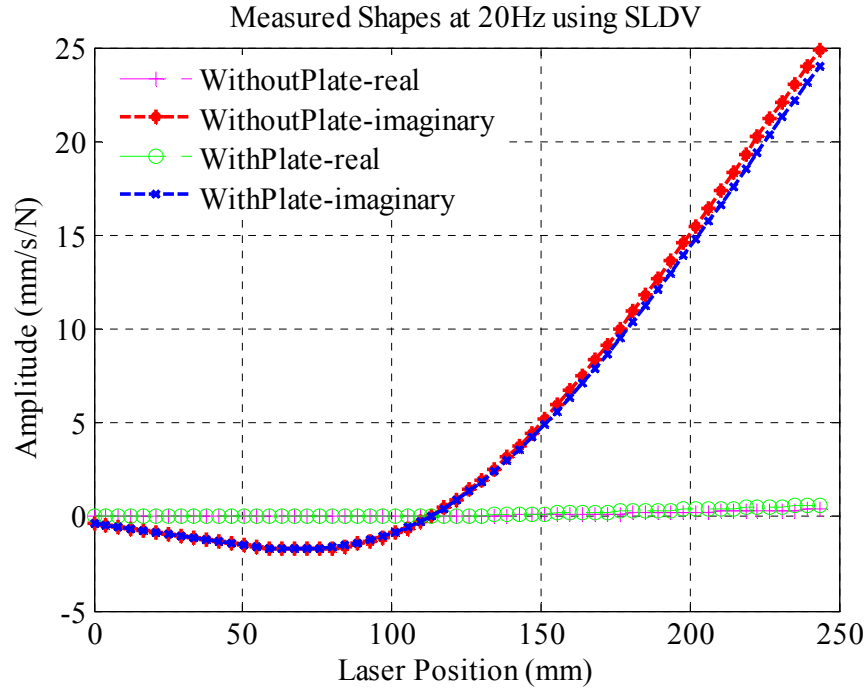


Figure 9 Measured operational shapes at 20Hz using conventional scanning LDV

3.4.2 Continuous-scan Laser Doppler Vibrometry

The laser then continuously scans over the same length of the beam at 3Hz for 102.4s to measure the operational mode shape, while other parameters remain the same as in the point-by-point scan test. Figure 10 compares the spectra of measured velocities from both the point-by-point scan and the continuous-scan when the beam is point supported. In the first plot the laser was kept at a stationary point at the tip of beam. The spectrum contains the excitation frequency component at 20Hz as well its harmonics at 40Hz, 60Hz, etc., which may arise due to the nonlinearity of the shaker. In contrast, when the laser is continuously scanning, a number of harmonics appear around 20Hz, each separated by the scan frequency at 3Hz. The harmonics from $n = -10 \dots 10$ are shown in the plot. Note that the harmonics from $n = -10 \dots -7$ have negative frequencies but are ‘reflected’ to the positive axis. These harmonics are obviously

incurred by the continuously moving laser position, which can be thought of as modulating the acquired velocity with the sweeping frequency.

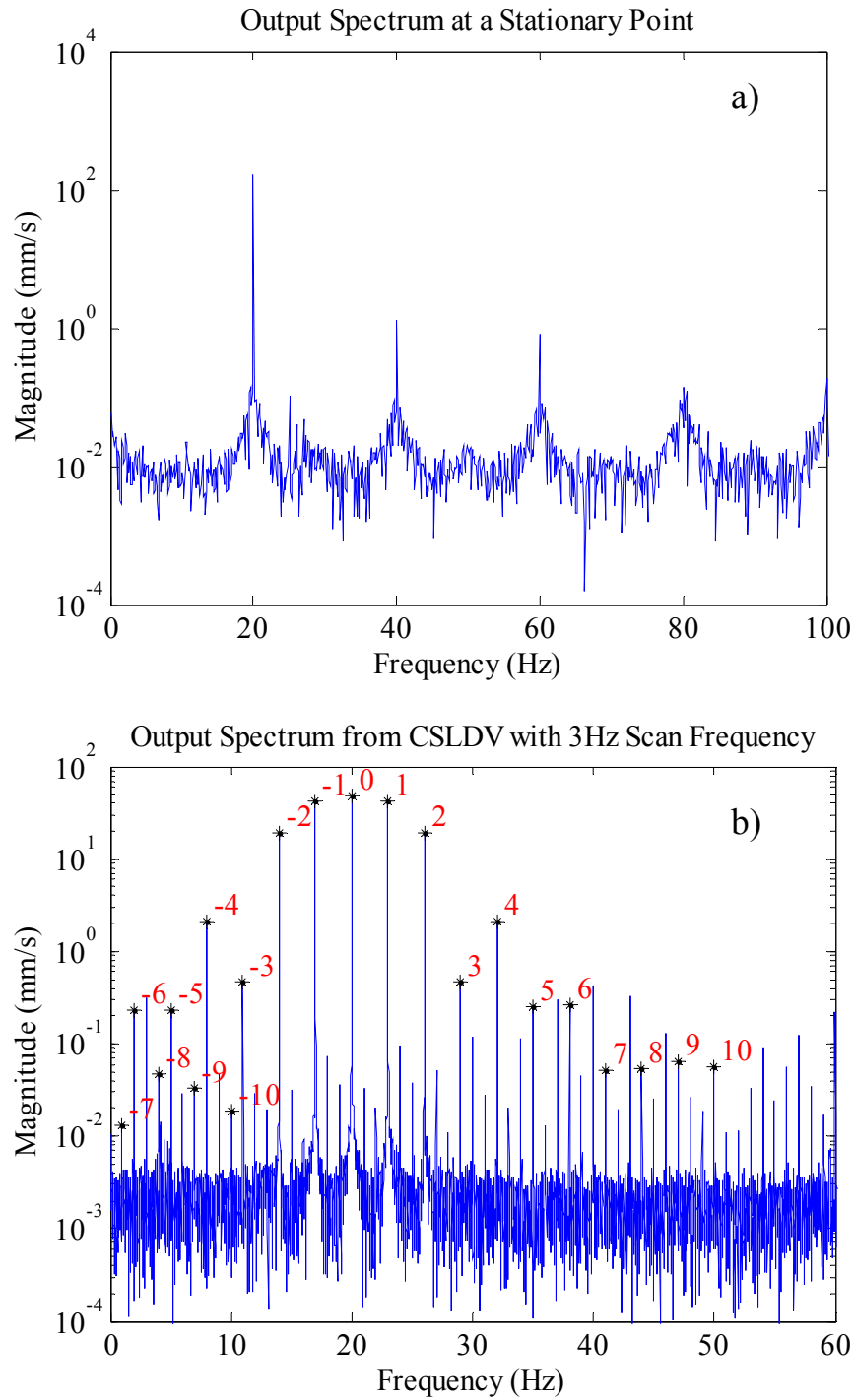


Figure 10 Measured output spectrum (a) At a stationary point, (b) CSLDV with 3Hz scan frequency

The acquired velocity signal from CSLDV is exponentially modulated to compute the harmonic transfer function, as $y_n(t) = y(t)e^{jn\omega_A t}$, where $n = -6 \dots 6$ and ω_A is the scan frequency. The reason for selecting $n = -6 \dots 6$ will be discussed in the next section. Figure 11 shows the spectra of modulated outputs when the beam is supported with the ball screw (point support). The modulation is essentially a process of creating frequency shifted copies (by $n\omega_A$) of the output spectrum. After modulation, all sideband harmonics are moved to the frequency line corresponding to the natural frequency of each mode, so conventional identification tools for LTI systems such as peak-picking and curve-fitting can be used to extract natural frequencies, damping ratios and mode shapes of the underlying LTI structure from the CSLDV measurements.

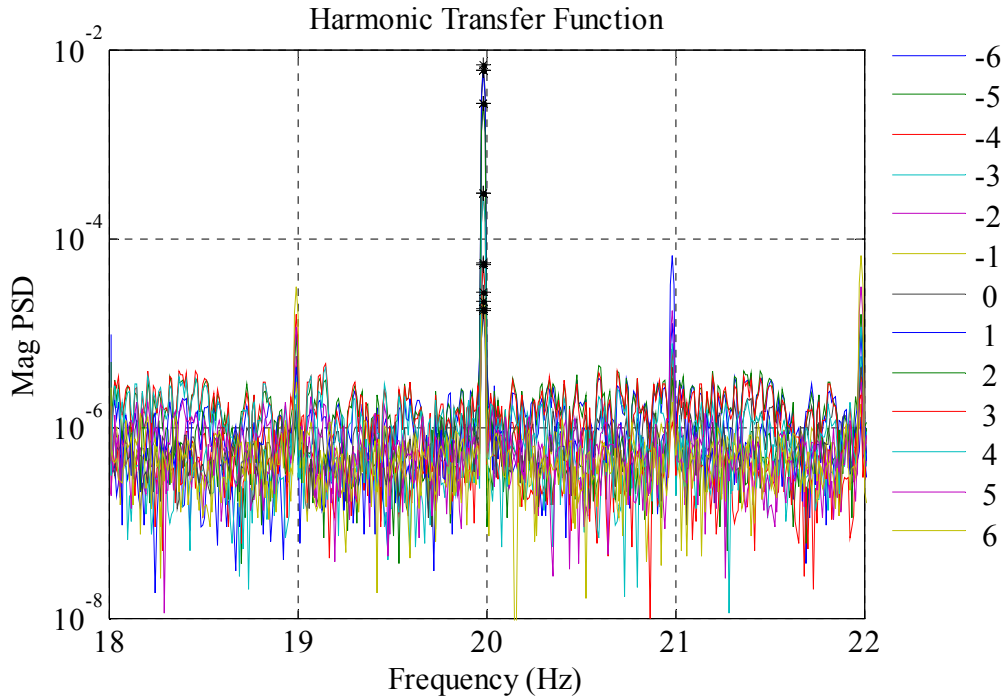


Figure 11 Harmonic transfer function

The peak-picking method was used to identify the mode vector at the excitation frequency of 20Hz. The acquired Fourier coefficients were then used to construct the

operational shape along the laser path using Eq. (33). Figure 12 shows the reconstructed shapes when the beam was supported with and without the load spreader plate. The operational shapes agree well with those from the point-by-point test but have much higher spatial resolution. In continuous-scan, the sampling frequency was 5120Hz and the scan frequency was 3Hz, resulting in 1708 points per scan cycle after resampling, while the point-by-point scan only measures 59 points. The shapes from CSLDV have a smaller imaginary part as well, indicating that the noise level might be smaller than in the point-by-point scan. Details about the uncertainty in the reconstructed mode shape will be discussed in the next section.

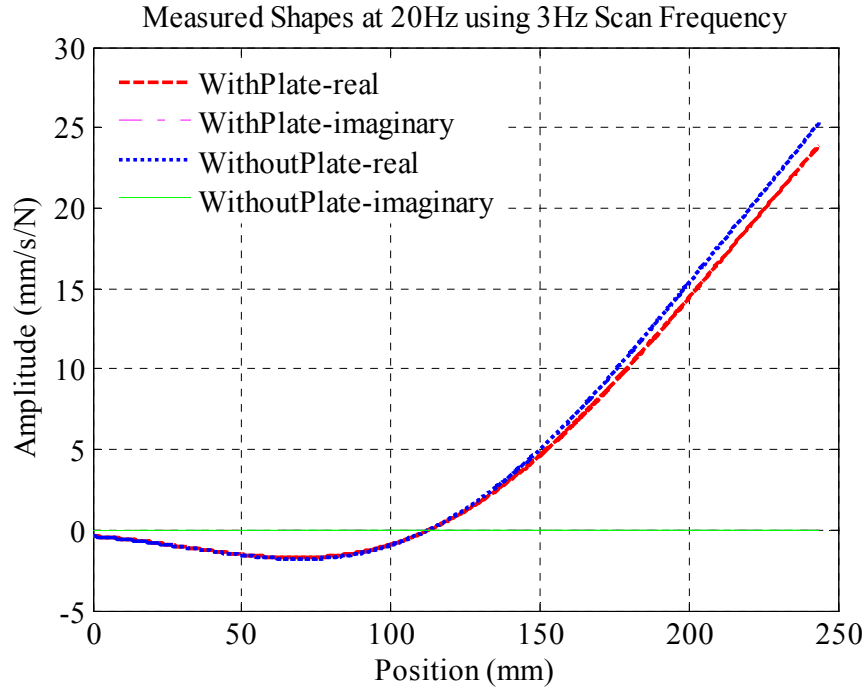


Figure 12 Mode shapes acquired using harmonic transfer function

The polynomial approach was used to identify the operational shapes of the beam from the same data set. In the polynomial approach, the amplitude and phase at each harmonic are obtained by frequency response analysis [51]. Since the excitation frequency ($\omega = 20\text{Hz}$) and the scan frequency ($\omega_A = 3\text{Hz}$) are exactly known, the frequency line of each harmonic can be

located with $\omega - n\omega_A$, where n is the harmonic order used to reconstruct the operational shape. The amplitude and phase at each harmonic are then obtained by computing the correlation function between the measured velocity and a sine (or cosine) signal at the harmonic frequency $\omega - n\omega_A$. Note that the phase at each harmonic should be corrected with an integer multiple of the mirror phase angle according to the harmonic order, as described in Eq. (6). The amplitude is then assigned either a '+' or '-' sign according to the corrected phase at the harmonic. The amplitudes at the harmonics from 0 to the n^{th} order are then transformed to the polynomial coefficients using Eq. (7), and the operational shapes at 20Hz are reconstructed using Eq. (5), as shown in Figure 13. The shapes are almost identical to those obtained via the harmonic transfer function except for the scale differences. The reason is because the polynomial approach only processes the output velocity signal while the harmonic transfer function processes the velocity signal and the forcing signal together in a transfer function manner.

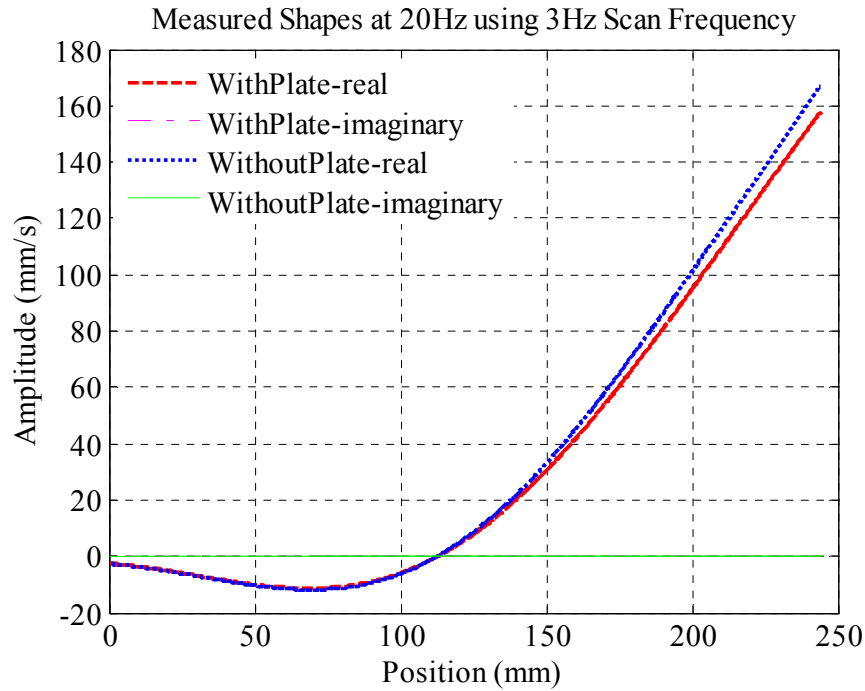


Figure 13 Mode shapes acquired using polynomial approach

The same data set was processed with the lifting approach. The measured velocity signal was resampled to generate 1708 samples per scan cycle. After resampling, the responses at the same location along the laser path were grouped together to form 1708 sets of signals. The lifted responses have a constant time delay between each set and the sampling frequency in each set becomes the laser scan frequency at 3Hz. Since the beam was excited at 20Hz, the lifted responses at each measurement location vibrate at 20Hz as well. Hence, a 20Hz sinusoidal signal was fitted to each set to find the vibration amplitude and phase. Then, these amplitudes were divided by the amplitude of the excitation force to compute the transfer functions. Figure 14 shows the acquired operational shapes from the lifting approach. The shapes are slightly noisier compared to those from the harmonic transfer function or the polynomial approach. However, this does not prove that the lifting approach is not as accurate. The harmonic transfer function and the polynomial approach use a truncated Fourier series or polynomial function to approximate the operational shape. Therefore, the reconstructed shapes are always smooth due to the nature of the Fourier series representation and the polynomial representation. On the other hand, the lifting approach can be thought of as a ‘discrete’ method that automatically includes all harmonics at each measurement location, because these harmonics are aliased to a single frequency between zero and half of the scan frequency. If there were discontinuities along the laser path, e.g., a hole, high order harmonics are necessary to accurately describe the mode shapes, and these higher order harmonics are usually contaminated with noise. With the lifting approach, the responses at the discontinuities can simply be discarded and do not affect the accuracy of the reconstructed mode shape.

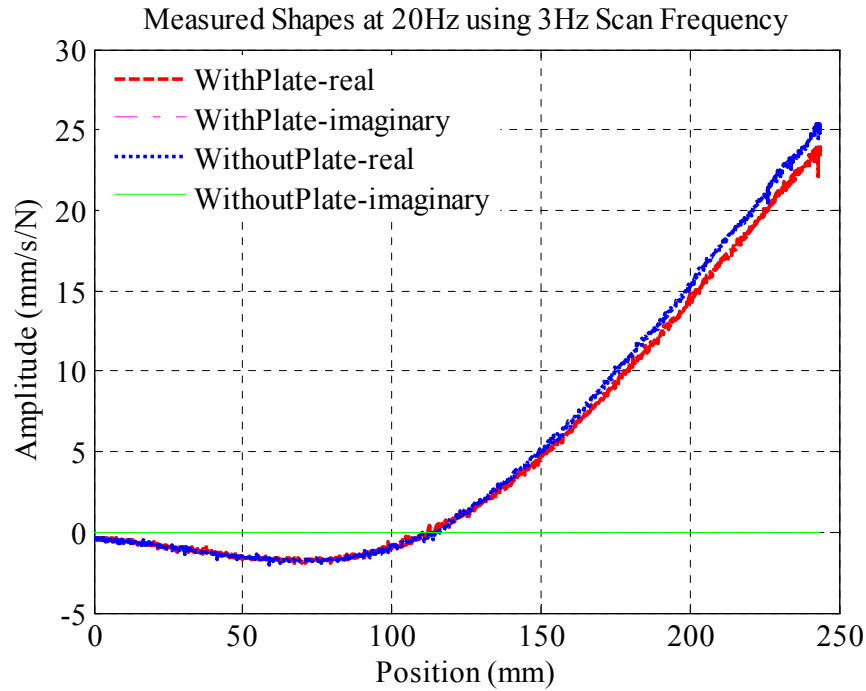


Figure 14 Mode shapes acquired using lifting approach

Table 2 compares the Modal Assurance Criteria [72] (MAC) values between the reconstructed operational shapes from CSLDV and the operational shape from the scanning LDV. The MAC values are almost 1 for the shapes from all three signal processing approaches, indicating any of them is capable of acquiring mode shapes as accurate as the scanning LDV. However, the advantages of continuous-scan are obvious. CSLDV took only 102.4s to acquire an operational shape with 1708 points, while scanning LDV took 24mins to measure only 59 points. The shape changes after installing the load spreader were computed in the same manner as in the point-by-point test. The maximum changes identified using CSLDV tests are slightly larger than 5%, while the maximum change identified by scanning LDV is about 3.67%. The difference might be due to the problem that the continuous-scan and point-by-point scan do not cover the same length of the beam.

Table 2 MAC values and maximum changes in mode shapes

Method	MAC-No Plate	MAC-With Plate	Max Change
Scanning LDV	1	1	3.67%
Polynomial Approach	1.0000	1.0000	5.59%
Harmonic Transfer Function	1.0000	1.0000	5.67%
Lifting approach	0.9999	0.9999	5.20%

3.5 Uncertainty in Reconstructed Operational Shape

The spatial resolution of the identified mode shape from CSLDV depends on the sampling frequency and the scan frequency, therefore it can be surprisingly high because the laser is capable of sampling up to 10MHz. However, since the mode shape is built from a truncated Fourier series representation, the accuracy of the reconstructed shape depends on the number of harmonics that stand out above the noise floor.

To study the uncertainty in the reconstructed operational shape, $n = -10 \dots 10$ was used to modulate the measured velocity signal. Figure 15 shows the amplitudes and phases of the Fourier coefficients picked at 20Hz from the harmonic transfer function. Note that the modulation is essentially a process of shifting all sideband harmonics in Figure 10 to the frequency line at 20Hz, so the identified Fourier coefficients actually represent the values at these harmonics. It seems that these Fourier coefficients are not of equal quality, some strongly excited ($n = -2 \dots 2$) by the 20Hz forcing signal, while others may be contaminated by the speckle noise ($n = -10 \dots -7, 7 \dots 10$). For a lightly damped structure such as the aluminum beam, the mode shape is mostly real, so the Fourier coefficients should be symmetrical about the center line ($n = 0$) in Figure 15. However, as listed in the table, the amplitudes and phases of the Fourier coefficients after the 6th order differ dramatically from those of the corresponding

negative order. It is obvious that the Fourier coefficients (or the harmonics) after the 6th order are mostly dominated by noise, therefore $n = -6 \dots 6$ was used to construct the operational shape in the previous section. In addition, to form a real mode shape, the phase difference between any two Fourier coefficients should be either 0° or 180° . For example, the phase at the 1st harmonic is 80.18° , and the phase at the 2nd harmonic is 78.79° , about 1.39° apart. The phase at the 3rd harmonic is -99.42° , about 179.21° from the 2nd harmonic. These small phase differences could be from the mirror phase lag or the speckle noise [73], and can be automatically compensated for by rotating the Fourier coefficient vector in the complex plane.

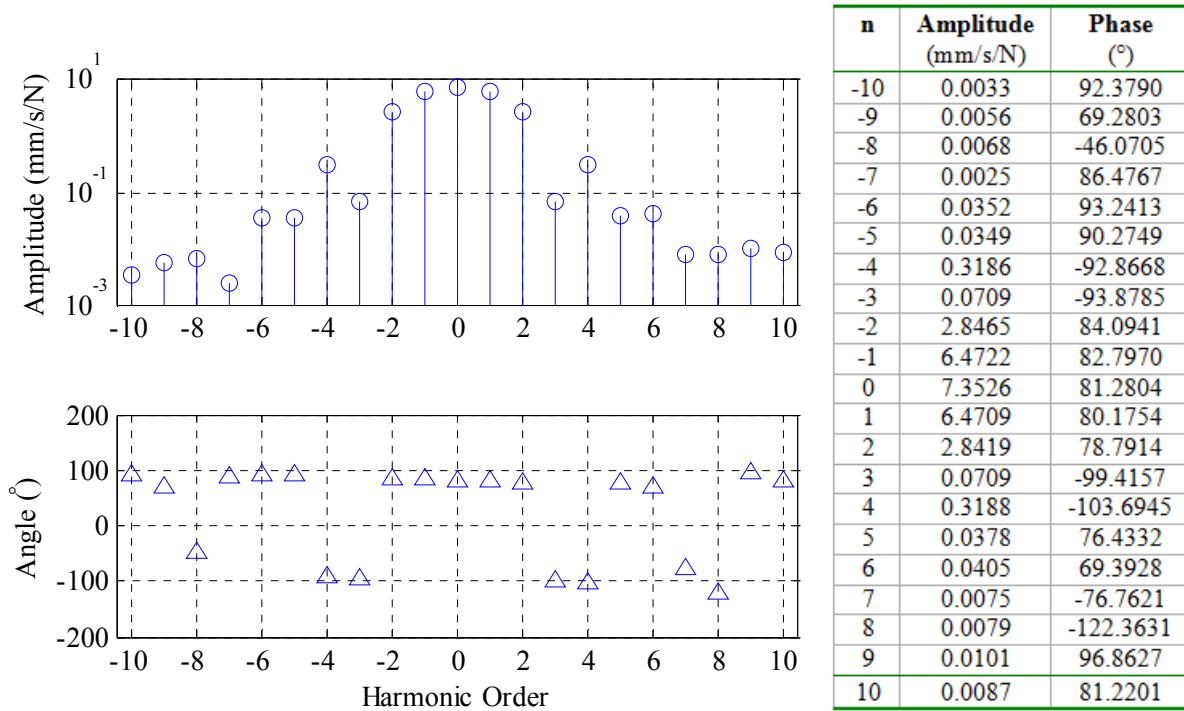


Figure 15 Amplitude and harmonic of the operational mode at 20Hz

The Fourier coefficients in Figure 15 were used to construct the operational shape at

20Hz using $\Phi(t) = \sum_{n=-p}^p C_n e^{jn\omega_A t}$, where ω_A is the laser scan frequency. Figure 16 shows the

reconstructed operational shape with different orders of Fourier coefficients and the number in

the legend indicates the highest harmonic order included in the reconstruction. When the Fourier coefficients up to the 3rd order are used, the operational shape is noisy and inaccurate because a strong harmonic (the 4th order) is missing. As the number of Fourier coefficients increases, the reconstructed operational shape converges to a more accurate shape.

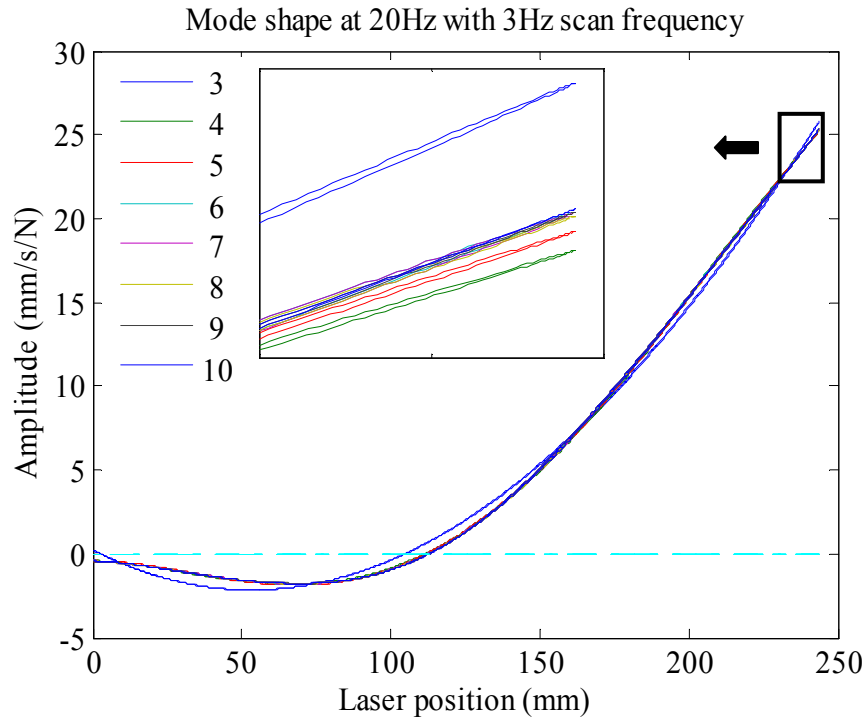


Figure 16 Reconstructed operational shape using different order of harmonics

However, this does not indicate that one should include as many harmonics as possible in the reconstruction. Revisiting the Fourier series description of the time periodic mode shape, in practice, the complex Fourier coefficient C_n may be contaminated with noise. Assuming $C_n = \bar{C}_n + \tilde{C}_n$, where \bar{C}_n is the accurate Fourier coefficient and \tilde{C}_n is the noise incurred by the mirror or laser speckle, if all important harmonics are included with $n = -p \dots p$, then the noise in the reconstructed shape is smaller than $(2p+1) \left| \tilde{C}_n \right|_{\max}$ plus some truncation errors of the Fourier series expansion. Figure 17 show the reconstructed mode shape using the harmonics up to the 7th

order (blue line). The noise level in CSLDV is assumed to be 0.01mm/s/N , which is about the amplitude of the 7th Fourier coefficient in Figure 15, though the real noise level is probably an order of magnitude smaller. A Monte Carlo simulation is performed with the noise \tilde{C}_n having a random phase and random amplitude smaller than 0.01mm/s/N , and the reconstructed operational shapes are plotted with red dots in Figure 17. It is obvious that even in the worst scenario the reconstructed mode shapes are still accurate. The maximum noise of the reconstructed operational shape is 0.15mm/s/N using the Fourier coefficients $n = -7 \dots 7$. Since the maximum amplitude of the normalized shape is about 26mm/s/N , the noise takes about 0.6% of the maximum vibration amplitude, which is similar to the noise level when the laser scans on a stationary beam.

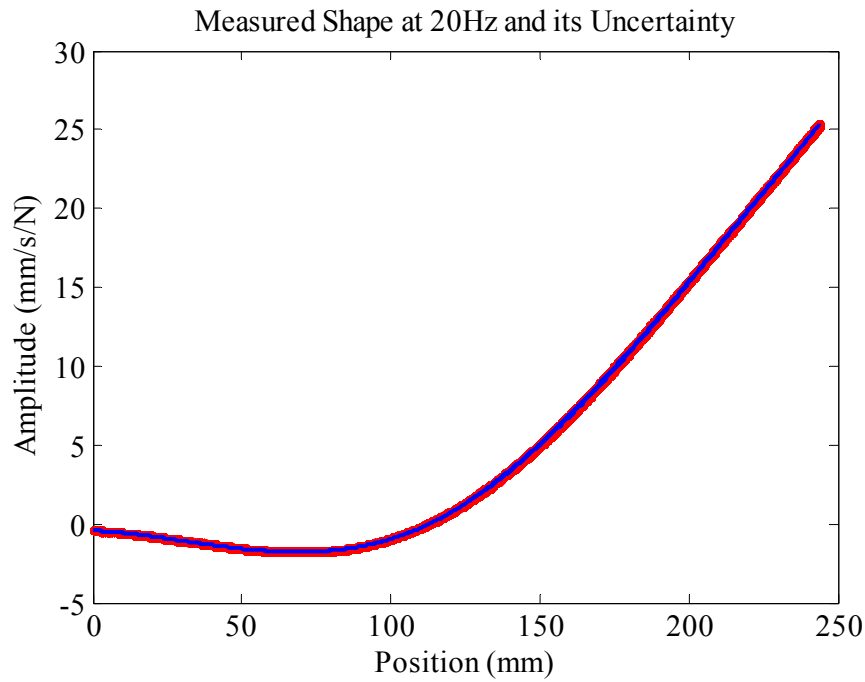


Figure 17 Operational shape reconstructed with random noise

3.6 *Summary*

This chapter explored the use of CSLDV and the harmonic transfer function in extracting the operational shape of a cantilever beam under sinusoidal excitation. Two boundary conditions were studied; one with a point support in the middle of the beam, the other with an additional load spreader added. The speckle noise was evaluated when the beam was kept stationary. It was found that the speckle noise level and the standard deviation increase with scan frequency. The noise increases from 0.70mm/s to about 10mm/s as the scan frequency increases from 0Hz to 100Hz. The actual noise level also depends on the surface properties and the sensitivity setting, but the numbers at least give an idea of the noise level and the capability of CSLDV to detect and measure minute motion.

Then, the responses of the beam under the two boundary conditions were measured with CSLDV. The harmonic transfer function, polynomial approach and lifting approach were used to extract the operational shapes from the same data set. The acquired operational shapes were compared with those from a conventional point-by-point scanning test. It was found that the harmonic transfer function and the polynomial approach provide almost identical operational shapes. However, the polynomial approach uses only the output signal, therefore needs special handling to obtain the normalized shape. The operational shapes from the lifting approach are noisier. However, this does not indicate that this method is less accurate than the harmonic transfer function or the polynomial approach. The accuracy of the reconstructed mode shape depends on the number of harmonics that stand out above the noise floor. In the harmonic transfer function and polynomial approach, a truncated set of sideband harmonics are used to form the operational shape, using either a Fourier series or polynomial function. In contrast, the lifting approach aliases all sidebands to a single frequency between zero and half of the scan

frequency. Therefore, the lifting approach automatically includes all harmonics when computing the operational amplitude at each pseudo-measurement location. The lifting approach may also be beneficial when the operational shape is no longer smooth, e.g., a hole exists on the laser path. In this case, high order harmonics (usually noisy) are necessary to reconstruct an accurate operational shape, whereas in the lifting approach one can just delete the responses at the discontinuity.

This chapter also provides guidance to improve the speckle noise in future tests using CSLDV. The scan frequency and sampling frequency should be as small as possible but still sufficient to identify all frequencies of interest. The laser sensitivity should be selected such that the maximum velocity is around 50%~60% of the full measurement range. If possible, the test should be performed on retro-reflective tape at the optimal standoff distance of the laser to achieve higher signal to noise ratio.

4 Measuring Translational and Rotational Velocities using CSLDV

In this chapter, the harmonic transfer function was used to process measurements from a continuous circular-scan. The speckle noise on various surfaces was studied using different scan frequencies and circle sizes. The translational and rotational velocities of a downhill ski were identified.

4.1 Introduction

A laser Doppler vibrometer typically measures the translational velocity at a point along the direction of incident light, but it can also be used to measure the rotational velocities of a structure. Ewins et al. [52] proposed a continuous-scan scheme using a short line or a small circle to measure the translational and the rotational vibration simultaneously. He proved that the translational and rotational velocities are related to the central harmonic and its two sidebands in the measured velocity spectrum. The forcing signal was used as a reference to compute the transfer function of the translational velocity, while the product of the forcing signal and mirror driving signal was used for the transfer functions of the rotational velocities. This procedure was later adopted by Salman et al. to study the vibration of a human hand [74]. In both of these works the authors used a demodulation technique to recover the translational and rotational velocities from the center and sideband responses.

This work aims to develop an alternative algorithm based on the harmonic transfer function concept that was introduced in Section 2.3. It has been shown in Section 1.5 that when the laser scans a closed periodic pattern, e.g., a circular path, the measurement from CSLDV can be treated as periodic, and therefore processed with the harmonic transfer function that allows

normalized velocities to be extracted under virtually any type of input. With this algorithm, the translational and rotational velocities are related to the 0th and 1st order Fourier coefficients in the acquired mode vector from the harmonic transfer function, and measured velocities at multiple points can be easily stitched together to create mode shapes of the underlying structure. This is exactly like acquiring mobility in conventional experimental modal analysis, except that with a circular-scan pattern, both the translational and rotational velocities are measured simultaneously. Moreover, speckle noise is always a key consideration in CSLDV. Laser speckle is formed when coherent light scatters from an optically rough surface and interferes on the photo detector. The effect of focus size, target surface roughness, scan speed, etc. on speckle noise level has been investigated extensively [36, 38, 71, 75-77]. In this work, the influence of circle size, scan frequency and surface quality on the speckle noise level in the circular-scan will be studied, in order to provide guidance for future tests.

The rest of this chapter is organized as follows: Section 4.2 reviews the harmonic transfer function concept with particular emphasis on how to interpret the response spectra of a continuous scan measurement; Section 4.3 discusses the influence of circle size and scan frequency on noise level in circular-scan. In Section 4.4, the circular-scan approach is used to identify the deflection mode shapes of a downhill ski. The results are compared with those from a conventional point-by-point scanning LDV. In Section 4.5, rotational velocities and the local slopes are obtained from the circular-scan test with retro-reflective tape. Section 4.6 summarizes this chapter.

4.2 Measuring Rotational Velocities using CSLDV

Stanbridge and Ewins proposed that local rotational velocities could be obtained by scanning a short line or a small circle around the point of interest [52]. Figure 18 shows the scheme of employing a circular-scan pattern to measure translational and rotational velocities simultaneously. The basis for a line scan pattern is similar but simpler, and therefore not introduced in this work. Assuming the standoff distance from the laser source to the point of interest is large compared to the scan radius R , the incident laser beam can be treated as perpendicular to the surface during the scan. In addition, if the circle size is small, out-of-plane deformation inside the circle can be neglected. So, the vibration at the point of interest consists of only rigid body translation and rigid body rotation.

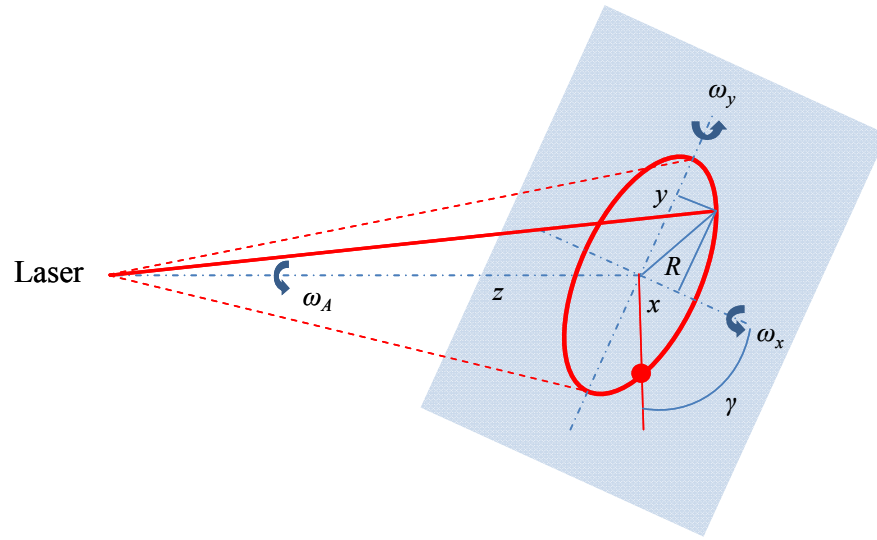


Figure 18 Scheme of measuring translational and rotational velocity using CSLDV

This work presents a methodology that works for any type of excitation, but the basic concept is easiest to explain if the structure is under sinusoidal excitation. In this case, the translational motion along the direction of the laser beam can be written as

$$V_z(t) = Z \cos(\omega t + \alpha) \quad (64)$$

where Z is the amplitude of the translational velocity, ω is the oscillating or the driving frequency, and α is the initial phase of the rigid translation. The angular motion at that point can be decomposed into two orthogonal principal rotations that have a 90° phase difference,

$$\begin{aligned}\omega_i &= \Theta_A \cos(\omega t + \beta) \\ \omega_j &= \Theta_B \sin(\omega t + \beta)\end{aligned}\tag{65}$$

Θ_A and Θ_B are the amplitudes of the principal rotations along the i and j principal axes, respectively, as shown in Figure 19. β is the initial phase of the rotational motion. Note that the principal axes i and j may not be the same as the inertial axis x and y . Their orientation with respect to the inertial reference frame x - y is denoted γ , and this is not known a priori and may be different at each measurement location.

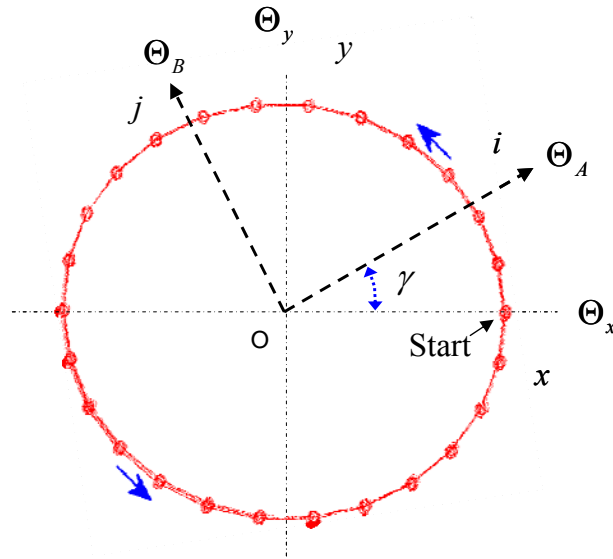


Figure 19 Circular-scan pattern (dots represent measurement locations)

The CSLDV signal is acquired digitally. In Figure 19 the red dots represent the locations on the circle path where the laser measurement is sampled. The number of samples in each cycle depends on the sampling frequency and the scan frequency (sometimes requiring resampling to

obtain an integer number). Suppose the laser starts scanning counterclockwise at the red dot on the x axis with a constant speed of ω_A , the measured velocity $V(t)$ contains three components; the translational velocity $V_z(t)$ along the incident laser, the velocity component along the laser beam introduced by the rotation $\omega_x(t)$, and the velocity component along the beam introduced by the rotation $\omega_y(t)$.

$$V(t) = V_z(t) + \omega_y(t)R \cos(\omega_A t) + \omega_x(t)R \sin(\omega_A t) \quad (66)$$

The rotational velocities along the x and y axis can be obtained using a rotation transformation about the z axis,

$$\begin{aligned} \omega_x &= \omega_i \cos(\gamma) - \omega_j \sin(\gamma) \\ \omega_y &= \omega_i \sin(\gamma) + \omega_j \cos(\gamma) \end{aligned} \quad (67)$$

Substitute Eq. (64), (65) and (67) into Eq. (66), and then simplify Eq. (66) using trigonometric functions,

$$V(t) = Z \cos(\omega t + \alpha) + R \frac{\Theta_B + \Theta_A}{2} \sin((\omega + \omega_A)t + \beta + \gamma) + R \frac{\Theta_B - \Theta_A}{2} \sin((\omega - \omega_A)t + \beta - \gamma) \quad (68)$$

Hence, the measured velocity $V(t)$ using circular-scan includes all translational (Z) and rotational velocities (Θ_A and Θ_B) at the point of interest. Figure 20 shows an example of the measured spectrum when the laser scans a small circle at ω_A (150Hz) on a beam that is excited at ω (13Hz). According to Eq. (68), the translational velocity Z and its phase α are obtained from the peak at ω . The rotational velocities Θ_A and Θ_B are recovered from the two harmonics at $\omega_A - \omega$ (137Hz) and $\omega_A + \omega$ (163Hz).

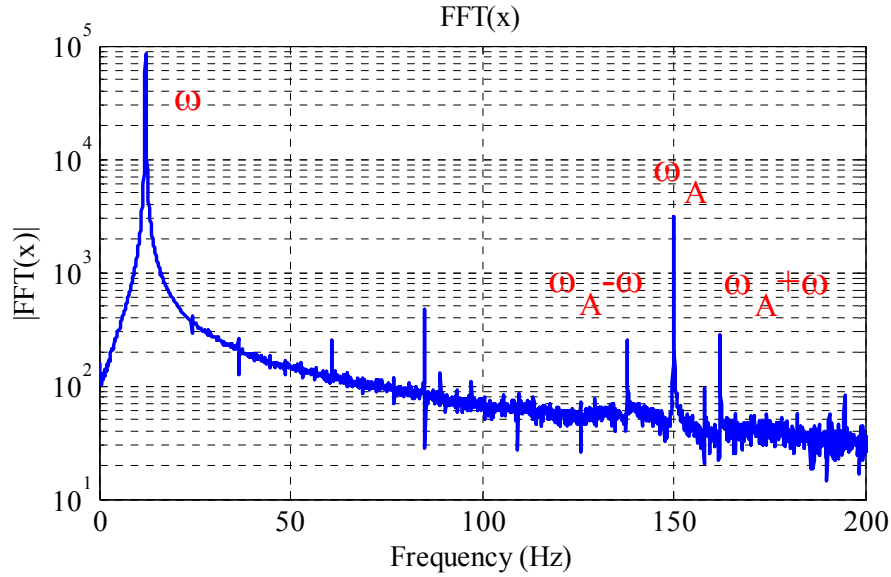


Figure 20 Spectrum of measured CSLDV signal with a 150Hz scan frequency

In Ewins' work [52], the forcing signal was used directly as a reference to compute the transfer function (or mobility) between the measured translational velocity and the input force. In contrast, to compute the rotational transfer function, the forcing signal was multiplied with the mirror driving signal and used as the reference. While this method was effective, it is more convenient to define a transfer function that directly relates both the translational and rotational velocities to the input force. The harmonic transfer function of linear time periodic systems is an alternative to describe this relationship. Since the noise is mostly from the speckle noise in the laser signal, an H1 estimator is used to experimentally estimate the harmonic transfer function, as follows,

$$\mathbf{G}(\omega) = \frac{E(\mathbf{Y}(\omega)U_0^H(\omega))}{E(U_0(\omega)U_0^H(\omega))} \quad (69)$$

Here $E()$ indicates the expected value. $\mathbf{Y}(\omega)$ is the exponentially modulated velocity signal, and $U_0(\omega)$ is the input spectrum. Note that for a general linear time periodic system, the

denominator would be a matrix of the cross power spectrum of the modulated inputs. In this case, at least several averages are required for the spectrum matrix to be invertible.

4.3 *Speckle Noise in Circular-scan*

The experimental validation of the proposed circular-scan algorithm was performed on a downhill ski. A ski is a complex structure formed by laminating several materials, and hence can be very challenging to model accurately. Figure 21 shows the experimental setup. The ski was hung using two soft bungee cords to obtain free-free boundary conditions. A shaker with a function generator was used to excite the ski. A load cell was installed on the tip of the stinger to record the input force applied to the ski, as shown in Figure 21b. The Polytec® PSV-400 (633nm laser) vibrometer with an external x-y mirror system [58] was used.

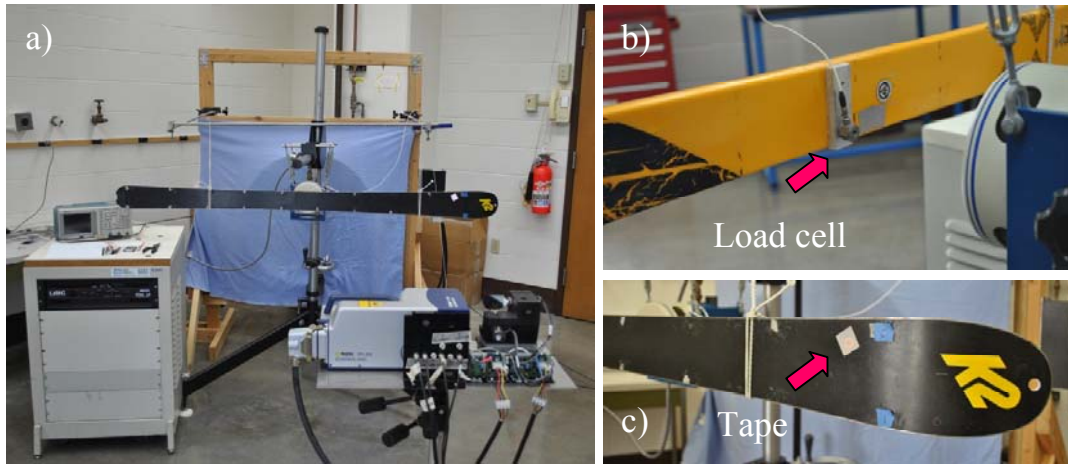


Figure 21 Experimental set up. (a) Testing scheme, (b) Load cell, (c) Retro-reflective tape

This section investigates the speckle noise in a circular-scan, specifically, the influence of scan frequency, circle size and surface quality on the noise level, such that a set of optimal experimental parameters can be selected for the following circular-scan tests. The scan frequencies tested were 20Hz to 300Hz in 20Hz steps. The mirror system used in this study was found to be significantly nonlinear when the scan frequency was higher than 300Hz. The scan

circle diameters ranged from 0mm to 12.8mm in 1.6mm steps, where diameter 0mm means the laser was kept at a stationary point. When the circle size is larger than 12.8mm, strong high order harmonics (>1) appear in the measurement spectrum, indicating significant elastic deformation along (or inside) the circle path. The ski was driven at 19Hz, and tests were repeated on three different surfaces; the black bottom of the ski, the yellow top of the ski and 3M[®] 7610 High Gain retro-reflective tape.

To estimate the noise level, a linear mode was fitted to the mode at 19Hz using the algorithm of mode isolation [78]. This linear mode was subtracted from the measured spectrum. Then, the harmonics that corresponded to rotational velocities were removed manually (See Figure 20). The rest was considered to be pure noise and transformed via an inverse FFT to the time domain. Figure 22 shows the measured velocity signals from the ski excited at 19Hz with the laser scanning an 8mm circle at 40Hz and 200Hz scan frequencies, respectively. The blue line is the original velocity time history, while the red line is the noise after removing the frequency component at 19Hz as well as the frequency components at the rotational velocities. The noise in the second plot is much higher, and is dominated by the 200Hz scan frequency. The mean value and the standard deviation of the absolute noise signals were computed for analysis.

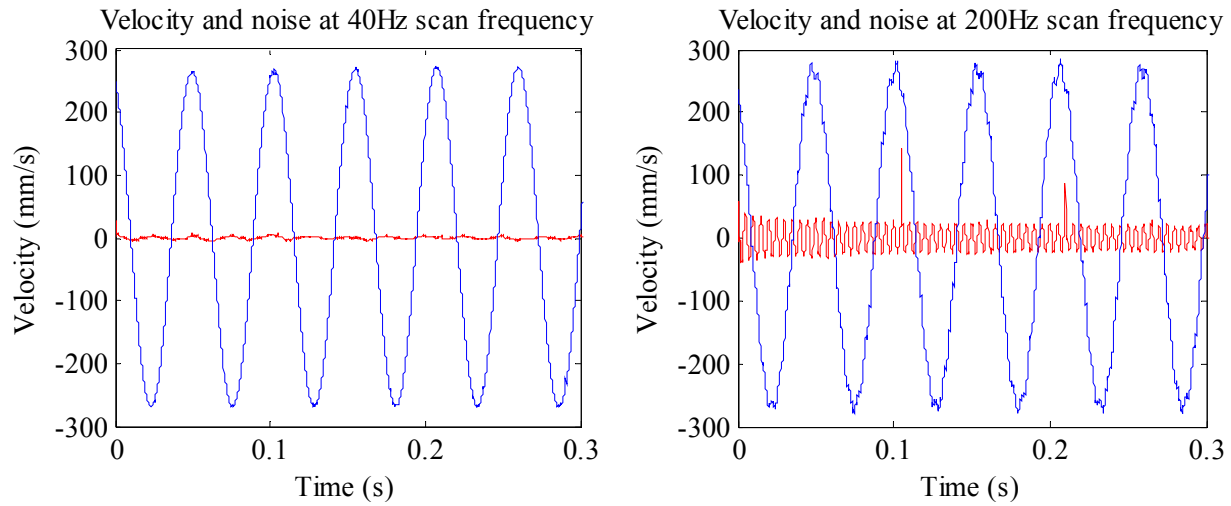


Figure 22 Noise level at 40Hz and 200Hz with an 8mm circle size. Blue line-measured velocity signal, Red line-noise in measured signal

Figure 23 shows the mean and the standard deviation of the noise when the laser scans on the retro-reflective tape. The tape is coated with micro-scale glass beads that reflect most of the light in a concentrated cone back to the detector [39]. The dashed horizontal lines in both plots represent the value from the stationary point test, where the noise level and standard deviation are the smallest among all tests. When the laser is continuously scanning, the noise level and the standard deviation increase with the scan frequency and the circle size. This phenomenon agrees with what was found in a previous work [71]. When the laser scans on a periodic path, the measured speckle noise contains mostly periodic components. The magnitude of this periodic noise increases severely with surface velocity, which is related to the scan frequency and the diameter of the scan circle.

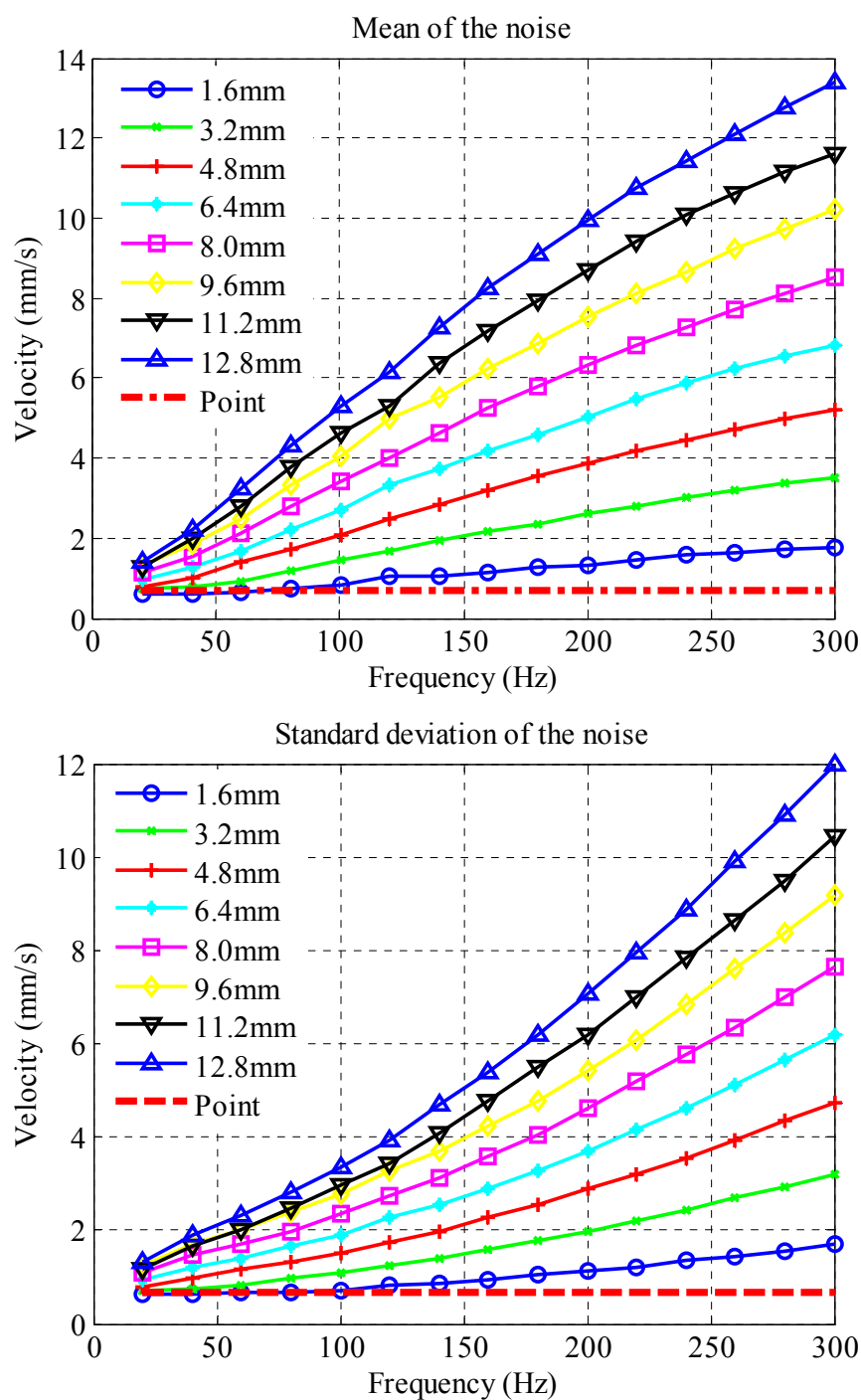


Figure 23 Noise level and standard deviation on retro-reflective tape

Figure 24 shows the mean and the standard deviation of the noise when scanning on the dark bottom surface of the ski. The noise pattern is similar to what was observed on the retro-reflective tape except for the first portion. On this surface, the mean of the noise at a stationary point is higher than some of the circular-scan results. When the laser hits a stationary point on a rough surface, the light is scattered in all directions randomly so only a small portion travels back to the detector. The laser could be located at a point where the light is dominated by a dark speckle so that little light returns to the detector until the sample or the laser spot moves. This may cause a dramatic change in noise level that partially explains the jagged nature of the noise level when the circle size is as small as 1.6mm. In contrast, when the circular-scan approach is adopted with an appropriate circle size, the signal level is always likely to be large over at least some portion on the circle path, so the total noise level seems to be reduced due to this ‘averaging’ effect. This would explain why the noise level and standard deviation decrease when the scan frequency increases to 60Hz. After 60Hz, increasing speckle noise becomes dominant, so the overall noise level increases again. In addition, it should be noted that the standard deviation of a circular-scan is, in general, much smaller on the black bottom surface, indicating a steady velocity signal in a circular-scan. This may be helpful in identifying translational and rotational velocities.

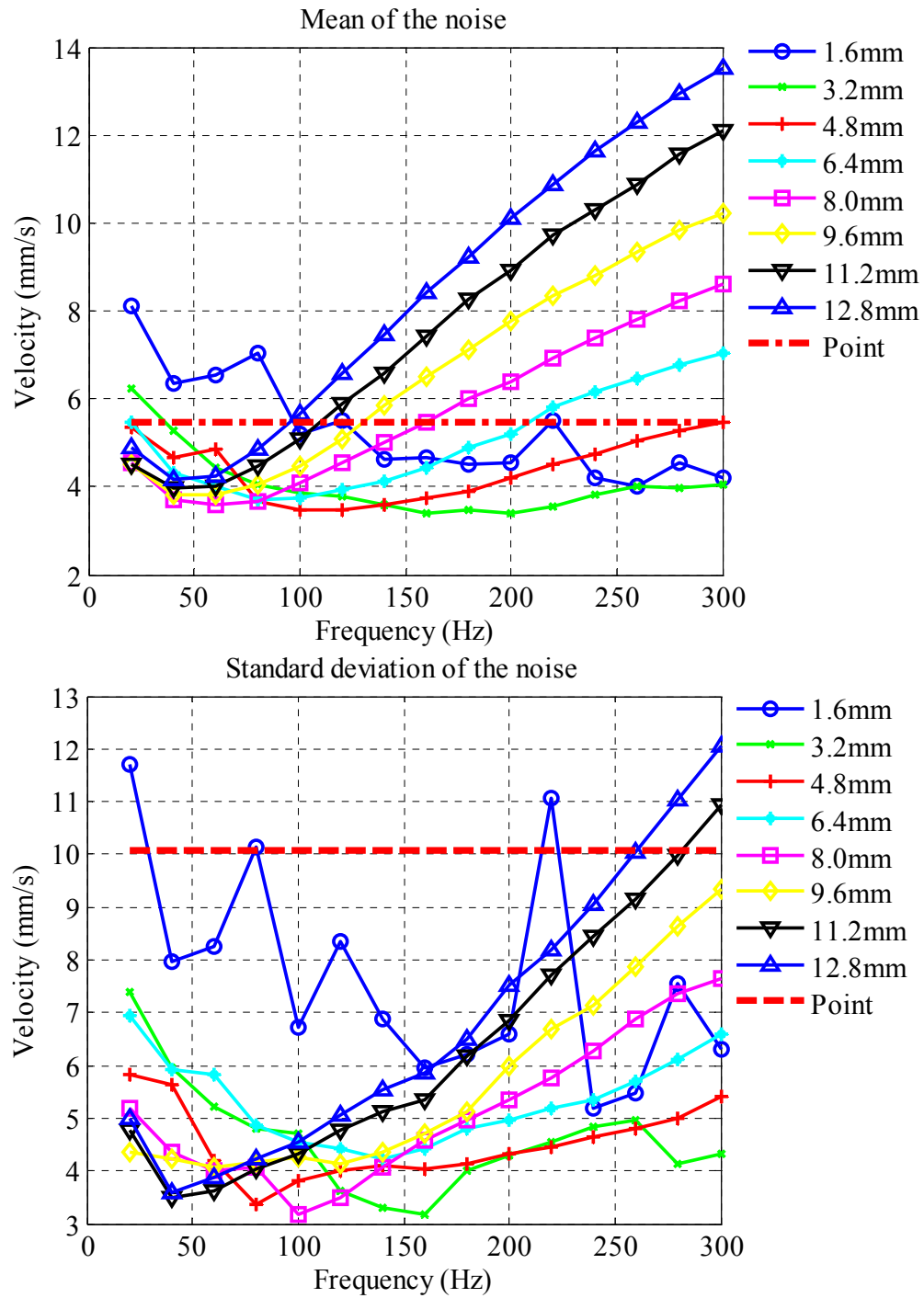
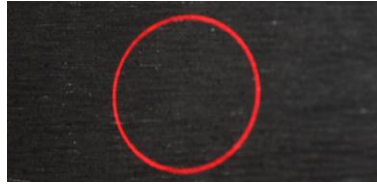


Figure 24 Noise level and standard deviation on black bottom surface of the ski

On the yellow surface, the noise level decreases more severely as the scan frequency increases from 0Hz to 120Hz, as shown in Figure 25. The noise and its deviation are much higher when the laser is kept stationary. The noise is smallest on this surface when scanning at 120 Hz with a circle size of 8mm. When the scan frequency is larger than 160Hz, the mean and standard deviation of the speckle noise again increase with the scan frequency and the circle size, suggesting that any gains in signal strength from scanning the laser are overcome by increased speckle noise. In addition, the overall noise level on the smooth yellow top surface is larger than those from the dark bottom surface or the retro-reflective tape. This difference is due to the mirror-like behavior of the optically smoother yellow surface, which leads to loss of signal especially when the incident angle is large. Insight into this result can be gained from previous studies on speckle noise and surface roughness [38, 39], where measurements on highly reflective surfaces are not recommended.

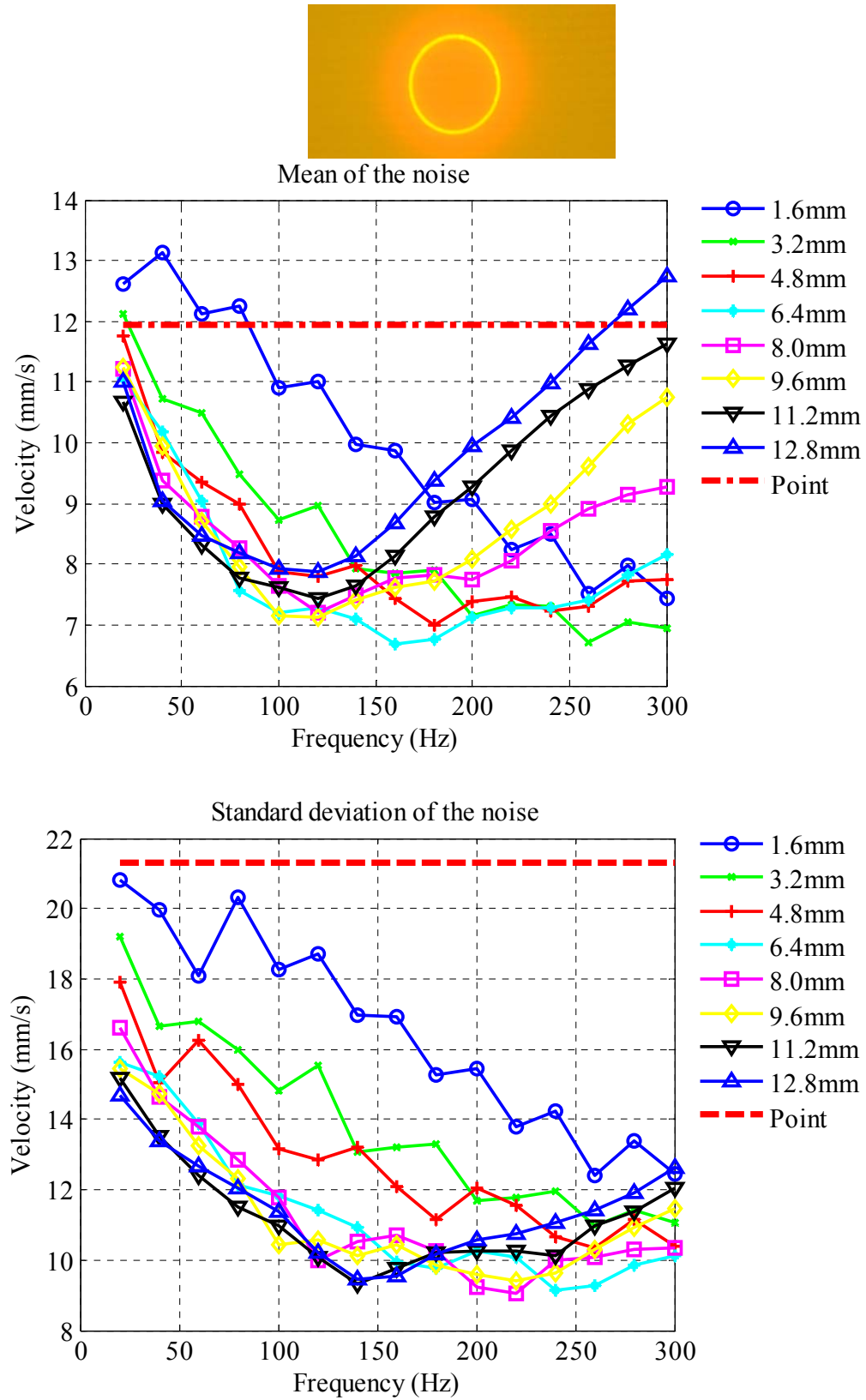


Figure 25 Noise level and standard deviation on Yellow top surface of the ski

This section has validated the hypothesis that laser speckle noise can be reduced on some surfaces by scanning a small circle rather than a stationary point. On the other hand, the lowest signal to noise level was found when scanning on retro-reflective tape so that this type of surface treatment is preferred whenever practical. In the following section, a set of circular-scan tests will be conducted on the black bottom surface directly to reconstruct the mode shapes of the ski under a swept-sine excitation. A scan frequency of 200Hz and a circle size of 8mm were selected so that both the noise level and standard deviation are at acceptable values.

4.4 Deflection Mode Shapes

Prior to the circular-scan test, a conventional hammer test was performed to identify the natural frequencies of the ski. Several frequency components were identified at 19Hz, 42Hz and 75Hz. A point-by-point Fast Scan was performed on the black bottom surface using the Polytec[®] software when the ski was excited at each of these natural frequencies. The laser scanned three lines along the ski with 40 points in each line, and 12 seconds at each point with a standoff distance of 2.6m. Figure 26 shows the acquired shapes. It is clear that the mode at 19Hz is the first bending mode of the ski (Figure 26a), and the mode at 42Hz is the second bending mode (Figure 26b). Note that the second bending mode has a node around the center of the ski. The shaker was installed slightly off-center to better excite this mode. The mode at 75Hz is the third bending mode (Figure 26c). An issue noticed in all identified mode shapes is that the amplitudes of the vibration shapes are close to zero at both ends of the ski. This is thought to be caused by the large angle between the incidence of the laser beam and the bending direction of the ski (the ski has curved ends). The detector may have lost most of the reflected laser signal, and the amplitudes of the shapes appear to be zero.

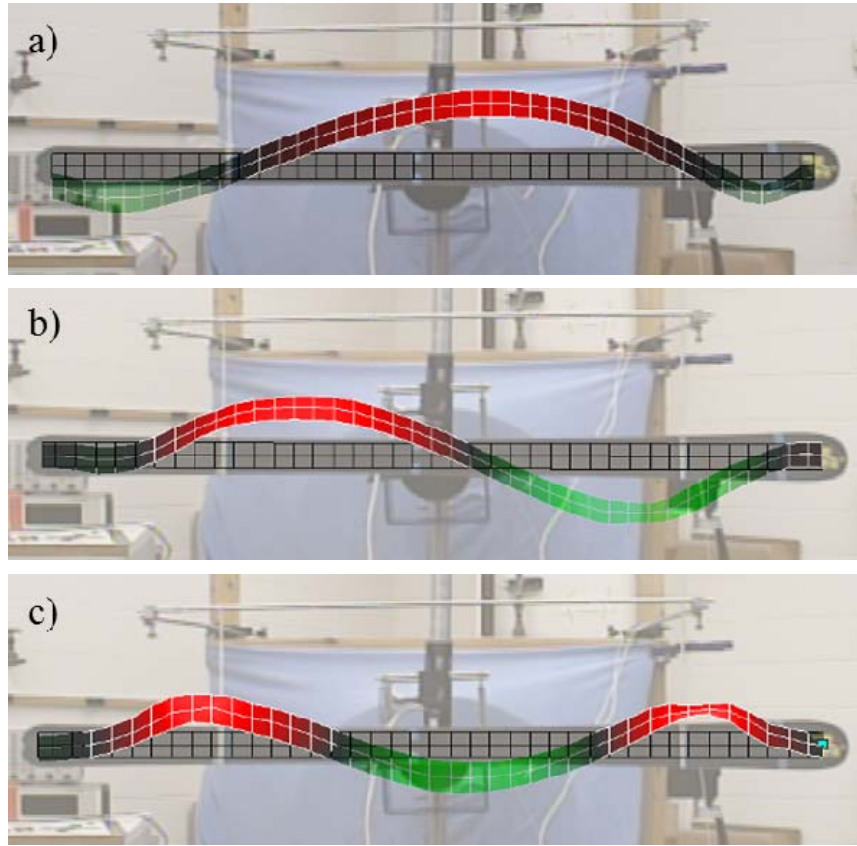


Figure 26 Identified mode shapes using fast scan. (a) 1st bending mode at 19Hz, (b) 2nd bending mode at 42Hz, (c) 3rd bending mode at 75Hz

The conventional scanning LDV test provides the basic mode shapes of the ski. A linear swept-sine test was then performed to validate the proposed circular-scan algorithm based on the harmonic transfer function. The shaker swept from 30Hz to 100Hz so only the second and third bending modes are well excited. The sweep time was 15 seconds from 30Hz to 100Hz and 15 seconds for the return. Only half of the ski was tested in order to keep the angle of the laser small and eliminate the distortion that was seen above near the ends of the ski. The measurement grid included 2 lines of points with 28 measurement points along each line. The total test duration at each point was 200 seconds to allow multiple averages.

Figure 27 shows the normalized mode shapes measured using the point-by-point scan approach as well as the circular-scan approach, with a 200Hz scan frequency and a circle size of 8mm. The zero position represents the location of the shaker. The identified second and third bending mode shapes agree well with the corresponding shapes from the scanning LDV test in Figure 26. However, it is obvious that the mode shapes from circular-scan test are much smoother than those from the point-by-point test. The reason for this difference is that the circular-scan approach provides a better signal to noise ratio on the rough surface of the ski (with the appropriate scan frequency and circle size, as was discussed in detail in the previous section). For example, with the conventional method, the measurement is inaccurate when the point is on the bungee cord. On the other hand, when the laser was scanning a circle around the point at $x=0.5\text{m}$ from shaker, part of the circle landed on the bungee cord but part does not. So although there is some error in the second bending mode shape near $x=0.5\text{m}$ in Figure 27b, it is not as severe as that from the traditional method.

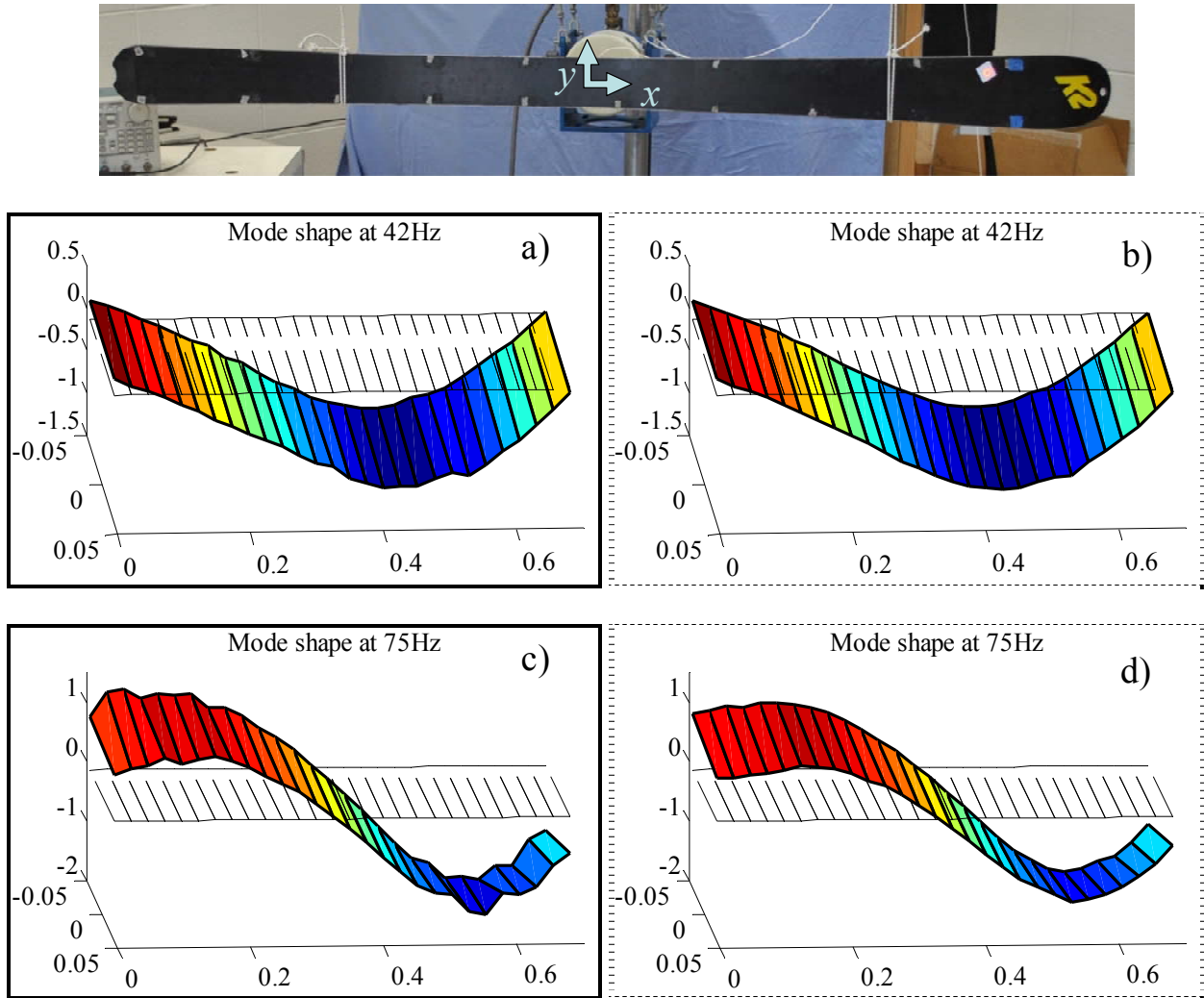


Figure 27 Identified mode shapes of half-ski(vertical axis is amplitude) (a) Mode at 42Hz by point measurement, (b) Mode at 42Hz by circular-scan, (c) Mode at 75Hz by point measurement, (d) Mode at 75Hz by circular-scan

4.5 Rotational Velocity and Local Slope

This section makes use of the harmonic transfer function to interpret measurements from the circular-scan, in order to compute the translational and rotational velocities simultaneously. To estimate the harmonic transfer function, $n = -2:2$ was used to form the exponentially

modulated output signals as $y_n(t) = y(t)e^{(i\omega + in\omega_A)t}$, where $y(t)$ was the measured signal. An accurate scan frequency ω_A is critical in this process. The phase errors in $e^{(i\omega + in\omega_A)t}$ accumulate with time if the scan frequency is inaccurate, which is usually the case when the scan frequency is high. Therefore, a multi-sine signal was fitted to the recorded mirror output signal to find the accurate scan frequency. This revealed that when the mirror was driven at 200Hz, the scan frequency was actually 200.0153Hz. The mirror signals, velocity signal and the input force were then resampled so that there were an integer number of measurement points in each scan cycle. For example, when the laser scanned at 200.0153Hz, the resampled measurement had 26 points on each circle, as shown in Figure 19,

The input signal and 5 modulated output signals were then broken into 30 second-long sub-blocks with approximately 75% overlap between neighboring blocks, producing 23 sub-blocks over the 200 second time history. These 23 sub-blocks must each start at the same location on the scan cycle to maintain a constant orientation angle γ of the rotational velocities (as seen in Figure 19). Therefore, the previous resampling procedure of generating integer number samples in each cycle is necessary. A Hanning window was applied to each block to reduce the leakage. Once the principal rotational velocities Θ_A and Θ_B of a mode were identified from the sidebands, the slope of the deflection shape along the x axis could be obtained by projecting the principal rotational velocities to the y direction using the phase angle γ at each measurement location, and similarly for the slope along the y axis.

Figure 28 shows the harmonic transfer functions on the dark bottom surface and on the retro-reflective tape measured at the same point close to the shaker. As was discussed earlier, the form of a harmonic transfer function is similar to the transfer function of a single-input multiple-output linear time invariant system. The harmonic transfer function between the output Y_i and

input U_0 is $G_{i,0}$, which corresponds to the i^{th} line in Figure 28. The amplitudes of $G_{-1,0}$ and $G_{1,0}$ are related to the principal rotational velocities, and have much smaller amplitudes compared to the translational velocity at $G_{0,0}$. Therefore, rotational velocities are more vulnerable to the speckle noise than translational velocities. Theoretically, according to Eq. (68), the amplitudes of $G_{-2,0}$ and $G_{2,0}$ should be zero when the elastic deformation is neglected. However, this is usually not the case experimentally, as shown in Figure 28a. The amplitudes of $G_{-2,0}$ and $G_{2,0}$ are close to those of $G_{-1,0}$ and $G_{1,0}$. This is because the speckle noise level is larger on the black bottom surface than that on the retro-reflective tape. Therefore, even though the circular-scan could reduce the noise level, the identified rotational velocities would be more accurate on retro-reflective tape.

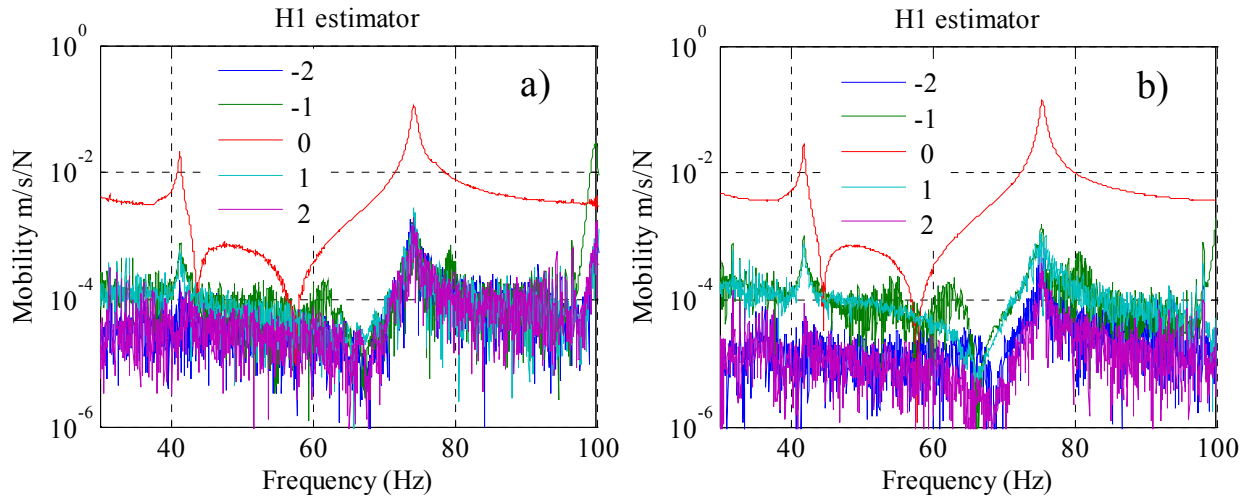


Figure 28 Harmonic transfer functions of circular-scan at the same point, (a) On black bottom surface, (b) On retro-reflective tape

Figure 29 shows the harmonic transfer function in Figure 28b that is fitted with the algorithm of mode isolation [9]. It appears that the identified modes reduce the harmonic transfer function essentially to noise (red line in Figure 29). The identified amplitudes and phase for the second and third bending modes are listed in Table 3. The amplitudes of the $G_{-1,0}$ and $G_{1,0}$

terms, which correspond to rotation, are an order of magnitude smaller than that of the $G_{0,0}$ term, which corresponds to the translational velocity at that measurement location.

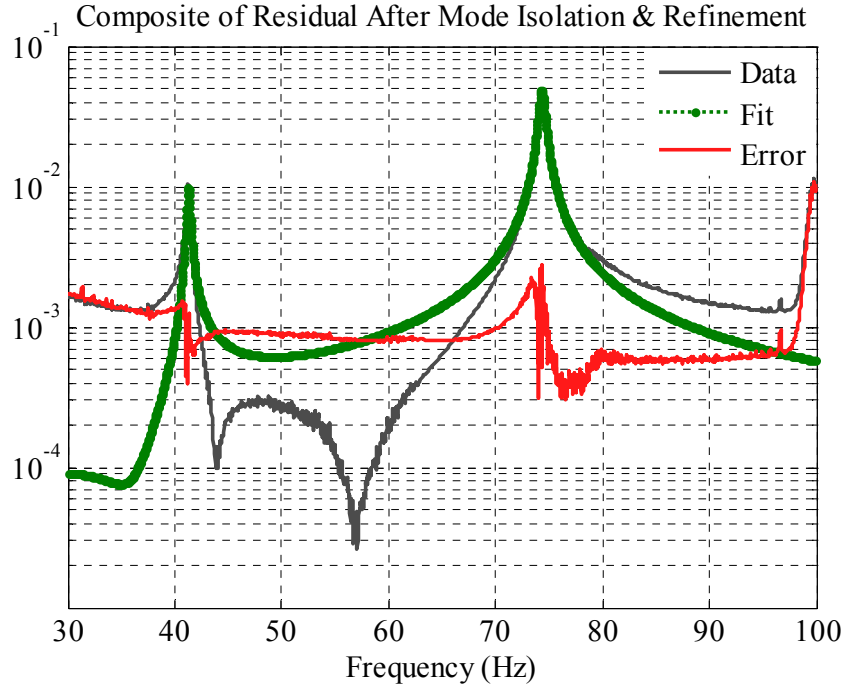


Figure 29 AMI fit of the harmonic transfer function

The rotational and translational velocities were computed according to Eq. (68), and the velocities are listed in Table 3 as well. It was found that for the second bending mode at 42Hz, the principal rotational velocity Θ_A is the dominant rotation at the measurement location close to the shaker. It has a magnitude of 0.3816rad/s/N and is orientated approximately 80 degrees from the longitudinal direction of the ski. The principal rotational velocity Θ_B has the magnitude of 0.0641 rad/s/N and is oriented 90 degrees from Θ_A . This result agrees with the experimental observation that the rotational motion associated with bending modes should be perpendicular to the longitudinal direction of the ski. The rotational velocities of the third bending mode at 75Hz have larger angles with respect to the longitudinal direction of the ski. The principal rotational

velocity Θ_A has a magnitude of 0.8053 rad/s/N and an orientation of 34 degrees, and has a slightly higher noise level.

Table 3 Measured translational and rotational velocities from circular-scan

Mode at 42Hz					
Mode shape	Amplitude (mm/s/N)	Phase angle (degree)	Velocities	Amplitude	γ Angle (degree)
$G_{-1,0}$	0.9	16.0369	Θ_A	0.3816 rad/s/N	79.9076
$G_{0,0}$	26	-166.4050	Z	26 mm/s/N	/
$G_{1,0}$	0.6	-4.1478	Θ_B	0.0641 rad/s/N	169.9076
Mode at 75Hz					
Mode shape	Amplitude (mm/s/N)	Phase angle (degree)	Velocities	Amplitude	γ Angle (degree)
$G_{-1,0}$	22	25.7603	Θ_A	0.8053 rad/s/N	34.0818
$G_{0,0}$	252.3	-0.5437	Z	252.3 mm/s/N	/
$G_{1,0}$	10	-86.0761	Θ_B	0.2872 rad/s/N	124.0818

The above results are from the measurement at a single point. The measurement was repeated on the retro-reflective tape in a 4×10 grid that was evenly distributed along one half of the ski. The translational and rotational velocities at all points were computed in the same manner. Note that the orientations γ of principal rotational velocities are different from one point to another. Figure 30 shows the orientations and amplitudes of principal rotational velocities at all measurement locations for the second bending mode at 42Hz. The first plot overlaps the rotational velocities with the deformation shape (Figure 30a, the color representing the amplitude of deformation). It can be seen that the orientations and amplitudes of principal rotational velocities are consistent with the observed shape at most points.

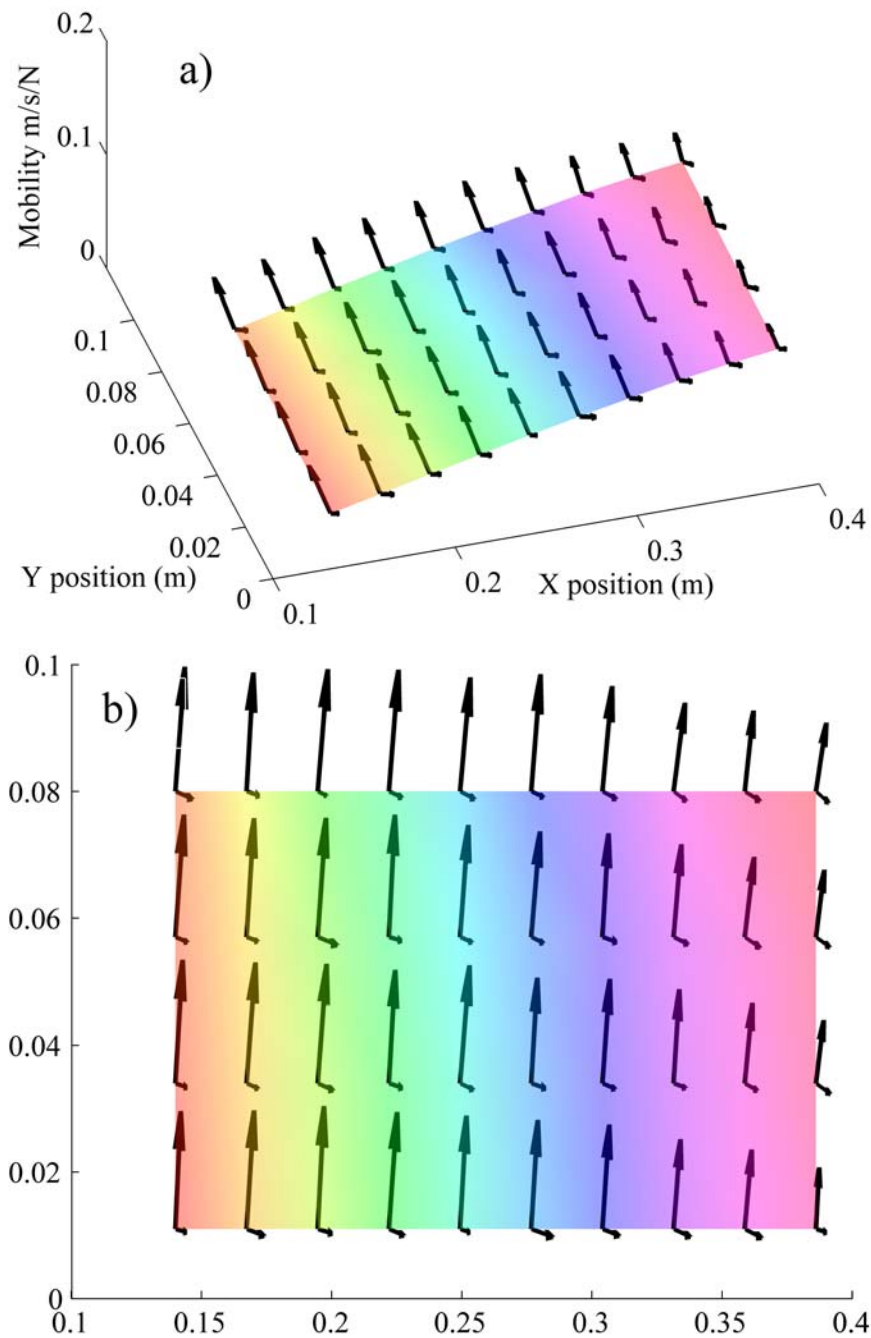


Figure 30 Translational and rotational velocities for the first mode

The ski has a large principle rotation (about 80 degrees from the x axis) that is caused by the deflection in the longitudinal direction. The amplitude of this principle rotation decreases from the center of the ski to the edge. A very small rotation was observed (about -10 degrees

from the x axis), which could be the torsional motion of the ski due to the misalignment of the shaker. The amplitude of this rotation seems to increase from the center of the ski to the edge. Note that the short arrows in Figure 13 corresponding to this rotation were scaled to twice their original length.

To more easily visualize these results, the shapes of each mode were extracted along a single line and the curvature along that line was calculated in the bending direction. The result is shown in Figure 31 for the second and third bending modes along the top line. The principal rotational velocities at each measurement location were projected to the y axis to compute the local slopes along the longitudinal direction of the ski, which are shown as short red lines. The results suggest that the measured slopes agree very well with what would be expected based on the overall curvature of the mode shape. However, some errors are presented at the first three measurement locations in the third bending mode around 75Hz. This is perhaps due to the large amplitudes of $G_{-2,0}$ and $G_{2,0}$ as seen Figure 28b. The circle size may be too large for the second mode in this region and the laser picked up some higher order harmonics along the circle, causing the principal rotational velocities to be inaccurately estimated.

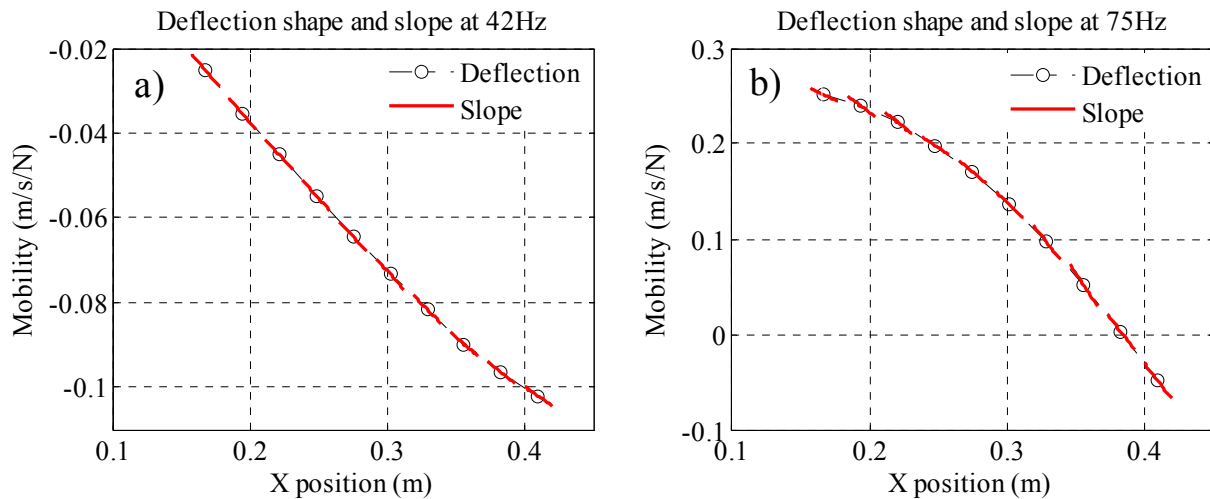


Figure 31 Measured deflection shape and local slope using the circular-scan approach

4.6 *Summary*

Signals measured using continuous scan laser Doppler vibrometry can be represented as the output of a linear time periodic system when a closed, periodic scan pattern is used. This work proposed an algorithm based on the harmonic transfer function to process measurements from a circular-scan, allowing the translational and rotational velocities to be extracted simultaneously. Using this new approach, a circular-scan approach can be used at every point in a measurement grid to acquire the translational and rotational velocities at each point in the same amount of time that is usually required to obtain only the translational velocity.

This algorithm was validated on a downhill ski that was hung to simulate free boundary conditions. The ski is a complex structure that can be very challenging to model accurately. This work studied the influence of the scanning rate, circle size, and surface quality on the noise level in measured velocity signal from CSLDV. The results showed that the circular-scan approach can provide a lower noise level and standard deviation than the conventional point approach, if the scan frequency and circle size are chosen appropriately. It appears that by scanning in a circle, one can avoid the possibility of the detector area being dominated by a dark speckle, or by a region where speckle noise is especially severe, and thus reduce the speckle noise and the potential for signal dropouts.

The circular-scan approach was then applied over a grid of circles (points) to measure the mode shapes on the black bottom surface of the ski. A 200Hz scan frequency and an 8mm circle size were selected based on the previous study. The circular-scan approach was found to provide smoother and more reliable mode shapes than the conventional point-by-point approach. This occurs because each circular-scan has a higher signal-to-noise ratio than a corresponding point measurement. The harmonic transfer function concept was also used to extract the principal

rotational velocities of the ski. Although the circular-scan can improve signal-to-noise ratio, the noise level is still too high to measure rotational velocities because the amplitudes are much smaller than those of the translational velocities. Hence, retro-reflective tape was applied in these tests. The acquired rotational velocities were used to compute the slope of the mode shape at different measurement locations. The results were found to agree well with the trend of the shapes found by measuring the translational velocity, suggesting that the method is accurate.

The circular-scan approach may be helpful in constructing a more accurate curvature shape. The curvature is widely used in damage detection but is vulnerable to the noise in deflection shape because of the finite difference approach involved in computing the curvature [79]. Circular-scan, on the other hand, not only provides a spatially detailed mode shape, but also identifies the additional slope information about the shape. Therefore, it is expected to improve the accuracy of curvature estimation and hence the accuracy of damage detection.

5 Output-only Modal Analysis using CSLDV

The harmonic power spectrum is used to extract the natural frequencies and mode shapes of a free-free beam under random excitation. One key consideration, the choice of scan frequency, is explored. The method is then applied to identify the mode shapes of a parked 20kW wind turbine using a ground based laser and with only a light breeze providing excitation.

5.1 Introduction

All of the previously discussed CSLDV algorithms are valid only for the case where the input is either zero (free response) or follows a specific form and is carefully controlled (e.g., sinusoidal). In practice one cannot always apply an input of one of these forms to a structure, but unmeasured random input forces may be present. For example, wind turbines are difficult to adequately excite due to their large size and mass, yet the wind provides a convenient, broadband source of ambient excitation. Output-only modal analysis, also known as operational modal analysis, extracts modal parameters of a structure based only on the response under unmeasured ambient excitations, providing dynamic characteristics about the structure under actual operating conditions with real boundary conditions.

Previous signal processing techniques of CSLDV, as presented in Chapter 1, are based on intuition and only work for controlled inputs. This chapter combines the output-only modal identification algorithms developed for LTP systems with CSLDV. As a result, for the first time, CSLDV can be used to extract modal parameters of Linear Time Invariant (LTI) structures under ambient excitation. It was shown that when the laser scans a closed and periodic pattern on an LTI structure, the measured signal can be treated as that from an LTP system. Thus, output-only

identification theory for LTP systems can be used to extract natural frequencies, damping ratios and mode shapes from CSLDV measurements of a structure under unmeasured, random input. Though this chapter is dedicated to CSLDV, the signal processing and results interpretation could be easily extended to the processing of measurements from general LTP systems.

The rest of this chapter is organized as follows: Section 5.2 demonstrates the proposed technique on a free-free beam by extracting the natural frequencies and mode shapes; Section 5.3 discusses the effect of the chosen scan frequency on the performance of CSLDV. In Section 5.4, the method is applied to identify the first few modes of a parked wind turbine under wind excitation. Section 5.5 summarizes the conclusions.

5.2 CSLDV Measurements from a Free-free Beam

In order to validate the new algorithm based on the harmonic power spectrum, CSLDV was used to measure the modes of a free-free aluminum beam, as shown schematically in Figure 32. The beam was suspended by flexible bungee cords, which were made as soft as possible and placed at the nodes of the first analytical bending mode to minimize the effect of the support stiffness on the beam's modes. A 5.2 gram accelerometer (PCB J351B11) was attached at the left end of the beam ($x = 6.3\text{mm}$). The signal from the accelerometer was not used in any of the following, but the accelerometer does mass load the beam and this is accounted for by the analytical model; the mode shapes extracted in this work are expected to be identical to those predicted by the analytical model.

random, although it drops to -3m/s periodically. The laser remains on the beam and retro-reflective tape during the measurement so these are not the reasons for the drop-out; this phenomenon seems to have been caused by the analog VD-03 velocity decoder in the Polytec system, although its cause is not known (the same phenomenon was noted when using a 3Hz scan frequency). These dropouts did not occur with the digital VD-08 decoder. Unfortunately, the VD-08 decoder had too small of a range for the systems studied in this work, so it would overload during the tests and could not be used. The output signal, including these dropouts, was used in the following analysis without any special treatment and reasonable results were still obtained in spite of that contamination.

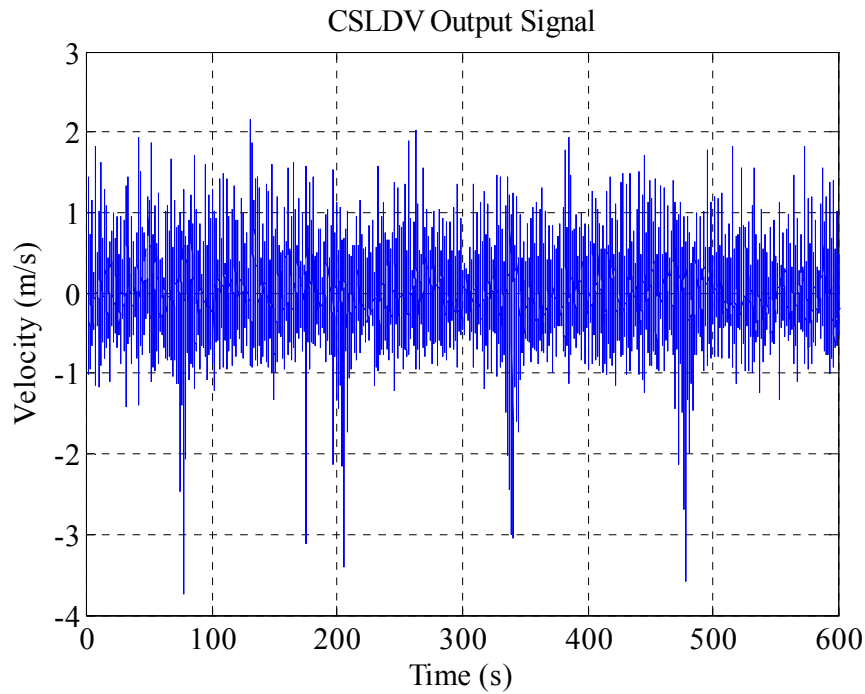


Figure 33 CSLDV output signal under random excitation (1.5Hz scan frequency)

To form the exponentially modulated periodic output signal $\mathbf{Y}(\omega)$ in Eq. (40), the vibrometer signal was modulated with harmonics $n = -6 \dots 6$ according to the formula in step 4. The 13 modulated CSLDV output signals were then decomposed into 20 second blocks with

75% overlap and a Hanning window was applied to each of the blocks. This resulted in 104 blocks that were averaged to compute $S_{YY}(\omega)$. The result is a $[13 \times 13 \times 16385]$ harmonic power spectrum matrix, where 16385 is the number of frequency lines. As mentioned previously, one row or column of $S_{YY}(\omega)$ is all that is required. Here, the primary column $S_{YY}(\omega)_{n,0}$ is computed and each of the elements for $n = -6 \dots 6$ are shown in Figure 34.

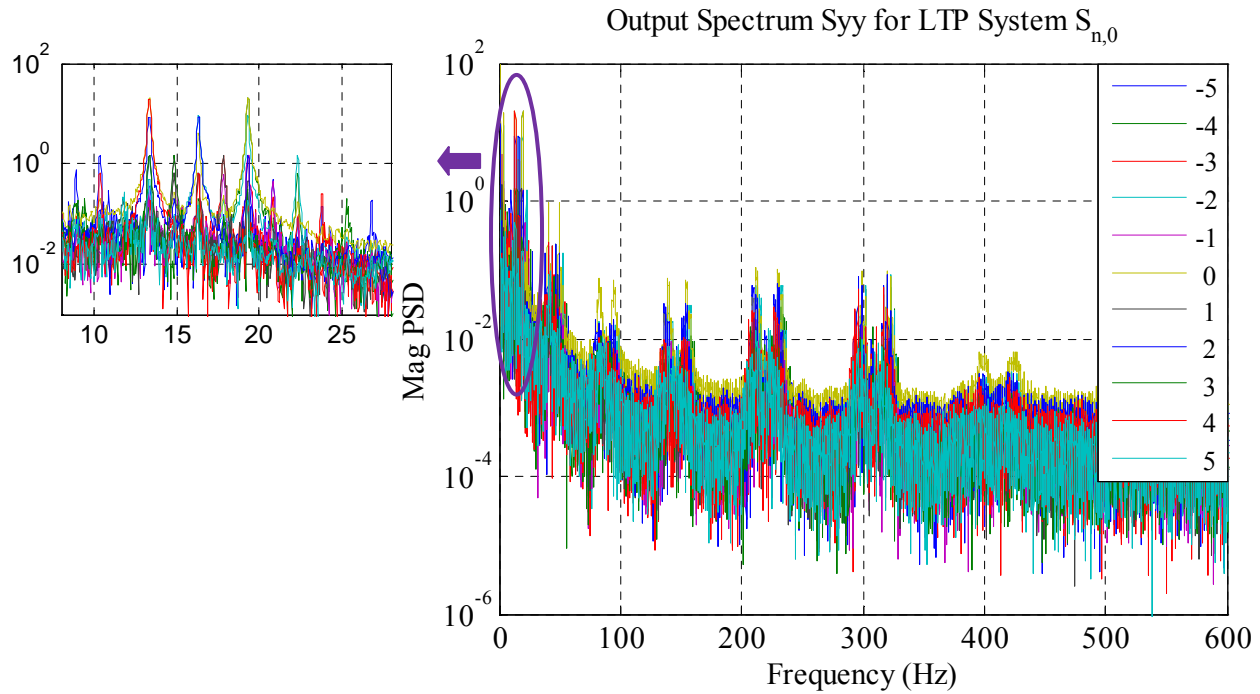


Figure 34 Harmonic power spectrum of CSLDV measurement at 1.5Hz scan frequency. The pane on the left shows an expanded view of the measurement near 16 Hz.

The harmonic power spectrum shows clusters of strong harmonics centered at various frequencies, for example 16 Hz, 45 Hz, 90 Hz, etc. One can deduce that these are the natural frequencies of the system, and since the scan frequency is small relative to the natural frequencies, the peaks for each $\bar{C}_{r,l}$ in Eq. (45) occur in a cluster near each natural frequency. The view on the left focuses on the 1st mode, whose natural frequency is 16.34Hz. Besides the peak at 16.34Hz, the 1st mode is also responsible for the harmonics in the spectrum at 13.34Hz,

14.85Hz, 17.85Hz, 19.34Hz, etc, all separated by multiples of 1.5Hz, which is the scan frequency. The peak picking method can be used to identify the Fourier coefficient vectors $\bar{\mathbf{C}}_{r,l}$ from the power spectra in Figure 34, and this approach was found to provide good accuracy in most of the cases considered here. However, somewhat better results were obtained by fitting the measurements to single degree-of-freedom modes using the Algorithm of Mode Isolation (AMI) [78]. This algorithm was modified from the version in [78] to fit squared modes to the power spectrum near each peak. The AMI algorithm identified the natural frequencies and residue vectors, which are proportional to the mode shapes $\bar{\mathbf{C}}_{r,l}$, for each of the peaks in the spectrum.

Figure 35 shows a curve fit to several of the peaks arising from the 1st mode. The black solid line indicates the composite harmonic power spectrum, which is the average of the 13 harmonic power spectra in Figure 34, and the green dash-dot line is the curve fit found by AMI. A third curve shows the composite of the difference between the measurement and the reconstruction. The five dominant peaks in the spectrum are well approximated by the reconstructed spectrum; the difference between the measurement and the curve fit is fairly small relative to the maximum value at each peak, but it still does stand above the noise by about one order of magnitude. This is thought to occur due to distortion from the Hanning window or perhaps because the noise in the LDV measurement is not perfectly white.

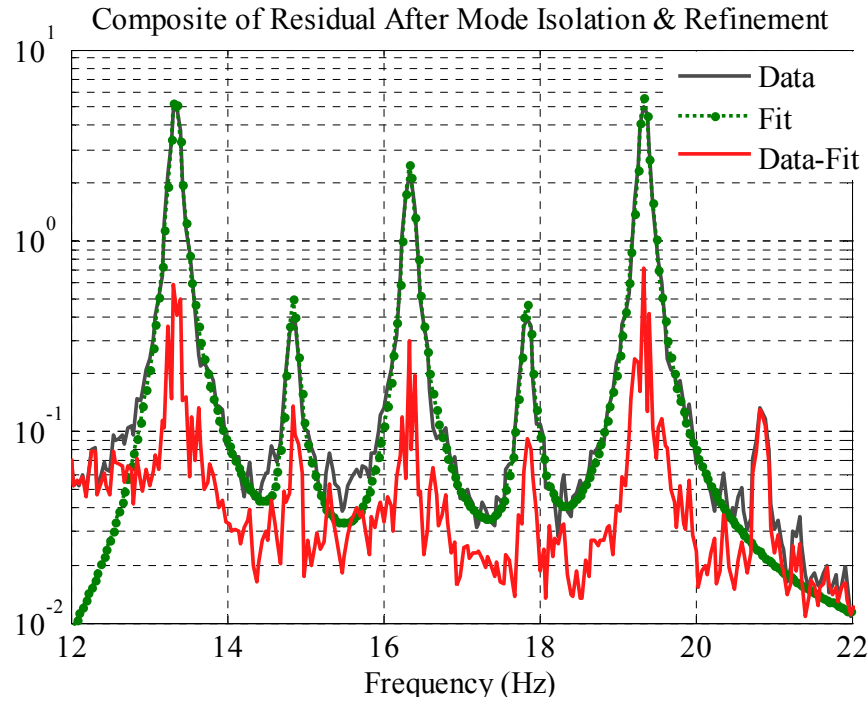


Figure 35 AMI fit of the 1st mode using a 1.5Hz scanning frequency

Table 4 shows the Fourier coefficient vectors identified from the 5 harmonics in Figure 35. The vector that was computed with the weighted average procedure, $\bar{\mathbf{C}}_1^{\text{AVG}}$, is also listed, which is normalized to its maximum value. The first column gives the Fourier coefficient that each term corresponds to. Higher order terms ($n = -8 \dots -5$ and $n = 5 \dots 8$) are dominated by noise and therefore not included in the averaging. There are significant discrepancies between each of the estimates of the terms $C_{1,-3}$, especially for the $\bar{\mathbf{C}}_{1,1}$ vector, apparently because that term overlaps with the harmonic of a neighboring rigid body mode. However, the error in this coefficient has little effect on the average because the $\bar{\mathbf{C}}_{1,1}$ vector carries a small weight in the average. The singular value decomposition produced mode shape coefficients that were within 2% of the values from weighted averaging, as shown in Table 5. In all cases studied in this work, the singular value decomposition and weighted averaging methods gave essentially

identical results, so either seems to be valid and they will not be compared further in subsequent examples.

Table 4 Shifted Fourier coefficient vectors of the 1st mode under 1.5Hz scanning frequency

	Averaged	SVD	Harmonics of 1 st mode				
Frequency	16.34	16.34	13.34	14.84	16.33	17.84	19.34
Weight ($\alpha_{r,l}$)	1	-	0.39	0.03	0.17	0.03	0.38
-	$\bar{\mathbf{C}}_1^{\text{AVG}}$	$\bar{\mathbf{C}}_1^{\text{SVD}}$	$\bar{\mathbf{C}}_{1,2}$	$\bar{\mathbf{C}}_{1,1}$	$\bar{\mathbf{C}}_{1,0}$	$\bar{\mathbf{C}}_{1,-1}$	$\bar{\mathbf{C}}_{1,-2}$
$C_{1,-8}$	-	-	$0.01 + 0.00i$	-	-	-	-
$C_{1,-7}$	-	-	$-0.01 + 0.00i$	$0.03 + 0.08i$	-	-	-
$C_{1,-6}$	-	-	$0.01 - 0.01i$	$0.05 + 0.01i$	$-0.00 - 0.01i$	-	-
$C_{1,-5}$	-	-	$-0.01 + 0.01i$	$0.00 + 0.00i$	$-0.01 + 0.01i$	$0.00 + 0.03i$	-
$C_{1,-4}$	$-0.06 + 0.01i$	$-0.06 + 0.01i$	$-0.05 + 0.01i$	$0.03 + 0.00i$	$-0.06 + 0.02i$	$0.00 + 0.07i$	$-0.06 + 0.03i$
$C_{1,-3}$	$0.00 - 0.01i$	$0.00 - 0.01i$	$0.00 - 0.01i$	$0.12 - 0.05i$	$-0.00 - 0.01i$	$0.00 - 0.02i$	$0.00 - 0.02i$
$C_{1,-2}$	1.00	1.00	$1.00 + 0.04i$	$0.94 + 0.05i$	$0.99 - 0.13i$	$0.99 - 0.13i$	$0.96 - 0.29i$
$C_{1,-1}$	$-0.07 - 0.00i$	$-0.07 + 0.00i$	$-0.07 - 0.00i$	$-0.15 - 0.04i$	$-0.07 + 0.01i$	$0.03 + 0.01i$	$-0.07 + 0.02i$
$C_{1,0}$	$0.43 + 0.07i$	$0.44 + 0.07i$	$0.43 + 0.09i$	$0.41 + 0.11i$	$0.44 + 0.01i$	$0.40 + 0.01i$	$0.44 - 0.06i$
$C_{1,1}$	$-0.08 - 0.01i$	$-0.07 - 0.01i$	$-0.07 - 0.02i$	$-0.12 - 0.02i$	$-0.08 - 0.01i$	$-0.11 + 0.00i$	$-0.07 + 0.01i$
$C_{1,2}$	$0.94 + 0.31i$	$0.94 + 0.30i$	$0.92 + 0.34i$	$0.93 + 0.38i$	$0.98 + 0.17i$	$0.95 + 0.17i$	$1.00 + 0.02i$
$C_{1,3}$	$0.01 + 0.02i$	$0.01 + 0.02i$	$0.01 + 0.02i$	$0.07 + 0.04i$	$0.01 + 0.02i$	$0.04 + 0.03i$	$0.01 + 0.01i$
$C_{1,4}$	$-0.05 - 0.03i$	$-0.06 - 0.03i$	$-0.06 - 0.03i$	$0.02 - 0.03i$	$-0.06 - 0.02i$	$-0.07 - 0.03i$	$-0.06 - 0.01i$
$C_{1,5}$	-	-	-	$0.00 - 0.03i$	$-0.01 - 0.00i$	$-0.00 + 0.00i$	$-0.00 - 0.00i$
$C_{1,6}$	-	-	-	-	$0.00 + 0.01i$	$0.02 - 0.01i$	$0.00 + 0.01i$
$C_{1,7}$	-	-	-	-	-	$0.01 - 0.02i$	$-0.00 + 0.00i$
$C_{1,8}$	-	-	-	-	-	-	$-0.00 - 0.00i$

To further explore the differences between each of the estimates for the mode shape that the vectors $\bar{\mathbf{C}}_{1,l}$ provide, the highlighted terms in the table above were used to reconstruct an estimate of the mode shape for each $l = -2 \dots 2$. These mode shapes, as well as the weighted averaged mode shape, are plotted in Figure 36 versus the position of the laser spot, which is a cosine function of time. It can be seen that the mode shapes from the -1 and 1 harmonics show

some discrepancy while the others from the -2, 0, and 2 harmonics all agree very closely. This is to be expected since the amplitudes of the -1 and 1 harmonics are 10 times smaller than those of -2, 0 and 2 harmonics, as shown in Figure 35, so they are much more influenced by noise. Any of the other harmonics gives a reasonable estimate of this mode's shape. The maximum differences between the weighted average shape and shapes from each harmonic are: 1.42%, 3.76% and 1.27% at the -2, 0, and 2 harmonics respectively, and 11.10%, 8.12% at -1 and 1 harmonics respectively.

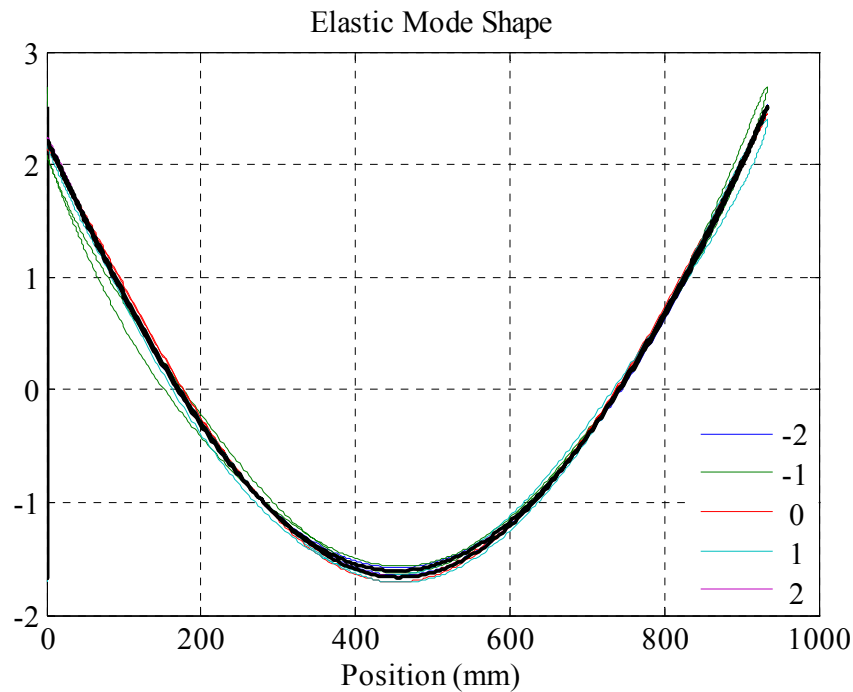


Figure 36 Mode shapes reconstructed from each of the five groups of harmonics in
The solid black line shows the mode shape computed from the weighted average method

The reason for choosing $n = -6 \dots 6$ also requires some explanation at this juncture. The number of harmonics required to accurately describe each mode shape is not known a priori. If too small a number is used, the Fourier coefficient terms may not be sufficient to describe the time varying function $C(t)\psi_r$ in Eq. (33), and therefore cannot capture the true variation in the mode shape along the scan path. On the other hand, choosing too large a number of harmonics may bring terms that are dominated by noise or by neighboring modes into the mode vectors,

making the reconstructed mode shapes unreliable. In this work, the authors selected a large number of harmonics (i.e. $n = -25 \dots 25$) to form the exponentially modulated periodic signal, then the number of terms retained in the identified vectors $\bar{\mathbf{C}}_{r,l}$ for each mode was determined manually based on the observation that the noise level was about 2% of the maximum signal in Figure 34. For each mode, the higher order terms in $\bar{\mathbf{C}}_{r,l}$ that are dominated by noise are deleted. For the first mode only the terms $C_{1,-4}$ to $C_{1,4}$ were retained in each $\bar{\mathbf{C}}_{r,l}$, so the harmonic power spectrum was only shown in Figure 34 for $n = -6 \dots 6$ in order to more easily demonstrate the signal processing procedure.

All of the other modes were identified in a similar manner. Table 5 shows the natural frequencies of all of the modes that were identified from the harmonic spectra. The value in the column labeled “OMA-CSLDV Freq (Hz)” is the average of the natural frequency estimated at each of the harmonics, after shifting each by an integer multiple of ω_A . The standard deviation (STD) of the natural frequency estimates is also shown, which is very small in all cases, revealing that each of the harmonics gives a very similar estimate of the natural frequency. The values in the column labeled “Analytical” are the natural frequencies of a tuned analytical model, which is an Euler-Bernoulli beam model that was adjusted to account for the mass of the accelerometer. All of the identified natural frequencies from the output-only modal analysis agree well with the analytical values. The largest difference is a few Hz for the higher modes, but the analytical model was found to be somewhat inaccurate for these modes in [54], so the result from output-only modal analysis is still within the margin of error for the analytical model. As noted in the table, the 1.5Hz scan frequency (data in Figure 34) was used for the first two modes, while the rest were extracted from the measurements with the 3Hz scan frequency. The

reason for using a 3Hz scan frequency for modes 3-7 is explained in the next section. A larger number of Fourier coefficient terms were used for modes 2 through 7 since there were more terms that stood out above the noise. These mode shapes are more complicated spatially, and hence require a larger number of terms to capture $C(t)\psi_r$.

Table 5 Comparison of analytical modes and those found with CSLDV for aluminum beam

<i>No.</i>	<i>Analytical Freq (Hz)</i>	<i>OMA-CSLDV Freq (Hz)</i>	<i>STD</i>	<i>n</i>	<i>Scan Freq (Hz)</i>	<i>MAC</i>
1	16.38	16.34	0.00	-4...4	1.5	1.00
2	45.35	45.11	0.06	-5...5	1.5	1.00
3	89.23	88.76	0.07	-8...8	3	0.98
4	147.99	146.97	0.05	-11...11	3	0.97
5	221.71	221.07	0.01	-12...12	3	0.97
6	310.49	309.52	0.01	-14...14	3	0.96
7	414.37	411.58	0.10	-15...15	3	0.95

Figure 37 shows the mode shapes of each of the identified modes, as well as the shapes from the tuned analytical model from [54]. Uncertainty in the measurement position is neglected since the mirror system positions the laser accurately at the scan frequencies used in this work. The velocity error due to laser misalignment is also very small (less than 1%). From Figure 37 we can see that the mode shapes agree very well with the analytical model, except for the 3rd and 7th modes which show some noticeable discrepancies. The 3rd mode was more heavily damped than the other modes and the harmonics overlapped with each other, as discussed in section 5.3, so it was difficult to identify its Fourier coefficients accurately. The 7th mode was weakly excited because the hammer force had rolled off significantly near its natural frequency, so it did not stand out well above the noise. This mode was also difficult to identify in the author's prior

work, as described in [53], since the hammer tip used does not excite it strongly. The Modal Assurance Criteria (MAC) values between the analytical mode shapes and the CSLDV mode shapes are listed in Table 5; the worst MAC values occur for the 6th and 7th modes, but those values are still above 0.95.

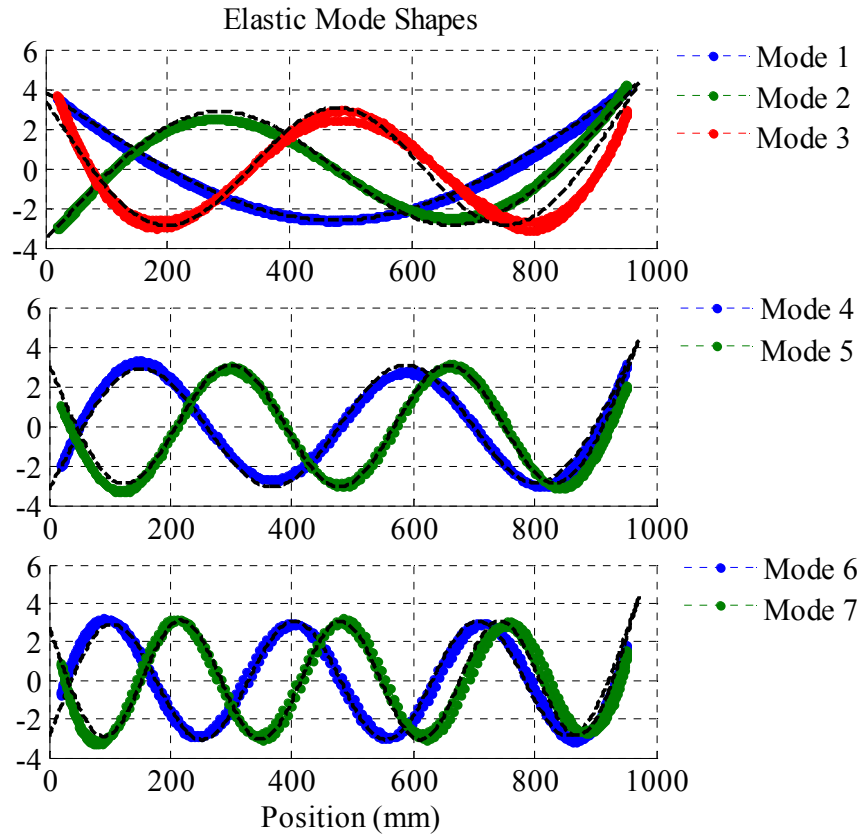


Figure 37 Mode shapes identified by CSLDV at 1.5Hz and 3Hz scanning frequencies. Solid black lines denote the analytical shapes; dots show the shapes from output-only modal analysis.

5.3 Effect of Scan Frequency

Low scan frequencies were used in the results in Section 5.2 so that the harmonics of each mode would occur in an easily located cluster, as illustrated in Figure 34. One additional consideration for this selection is the speckle noise, which increases with the scan frequency.

However, the scanning frequency must be large relative to the half power bandwidth of each mode; otherwise the harmonics may be difficult to distinguish. Figure 38 explores this issue by comparing the spectrum near the heavily damped 3rd mode for 1.5Hz and 3Hz scanning frequencies. The harmonics of this mode are seen to overlap significantly when a 1.5Hz scanning frequency was used, so much so that it appears that only two harmonics are present. One might still be able to identify the natural frequency and mode shape of the 3rd mode from this measurement, however, the shape at each peak is likely to be contaminated by the neighboring peaks. A better estimate of the mode shape is obtained with a 3Hz scanning frequency. Its harmonics are found to be better separated so the Fourier coefficients estimated from each peak are not as strongly affected by the neighboring peaks.

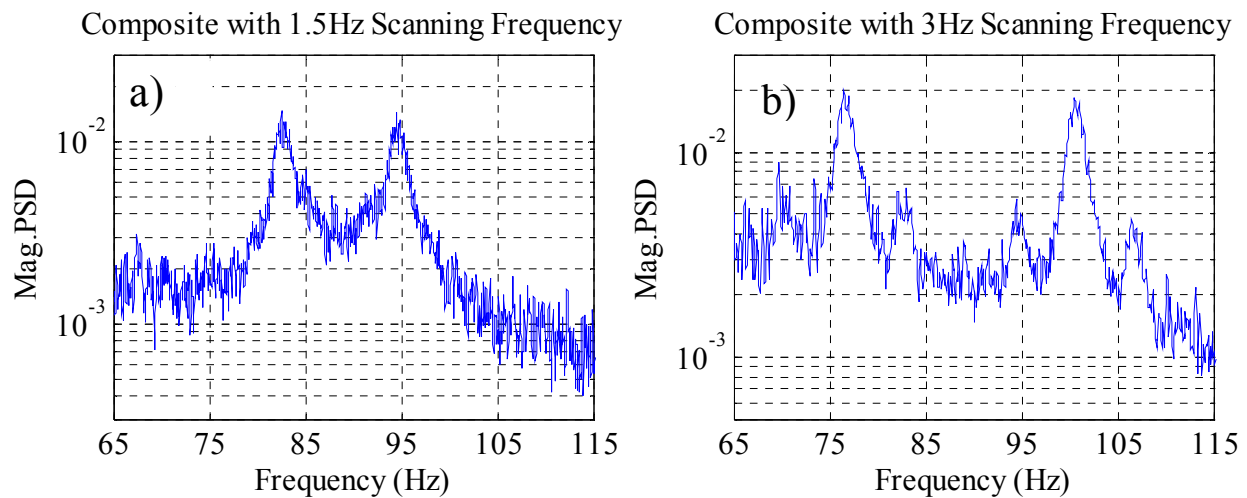


Figure 38 Composites of the harmonic power spectrum near the 3rd mode with 1.5Hz (a) and 3Hz (b) scanning frequencies.

On the other hand, if the scanning frequency is too large, the harmonics of one mode may overlap with those of the neighboring modes, especially when the modes are close to each other. As shown in Figure 39, when the scan frequency changes from 1.5Hz to 3Hz, sidebands of the first (red block, left) and the second (green block, right) bending modes start to overlap, so the

estimates of $\bar{C}_{r,l}$ could be contaminated. A similar issue was noted by Stanbridge [45, 46, 73, 80] and Sriram [44] in their works.

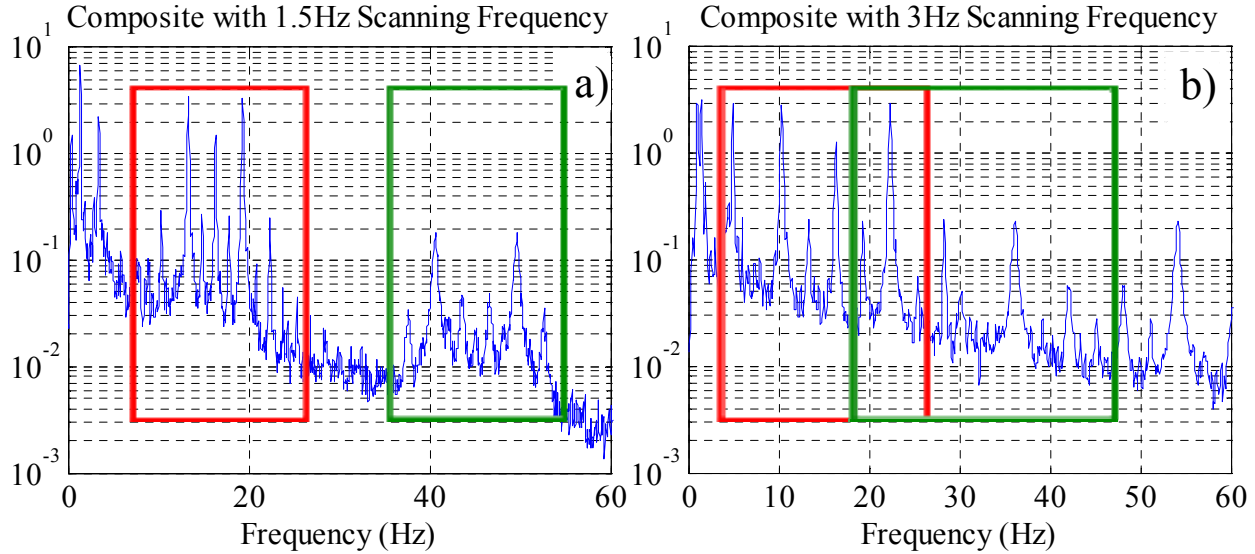


Figure 39 Composites of the harmonic power spectrum near first and second modes with 1.5Hz (a) and 3Hz (b) scanning frequencies.

One alternative to this dilemma is to select a scan frequency that is greater than twice the natural frequency of the highest mode that is excited. This ensures that all of the harmonics in Eq. (45) occur at distinct frequencies. The disadvantage of this approach is that it may result in increased speckle noise with current lasers [36, 76], and for some structures the scan frequency needed may exceed the capabilities of the mirror system (maximum scan frequency 500Hz). A high scan frequency also produces a spectrum that is more difficult to visually interpret than those shown above, since harmonics for all of the modes are spread throughout the bandwidth of the measurement. In previous works the authors circumvented this difficulty by lifting the measurements, which effectively aliases the CSLDV signal, producing a collection of signals that are limited to $0 < \omega < \omega_A/2$ [53]; each mode occurs as a single peak in the aliased spectrum. This technique will be demonstrated in the next section.

Figure 40 shows a measurement where a 56Hz scanning frequency was used, which seemed to provide a good balance between speckle noise and minimizing overlap of the various modes. Black star markers were added where harmonics of the first mode ($f_1 = 16.34\text{Hz}$) were expected to occur. The harmonics of this mode no longer appear in a cluster, as in Figure 34, but throughout the band for $16.34\text{Hz} \pm l \times 56\text{Hz}$. Some of the harmonics for positive l fold about zero frequency occurring at positive frequencies $|16.34\text{Hz} - l \times 56\text{Hz}|$, complicating matters further. Nevertheless, the same identification procedure can still be applied as long as the harmonics of each mode can be located. When reconstructing the mode shapes, one should be aware that the folded harmonics actually correspond to positive-frequency harmonics of the complex conjugate eigenvalue, so the Fourier coefficient vectors at these folded harmonics are complex conjugates of the identified $\bar{C}_{r,l}$, and the order of the Fourier coefficients $C_{r,n}$ within those vectors is reversed.

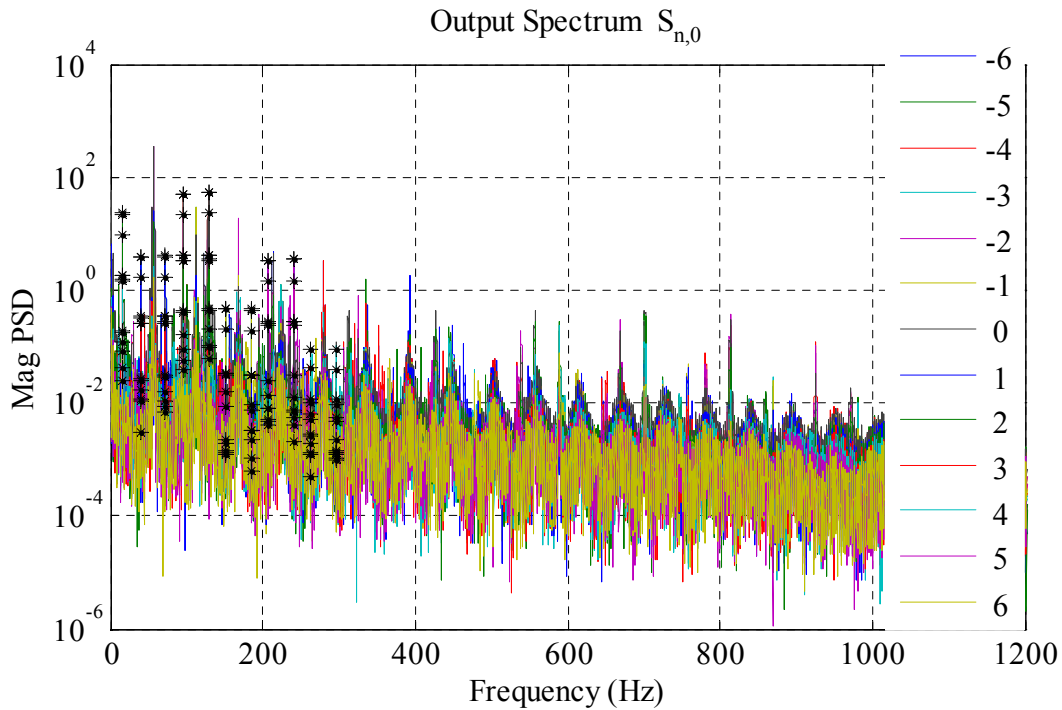


Figure 40 Harmonic power spectrum of CSLDV measurement at 56Hz scan frequency

Figure 41 shows the mode shapes that were identified from the harmonic power spectrum of the measurement with a 56Hz scan frequency. The number of Fourier coefficient terms selected to describe each mode were the same as listed in Table 5. The peak picking method was used to obtain the Fourier coefficient vector at each harmonic instead of AMI in this case. This was done for two reasons; first to demonstrate that the peak picking method gives quite acceptable results when the modes are widely spaced and the scan frequency is high and, second, because the AMI algorithm becomes somewhat inconvenient when there are so many peaks over such a wide frequency range.

As with the measurements at 1.5 and 3Hz scan frequencies, the reconstructed mode shapes from the measurement at the 56Hz scan frequency agree very well with the analytical ones. The mode shapes in Figure 41 were plotted with fewer points along the length of the beam than in Figure 37 in order to reflect the fact that the 2560Hz sampling rate only produces 46 samples per period at a 56Hz scan frequency. In fact, one is actually estimating a continuous, Fourier series description of the mode shapes. The Fourier series could actually be plotted with any desired resolution in time, but doing so would mask the fact that the signal used to obtain it has finite resolution. The mode shapes obtained using a 56Hz scan frequency agree very well with those shown previously, although the discrepancies between the measured and analytical shapes are visibly larger for some of the modes, especially the weakly excited third and seventh modes.

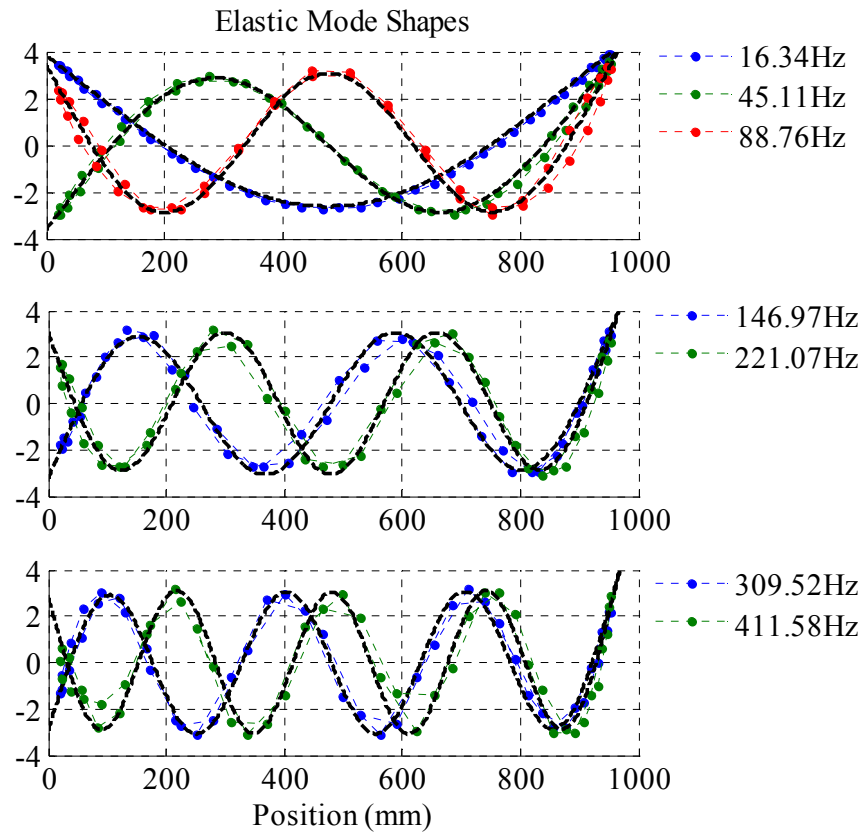


Figure 41 Mode shapes identified by CSLDV at 56Hz scanning frequency. Solid black lines denote the analytical shapes; dots show the shapes identified by output-only modal analysis.

5.4 Application to Wind Turbine

The proposed method was applied to identify the natural frequencies and mode shapes of a 20kW wind turbine blade as depicted in Figure 42. This turbine, manufactured by Renewegy, LLC, has a rotor diameter of 9.5m, nominal rotor speed of 100rpm, generator speed of 600rpm, and produces power for wind speeds ranging from 3.5 to 25m/s. The blade is one of three that comprise the turbine rotor. For all of the tests described here, the turbine rotor was locked by applying the brake and the blade of interest was pitched so that the laser was nominally perpendicular to the chord of the blade (i.e. measuring in the flapwise direction). The laser

scanned over as much of the 4.3m long blade as was possible. For the results shown here the laser was 66m from the base of the tower and the tower height was 30m, so the total distance from the laser head to the blade was approximately 72.5m. A long strip of retro-reflective tape was applied on the blade to increase the signal strength. This tape was necessary to obtain a reasonable signal from the vibrometer at such a large stand off distance, and the increased reflectivity made the laser spot easy to locate visually. The blade was excited purely by the wind, whose maximum speed was about 3.5m/s during the tests.

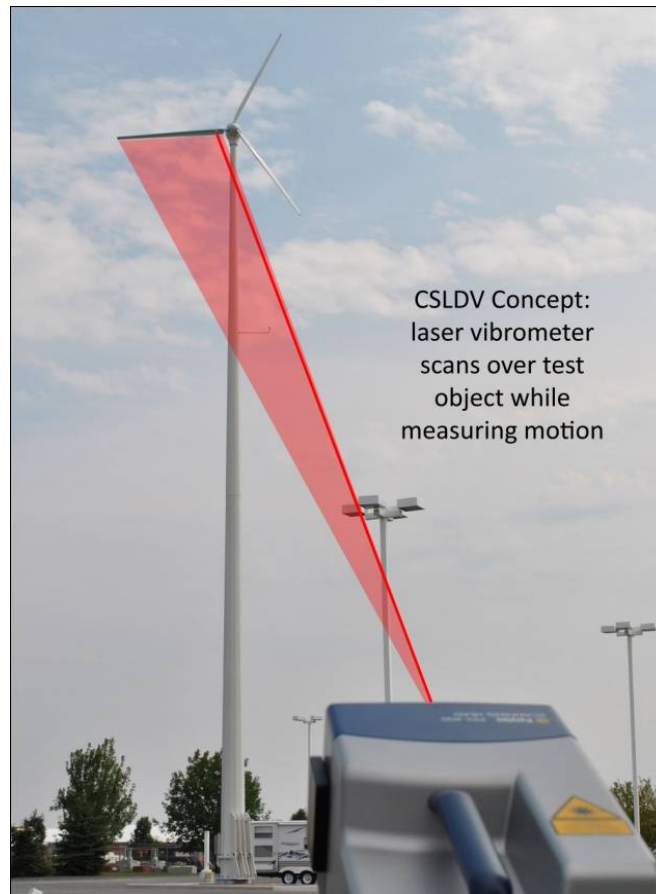


Figure 42 Photograph from CSLDV test of a wind turbine blade with a graphic illustrating the scan pattern.

Before acquiring CSLDV measurements, the laser spot was fixed near the tip of the blade and the power spectrum was estimated over about a 10 minute period. The resulting spectrum is

shown in Figure 43. At least seven peaks are seen in the spectrum, each of which is presumed to correspond to a natural frequency of the wind turbine. The frequencies of each of these peaks are listed in Table 6. Beyond 25Hz the wind apparently does not excite the system significantly. The seven modes seen in Figure 43 are not expected to be seven bending modes of a simple beam. The turbine is comprised of three nominally identical blades so each blade bending mode occurs three times, at two or three distinct frequencies depending on the stiffness properties of the tower and nacelle.

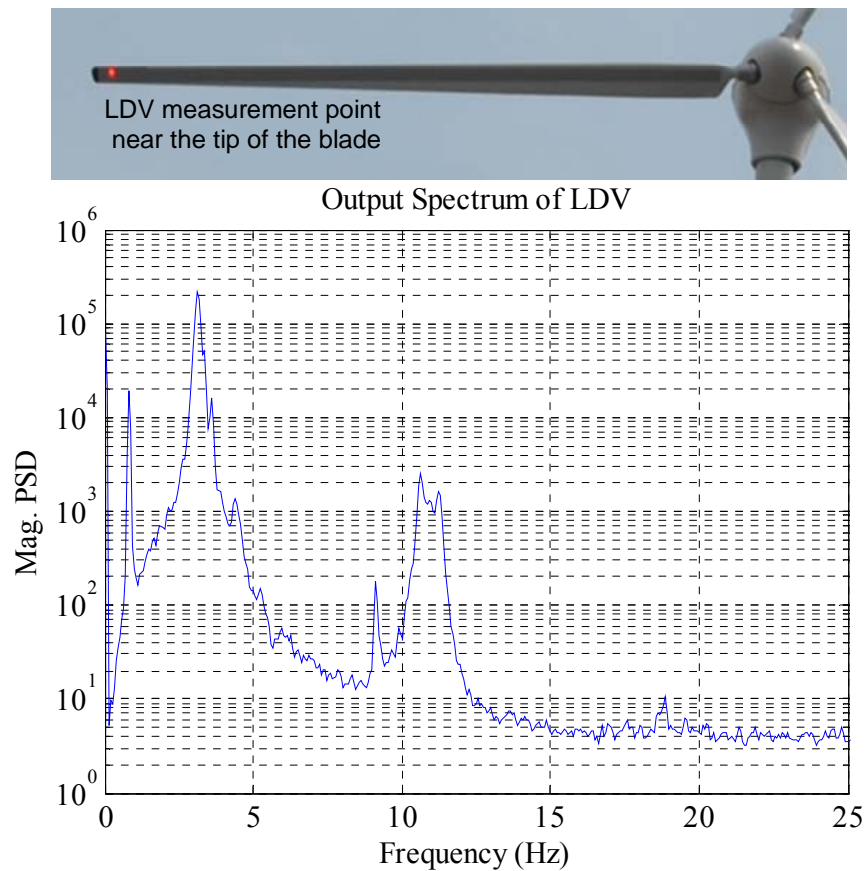


Figure 43: Power spectrum of LDV output signal with the laser measuring at a fixed point near the tip of the blade

The LDV was then set to continuously scan over the blade for 10 minutes at a time at several different scan frequencies ranging from 0.8Hz to 9.3Hz. Scan frequencies were selected

as discussed in Section 5.3, large enough to render the mode peaks distinct but small enough to limit speckle noise. Also the specific frequencies seen in Figure 43 and their harmonics were avoided since this would introduce noise at a frequency of interest. The sampling frequency for these tests was 2560Hz, which was sufficient to capture the highest mode excited by the wind even at the 9.3Hz scanning frequency.

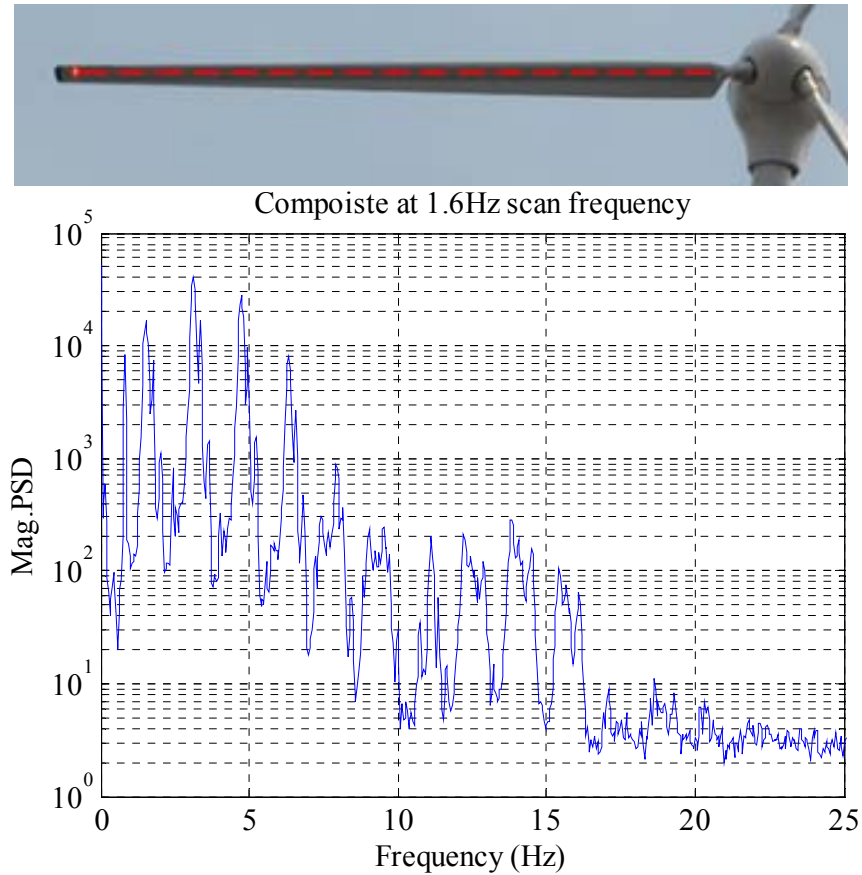


Figure 44: Composite of harmonic power spectrum of the CSLDV measurement with 1.6Hz scanning frequency

Figure 44 shows a composite of the power spectra $S_{\mathbf{y}\mathbf{y}}(\omega)_{n,0}$ when a 1.6Hz scanning frequency was used. The harmonics $n = -6 \dots 6$ were used to create the harmonic power spectrum, and the Fourier coefficient terms from $C_{1,-3}$ to $C_{1,3}$ were used to represent the mode

shapes. The spectrum again seems to reduce to noise above about 25Hz. The harmonics of several modes are visible in the spectrum, but it is difficult to determine which harmonics go with each natural frequency since they are all so closely spaced. Therefore, the point measurement in Figure 43 was used to determine which frequencies correspond to each of the system's modes. The natural frequencies that were found to be present in the harmonic spectra are listed in Table 6, along with the seven frequencies identified from the tip spectrum. Also listed are the first two bending modes obtained by a conventional hammer-accelerometer test on a different blade of nominally identical design when it was mounted in a stiff fixture on the ground. The differences in the natural frequencies between the tip measurement on the tower and the measurements in the fixture could be attributed to the fact that the boundary conditions were significantly different.

The mode shapes of the turbine were found using the weighted averaging method and are shown in Figure 45. The mode shapes reveal that the mode at 0.82Hz is predominantly a tower bending mode, where the tower bends and the blade moves as a rigid body. The next three modes identified by output-only modal analysis were at 3.13, 3.36 and 3.63Hz. The first bending mode of the single blade in a stiff fixture was 3.36Hz, which is close to these frequencies. Each of these modes shows the blade bending with the familiar shape reminiscent of the first mode of a cantilever beam. However, the mode shape of the 3.63Hz mode seems to show some displacement at the root of the blade. This would seem reasonable since the symmetric flapwise mode (where all three blades bend in phase in their softer bending direction) of a horizontal axis wind turbine such as this tends to occur at higher frequency than the yaw and tilt flapwise modes (see, e.g., [81, 82]). The symmetric flapwise mode also typically involves larger translation of the nacelle since it merely rotates about the top of the tower in the yaw and tilt modes. The

mode seen at 4.38Hz in the tip measurement was not identifiable in the harmonic autospectrum, so its mode shape could not be determined. The first edgewise mode of this blade occurred at 5.24Hz when the blade was mounted in the stiff fixture, so this peak in the tip spectrum may come about due to edgewise motion of the blade and the fact that the blade twists from root to tip. A 9.13Hz mode was also seen in the fixed point LDV test and not in the CSLDV test, this mode seems to have been buried in the sidebands of the neighboring modes, or perhaps it was not excited significantly in this time record. The last three modes that were identified have shapes that are similar to the second bending mode of a cantilevered beam, and their frequencies at 10.62Hz, 10.86Hz and 11.29Hz are all close to the frequency of the second flapwise mode of the blade in the fixture.

Table 6 Natural frequencies of wind turbine blade

Mode	Conventional test in stiff fixture	Fixed point OMA on tower	CSLDV OMA on tower ($f_A=1.6$ Hz)
-	-	0.81Hz	0.82Hz
		3.13Hz	3.13Hz
Flap Wise Bending 1	3.36Hz	3.37Hz	3.36Hz
		3.63Hz	3.63Hz
Edge Wise Bending 1	5.24Hz	4.38Hz	-
-	-	9.13Hz	-
		10.63Hz	10.62Hz
Flap Wise Bending 2	11.40Hz	10.94Hz	10.86Hz
		11.25Hz	11.29Hz

All of these results were obtained from the CSLDV measurement at the 1.6Hz scan frequency. A similar set of results was obtained at the 9.3Hz scan frequency as well, although the mode shapes were somewhat noisier at that scan frequency. Due to space limitations those results are not shown here.

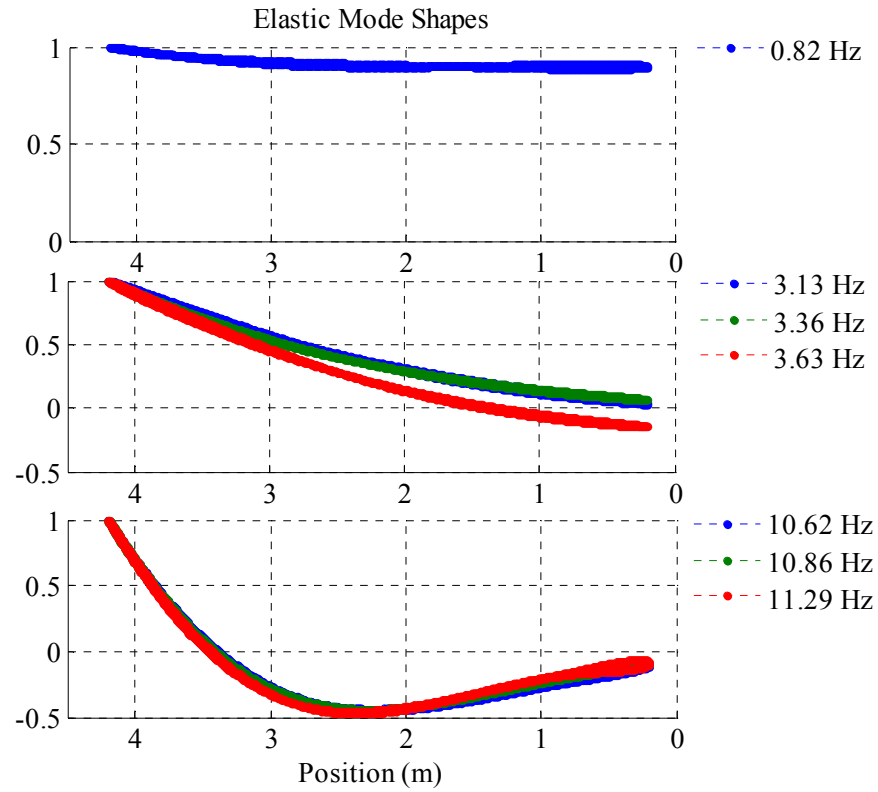


Figure 45: Mode shapes of wind turbine blade identified by CSLDV at 1.6Hz scanning frequency.

5.5 Summary

In this chapter, continuous scan laser Doppler vibrometry was extended to output-only measurements by capitalizing on the system identification methodology for linear time-periodic systems. As with conventional output-only modal analysis, the method assumes that the forces exciting the system are random white noise, and they sufficiently excite all of the modes of interest. Theoretical development reveals that when CSLDV is used, each mode appears at several peaks in the power spectrum. To apply the output-only identification algorithm for LTP systems, the measured CSLDV signal is first exponentially modulated to create what is called a harmonic power spectral density function, and then a standard output-only algorithm such as

peak-picking can be used to identify the modes of the system. Each identified mode is comprised of a set of Fourier coefficients that describe the variation of the mode shape as a function of time as the laser scans periodically over the structure. In this work, the harmonic spectrum was processed both by peak-picking and by curve fitting using the Algorithm of Mode Isolation. Both methods gave good results for the systems studied here.

The new output-only algorithm for CSLDV was first validated on a free-free beam in a laboratory setting. The algorithm was found to give results that were very similar to a tuned analytical model of the beam. Various scan frequencies were investigated and their associated issues were discussed. The output spectra shown in this chapter seemed to be considerably noisier than the spectra of the free-response (to a single hammer strike) that was processed in a prior work [54], but the same has been observed when comparing any conventional output-only modal analysis with experimental modal analysis methods where the input forces are measured and controlled. The methodology presented here was further explored by using it to measure the modes of a parked wind turbine. The vibrometer was used to measure the spectrum of the response at the tip of the blade (conventional fixed-point output-only modal analysis) and CSLDV measurements were also acquired with the laser scanning along the length of one blade to identify the mode shapes. Qualitatively reasonable results were obtained for seven modes of the turbine, which were found to correspond to a tower bending mode and the first two bending modes of the blades.

6 Lifting Approach on Output-only Modal Analysis

In this chapter, the positive harmonic correlation function is lifted to simplify output-only modal analysis. The proposed output-only algorithm is demonstrated on a simulated beam and compared with the previous algorithms based on the harmonic power spectrum. Then, the lifting approach is validated on a wind turbine under ambient excitation using a new long range laser vibrometer.

6.1 Introduction

In Chapter 5, the CSLDV was extended to the output-only modal analysis where the input forces are unmeasured and random using the harmonic power spectrum. While this method has proved effective, the identification procedure is somewhat labor intensive since a multitude of peaks are present in the harmonic power spectrum for each mode of the system. The resulting mode shapes can also vary depending on which peaks in the harmonic power spectrum are used to estimate them. On the other hand, the lifting method, as introduced in Section 1.4.2, allows one to extract mode shape from CSLDV measurements almost automatically. Using this approach, the responses at the same location along the laser path are grouped together. The re-organized responses then appear to be from a set of pseudo transducers distributed along the scan path, except that each sensor samples only one time over each scan period, and there is a constant time delay between the measurements at each point. As a result, according to the sampling theorem, all modes of the system and their harmonics are aliased to the range from zero to half of the scan frequency. The lifting approach produces a set of spectra that are mathematically equivalent to a single-input multiple-output system, and hence

conventional modal analysis routines can be used to extract the modal parameters from the CSLDV measurement. The lifting approach was used to extract the natural frequencies and mass-normalized mode shapes of a free-free beam under impact excitation in [54].

This chapter presents a variant on the output-only modal analysis using CSLDV by combining the lifting approach with the positive harmonic correlation function, which is analogous to the free response of a time periodic system. The spectrum after lifting is much simpler to interpret and can be readily curve-fit with virtually any modal parameter identification routine. The proposed algorithm is evaluated on a simulated beam and compared with the harmonic power spectrum algorithm. Later, the algorithm is used to identify the first several modes of a parked wind turbine under wind excitation, capturing the deformation shape along one blade in detail. A new long range Remote Sensing Vibrometer (RSV) from PolyTec® is employed for these measurements.

The rest of this chapter is organized as follows: Section 6.2 compares the harmonic power spectrum algorithms with the lifting approach using a simulated beam measurement. In Section 6.3, the new lifting approach is applied to the identification of a wind turbine under ambient excitation, using the new long range remote sensing vibrometer provided by PolyTec®. Section 6.3 presents the conclusions.

6.2 Comparison of Output-only Algorithms on a Simulated Beam

The parameters of the simulated beam are listed in Table 7. They are identical to the parameters of a real beam tested in [54]. The first five analytical bending modes were used to construct the mass and stiffness matrices by means of the Ritz method [83]. Each mode was also assumed to have 0.5% modal damping, which is close to the experimentally measured value.

The response of this simulated model to random excitation was obtained using the ‘*lsim*’ function in Matlab with a step size of 1/10240s (10240Hz) for 488 seconds. Responses at different locations along the beam were picked up sequentially at 128Hz to simulate the continuous scan, which generated 80 pseudo measurement points per scan cycle. Note that the scan frequency and the sampling frequency are both practical for the commercially available laser Doppler vibrometer.

Table 7 Parameters for the simulated CSLDV test

Beam geometry	L 971.6 mm × H 25.4 mm × W 3.2 mm
Density	2710 kg/m ³
Elastic modulus	66 GPa
Laser scan frequency	128 Hz
Laser sampling frequency	10240 Hz
Simulated duration	488 s

The simulated measurement was used to form the exponentially modulated output signal with $n=-10\ldots10$, as described in step 4. Trial and error revealed that $n=-10\ldots10$ was necessary to include all important harmonics that describe the bending modes up to the 5th order. Then, each of these modulated time histories was divided into 150 sub-blocks of 6.4 seconds, each with 50% overlap, and a Hanning window was applied. After that, each sub-block was zero-padded to twice its original length. The linear power spectra between the 21 modulated signals and the original time history (unmodulated signal) were computed and averaged over the 150 sub-blocks, resulting in the primary column of the harmonic power spectrum, $S_{YY}(\omega)_{n,0}$, as shown in Figure

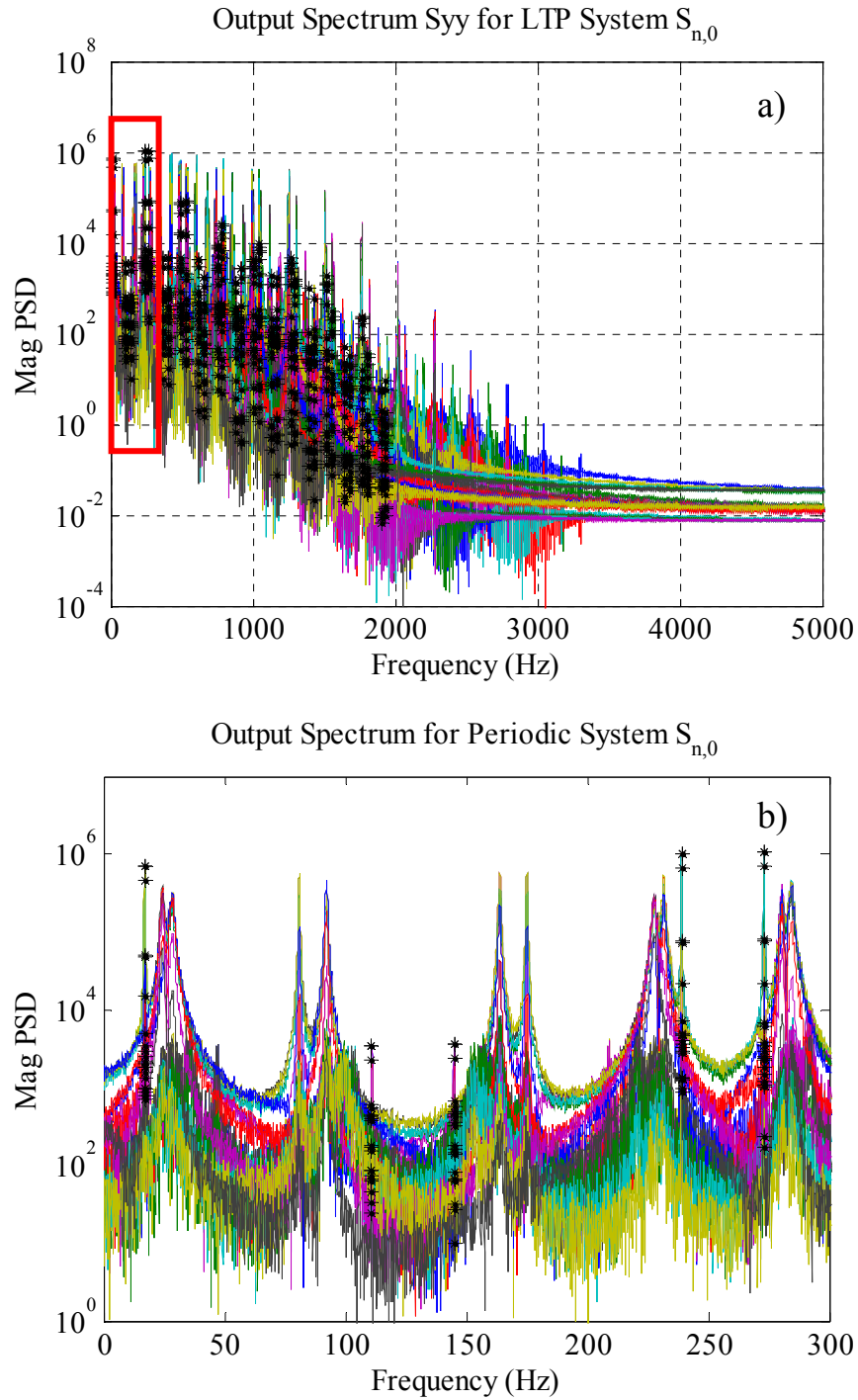


Figure 46 Primary column of the harmonic power spectrum, $S_{YY}(\omega)_{n,0}$.

(a) Harmonics of the 1st mode (dark stars), (b) Zoom-in plot for the harmonics of the 1st mode.

Though the beam model contains only five bending modes, there are tens if not hundreds of harmonics in the harmonic power spectrum due to the moving laser position, as shown in Figure 46a, where the dark stars represent the harmonics of the 1st bending mode at 17.06Hz. These harmonics, separated by the 128Hz scan frequency, spread over a wide frequency range. Figure 46b shows the first few harmonics of the 1st bending mode. The harmonics at around 111Hz and 239Hz are from the negative harmonics but folded to the positive axis [57]. The mode vector can be estimated from each peak using peak-picking, and the physical mode shape can then be constructed according to step. However, the mode shapes were found to vary significantly depending on which peaks were included in the peak-picking. Indeed, this procedure requires extensive user input to discard noisy harmonics. Nevertheless, identification is possible and the identified natural frequencies and damping ratios are listed in Table 8. The damping ratios were obtained by curve fitting a few of the dominant peaks in the harmonic power spectrum. The modal assurance criterion (MAC) [72] was used to compare the reconstructed mode shapes with the analytical shapes, and the MAC values are also shown in Table 8.

The harmonic correlation function was obtained by taking a two-sided inverse FFT of the harmonic power spectrum $S_{YY}(\omega)_{n,0}$. A rectangular window was used to delete the negative harmonic correlation function, leaving the portion that contains only the stable poles of the system. Figure 47 shows the positive harmonic correlation functions that were obtained from the 21 harmonic power spectra. The positive harmonic correlation function has a similar decaying form as that of the free response of a linear time invariant system. The previous zero-padding process was employed to ensure the positive harmonic correlation function has the same length as the original time history in each sub-block.

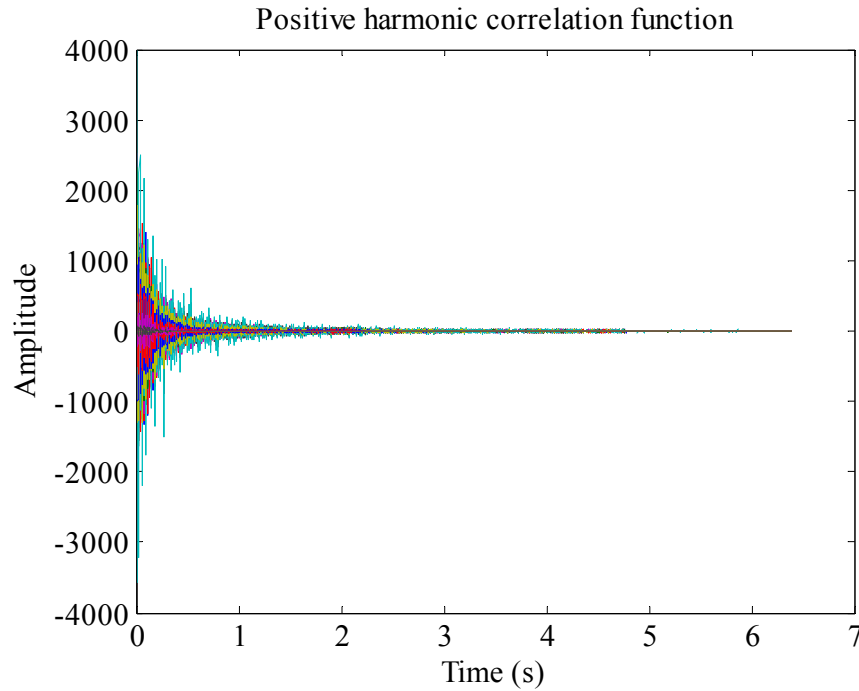


Figure 47 Positive harmonic correlation function

The lifting approach was then employed to lift the positive harmonic correlation function, which has 80 pseudo measurement points in each scan cycle. The responses at the same location along the beam are grouped to form a single-input multiple-output system, which can be viewed as having 80 pseudo sensors and 21 degrees of freedom at each sensor due to the modulation ($n = -10 \dots 10$). Figure 48 shows the composite (averaged) spectrum of the lifted positive harmonic correlation function. The lifting approach aliases all sidebands of one mode to a single frequency between zero and half of the scan frequency. As a result, the lifted spectrum contains only one peak for each mode, and the averaged spectrum looks very clean compared to the harmonic power spectrum in Figure 46. However, after aliasing, the modes are closely spaced, so the 128Hz scan frequency might be too low to separate the 5 bending modes if the damping in the system were higher. The experimental data (gray solid line) was curve fitted using Algorithm of Mode Isolation (AMI) [78] to identify the natural frequencies, damping ratios and

mode shapes. The red line in Figure 48 shows the difference between the fitted response and the original data. The reconstructed FRF (dotted line) compared well with the measurements. The identified mode shapes were processed using a least squares approach, as in step 14, and the optimal estimate of the Fourier coefficient vector was extracted. The physical mode shapes were reconstructed by plotting the time periodic shapes versus the laser path. The MAC values between the reconstructed mode shapes and the analytical shapes are given in Table 8 as well.

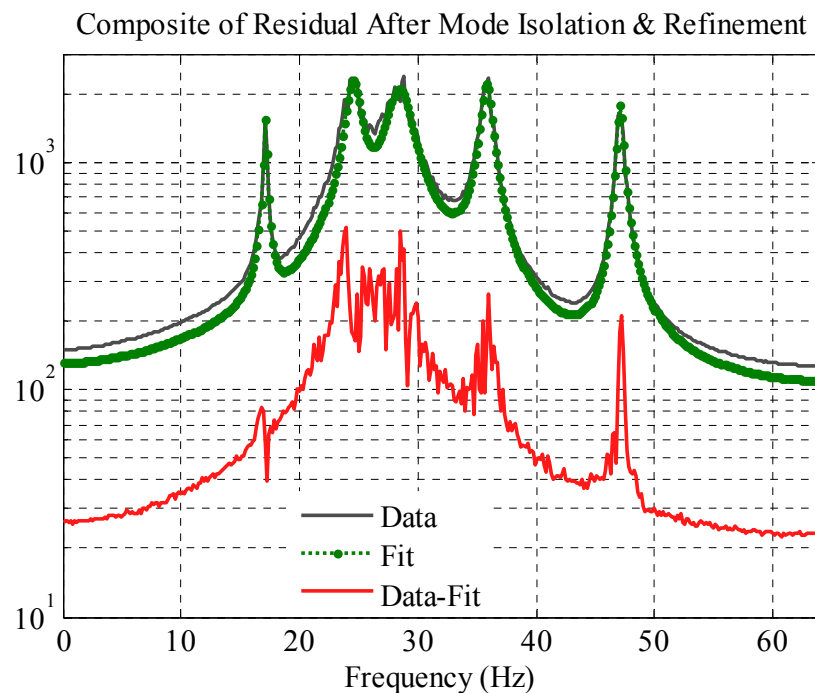


Figure 48 Lifted positive harmonic correlation function fitted with AMI

Figure 49 shows the reconstructed 1st bending mode at 17.06Hz using the harmonic power spectrum and the lifting approach. The blue dashed line represents the analytical shape. The identified shapes using both methods agree very well with the exact shape. Table 8 compares all identified natural frequencies and damping ratios to the exact properties of this simulated beam. It can be seen that the natural frequencies are all within 1% of the actual values. The MAC values are all close to one as well. This indicates that the lifting approach has successfully identified all modal parameters of the beam, and is as effective as the harmonic

power spectrum algorithm. One should note that the identified damping ratios are less accurate; the error is about 46% for the 1st bending mode, and up to 15% for other modes. These large errors are most likely due to distortion caused by the Hanning window [84].

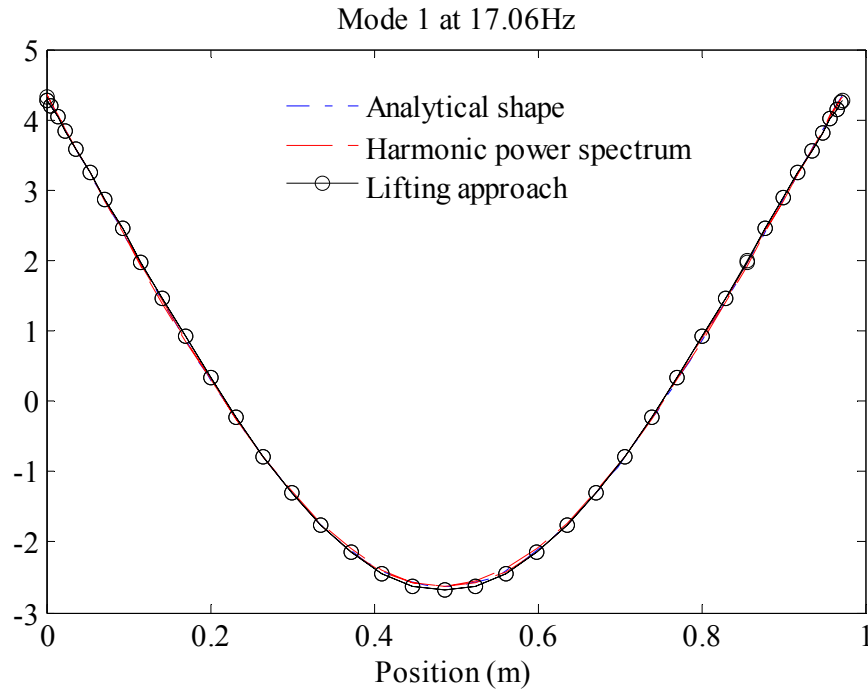


Figure 49 Comparison of mode shapes reconstructed from different algorithms

Table 8 Comparison of modes identified by different algorithms

Mode	Analytical		Harmonic power spectrum			Lifting approach		
	Frequency (Hz)	Damping (%)	Frequency (Hz)	Damping (%)	MAC	Frequency (Hz)	Damping (%)	MAC
1	17.06	0.5	17.06	0.73	1.0000	17.07	0.66	1.0000
2	47.04	0.5	47.02	0.57	0.9996	47.08	0.57	1.0000
3	92.21	0.5	92.16	0.54	0.9997	92.12	0.55	1.0000
4	152.42	0.5	152.44	0.53	0.9996	152.36	0.49	0.9965
5	227.70	0.5	227.78	0.48	0.9979	227.79	0.43	0.9952

The simulated experiment indicates that the harmonic power spectrum and the lifting approach both give comparable results, but the lifting approach provides a much simpler

spectrum, which greatly reduces the effort required in modal identification. Moreover, the lifting algorithm might also be advantageous if the structure of interest contained modes with close natural frequencies, where multiple-input multiple-output measurements are necessary to distinguish these modes and determine the modal parameters.

6.3 Application to Wind Turbine using Remote Sensing Vibrometer

The lifting approach was used to identify the modes of a wind turbine blade mounted on the tower, as depicted in Figure 50. This wind turbine is the same as the turbine studied in previous work [57] except with a different set of blades. During the tests, the turbine was locked to prevent rotation, and the blade of interest was pitched so that the laser was nominally perpendicular to the chord of the blade (i.e. measuring in the flap-wise direction). A prototype of Polytec's new remote sensing vibrometer was used to acquire the measurements. The vibrometer incorporates a longer wavelength laser (1550nm, invisible) and higher laser power (10mW) than the Polytec PSV-400 that was used in [57], so it is optimal for long standoff distances. Using this vibrometer, a clean velocity signal was acquired at a standoff distance of 77m between the vibrometer and the turbine, without any surface treatment to the blade. In contrast, the measurements from the PSV-400 (1mW, 633nm laser) vibrometer were pure noise at this distance without retro-reflective tape applied to the blade. A customized x-y mirror system was used to redirect the laser from the remote sensing vibrometer to scan over as much of the 4.5m long blade as possible. The blade was excited purely by the wind, whose maximum speed was about 9m/s during the tests.

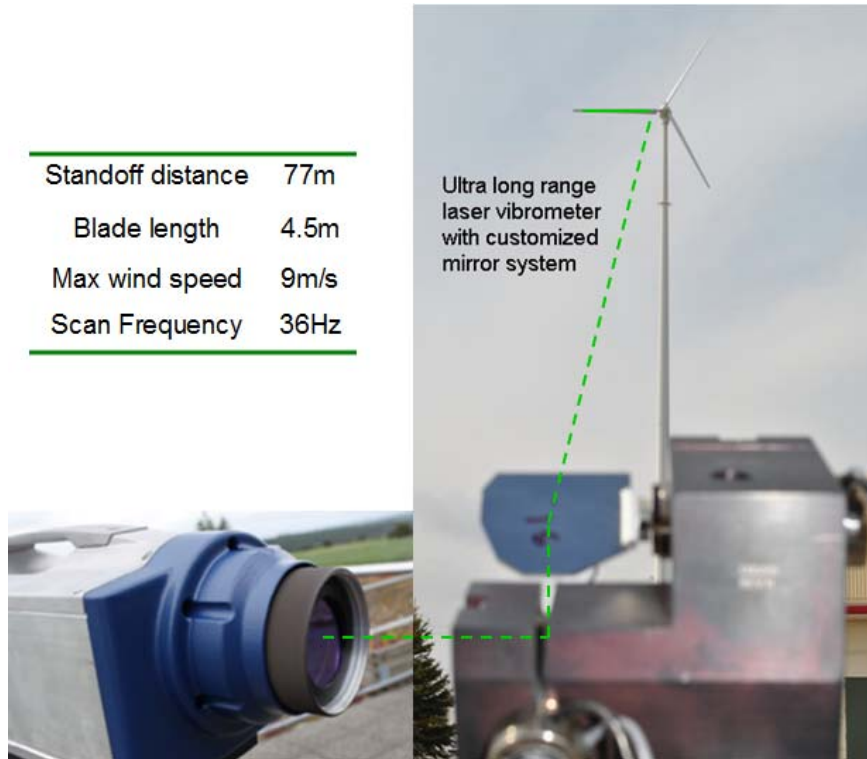


Figure 50 Schematic of experimental setup. The photograph on the left shows a generic photo of a remote sensing vibrometer.

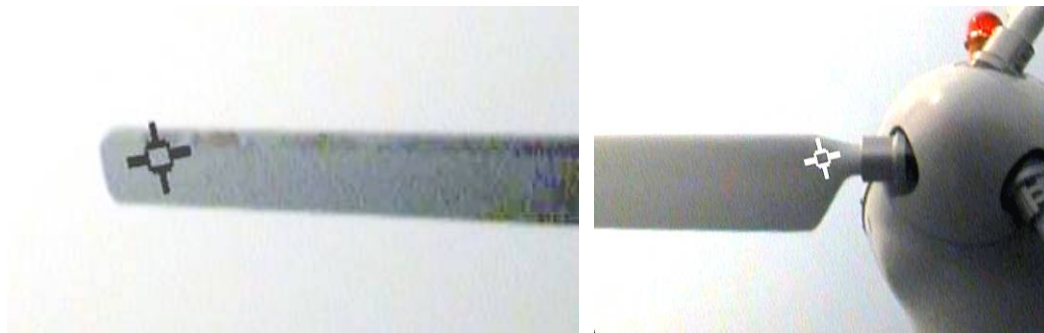


Figure 51 Photographs showing the position of the CSLDV measurement point at the extremes of its travel. The CSLDV scan path was a line connecting these two points.

The laser scanned a line over the blade for 410 seconds with a scan frequency of 36Hz and a sampling frequency of 2560Hz. Since the laser was not visible, and the guide laser was not available in the prototype, the scan path was defined by first determining the voltages to position the laser at both ends of the blade, as shown in Figure 51. These voltages were then used to

define a scan path that corresponded to a line between these two points. Figure 52 shows the measured velocity signal that has the appearance of random noise due to the random nature of the input. However, a closer look in Figure 52b indicates that the signal is dominated by a frequency component at 36Hz. There are clearly several other frequencies present in the response, presumably due to the vibration modes of the turbine.

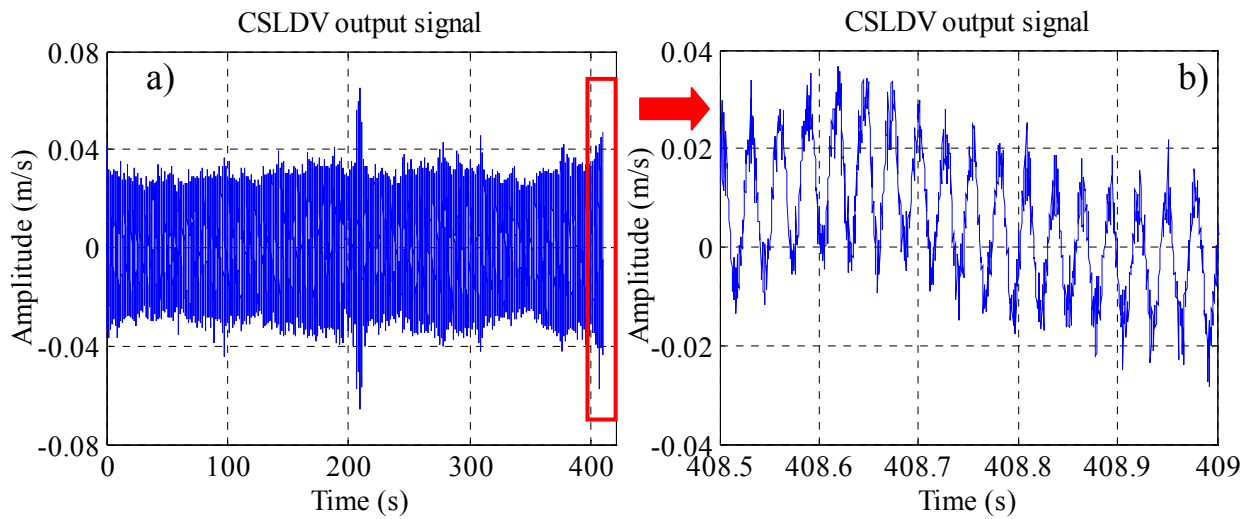


Figure 52 CSLDV output signal under random excitation (36Hz scan frequency). (a) Full time history (b) Time history from 408.5s to 409s

The entire measured time history was resampled at 2592Hz to generate 72 samples per scan cycle. Since only frequency components up to a few hundred hertz were of interest, the resampled signal was low pass filtered to 250Hz to reduce the high frequency noise. The frequency component corresponding to the 36Hz scan frequency was also deleted since it is known to be dominated by noise (e.g., speckle noise, noise due to mirror configuration and the time varying distance between the laser head and the measurement point). The resampled signal was then exponentially modulated with harmonics $n = -3 \dots 3$, resulting in 7 modulated time histories. Each of these modulated signals was decomposed into 25.6s sub-blocks with 50% overlap, generating 31 blocks, and a Hanning window was applied.

Figure 53 shows the harmonic power spectrum computed from the exponentially modulated periodic signals. The spectrum has many peaks for each mode, each separated by the scan frequency 36Hz. As was the case for the simulated beam in Section 6.2, the harmonic power spectrum is quite complicated, with many peaks from each mode, but with some care one can determine the number of modes and their modal parameters. In [57] these peaks and their harmonics were used to find the natural frequencies and mode shapes of the turbine blade using peak-picking, and for brevity, those results will not be repeated in the work.

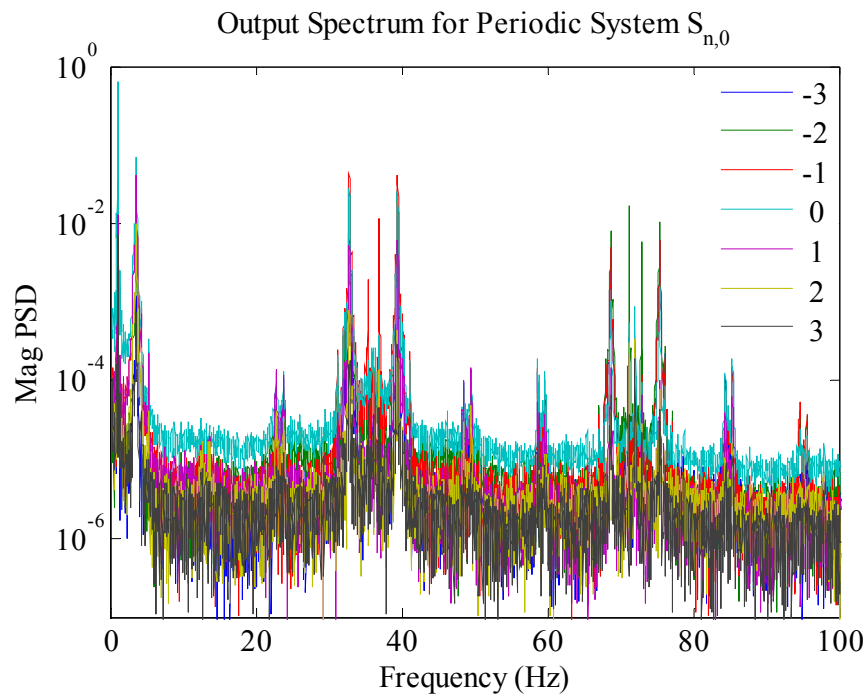


Figure 53 Harmonic power spectrum of the measured signal up to 100 Hz.

The harmonic correlation function was then obtained by taking the inverse FFT of the harmonic transfer function. A rectangular window was used to retain the positive harmonic correlation functions, as depicted in Figure 54. Here only one (0^{th} order or the center) of the 7 positive harmonic correlation functions is displayed, but all of the correlation functions have the appearance of a standard impulse response function with a dominant low frequency mode which

persists for more than 20s. Several higher frequency components exist as well but they disappear quickly after about 10s.

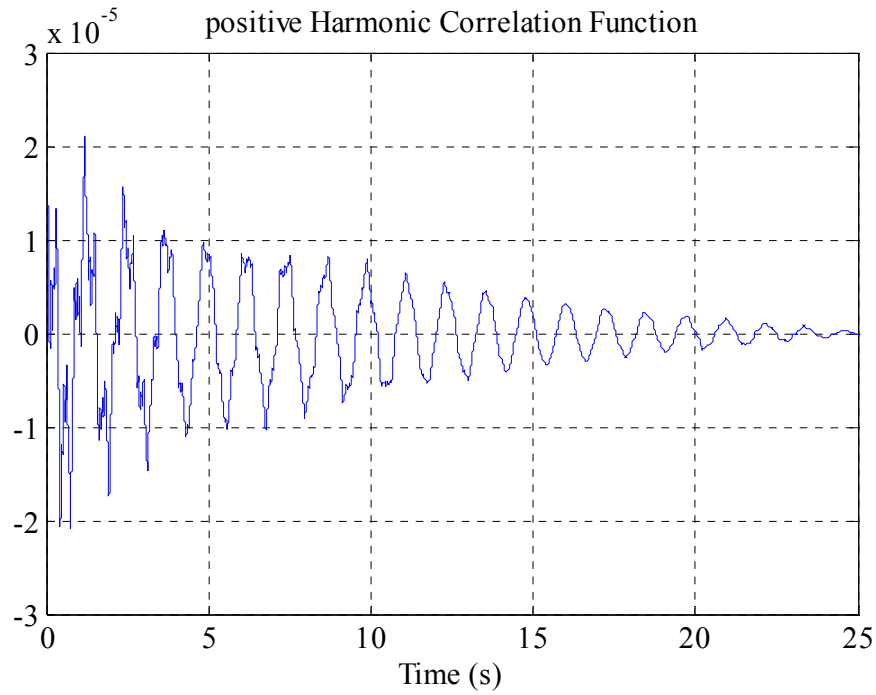


Figure 54 Positive harmonic correlation function

The positive harmonic correlation functions were lifted to create a single-input multiple-output system. Figure 55 shows the averaged spectrum of the lifted responses (solid grey line). The AMI algorithm was used to fit a modal model to the response (dotted line). Only two peaks at 0.81Hz and 3.3Hz are prominent in the plot. A mode was fit to each of these peaks and the natural frequencies and damping ratios are reported in Table 9. There appear to be other closely spaced modes near 3.3 Hz according to the residual. This is reasonable, as for a three-bladed turbine, the blade bending modes typically appear at three close frequencies due to the anisotropic rotor [14]. However, it was difficult to tell if these frequencies were meaningful since only one blade was measured, and these modes tend to differ in the relative amplitudes and directions in three blades, so they are not reported. A closer inspection reveals a few other peaks at 12.3 and 13.3 Hz, respectively. These peaks, which are only barely visible in the average

spectrum, are actually fairly prominent in the subtraction residual, and a mode was identified near each of these peaks.

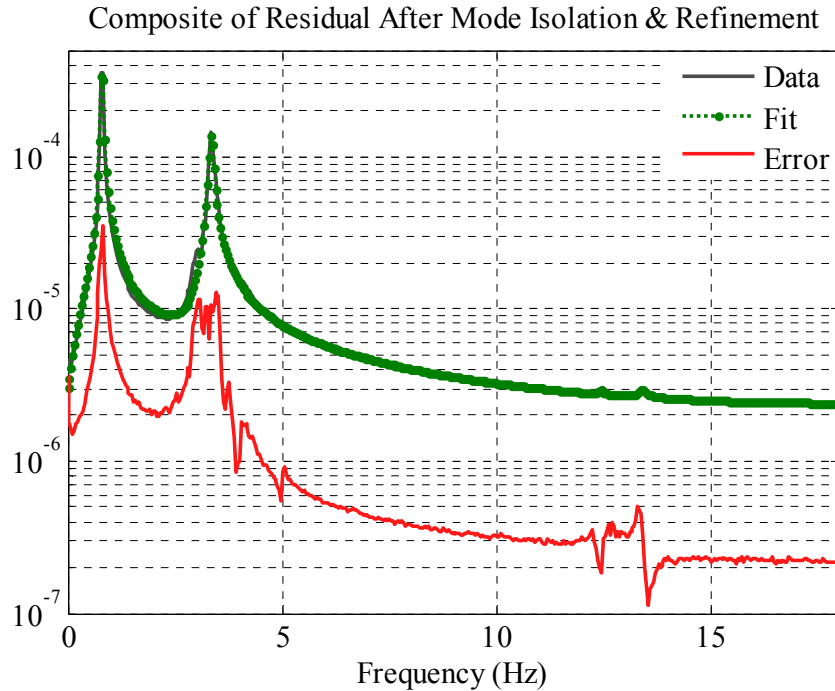


Figure 55 Averaged spectrum of the lifted response fitted with AMI

Next, the mode shapes were reconstructed from the Fourier coefficients that were identified using Eq. (56). Since AMI fits a complex mode model to the measurements, both the real and imaginary parts of the mode shapes are shown in Figure 56. However, a lightly damped structure such as this is expected to have real modes, so the imaginary parts most likely arise due to inaccuracy in the measurements or signal processing. The blade appears to move as a rigid body in the first mode, at 0.81Hz, suggesting that this mode primarily involves bending of the tower. The mode at 3.33Hz appears to be the first flap-wise bending mode of the blade. The 0.81Hz and 3.33Hz modes both have very small imaginary parts, and the shape estimated as the laser spot moved from root to tip agrees very well with the shape estimated as the laser spot returned from tip to root, suggesting that the shape is quite accurate. The third and fourth

identified frequencies are second bending modes of the blade. These modes can be seen to exhibit larger imaginary shapes, presumably due to noise considering the vibration amplitudes are two orders of magnitude lower than the dominant modes at 0.81Hz and 3.33Hz. Their general shape is similar to the second mode of a cantilever beam, as expected.

Table 9 *Modes identified from the lifted response*

Mode	Natural frequency	Damping
Tower Bending	0.81Hz	1.61%
Flap Wise Bending 1	3.33Hz	1.52%
Flap Wise Bending 2	12.42Hz	0.44%
	13.41Hz	0.70%

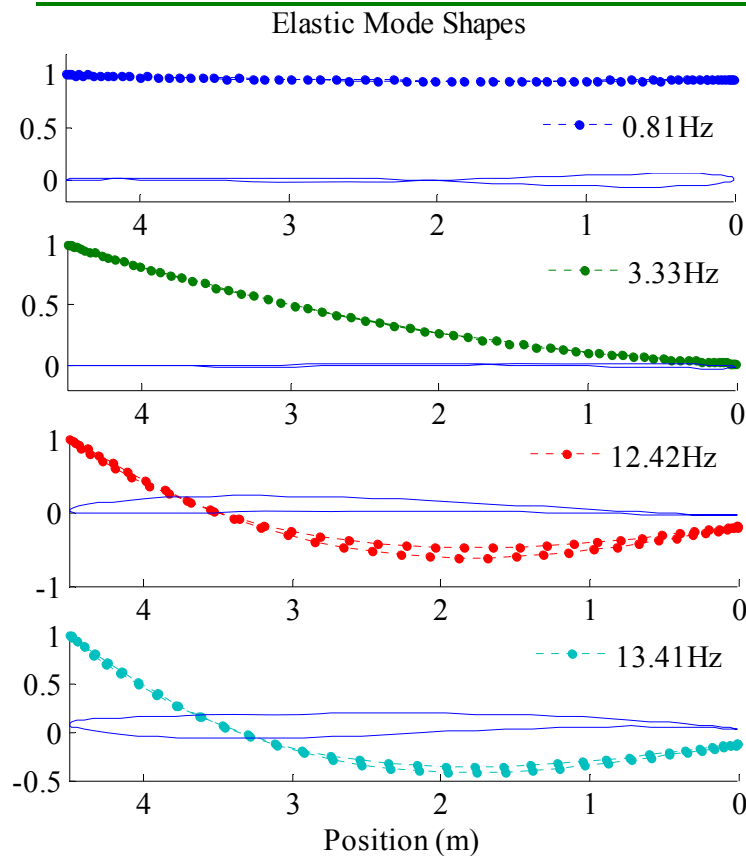


Figure 56 Real (dots) and imaginary parts (solid-line) of the mode shapes identified from the

CSLDV measurements.

For comparison, a standard output-only modal test was performed to estimate the blade's mode shapes. A patch of retro-reflective tape was applied to the tip of the blade and the PSV-400 vibrometer was pointed to this location as a reference. The remote sensing vibrometer laser was then positioned sequentially at five different points along the length of the blade to measure its response. The positions of the measurement locations were determined by measuring the angle of the mirror (which was fixed during each measurement). The cross power spectra of the measurements from two lasers were then computed and used to determine the natural frequencies and modes shapes of the turbine. As shown in Figure 57, only the modes below 20Hz were excited by the wind. Figure 58 shows the identified mode shapes using this conventional operational modal analysis test. The same rigid body mode was identified at 0.81Hz. Three modes that have similar shape were extracted near 3.3Hz. However, as was discussed previously, there is little evidence that the additional modes are meaningful since additional tests are required on all three blades simultaneously to determine the shape. Similarly, the second blade bending mode was identified around 13.0Hz, and since the turbine is known to have three blade bending modes, shapes were extracted at two other nearby peaks. The mode at 9.03Hz was found to be the second bending mode of the tower. The shape is similar to that of the rigid body mode at 0.81Hz, and hence not repeated in Figure 58.

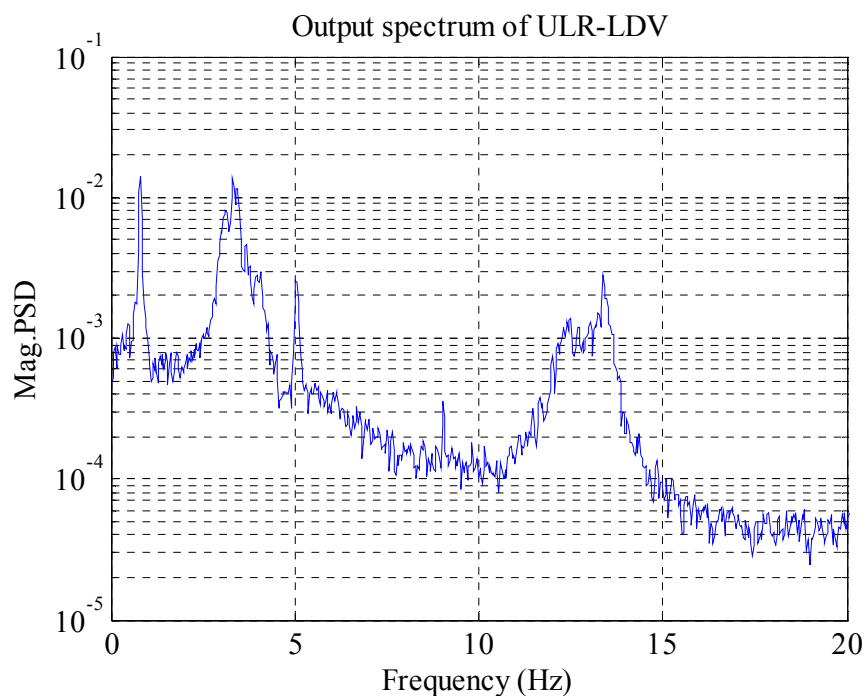


Figure 57 Composite output cross spectrum from a stand operational modal test

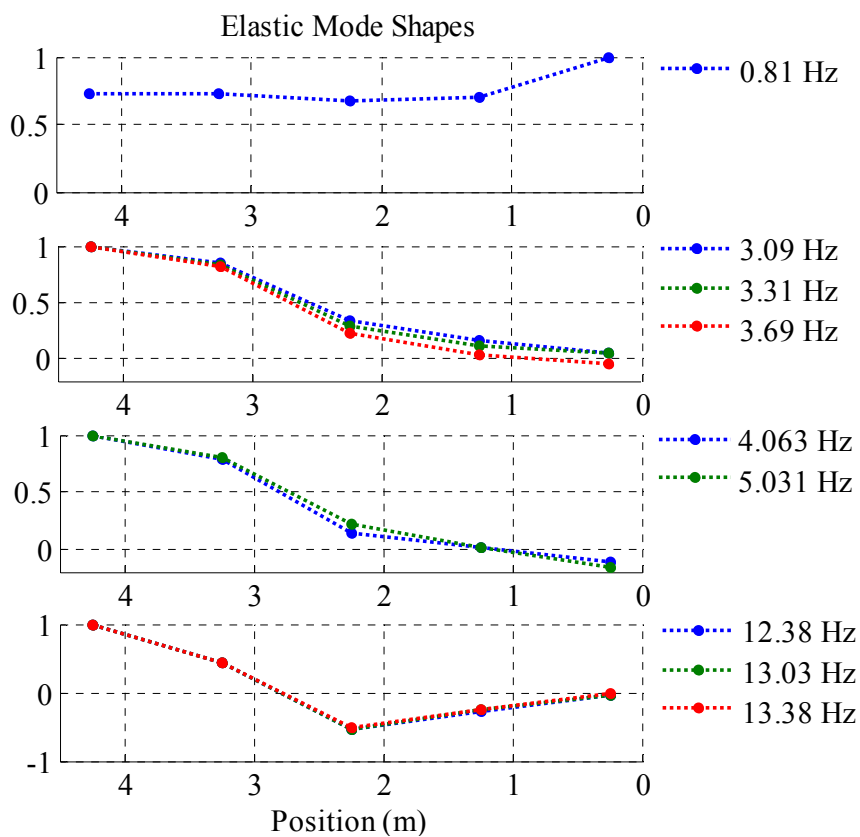


Figure 58 Mode shapes at five points obtained using a standard operational modal analysis.

It is informative to compare the results from the standard output-only modal test to those from the CSLDV. First, one should note that the standard approach required a second laser as the reference, adding tens of thousands of dollars to the cost. Second, the standard test required acquisition of time histories at five different locations, which would nominally increase the measurement time by a factor of five. For example, each of the measurements shown above took 5.3 minutes, which results in a total test time of 26.5 minutes. In contrast, the continuous-scan test only took 6.7 minutes. Third, the mode shapes obtained by the standard test agree fairly well qualitatively with those obtained by CSLDV, but there are several points which appear to be questionable in the standard test, e.g., the large deformation of the rigid body mode at the root of the blade. Anomalies such as these could possibly be caused by changes in the wind conditions from one measurement to the next, since the tests take so long. Fourth, the mode shapes obtained by the standard test have less spatial detail than those obtained by CSLDV, even though the test time was longer.

6.4 *Summary*

This chapter introduced a lifting approach to process CSLDV measurements from structures excited by unmeasured random inputs. The algorithm makes use of the positive harmonic correlation function that is analogous to the free response. The responses at the same location along the scan path are grouped together to form a single-input multiple-output system. This causes all of the sidebands in the spectrum to be aliased to a single frequency from zero to half of the scan frequency, greatly simplifying the identification compared to the algorithm fitting the harmonic power spectrum directly. Furthermore, using this approach one can use

standard model identification routines for time invariant systems, whereas the harmonic power spectrum requires an algorithm that is specialized to operational modal analysis.

The lifting approach was compared with the algorithm based on the harmonic power spectrum using simulated measurements from a free-free beam and real measurements from a parked wind turbine. The comparison revealed that similar results could be obtained with either of the approaches, but the lifting approach provided a much simpler spectrum that greatly reduced the effort required to extract the modal parameters. However, the sideband harmonics that capture each mode shape may overlap if the scan frequency is not carefully chosen. This was particularly noticeable for the wind turbine, where the higher frequency bending modes were initially buried in the tails of the first two modes and were not obvious in the spectrum until the dominant modes had been fit and removed.

This work also reported the first test of Polytec's new remote sensing vibrometer, which employs a longer wavelength and higher laser power than previous lasers. It is remarkable to note that excellent results were obtained with this laser even at a scan frequency of 36Hz. At this scan frequency, the peak surface velocity of the laser spot was about 500m/s, but the speckle noise in the measurements was still relatively small even though the surface was not treated with retro-reflective tape. A conventional output-only modal analysis test was performed with two LDVs, and those results were found to be comparable with the CSLDV results. However, this comparison highlighted many of the practical problems that are encountered when using laser vibrometers to perform standard output-only modal analysis on a large structure. The CSLDV approach would be even more attractive for large wind turbines where the natural frequencies are even lower (less than 10Hz) and hence the time required to obtain operational modal analysis data with a pair of lasers would be excessive.

7 Output-only Modal Analysis of Rotating Wind Turbine using Harmonic Power Spectrum

In this chapter, the harmonic power spectrum was used to identify the periodic modes of an operating wind turbine, which is modeled as an LTP system. The results are discussed and compared with those previously obtained from simulated turbines.

7.1 Introduction

All previous applications of the proposed identification algorithms focused on extracting modal parameters of Linear Time Invariant (LTI) structures measured with CSLDV. A CSLDV measurement is a special case of Linear Time Periodic (LTP) systems because the periodic output is only caused by the periodically changing laser position. For example, the parked wind turbine in Chapter 5 and Chapter 6 was assumed to be time invariant. However, wind turbines cannot be truly modeled as LTI systems, especially when operating. The blades are different from each other, so the rotor has different properties in each direction. This causes periodically changing boundary conditions when the rotor is rotating. Therefore, wind turbines have to be modeled as LTP systems to better characterize their behavior under different operating conditions. This greatly limits the applicability of well-established modal analysis methods for LTI systems in order to validate the numerical models of modern wind turbines.

The multi-blade coordinate transformation, also known as the Coleman transformation [85], has been used to identify the modal parameters of isotropic turbines (i.e., all blades are identical and symmetrically mounted) [14, 86]. The method converts the motion of individual blades described in the rotating frame into the ground-fixed frame using some special variables

that combine the deflections of all three blades with the instantaneous rotor azimuth. When the rotor is isotropic, this method eliminates all of the periodic terms in the equations of motion, thus making the system time invariant. As a result, modal analysis techniques for LTI systems, such as stochastic subspace identification, can be applied. The multi-blade coordinate transformation is built on the assumption that the rotor is isotropic. For anisotropic turbines [26], the transformed equations of motion still have periodic terms. Therefore, a more general approach known as the Lyapunov-Floquet transformation can be adopted [25]. The Floquet eigenvectors of the system matrix can be used as the basis to eliminate the periodic terms in the equations of motion. However, since the Floquet eigenvectors are not known a priori, the Lyapunov-Floquet transformation is only an analytical tool for simulated models and cannot be applied to the experimental identification of real turbines in operation. Recently, an improved multi-blade coordinate transformation was proposed that appears to work on anisotropic rotors with time-varying rotating speed [86]. It was used to study the stability of a simulated turbine under different operational conditions. However, no application of the modal identification using this improved multi-blade coordinate transformation has been reported yet.

In this chapter, the proposed harmonic power spectrum was used to process measurements from an operating turbine under pure wind excitation. The data was provided by Brüel & Kjær. The Vestas V27 wind turbine (225kW, rotor diameter 27m) was instrumented with accelerometers on the three blades. The blade pitch and rotor azimuth angles were also measured and recorded. When the turbine was parked, a conventional output-only modal analysis was performed to identify the natural frequencies and mode shapes of the blades in both flapwise and edgewise directions. Then, the measurements under operating condition were analyzed using the harmonic power spectrum. The identified periodic mode in edgewise

direction was discussed and compared with the simulated results of different turbines obtained by other researchers [14, 26, 63, 86, 87].

The rest of this dissertation is organized as follows: Section 7.2 introduces the wind turbine and sensor arrangement. In Section 7.3, the turbine was parked, and the modes in both edgewise and flapwise directions were identified using LTI techniques. In Section 7.4, the harmonic power spectrum was used to analyze the turbine when operating. Section 7.5 summarizes this work.

7.2 *Experimental Setup*

Figure 59 shows the sensor locations on the three-bladed Vestas 27 wind turbine. Twelve accelerometers were installed on each blade to measure the flapwise and edgewise vibration. On the nacelle there are three triaxial accelerometers (center plot in Figure 59), recording the vibration in the front, rear left and rear right side of the nacelle, respectively. Two DC accelerometers (not visible in Figure 59) were installed 90° from each other on the rotor's hub. The signals from these accelerometers were used to calculate the instantaneous rotor position (azimuth) and rotor angular speed. In order to improve azimuth calculations, a tachoprobe was installed on the high-speed shaft (the output of the gearbox). The tachoprobe provides one pulse per revolution of the high-speed shaft, and 23.3333 (gear ratio) revolutions correspond to one revolution of the rotor. A pitch sensor was installed inside the hub; its readings were used for selecting recordings with no or relatively small pitch activity. In this case, the edgewise motion of the blades are in the plane of wind turbine blades, and the flapwise motion of the blades are out-of-plane. In addition, two IRIG-B signals were used to synchronize signals from the rotor

and nacelle sensors. In total, 51 channels were recorded at a sampling frequency of 4096Hz. Additional details regarding the measurement setup can be found in [87].

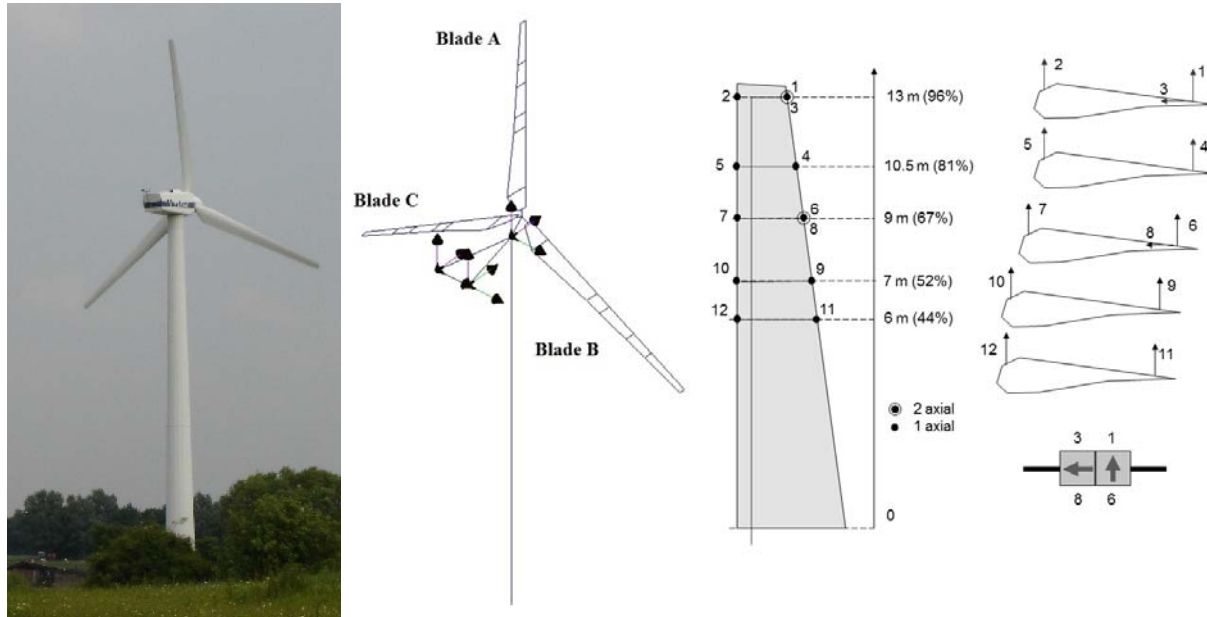


Figure 59 Accelerometers location on the blade (pictures from [87] authorized by the author)

Two different boundary conditions of the wind turbine were analyzed. In the first case the brake was applied, and the parked turbine was approximated as an LTI system. A conventional output only modal analysis was performed using peak-picking. In the second case, the turbine was rotating and had to be modeled as an LTP system. The harmonic power spectrum was used to identify periodic modes of the rotating turbine blades. However, in the harmonic power spectrum the phase error of the exponential component $e^{-jn\omega_A t}$ accumulates with time for an inaccurate rotating frequency ω_A . This would then distort the modulated periodic output signal, especially for a long time history. Therefore, an accurate and steady rotating speed is the key in the modal analysis of the turbine blades. Unfortunately, the rotating speed is rarely constant in practice. Figure 60 shows a portion of the time history of rotating speed computed from one of the DC accelerometers. The average rotating speed in every 0.125 revolution was

obtained. During the 300s period, the maximum rotating speed was 0.5435Hz, the minimum rotating speed was 0.5271Hz, and the standard deviation was 0.0018Hz.

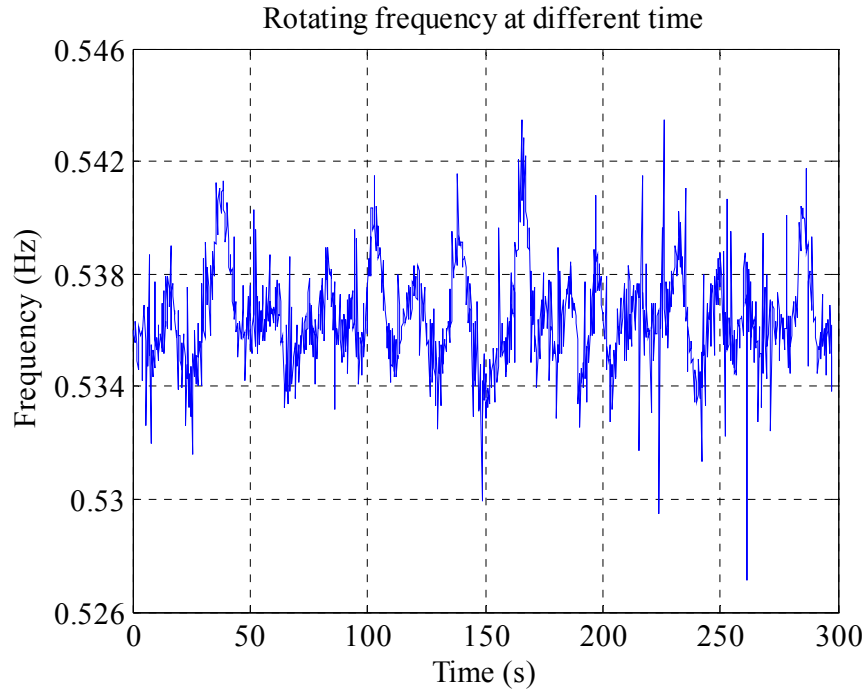


Figure 60 Time history of rotating frequency

Therefore, the first step is to locate a time history where the rotating speed is the steadiest. Furthermore, the vibration of the blades needs to be as large as possible. With this in mind, the data taken at Dec.16, 2012 was selected (20 minutes). The rotating speed, pitch angle and wind speed (30m above the ground) are listed in Table 10. It can be seen that the rotating speeds from the two DC accelerometers slightly differ from each other; this is perhaps due to the installation error. The rotating speed from the tachoprobe appears to be the most accurate. A line was used to cut through all spikes in the tachoprobe signal in order to find a more accurate time interval between any two neighboring peaks, which was then divided by the gear ratio to obtain the rotating speed. The average rotating speed was found to be 0.536893867Hz with a standard deviation of 0.0007Hz. The average pitch angle of all three blades in 20 minutes was -

0.215°, and the standard deviation was 0.085°. The average wind speed at 30m above the ground was 4.73m/s.

Table 10 Testing parameters of slected data

	DC1 (Hz)	DC2 (Hz)	Tacho (Hz)	Pitch Angle (°)	Wind speed (m/s)
Mean	0.5370	0.5370	0.5369	-0.2150	4.7300
Maximum	0.5536	0.5548	0.5385	-0.0525	6.6850
Minimum	0.5228	0.5159	0.5352	-0.4925	2.6250
Standard deviation	0.0064	0.0074	0.0007	0.0850	0.6710

7.3 Output-only Modal Analysis of Parked Turbine

The turbine was modeled as an LTI system when parked and excited with pure wind. The conventional modal identification routine, peak-picking, was used to identify the natural frequencies and mode shapes in order to provide references for the modal identification when the turbine is rotating. The data was 15 minutes long, sampled at 4096Hz. Each of the time histories from the sensors on three blades was divided into 32s (17.5 revolutions) sub-blocks with 85% overlap. This resulted in 187 sub-blocks at each sensor. Then, the conventional cross power spectrum of each sensor was computed using sensor 1 on blade A as the reference. The expected value of the cross spectrum was obtained by averaging over all sub-blocks. Figure 61 shows the averaged power spectra in the edgewise and flapwise directions of the three blades. Low frequency components below 25Hz are of primary interest in wind turbine analysis, and the modes were identified using peak-picking (only the modes below 100Hz were strongly excited). In general, the flapwise motion has larger amplitude. Some of the flapwise modes also appear in the edgewise direction perhaps because the surfaces where the sensors are installed are slightly tilted with respect to the rotating plane (see Figure 59).

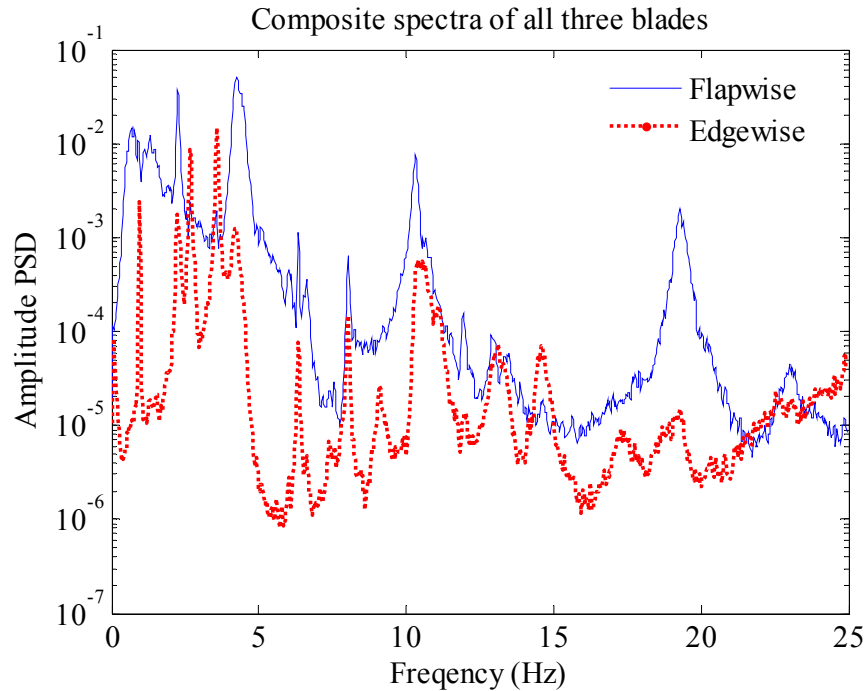
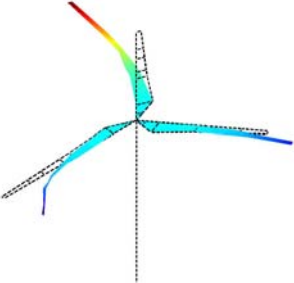
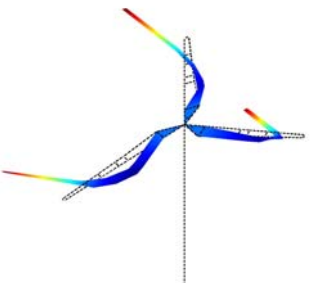
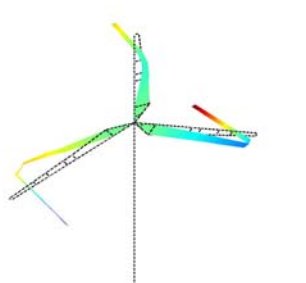
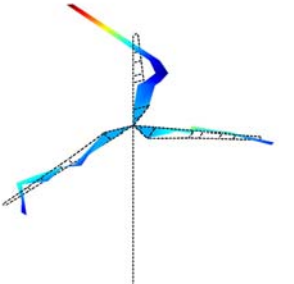
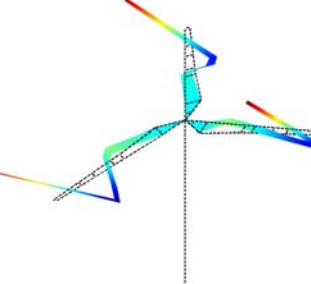
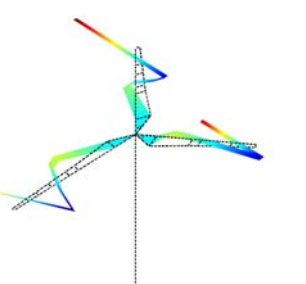
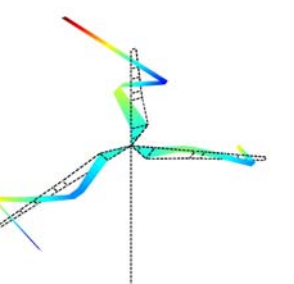
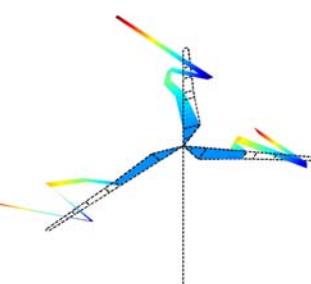
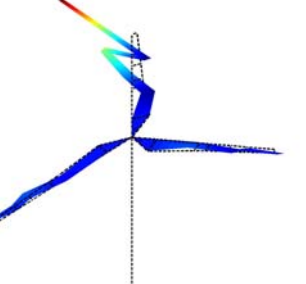


Figure 61 Averaged power spectra in both edgewise and flapwise directions

Table 11 lists the identified blade modes in the flapwise direction (out-of-plane). For a three-blade turbine, each mode may appear at three frequencies that are closely spaced due to the similarity of the blades (the blades are not identical). The first bending mode in the flapwise direction appears at 2.25Hz, where two of the three blades move in the same direction and the third one moves in the opposite direction. The second bending mode occurs at 4.22Hz and 6.34Hz. At 4.22Hz all three blades move in the same direction, and at 6.34Hz only two of them move in the same direction. The second bending mode also appears at 8.03Hz but seems to be coupled with the torsional modes of blade B and C. The third bending mode appears at three frequencies; at 10.31Hz and 11.94Hz where the three blades move in the same direction, and at 12.88Hz where the blade C moves in the opposite direction with respect to the other two. The 4th mode occurs at 19.28Hz. It also appears at 23Hz where it is coupled with another torsional mode.

Table 11 Identified flapwise mode shapes of the parked turbine

Mode at 2.2500 Hz 1 st Bending mode	Mode at 4.2188 Hz 2 st Bending mode	Mode at 6.3438 Hz 2 nd Bending mode
		
Mode at 8.0313 Hz 2 nd Bending mode + Torsion mode	Mode at 10.3125 Hz 3 rd Bending mode	Mode at 11.9375 Hz 3 rd Bending mode
		
Mode at 12.8750 Hz 3 rd Bending mode	Mode at 19.2813 Hz 4 th Bending mode	Mode at 23 Hz 4 th Bending mode+ Torsion mode
		

The modes in the edgewise direction were extracted using peak-picking as well. Only those modes which did not show up in the flapwise direction (see Figure 61) were identified, and their shapes are shown in Figure 62. Note that the vibration amplitude at the hub was assumed to be zero in Figure 62 in order to demonstrate the relative position of each blade. The real vibration amplitude at the hub was not available. All three blades move in the same direction at 0.97Hz. This mode could be from the motion of the tower, which was known to have its first bending mode around this frequency. Blade A has the largest amplitude perhaps because its height is larger than blade B and C. At 2.69Hz two blades move in the same direction while the third one moves in the opposite direction. This mode may be incurred by the first bending mode in the flapwise direction at a similar frequency. The mode at 3.56Hz has all three blades moving in the same direction with similar amplitudes. When the blades and hub assembly were placed on the ground, the first edgewise bending modes were found at 3.28Hz and 3.34Hz respectively. Therefore, the mode at 3.56Hz could be the first bending mode of the blades in the edgewise direction. The frequency increases perhaps due to the change of boundary condition after the blades were installed on the tower. The amplitudes of the 9.09Hz mode are almost zero at 9m from the blade roots. At this frequency, blade A and B have similar amplitude at the tip but they move in opposite directions. This mode could be due to a nearby flapwise mode. At 14.6Hz, two blades move in the same direction while the third one moves in the opposite direction. This mode could be another edgewise bending mode because the amplitude is larger in the edgewise direction. At 17.3Hz, blade A and C move in the opposite directions, while blade B moves in the same direction as blade C but with much smaller amplitudes. This mode could be caused by a flapwise mode as well. Unfortunately, since there were only two accelerometers in the edgewise direction, it is difficult to accurately determine which modes these frequencies belong to.

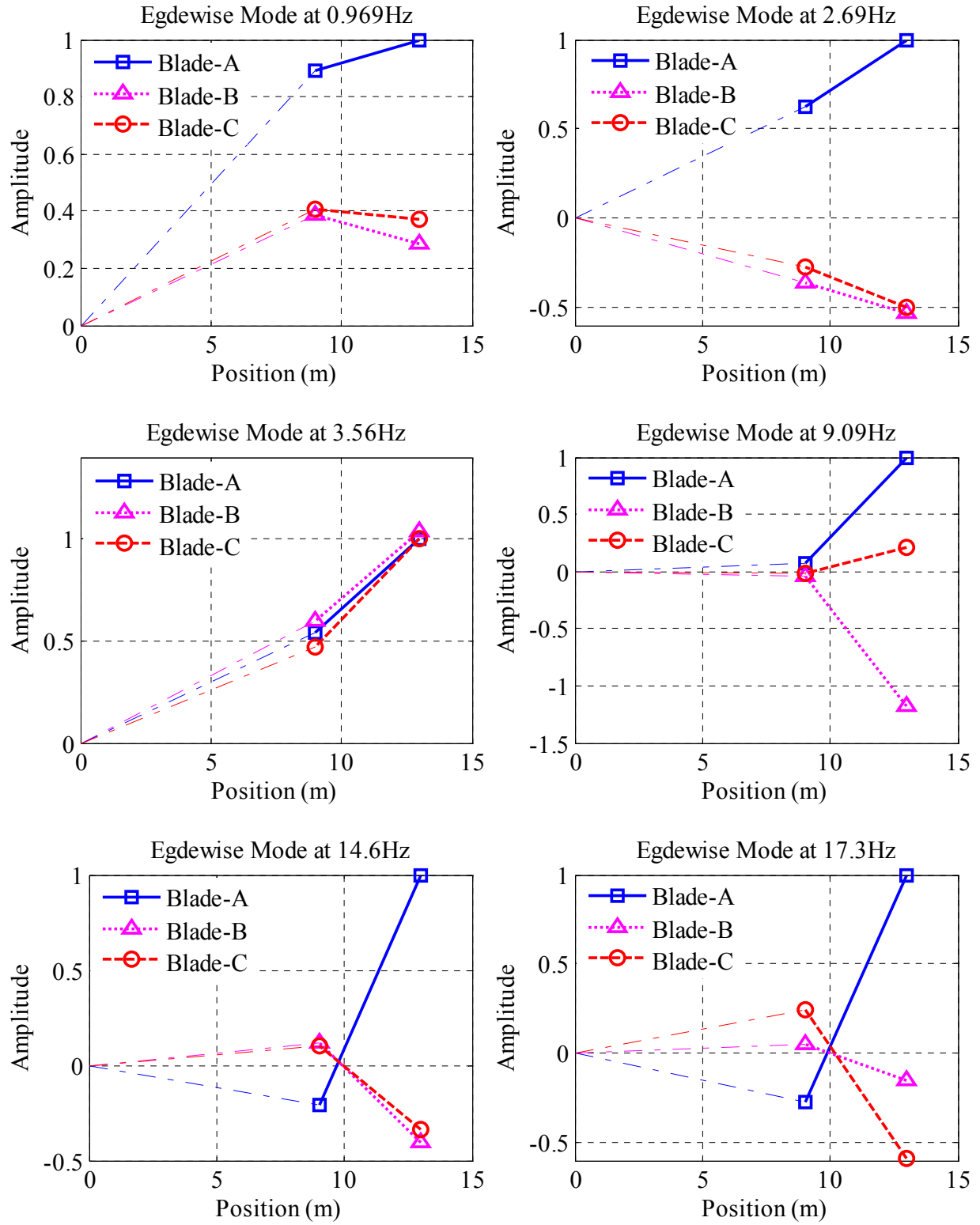


Figure 62 Mode shapes of the parked turbine in the edgewise direction

7.4 *Output-only Modal Analysis of Operational Turbine*

The wind turbine has to be modeled as an LTP system when operating. The periodic coefficients may be introduced by the asymmetric blades and the periodically changing boundary conditions. As a consequence, the conventional multi-blade coordinate transformation may no longer be valid on this turbine. In this section, the harmonic power spectrum will be used to process the periodic response of the wind turbine. As a frequency domain method, the harmonic power spectrum allows averaging and windowing to reduce the uncertainties in the identified modal parameters.

7.4.1 *Analysis of a Single Point*

The turbine rotated at an average speed of 0.5369Hz with a standard deviation of 0.0007Hz. The measured response at the tip of blade A (sensor 3) was exponentially modulated with $n = -4 \dots 4$ using Eq. (33). Then, the modulated signals were split into 123 sub-blocks with a block size of 60s (32.2 revolutions) and 85% overlap. A Hanning window was applied to reduce the leakage. Figure 63 shows the harmonic power spectrum (up to 25Hz) in the flapwise direction. The magenta line is the center spectrum $S_{0,0}$ -the spectrum one would obtain using the conventional output-only modal analysis. Many harmonics appears at the rotating frequency and its multiples up to 10Hz. Some of these harmonics overlap with the peaks that could be the system modes, e.g., the peaks at 2.1476Hz and 2.6845Hz, making these modes almost impossible to be extracted. One can also observe a cluster of harmonics around 12.52Hz, which is found to be the blade vibration introduced by the gearbox ($12.52\text{Hz}/23.3333 \approx 0.5365\text{Hz}$). This vibration component at 12.52Hz was measured by accelerometers attached to the rotating blades so many sidebands appear around this frequency, each separated by a multiple of the rotating frequency.

Two strong modes arise at 5.469Hz and 6.711Hz; they could be the second bending modes in the flapwise direction according to the output-only modal analysis when the turbine was parked. The increased modal frequencies may be attributed to the centrifugal stiffening when the turbine is rotating. In addition, these two modes do not have obvious sideband harmonics, indicating that they could be the time invariant modes or the sideband harmonics are too weak to be observed. Thus, a conclusion can be made that there is limited periodic behavior in the flapwise direction in the selected data. This is reasonable because strong periodic behavior is more likely to happen in the edgewise direction [63].

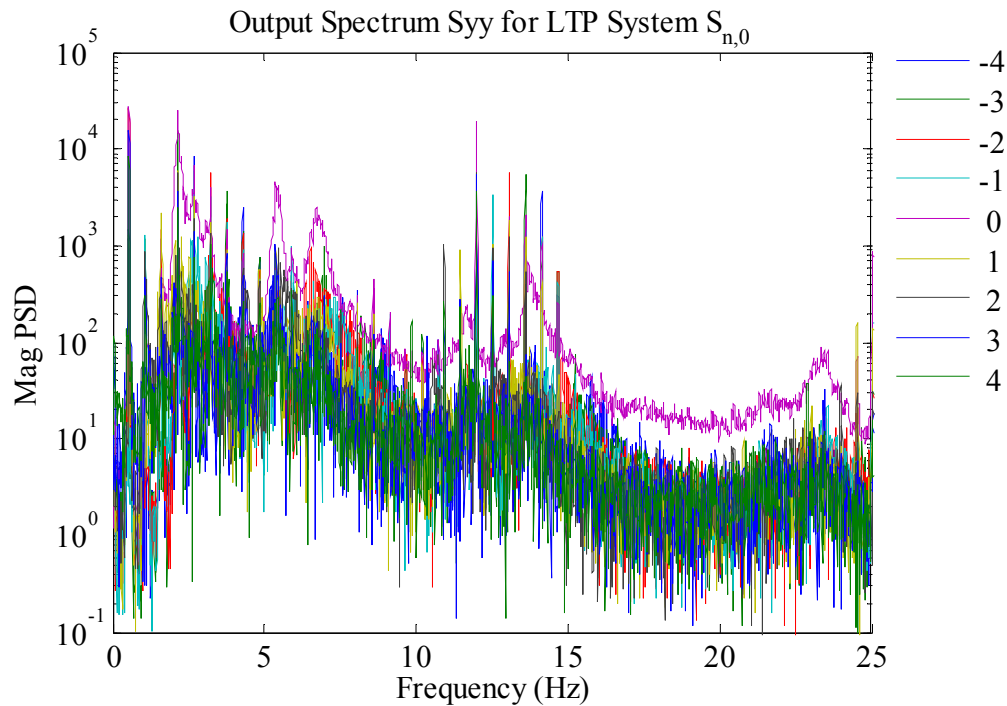


Figure 63 Harmonic power spectrum in the flapwise direction at the tip of blade A

Figure 64 shows the harmonic power spectrum at the tip of the same blade but in the edgewise direction (in-plane). The same cluster of harmonics around 12.52Hz can be observed. One can also see a periodic pattern around 3.59Hz with the strong sideband harmonics, each separated with the rotating frequency. A similar periodic pattern appears around 8.219Hz, but

the response at this frequency is much weaker and may be severely contaminated by the noise. Therefore, this work primarily focuses on the periodic modes in the edgewise direction near 3.59Hz.

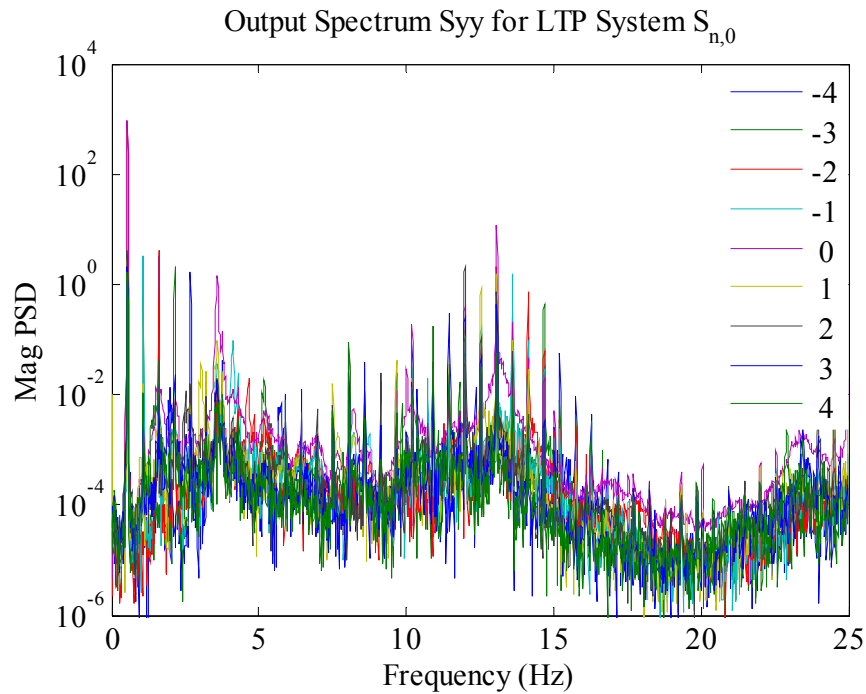


Figure 64 Harmonic power spectrum in the edgewise direction at the tip of blade A

Figure 65 shows the zoom-in plot of the harmonic power spectrum in the edgewise direction. The dashed vertical lines indicate the harmonics of the rotating frequency so they can be more easily distinguished from the modes. A few frequency components appear around 3.59Hz. The complex modal indicator function [88], as shown in Figure 66, was formed to determine whether any of the peaks corresponded to modes with very close natural frequencies. The edgewise sensors at all three blade tips were used as the references. The 1st singular value curve (blue) has two peaks around 3.59Hz, suggesting that there are at least two modes around this frequency. This curve also has similar patterns around 3Hz, 4.1Hz and 4.6Hz; these frequency components could be the harmonics of the modes around 3.59Hz. In any event, the

mode vectors at these peaks were identified using peak-picking. One should note that the identified mode vector at each peak is no longer the physical deformation at different measurement locations, but the Fourier coefficients that describe the time periodic mode at this peak.

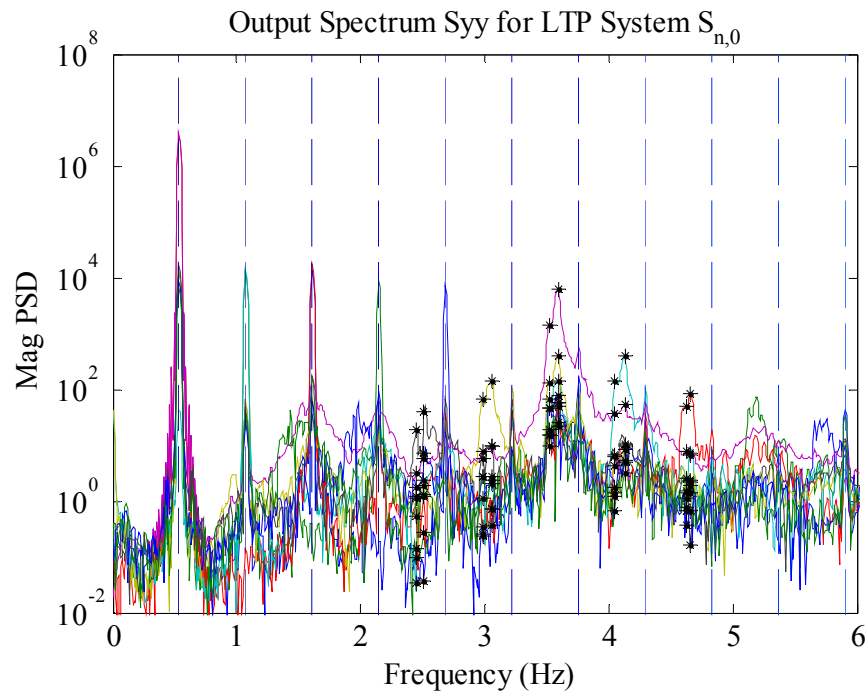


Figure 65 Time periodic mode at 3.59Hz in the edgewise direction

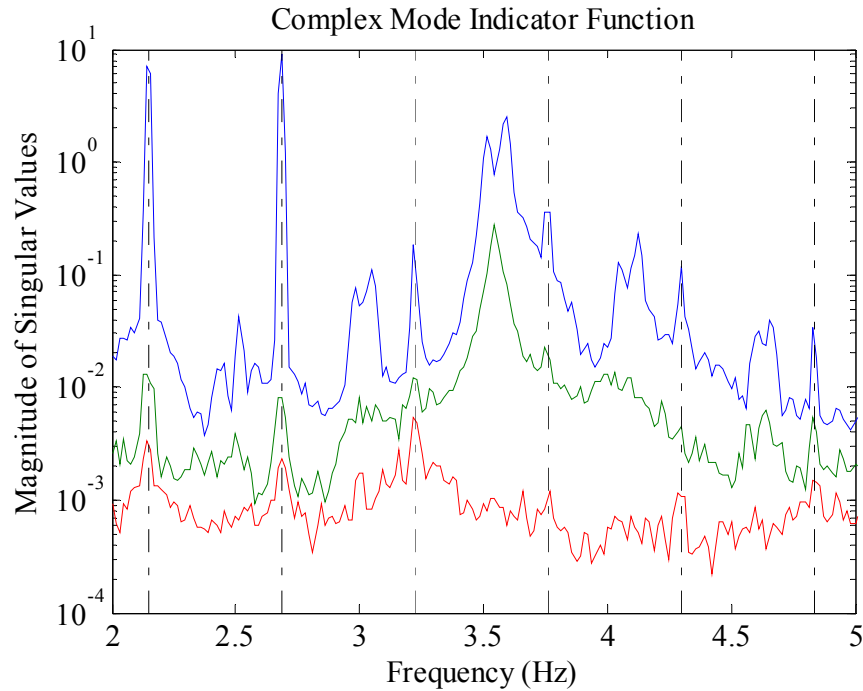


Figure 66 Complex mode factor of the mode at 3.59Hz

The identified Fourier coefficient vectors are listed in Table 12. These vectors were shifted such that each element was in the correct position, as explained in Section 2.7. Then, these coefficient vectors were normalized to the maximum value in each vector in order to compare with each other. Only the Fourier coefficient vectors identified from the harmonics at $n = -2 \dots 2$ are listed here ($n = -4 \dots 4$ was used to modulate the periodic signal). The amplitudes at higher order harmonics are so small that they could be considered as noise. According to Figure 66, the frequency components around 2.5Hz, 3Hz, 4.1Hz and 4.6Hz are most likely the harmonics of the first edgewise bending modes around 3.59Hz. Therefore, the mode vectors identified at 2.4496Hz, 2.9865Hz, 4.0519Hz and 4.6055Hz describe the same shape as the mode vector at 3.5234Hz, though they are scaled with unknown complex scalars (see Eq. (46)), and similarly for the harmonics of the mode at 3.5905Hz. Singular value decomposition was used to find the best estimates of the mode vectors at 3.5232Hz and 3.5905Hz from these peaks. The

results are shown in Figure 67, where the x-axis indicates the harmonic order. It can be observed that the amplitudes of the sideband harmonics are at least an order of magnitude smaller than the 0th (center) harmonic. Details about these two modes will be discussed later.

Table 12 Measured Fourier coefficients at the tip of the blade

Natural frequency	2.4496 Hz	2.5167 Hz	2.9865 Hz	3.0536 Hz	3.5234 Hz
-2	-0.1379 - 0.0964i	0.1239 + 0.0072i	-0.0095 - 0.0136i	0.0127 - 0.0061i	-0.0112 - 0.0078i
-1	0.0539 - 0.0243i	0.0409 + 0.0032i	0.1110 - 0.0081i	0.0601 - 0.0276i	0.0487 - 0.0036i
0	1	1	1	1	1
1	-0.0896 + 0.0050i	-0.1232 - 0.1112i	-0.0806 + 0.0252i	-0.0627 - 0.0296i	-0.0959 + 0.0059i
2	0.0569 + 0.0323i	0.0338 - 0.0245i	0.0240 - 0.0342i	0.0076 - 0.0149i	0.0273 - 0.0168i
Natural frequency	3.5905 Hz	4.0519 Hz	4.1274 Hz	4.6055 Hz	4.6559 Hz
-2	0.0082 + 0.0005i	-0.0107 - 0.0071i	0.0208 - 0.0001i	-0.0177 + 0.0016i	0.0215 + 0.0091i
-1	0.0218 - 0.0100i	0.0473 + 0.0069i	0.0248 - 0.0049i	0.0492 + 0.0084i	0.0287 + 0.0037i
0	1	1	1	1	1
1	-0.0515 - 0.0411i	-0.2618 + 0.0313i	-0.1019 - 0.0814i	-0.0725 - 0.0107i	-0.0344 - 0.0802i
2	0.0108 - 0.0079i	0.0261 - 0.0178i	0.0118 - 0.0175i	0.1368 - 0.0600i	0.0717 - 0.0357i

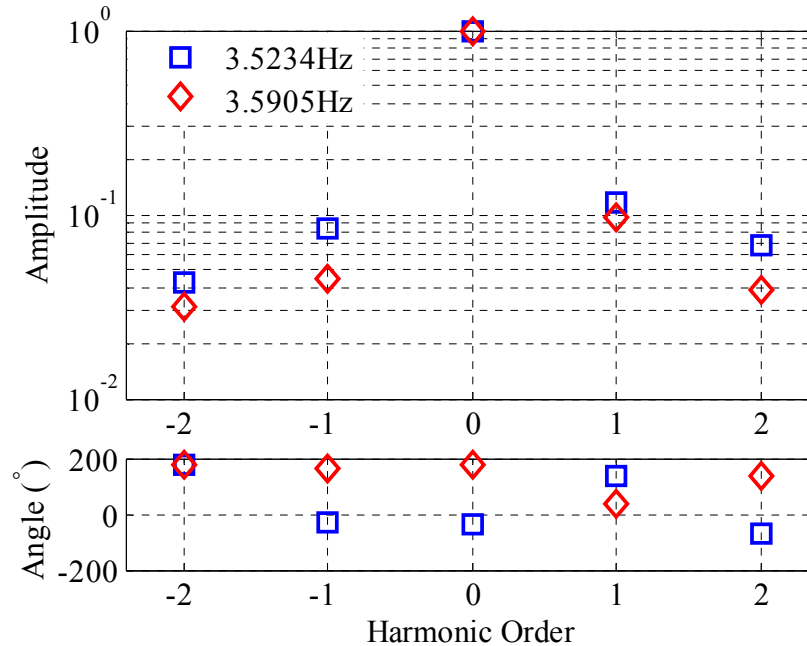


Figure 67 Identified Fourier coefficients at different frequencies.

7.4.2 Discussion

Equation (70), taken from [14], gives the blade response of an isotropic turbine measured in the rotating frame. Here $A_{i,r}$ is the modal amplitude, and $\alpha_{i,k}$ is the modal phase, ζ_r is the modal damping. The integers i, r are the blade number and mode number respectively.

$$\begin{aligned}
 x_{i,r} = & A_{i,r}^0 e^{\zeta_r t} \cos(\omega_r t + \alpha_{i,r}^0) \\
 & + \frac{1}{2} A_{i,r}^{\text{FW}} e^{\zeta_r t} \cos((\omega_r - \omega_A)t + \frac{2}{3}\pi(i-1) + \alpha_{i,r}^{\text{FW}}) \\
 & + \frac{1}{2} A_{i,r}^{\text{BW}} e^{\zeta_r t} \cos((\omega_r + \omega_A)t - \frac{2}{3}\pi(i-1) + \alpha_{i,r}^{\text{BW}})
 \end{aligned} \tag{70}$$

The blade response has three components for each mode; a symmetric component at ω_r , a forward whirling component at $\omega_r - \omega_A$, and a backward whirling component at $\omega_r + \omega_A$, where ω_A is the turbine rotating frequency. The whirling components are separated by $2\omega_A$, and they appear because the blade responses were measured by the sensors attached to the blade-fixed rotating frame. The phases of the backward or forward whirling component of any two blades differ by 120° , and the phases of the three components of the same blade differ by 120° plus some constant phase angle $\alpha_{i,k}$ of each component. The multi-blade coordinate transformation converts the blade responses in Eq. (70) to an inertial frame using some special variables that combine the deflections of all three blades with the instantaneous rotor azimuth. The system then becomes linear time invariant and can be identified using conventional modal identification routines.

Unfortunately, if the turbine is anisotropic, the blade response may contain more than three harmonic components [26]. This is similar to what was observed in Figure 65; the frequency components in the edgewise direction at 3.5234Hz and 3.5905Hz are distinct modes

and have -2 and 2 harmonics. Thus the multi-blade coordinate transformation may no longer be valid because the transformed equations of motion will have the periodic terms. In addition, one should note that the spectrum in Figure 65 is different from that obtained from simulated wind turbine models [14, 26, 64], where the symmetric and whirling modes appear in the measured response simultaneously. A in-depth discussion of the symmetric and whirling modes can be found in [89]. The two frequencies at 3.5234Hz and 3.5905Hz could be the first bending modes of the blades in the edgewise direction. The fact that they are 0.0671Hz apart might be attributed to the slightly asymmetrical blades, and this frequency difference agrees with that from a ground test (edgewise bending modes at 3.28Hz and 3.34Hz on the ground). Therefore, these two frequencies are most likely the symmetric modes of the blades in the edgewise direction, and no obvious backward or whirling mode can be observed in the output spectrum. Note that for an anisotropic turbine, the symmetric modes at 3.5234Hz and 3.5905Hz may not be pure [26], i.e., there might be harmonics of the whirling modes in the mode vector of symmetric mode. However, the phase difference between the -1st harmonic and 1st harmonic in Figure 67 is around 150° for both modes at 3.5234Hz and 3.5905Hz. Furthermore, the 0th harmonic and -1st harmonic have the same phase, which contradicts with the 120° phase difference as discussed previously. Therefore, the -1st and 1st harmonics are dominated by the symmetric modes at 3.5234Hz and 3.5905Hz.

The periodic shapes at 3.5234Hz and 3.5905Hz were reconstructed using Eq. (33) with the identified Fourier coefficients in Figure 67, and the results are shown in Figure 68, where the x -axis is the azimuth. The frequency components at 3.5234Hz and 3.5905Hz have their phases about 180° apart, indicating that the blade vibrates in opposite directions at these two frequencies. The harmonic power spectrum directly identifies a periodically varying state

variable that describes the motion of the blade in the rotating frame. The state variable can be further used to identify the system matrix of this turbine for model verification purposes using the stochastic subspace identification or other realization techniques. However, this part is beyond the scope of this dissertation and therefore will not be discussed.

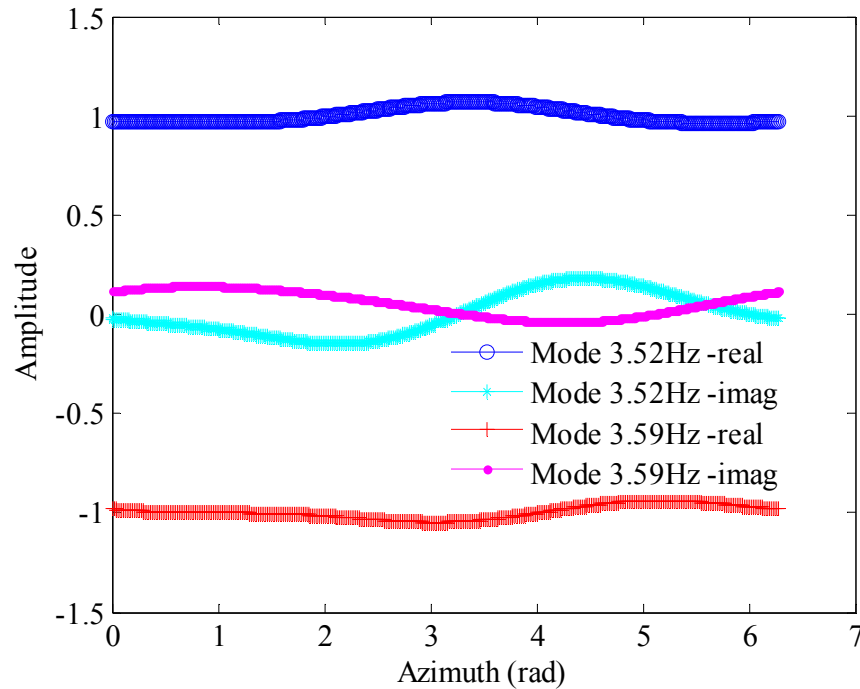


Figure 68 Time periodic mode amplitude in edgewise direction at sensor 3 on blade A

7.4.3 Analysis of Multiple Blades

The same analysis was repeated at all the edgewise sensors on the blades. The cross harmonic power spectra were computed between the modulated periodic signals of all the sensors and the original time history from sensor 3 on blade A. Figure 69 shows the averaged cross harmonic power spectra in the edgewise direction. As in Figure 65, the response at each sensor is consisted of two symmetric components at 3.523Hz and 3.59Hz and their harmonics around 3Hz and 4.1Hz, etc.

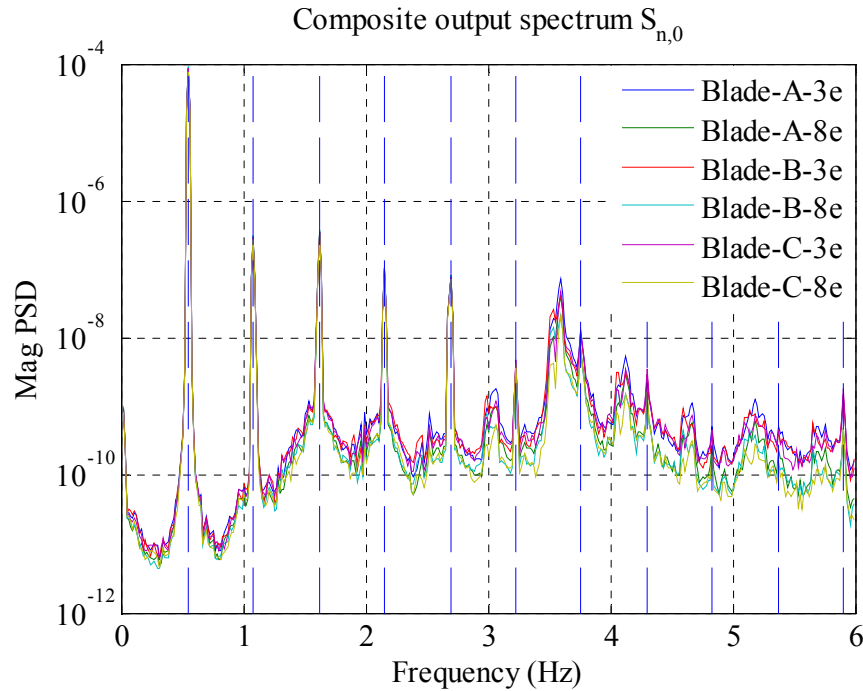


Figure 69 Average power spectra of different sensors. 'e' indicates edgewise direction

The mode vectors (or Fourier coefficient vectors) at these harmonics (-2...2) were identified using peak-picking. This resulted in a $6 \times 9 \times 10$ mode vector matrix, where the first dimension indicates the number of sensors, the second dimension indicates the number of modulated periodic signals ($n = -4 \dots 4$), and the third dimension is the number of identified modes. Then, the mode vectors of each mode of each blade were normalized using sensor 3 on blade A as a reference. For example, the mode vectors (6×9 matrix) of the fourth mode at 3.05 Hz were normalized using the [1, 5, 4] element in the $6 \times 9 \times 10$ mode vector matrix. The elements in the normalized Fourier coefficient vectors were shifted to the correct position, and singular value decomposition was used to extract the best estimates of the Fourier coefficient vectors at 3.523 Hz and 3.59 Hz respectively. The results are shown in Figure 70, where the x -axis is the harmonic order.

It can be seen that the amplitudes of the sideband harmonics are at least an order of magnitude smaller than that of the 0th harmonic at both frequencies. At the -1st harmonic of the mode at 3.523Hz, blade A and B have the similar amplitudes and phases. The amplitudes of blade C are much smaller, and the phase at sensor 8 on blade C is slightly off perhaps due to the noise. At the -1st harmonic of 3.59Hz, the three blades have distinct amplitudes but their phases appear to be similar. The phases at sensor 3 and sensor 8 on blade C differ about 360° (equals 0°), therefore the two sensors are actually in-phase. In addition, the phases of the -1st harmonic at 3.523Hz and at 3.59Hz differ about 180°. In theory, if the -1st harmonic were dominated by the forward whirling modes $\omega_r - \omega_A$, one would expect the phase difference between any two blades to be 120° [14]. Unfortunately, this does not appear to be the case for this anisotropic turbine. The 1st harmonics at both frequencies have larger amplitudes than those of the corresponding -1st harmonics, and the phase differences between different blades are slightly larger (not 120°). In an event, the phases (and perhaps amplitudes) at these harmonics of different blades indicate that the -1st and 1st harmonic are dominated by the harmonics of the symmetric modes rather than the harmonics of the whirling modes.

Figure 71 shows the 0th harmonics at 3.523Hz and 3.59Hz to help understanding the shapes of these two edgewise modes. The 0th harmonic is the shape one would obtain if a conventional output-only modal analysis were performed. The vibration amplitude at the hub (0m) is assumed to be zero in order to distinguish the blade motion. At 3.52Hz, blade B has the largest amplitude, and the phase of blade C is 180° from blades A and B, indicating that blade C moves in the opposite direction. At 3.59Hz, blade A has the largest amplitude. Blades A and B have a phase difference of about 360° so they are actually in-phase, and blade C still moves in the opposite direction. The phases of blade A and B at 3.523Hz are 180° from those at 3.59Hz.

Since the amplitudes of sideband harmonics are very small, the frequencies at 3.52Hz and 3.59Hz describe the same shape, and the only difference is the vibration direction of each blade.

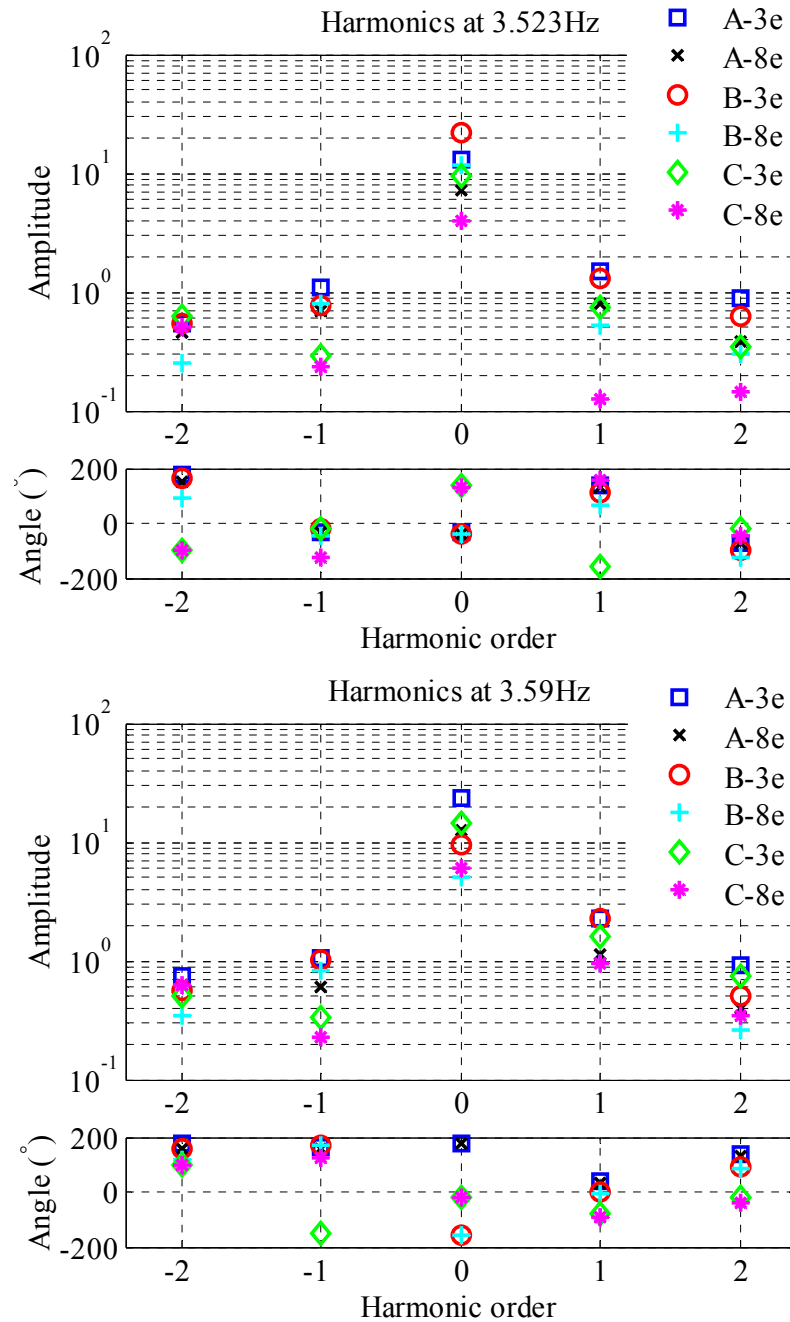


Figure 70 Identified Fourier coefficients on all the blades plotted against harmonic order

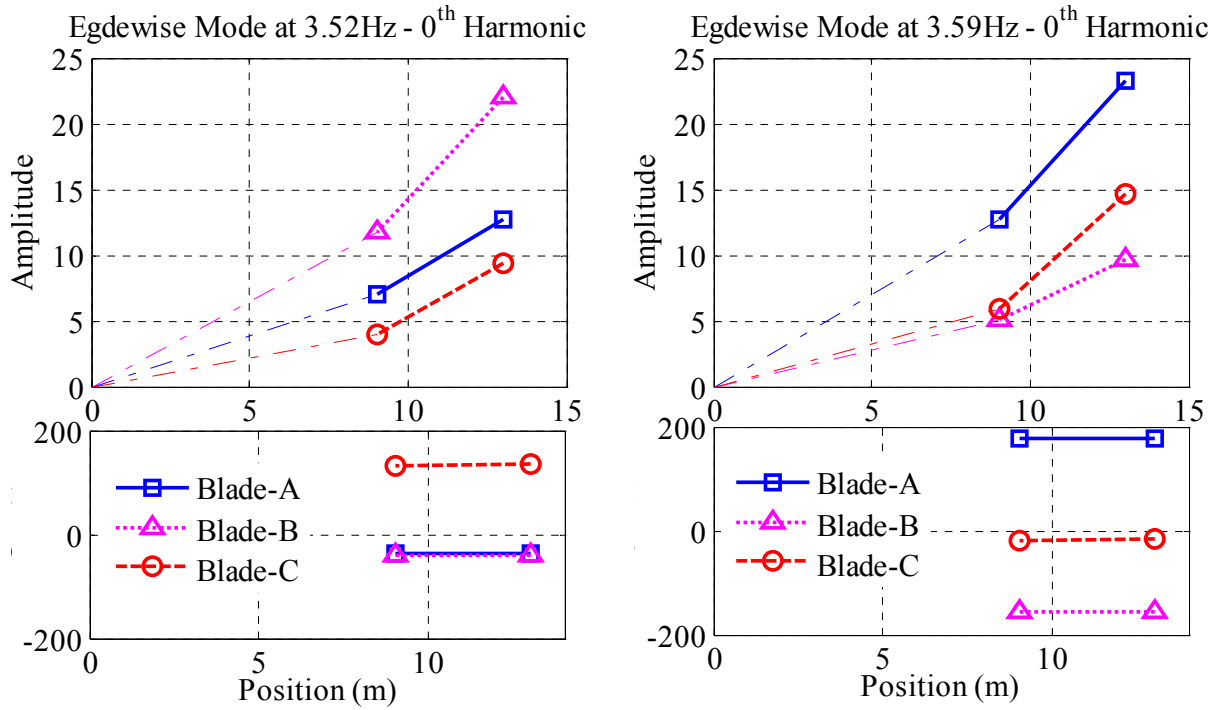


Figure 71 Identified forward whirling, symmetric and backward whirling modes at 3.52Hz and 3.59Hz.

7.5 Summary

In this chapter, the harmonic power spectrum was used to identify the periodic modes of an operating wind turbine instrumented with accelerometers. The turbine is anisotropic and has to be modeled as an LTP system, so the multi-blade coordinate transformation built on the assumption of isotropic rotors is no longer valid. Two edgewise (in-plane) bending modes were identified using the harmonic power spectrum. These modes were found to be the symmetric bending modes of the blades in the edgewise direction. The phases and amplitudes of the sideband harmonics of these two modes were investigated. It was found that the blade responses are different from those of the previously studied wind turbine models; no obvious backward or forward whirling mode could be observed in the acquired responses. The harmonics of the symmetric modes were identified, and they could be used to study the parametric resonance and

instability of this anisotropic turbine, i.e., an input at one frequency may cause the response at other frequencies, so that the actual vibration levels in the turbine can be much higher than expected based on an isotropic model. Validating the identified periodic modes would require a detailed output-only modal analysis of the same data using, perhaps, the modified multi-blade coordinate transformation [86]. However, this work at least proves that the harmonic power spectrum is a promising tool to analyze general LTP systems such as wind turbines.

8 Conclusion

A complete set of frequency domain algorithms were proposed for the modal identification of Linear Time Periodic (LTP) systems. These algorithms can be applied to experimental modal analysis of LTP systems under carefully controlled input, and also output-only modal analysis where the input cannot be directly measured but is assumed to be random white noise. The theory is completely analogous to modal identification theory of Linear Time Invariant (LTI) systems. Thus, the well-established identification routines for LTI systems can be used to extract modal parameters of LTP systems under virtually any type of input.

- The harmonic transfer function is analogous to the transfer function in the experimental modal analysis of LTI systems. Whereas a transfer function relates a single frequency output of an LTI system to the input at the same frequency, the harmonic transfer function relates the output of an LTP system at a collection of frequencies to the input at the same collection of frequencies, each separated by the fundamental frequency of the periodic system.
- The harmonic power spectrum has a similar modal summation form as the power spectrum in output-only modal analysis of LTI systems. As in LTI cases, the output-only modal analysis of LTP systems also assumes the input to be uniformly distributed random noise. The harmonic power spectrum contains both stable and unstable poles of an LTP system. Therefore, conventional curve-fitting routines for the frequency response function need to be modified to account for the unstable poles.

- The positive harmonic power spectrum, extended from the positive power spectrum of LTI systems, contains only the stable poles of an LTP system. The positive harmonic power spectrum has the appearance of an impulse response function, allowing conventional modal identification routines to extract modal parameters of the LTP system. This algorithm was demonstrated in [63].
- The lifting approach groups the responses at the same time instant in each period of a periodic response, so the sampling frequency of the lifted responses becomes the fundamental frequency. As a result, all sideband harmonics in the harmonic power spectrum are aliased to a single frequency according to the sampling theorem. Thus, the lifted spectra contain only one peak for each mode, and are far easier to interpret.

There are two notable differences between the modal identification theory for LTP system and the theory for LTI systems. First, an LTP system has an infinite number of harmonics for each mode. Each peak occurs near the imaginary part of the Floquet exponent plus some integer multiple of the fundamental frequency. All of these peaks have to be curve-fitted in order to obtain the best estimate of the mode vector. Second, the mode vector of an LTP system no longer describes the spatial deformation pattern at a certain frequency. Instead, the mode vector consists of the Fourier coefficients that describe the time periodic spatial deformation pattern. Once these differences have been addressed, conventional identification routines for LTI systems including peak-picking, curve-fitting, and stochastic subspace identification (not reported in this dissertation) can be used to extract modal parameters of LTP systems.

The proposed modal identification algorithms for LTP systems were employed to identify modal parameters of LTI structures measured with Continuous-Scan Laser Doppler Vibrometry

(CSLDV), where the laser continuously sweeps over a surface while recording the response along the laser path. Hence, the measurements from CSLDV appear to be periodic when the laser spot moves in a closed and periodic pattern. The harmonic transfer function was used to identify operational shapes of a cantilever beam under different boundary conditions from CSLDV measurements. The results were almost identical to those extracted from the same data using the polynomial approach and lifting approach. The noise in the reconstructed shape using CSLDV was only 0.6% of the maximum amplitude, similar to that of a point-by-point measurement, but the time saving using continuous-scan was remarkable. It took only 102.4s to obtain the operational shape consisted of 1708 points, while the point-by-point scan took 24mins to measure only 59 points.

Another application of the harmonic transfer function was to simultaneously measure the translational and rotational velocities of a small region by scanning a small circle around a point inside the region. With an appropriate circle size and scan frequency, the circular-scan was capable of providing a higher signal to noise ratio than that with a stationary laser spot. The deflection shape acquired using circular-scan was much cleaner, and the reconstructed slope from the rotational velocities agrees well with the trend of the deflection curve.

The harmonic power spectrum was combined with CSLDV to perform output-only modal analysis of LTI structure under random excitation. The algorithm was validated on a free-free beam in a laboratory setting, and was found to give results that were very similar to a tuned analytical model of the beam. CSLDV was then employed to measure a blade of a parked wind turbine from a 77m standoff distance to identify the mode shapes, and qualitatively reasonable results were obtained for seven modes of the turbine.

The lifting approach was employed to simplify the output-only modal analysis using the positive harmonic correlation function, which is similar to the impulse response of LTP systems. Simulated measurements from a free-free beam indicated that the harmonic power spectrum and lifting approach provided equivalent results, but the identification using the lifting approach was far simpler. The Polytec's new remote sensing vibrometer was used to measure the same turbine but with a different set of blades. A conventional output-only modal analysis test was performed with two LDVs, and those mode shapes were found to be comparable with the CSLDV results using the remote sensing vibrometer.

Finally, the harmonic power spectrum was used to analyze the dynamic behavior of an operating wind turbine instrumented with accelerometers. The turbine is anisotropic and has to be modeled as an LTP system, so the conventional multi-blade coordinate transformation built on the assumption of isotropic rotors is no longer valid. One periodic mode in the edgewise direction (in-plane) of the blades was identified, and the results are related to those one would obtain using a Lyapunov-Floquet transformation. The analysis of the dynamics of an anisotropic wind turbine indicates that the proposed modal identification algorithms provide effective tools to experimentally extract modal parameters of general LTP systems.

9 Future work

Many nonlinear systems tend to have periodic responses, for example, human gait modeled with inverted pendulum models [17]. When walking with appropriate conditions (e.g., at a steady pace), the motion of the models appears to be in a periodic orbit. Other examples include rotor systems with a periodic excitation due to the bearing clearance [90]. In practice, it is typical to study a nonlinear system using a single tone excitation so the system can be linearized about a stable periodic orbit. Sracic proposed an experimental technique to indentify the LTP model of a cantilever beam with a nonlinear stiffness at the tip, as shown in Figure 72, using the perturbed response from the periodic orbit of the beam [91].

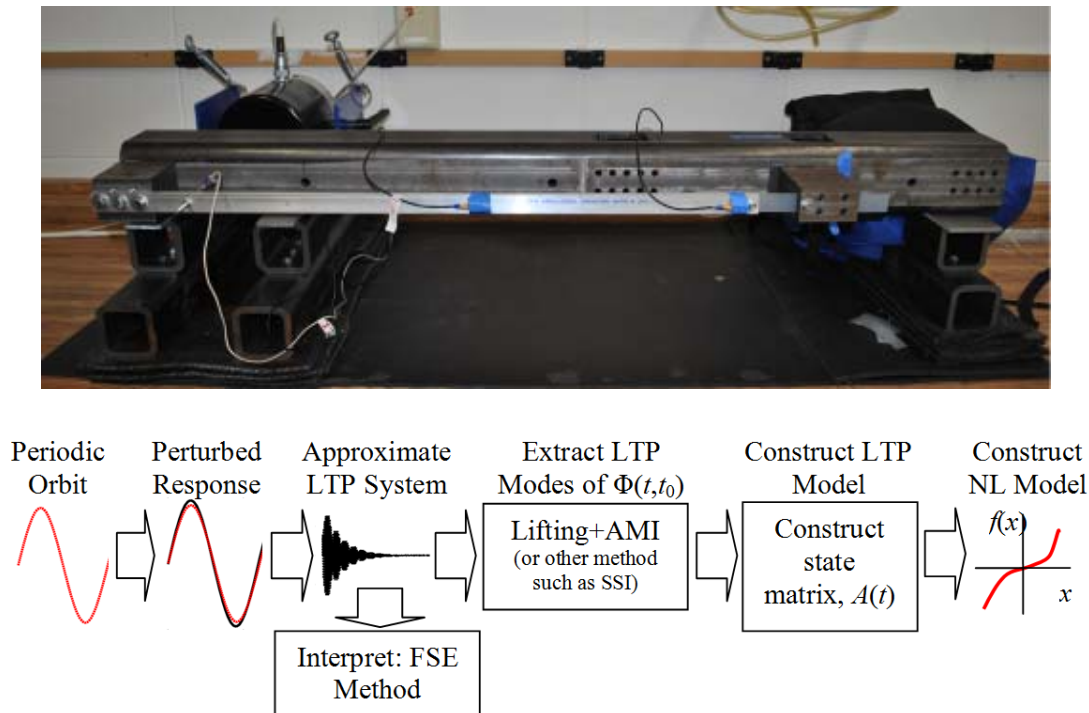


Figure 72 Study a cantilever beam with nonlinear stiffness. (Pictures from [Mike Sracic, PhD Thesis])

The perturbation causes the response to deviate from the periodic orbit. If the perturbation is sufficiently small, the response will eventually return to the periodic orbit because the orbit is stable. The periodic orbit is then subtracted from the perturbed response to obtain a transient response of the periodic model. Then, experimental modal identification techniques for LTP systems, e.g., the lifting approach and Fourier series expansion, were used to extract the time periodic modes. Once the time periodic modes have been identified, the state transition matrix and the system matrix of the LTP system can be reconstructed [92]. Then the nonlinear function describing the nonlinear system around the periodic orbit can be obtained by an integration of the system matrix.

One of the major challenges of these experimental techniques is to apply a perturbation that is small enough but still measurable to keep the nonlinear system around the stable periodic orbit. Meanwhile, the perturbation needs to sufficiently excite all periodic modes of interests. A perturbation from the periodic orbit is necessary for both lifting approach and Fourier series expansion to extract the periodic modes because these methods only apply to the free response of an LTP system. In addition, without an input-output relationship described by the transfer function, the results could be noisy since averaging multiple measurements is not applicable. The proposed frequency domain identification algorithms for LTP provide promising tools to analyze this nonlinear structure. These algorithms allow the use of the perturbation forces to form the harmonic transfer function, and random perturbation signals can be applied as well. In addition, one may take advantage of the high precision measurements provided by CSLDV. This part of the work will be explored by another PhD student in the lab.

References

- [1] C.-T. Chen, *Linear system theory and design*, 3rd edition ed.: Oxford University Press, Inc, 1999.
- [2] G. Floquet, "Sur Les Equations Lineaires a Coefficients Periodiques," *Ann. Sci. Ecole Norm. Sup.*, vol. 12, pp. 47-88, 1883.
- [3] J. Guckenheimer and P. Holmes, *Nonlinear Oscillations, Dynamical Systems, and Bifurcations of Vector Fields* vol. 42. New York: Springer-Verlag New York Inc., 1983.
- [4] P. Hartman, *Ordinary Differential Equations*. New York: John Wiley & Sons, Inc., 1964.
- [5] S. R. Ibrahim and E. C. Mikulcik, "Method for the direct identification of vibration parameters from the free responses," *Shock and Vibration Bulletin*, p. 197, 1977.
- [6] B. Peeters and G. De Roeck, "Reference Based Stochastic Subspace Identification for Output-Only Modal Analysis," *Mechanical Systems and Signal Processing*, vol. 13, pp. 855-878, 1999.
- [7] J. N. Juang and R. S. Pappa, "An eigensystem realization algorithm for modal parameter identification and model reduction," *Journal of Guidance, Control, and Dynamics*, vol. 8, pp. 620-627, 1985.
- [8] R. J. Allemang and D. L. Brown, "A Unified Matrix Polynomial Approach to Modal Identification," *Journal of Sound and Vibration*, vol. 211, pp. 301-322, 1998.
- [9] M. S. Allen, "Global and Multi-Input-Multi-Output (MIMO) Extensions of the Algorithm of Mode Isolation (AMI)," Doctorate, George W. Woodruff School of Mechanical Engineering, Georgia Institute of Technology, Atlanta, Georgia, 2005.
- [10] D. A. Peters, "Fast Floquet theory and trim for multi-bladed rotorcraft," *Journal of the American Helicopter Society*, vol. 39, pp. 82-89, 1994.
- [11] G. Bir and K. Stol, "Operating Modes of a Teetered-Rotor Wind Turbine," presented at the 17th International Modal Analysis Conference (IMAC XVII), Kissimmee, Florida, 1999.
- [12] D. J. Malcom, "Modal Responses of 3-Bladed Wind Turbines," *Journal of Solar Energy Engineering-Transactions of the ASME*, vol. 124, pp. 372-377, 2002.
- [13] K. Stol, M. Balas, and G. Bir, "Floquet modal analysis of a teetered-rotor wind turbine," *Journal of Solar Energy Engineering-Transactions of the ASME*, vol. 124, pp. 364-371, Nov 2002.
- [14] M. H. Hansen, "Improved modal dynamics of wind turbines to avoid stall-induced vibrations," *Wind Energy*, vol. 6, pp. 179-195, 2003.
- [15] J. B. Dingwell, J. P. Cusumano, P. R. Cavanagh, and D. Sternad, "Local dynamic stability versus kinematic variability of continuous overground and treadmill walking," *Journal of Biomechanical Engineering*, vol. 123, pp. 27-32, 2001.
- [16] J. B. Dingwell and K. Hyun Gu, "Differences between local and orbital dynamic stability during human walking," *Transactions of the ASME. Journal of Biomechanical Engineering*, vol. 129, pp. 586-93, 2007.
- [17] T. McGeer, "Passive Dynamic Walking [Two-Legged Machines]," *The International Journal of Robotics Research*, vol. 9, pp. 62-82, 1990.

- [18] M. W. Sracic and M. S. Allen, "Method for Identifying Models of Nonlinear Systems Using Linear Time Periodic Approximations," *Mechanical Systems and Signal Processing*, vol. 25, pp. 2705-2721, 2011.
- [19] F. Felici, J. W. van Wingerden, and M. Verhaegen, "Subspace identification of MIMO LPV systems using a periodic scheduling sequence," *Automatica*, vol. 43, pp. 1684-97, 2007.
- [20] C.-W. Lee, D.-J. Han, J.-H. Suh, and S.-W. Hong, "Modal analysis of periodically time-varying linear rotor systems," *Journal of Sound and Vibration*, vol. 303, pp. 553-574, 2007.
- [21] K. Liu, "Identification of linear time-varying systems," *Journal of Sound and Vibration*, vol. 206, pp. 487-505, 1997.
- [22] V. Verdult, M. Lovera, and M. Verhaegen, "Identification of linear parameter-varying state-space models with application to helicopter rotor dynamics," *International Journal of Control*, vol. 77, pp. 1149 - 1159, 2004.
- [23] J. J. Hench, "A technique for the identification of linear periodic state-space models," *International Journal of Control*, vol. 62, pp. 289-301, 1995.
- [24] L. H. Lee and K. Poolla, "Identification of linear parameter-varying systems via LFTs.," presented at the 35th IEEE Conference on Decision and Control, Kobe, Japan 1996.
- [25] S. C. Sinha, R. Pandiyan, and J. S. Bibb, "Liapunov-Floquet transformation: computation and applications to periodic systems," *ASME Journal of Vibration and Acoustics*, vol. 118, pp. 209-217, 1996.
- [26] P. F. Skjoldan and M. H. Hansen, "On the similarity of the Coleman and Lyapunov-Floquet transformations for modal analysis of bladed rotor structures," *Journal of Sound and Vibration*, vol. 327, pp. 424-439, 2009.
- [27] M. S. Allen, "Frequency-Domain Identification of Linear Time-Periodic Systems Using LTI Techniques," *Journal of Computational and Nonlinear Dynamics*, vol. 4, pp. 041004.1-6, 2009.
- [28] N. M. Wereley and S. R. Hall, "Linear time periodic systems: transfer functions, poles, transmission zeroes and directional properties," presented at the Proceedings of the 1991 American Control Conference, Boston, MA, USA, 1991.
- [29] N. M. Wereley and S. R. Hall, "Frequency Response of Linear Time Periodic Systems," presented at the Proceedings of the 29th Conference on Decision and Control, Honolulu, Hawaii, USA, 1990.
- [30] A. Siddiqui, "Identification of the Harmonic Transfer Functions of a Helicopter Rotor," M.S., Department of Aeronautics and Astronautics, Massachusetts Institute of Technology, 1999.
- [31] S. Hwang, "Frequency Domain System Identification of Helicopter Rotor Dynamics Incorporating Models with Time Periodic Coefficients," Doctor of Philosophy, Department of Aerospace Engineering, University of Maryland - College Park, 1997.
- [32] J. R. Bell and S. J. Rothberg, "Laser Vibrometers and Contacting Transducers, Target Rotation and Six Degree-Of-Freedom Vibration: What Do We Really Measure?," *Journal of Sound and Vibration*, vol. 237, pp. 245-261, 10/19 2000.
- [33] M. A. Rumsey, J. Hurtado, B. D. Hansche, T. W. Simmermacher, T. G. Came, and E. Gross, "In-Field Use of Laser Doppler Vibrometer on a Wind Turbine Blade," *AIAA Journal*, vol. 98, pp. 212-221, January 1998.

- [34] S. Vanlanduit, F. Prezniak, R. Longo, C. Vuye, and P. Guillaume, "Fluid flow measurements using a scanning laser Doppler vibrometer " presented at the 9th International conference on vibration measurements by laser and non-contact techniques and short course, Ancona, Italy, 2010.
- [35] M. S. Allen, H. Sumali, and P. C. Penegor, "DMCMN: Experimental/analytical evaluation of the effect of tip mass on atomic force microscope cantilever calibration," *Journal of Dynamic Systems, Measurement and Control*, vol. 131, p. 064501 (10 pp.), 2009.
- [36] S. J. Rothberg, "Laser vibrometry. Pseudo-vibrations," *Journal of Sound and Vibration*, vol. 135, pp. 516-522, 1989.
- [37] N. Shvartsman and I. Freund, "Speckle spots ride phase saddles sidesaddle," *Optics Communications*, vol. 117, pp. 228-34, 1995.
- [38] S. J. Rothberg and B. J. Halkon, "Laser vibrometry meets laser speckle," Ancona, Italy, 2004.
- [39] P. Martin and S. Rothberg, "Laser Vibrometry and the secret life of speckle patterns," in *Eighth Int. Conf. on Vibration Measurements by Laser Techniques: Advances and Applications*, 2008.
- [40] P. Martin, "Uncertainty due to speckle noise in laser vibrometry," Doctor of Philosophy, Wolfson School of Mechanical & Manufacturing Engineering, Loughborough University.
- [41] B. J. Halkon and S. J. Rothberg, "Vibration measurements using continuous scanning laser Doppler vibrometry: theoretical velocity sensitivity analysis with applications," *Measurement Science and Technology* vol. 14, 2003.
- [42] A. Gasparoni, M. S. Allen, S. Yang, M. W. Sracic, P. Castellini, and E. P. Tomasini, "Experimental Modal Analysis on a Rotating Fan Using Tracking-CSLDV," presented at the 9th International Conference on Vibration Measurements by Laser and Noncontact Techniques, Ancona, Italy, 2010.
- [43] P. Sriram, S. Hanagud, and J. I. Craig, "Mode shape measurement using a scanning laser doppler vibrometer," *International Journal of Analytical and Experimental Modal Analysis*, vol. 7, pp. 169-178, 1992.
- [44] P. Sriram, J. I. Craig, and S. Hanagud, "Scanning laser Doppler vibrometer for modal testing," *International Journal of Analytical and Experimental Modal Analysis*, vol. 5, pp. 155-167, 1990.
- [45] A. B. Stanbridge, M. Martarelli, and D. J. Ewins, "Measuring area vibration mode shapes with a continuous-scan LDV," *Measurement*, vol. 35, pp. 181-9, 2004.
- [46] A. B. Stanbridge and D. J. Ewins, "Modal testing using a scanning laser Doppler vibrometer," *Mechanical Systems and Signal Processing*, vol. 13, pp. 255-70, 1999.
- [47] A. B. Stanbridge, A. Z. Khan, and D. J. Ewins, "Modal testing using impact excitation and a scanning LDV," *Shock and Vibration*, vol. 7, pp. 91-100, 2000.
- [48] D. D. Maio, G. Carloni, and D. J. Ewins, "Simulation and validation of ODS measurements made using a Continuous SLDV method on a beam excited by a pseudo random signal," presented at the 28th International Modal Analysis Conference (IMAC XXVIII), Jacksonville, Florida, 2010.
- [49] S. Vanlanduit, P. Guillaume, and J. Schoukens, "Broadband vibration measurements using a continuously scanning laser vibrometer," *Measurement Science & Technology*, vol. 13, pp. 1574-82, 2002.

- [50] S. Vanlanduit and P. Guillaume, "An automatic scanning algorithm for high spatial resolution laser vibrometer measurements," *Mechanical Systems and Signal Processing*, vol. 18, pp. 79-88, 2004.
- [51] D. J. Ewins, *Modal Testing: Theory, Practice and Application*. Baldock, England: Research Studies Press, 2000.
- [52] A. B. Stanbridge and D. J. Ewins, "Measurement of translational and angular vibration using a scanning laser Doppler Vibrometer," *Vibration Measurement*, vol. 2358, pp. 37-47, 1994.
- [53] M. S. Allen and M. W. Sracic, "A New Method for Processing Impact Excited Continuous-Scan Laser Doppler Vibrometer Measurements," *Mechanical Systems and Signal Processing*, vol. 24, pp. 721-735, 2010.
- [54] S. Yang, M. W. Sracic, and M. S. Allen, "Two algorithms for mass normalizing mode shapes from impact excited continuous-scan laser Doppler vibrometry," *Journal of Vibration and Acoustics*, vol. 134, p. 021004, 2012.
- [55] M. W. Sracic, "A New Experimental Modal Analysis Method Using Continuous Scan Laser Doppler Vibrometry and Impact Excitation," Master of Science in Engineering Mechanics, Department of Engineering Physics, University of Wisconsin-Madison, Madison, 2008.
- [56] S. Yang and M. S. Allen, "Transfer Functions to Measure Translational and Rotational Velocities with Continuous-Scan Laser Doppler Vibrometry," presented at the IMAC XXXI, Garden Grove, CA, USA, 2013.
- [57] S. Yang and M. S. Allen, "Output-Only Modal Analysis Using Continuous-Scan Laser Doppler Vibrometry and Application to a 20kW Wind Turbine," *Mechanical Systems and Signal Processing*, vol. 31, August 2012 2011.
- [58] S. Yang and M. S. Allen, "A Lifting Algorithm for Output-only Continuous Scan Laser Doppler Vibrometry," presented at the AIAA, Hawaii, 2012.
- [59] S. Yang, D. Tcherniak, and M. S. Allen, "Modal Analysis of Rotating Wind Turbine using Multi-blade Coordinate Transformation and Harmonic power spectrum," presented at the IMAC XXXII, Orlando, Florida USA, 2014.
- [60] C. Chen, *Linear Systems Theory and Design*, 3 ed. New York: Oxford University Press, Inc., 1999.
- [61] N. M. Wereley, "Analysis and Control of Linear Periodically Time Varying Systems," PhD, Department of Aeronautics and Astronautics, Massachusetts Institute of Technology, Cambridge, 1991.
- [62] B. Cauberghe, "Applied Frequency-Domain System Identification in the Field of Experimental and Operational Modal Analysis," PhD, Faculteit Tegepaste Wetenschappen, Vakgroep Werktuigkunde, Vrije Universiteit Brussel, Brussels, Belgium, 2004.
- [63] M. S. Allen, S. Chauhan, and M. H. Hansen, "Advanced Operational Modal Analysis Methods for Linear Time Periodic System Identification," presented at the 29th International Modal Analysis Conference (IMAC XXIX), Jacksonville, Florida, 2011.
- [64] M. S. Allen, M. W. Sracic, S. Chauhan, and M. H. Hansen, "Output-Only Modal Analysis of Linear Time Periodic Systems with Application to Wind Turbine Simulation Data," *Mechanical Systems and Signal Processing*, vol. 25, pp. 1174-1191, 2011.

- [65] S. Yang, M. W. Sracic, and M. S. Allen, "Two algorithms for mass normalizing mode shapes from impact excited continuous-scan laser Doppler vibrometry," *Journal of Vibration and Acoustics*, vol. 134, April 2012.
- [66] N. M. Wereley, "Analysis and Control of Linear Periodically Time Varying Systems," PhD, Department of Aeronautics and Astronautics, Massachusetts Institute of Technology, Cambridge, 1991.
- [67] G. H. James, "Estimation of the Space Shuttle Rollout Forcing Function," presented at the 23rd International Modal Analysis Conference (IMAC XXIII), Orlando, Florida, 2005.
- [68] A. A. Uslu, K. Y. Sanliturk, and M. Gül, "Force estimation using vibration data," 28-31 AUGUST 2007 2007.
- [69] T. C. Chu, W. F. Ranson, and M. A. Sutton, "Applications of digital-image-correlation techniques to experimental mechanics," *Experimental Mechanics*, vol. 25, pp. 232-244, 1985.
- [70] B Pan, K Qian, H Xie, and A. Asundi, "Two-dimensional digital image correlation for in-plane displacement and strain measurement: a review " *Measurement Science and Technology*, vol. 20, 2009.
- [71] M. W. Sracic and M. S. Allen, "Experimental Investigation of the Effect of Speckle Noise on Continuous Scan Laser Doppler Vibrometer Measurements," presented at the 27th International Modal Analysis Conference (IMAC XXVII), Orlando, Florida, 2009.
- [72] R. J. Allemang, "The Modal Assurance Criterion –Twenty Years of Use and Abuse," *Sound and Vibration*, vol. 37, 2003.
- [73] M. Martarelli, "Exploiting the Laser Scanning Facility for Vibration Measurements," Ph.D. Ph.D., Imperial College of Science, Technology & Medicine, Imperial College, London, 2001.
- [74] M. Salman and K. G. Sabra, "Broadband measurement of translational and angular vibrations using a single continuously scanning laser Doppler vibrometer," *Journal of Acoustical Society of America*, vol. 132, pp. 1384-1391, 2012.
- [75] P. Martin and S. Rothberg, "Introducing speckle noise maps for laser vibrometry," *Optics and Lasers in Engineering*, vol. 47, pp. 431-42, 2009.
- [76] S. Rothberg, "Numerical simulation of speckle noise in laser vibrometry," *Applied Optics*, vol. 45, pp. 4523-33, 2006.
- [77] M. Martarelli and D. J. Ewins, "Continuous scanning laser Doppler vibrometry and speckle noise occurrence," *Mechanical Systems and Signal Processing*, vol. 20, pp. 2277-89, 2006.
- [78] M. S. Allen and J. H. Ginsberg, "A Global, Single-Input-Multi-Output (SIMO) Implementation of The Algorithm of Mode Isolation and Applications to Analytical and Experimental Data," *Mechanical Systems and Signal Processing*, vol. 20, pp. 1090–1111, 2006.
- [79] C. P. Ratcliffe, "A Frequency and Curvature Based Experimental Method for Locating Damage in Structures," *Journal of Vibration and Acoustics*, vol. 122, pp. 324-328, 2000.
- [80] C. W. Schwingshackl, A. B. Stanbridge, C. Zang, and D. J. Ewins, "Full-Field Vibration Measurement of Cylindrical Structures using a Continuous Scanning LDV Technique," presented at the 25th International Modal Analysis Conference (IMAC XXV), Orlando, Florida, 2007.

- [81] S. Chauhan, M. H. Hansen, and D. Tcherniak, "Application of Operational Modal Analysis and Blind Source Separation / Independent Component Analysis Techniques to Wind Turbines," presented at the 27th International Modal Analysis Conference (IMAC XXVII), Orlando, Florida, 2009.
- [82] J. Jonkman, "NREL 5 MW Baseline Wind Turbine," Technical report, NREL/NWTC, 1617 Cole Boulevard; Golden, CO 80401-3393, USA2005.
- [83] J. H. Ginsberg, *Mechanical and Structural Vibrations*, First ed. New York: John Wiley and Sons, 2001.
- [84] J. Wang, S. Qu, X. Hou, and J. Zhang, "Influences of Window Function on the Subsoil Damping Ratio," presented at the 2010 International Conference on ICEEE.
- [85] R.P.Coleman, "Theory of self-excited mechanical oscillations of hinged rotor blades," available from <ntrs.nasa.gov>, Langley Research Center1943.
- [86] G. Bir, "Multiblade Coordinate Transformation and Its Application to Wind Turbine Analysis," presented at the 2008 ASME Wind Energy Symposium, Reno, Nevada, 2008.
- [87] D. Tcherniak and G. C. Larsen, "Applications of OMA to an operating wind turbine: now including vibration data from the blades," presented at the 5th International Operational Modal Analysis Conference, Guimarães - Portugal, 2013.
- [88] R. J. Allemang and D. L. Brown, "A Complete Review of the Complex Mode Indicator Function (CMIF) with Applications," presented at the ISMA, Leuven, Belgium, 2006.
- [89] M. H. Hansen, "Aeroelastic stability analysis of wind turbines using an eigenvalue approach," *Wind Energy*, vol. 7, pp. 133-143, 2004.
- [90] G. T. Flowers, D. B. Margithu, and G. Szasz, "The Application of Floquet Methods in the Analyses of Rotordynamic Systems," *Journal of Sound and Vibration*, vol. 218, pp. 249-259, 1998.
- [91] M. W. Sracic, "A new experimental method for nonlinear system identification based on linear time periodic approximations," Ph.D., Engineering Physics, University of Wisconsin-Madison, 2011.
- [92] M. S. Allen and M. W. Sracic, "System Identification of Dynamic Systems with Cubic Nonlinearities Using Linear Time-Periodic Approximations," presented at the ASME 2009 International Design Engineering Technical Conferences & Computers and Information in Engineering Conference IDETC/CIE 2009, San Diego, California, USA, 2009.

Appendix 1: List of Publications

Journal Papers

- 1) **Shifei Yang**, Matthew S. Allen. Harmonic Transfer Function to Measure Translational and Rotational Velocities with Continuous-Scan Laser Doppler Vibrometry. ASME Journal of Vibration and Acoustics (Under review).
- 2) **Shifei Yang**, Matthew S. Allen. Lifting Approach to Simplify Output-only Continuous-scan Laser Vibrometry. Mechanical System and Signal Processing (Under review)
- 3) **Shifei Yang**, Matthew S. Allen. Output-Only Modal Analysis Using Continuous-Scan Laser Doppler Vibrometry and Application to a 20kW Wind Turbine. Mechanical System and Signal Processing, 3, pp 47-64 (2011)
- 4) **Shifei.Yang**, Matthew S. Allen, Michael W. Sracic. Two algorithms for mass normalizing mode shapes from impact excited continuous-scan laser Doppler vibrometry. ASME Journal of Vibration and Acoustics, 134, 021004 (2012)

Conference Papers

- 1) **Shifei Yang**, Dmitri Tcherniak, Matthew S. Allen, Modal Analysis of Rotating Wind Turbine using Multi-blade Coordinate Transformation and Harmonic power spectrum. (IMAC XXXII), Orlando, Florida USA, Feb. 3-6, 2014
- 2) David Ehrhardt, **Shifei Yang**, Matthew S. Allen, Mode Shape Comparison using Continuous Scanning Laser Doppler Vibrometry and High Speed 3D Digital Image Correlation. (IMAC XXXII), Orlando, Florida USA, Feb. 3-6, 2014
- 3) **Shifei Yang**, Matthew S. Allen, Measuring curvature for damage detection using continuous-scan laser Doppler vibrometry, 31st International Modal Analysis Conference (IMAC XXXI), Garden Grove, California USA, Feb. 11-14, 2013
- 4) **Shifei Yang**, Matthew S. Allen, A Lifting Algorithm for Output-only Continuous Scan Laser Doppler Vibrometry, 2012 AIAA Conference, Hawaii, 2012
- 5) Michael W. Sracic, **Shifei Yang**, Matthew S. Allen. Comparing Measured and Computed Nonlinear Frequency Responses to Calibrate Nonlinear System Models. 30th International Modal Analysis Conference (IMAC XXX), Jacksonville, Florida, Feb. 1-4, 2012
- 6) **Shifei.Yang**, Matthew S. Allen, Michael W. Sracic. Output-Only Modal Analysis Using Continuous-Scan Laser Doppler Vibrometry. 29th International Modal Analysis Conference (IMAC XXVIII), Jacksonville, Florida, Feb. 1-4, 2011
- 7) Andrea Gasparoni, Matthew S. Allen, **Shifei Yang**, et.al. Experimental Modal Analysis on a Rotating Fan Using Tracking-CSLDV. AIP Conference Proceedings, Volume 1253, pp. 3-16 (2010)

Appendix 2: Matlab Examples – A Simulated Free-free Beam

The codes simulate a CSLDV measurement of a beam model that has the same parameters as that in Section 6.2. Then the harmonic transfer function can be used to identify the modal parameters of the simulated beam under sinusoidal input, and the harmonic power spectrum can be used to analyze the beam under random input. The parameters in the codes can be modified to evaluate the proposed modal identification algorithms. Note that the codes can also be used to analyze a general LTP system. The readers can contact the author for the codes of positive harmonic power spectrum and lifting approach. There are not listed in the dissertation for brevity. The main and sub-functions listed are,

- Processing CSLDV measurements using harmonic transfer function
- Processing CSLDV measurements using harmonic power spectrum
- Sub-function that simulates CSLDV measurement on a beam model
- Sub-function that resamples a response to generate integer number of samples per period
- Sub-function that creates a periodic mode shape from the identified Fourier coefficients
- Sub-function that transforms a complex periodic shape to a real periodic shape

```

% This m-file process CSLDV measurement using harmonic transfer function
% Channel list
    % VibVelo - Vibrometer Velocity
    % MirXout - Mirror output signal in X channel
    % Force - Forcing signal signal from the load cell (DC)

clear;clc;close all

%% CLSDV Simulator - measuring a free-free beam

% one can also put real measurement from CSLDV here

ScanFreq = 128;
    wA = 2*pi*ScanFreq;
SampFreq = 10240;
    dt = 1/SampFreq;
% define the driving frequency at the first bending mode
fn = 227.70;
N = 1e5;
Force = sin(fn*2*pi*dt*[0:N-1].'); % number of samples in aquired signal
% sinusoidal input
% Run simulation to generate simulated measurement from CSLDV
[VibVelo,MirXout,xEx] = CSLDVSimulator(ScanFreq,SampFreq,Force,'debug');

%% signal conditioning
% 1. Find the accurate scanning frequency from mirror signal -Important for high scan
% frequency in real measurement
% 2. Resample to obtain integer number of samples per scan cycle

T = dt*(0:length(VibVelo)-1);
% Find accurate scan frequency
disp('Finding scanning frequency ...');
    MirXfft = fft(MirXout);
    MirXfft = MirXfft([1:(N/2+1)]);
    dw = 2*pi/(N*dt);
    MirXw = [0:dw:dw*N/2].';

    [~,ScanFreqind] = max(abs(MirXfft));
    f0 = MirXw(ScanFreqind)/2/pi; %integer scan freq as the initial guess

% Plot spectrum of mirror signal to check
figure(31)
subplot(3,1,1:2)
semilogy(MirXw/2/pi,abs(MirXfft)); grid on;
set(get(gca,'Children'),'LineWidth',2);
hold on; stem(f0,max(abs(MirXfft)),'ro','LineWidth',0.2);
title('FFT(x)');
xlabel('Frequency (Hz)'); ylabel('|FFT(x)|');
subplot(3,1,3)
plot(MirXw/2/pi,angle(MirXfft)*180/pi); grid on;
set(get(gca,'Children'),'LineWidth',2);
xlabel('Frequency (Hz)'); ylabel('Phase (FFT(x)) (^o)');
set(gcf,'Name','Mirror Angle X');
clear MirXfft MirXw

% use least squares to find a best estimate of the scan frequency
MirXout = MirXout(:);T = T(:);
f_obj = @(x) sum((MirXout - [cos(x*2*pi*T), sin(x*2*pi*T)]*...
    ([cos(x*2*pi*T), sin(x*2*pi*T)]\MirXout)).^2);
options = ['TolFun',1e-8,'TolX',1e-8];
ScanFreq = fminsearch(f_obj,f0,options)

% Find the delay in mirror drive signal
AB = ([cos(ScanFreq*2*pi*T), sin(ScanFreq*2*pi*T)]\MirXout);
Camp = AB(1)-sqrt(-1)*AB(2); % cosine amplitude - x(t) = real(Camp*exp(i*f0pt*2*pi*T))
th_delay = angle(Camp);

% resample and delete the initial delay in mirror signal

```

```

data = [VibVelo,Force,MirXout]; % ,SigLev
% clear VibVelo Force MirXout
% Consider the delay in fftresample. The delay is only the delay in MirX channel
[Trs, data_sync, NA] = FFTresample(T,data,ScanFreq,-th_delay,8); clear data T
Trs = Trs-Trs(1);
ts_cyc = Trs(1:NA);
t_cyc = ts_cyc - ts_cyc(1);
VibVelors=data_sync(:,1); Forcers=data_sync(:,2);
MirXoutrs=data_sync(:,3);
clear data_sync

%% harmonic transfer function to acquire mode shape

% one should select py such that all important harmonics are included

% here select the harmonics -10:10 to be safe
py = 10;
pys = -py:py;
Ny = length(pys);
Nt = length(VibVelors);

% creat exponentially modulated periodic signals
yexp = zeros(Nt,Ny); % EMP output
Hv = zeros(Nt,Ny); % spectrum of modulated signal

% Hanning window
window = 0.5*(1-cos([0:Nt-1].'*2*pi/Nt));
for k = 1:Ny
    yexp(:,k) = VibVelors.*exp(-li*pys(k)*wA*Trs);
    yw = yexp(:,k).*window;
    Hv(:,k) = fft(yw);
end

% define harmonic transfer function
F = fft(Forcers.*window);
Hv = Hv/max(F);
ws_est = [0:1:(Nt/2)]*2*pi/(dt*Nt);

% Manually Peak picking to find Fourier coefficient vector
band = find(ws_est<500*2*pi); % define the band up to 100Hz
figure(23);
semilogy(ws_est(band)/2/pi,abs(Hv(band,:)),'LineWidth',1);
title('Harmonic transfer function LTP System H_{n,0}');
xlabel('Frequency (Hz)'); ylabel('Mag PSD')
legend(num2str(pys.'));

grid on;

% pick the harmonics at selected driving frequency
[~,minindx] = min(abs(ws_est-fn*2*pi));
vs = Hv(minindx,:).';

%% Display the mode shape by plotting against laser path
shps = ltpFS2Phi(vs,pys.',wA,ts_cyc,'CSLDV'); % reconstructed mode shape
shps = res2real(shps. '); % rotate the shape to obtain real mode
shps = shps(:);
% Search for best phase delay based minimizing the area enclosed by the
% first shape.
shpints = zeros(400,1);
for k = 1:2000;
    x = cos(wA*ts_cyc+(k-1)*pi/2000);
    shpints(k) = sum(diff([x(end); x]).*real(shps(:,1)));
end
[junk,mind] = min(abs(shpints));
phi_delay = (mind-1)*pi/2000;
plt_txt = 'x = cos(wA*ts_cyc+phi_delay); plot(x,real(shps), x,imag(shps),':');';
figure(12); clf(12);
axes('Position',[0.13 0.169048 0.775 0.755952]); eval(plt_txt);
xlabel('\bf x position'); ylabel('Shapes');
title([num2str(fn),'Hz'])

```

```

grid on; % legend(num2str(ns));

% Add buttons to adjust phi
set(gca,'tag','Main');
PointsPerPixel = 72/get(0,'ScreenPixelsPerInch');
hf = gcf;
h1 = uicontrol('Parent',hf, ...
    'Units','points', ...
    'Position',[87 14.25 33.75 18.75]*PointsPerPixel, ...
    'Callback','phi_delay = phi_delay+2*pi/2000; eval(plt_txt)', ...
    'String','>>', ...
    'Tag','AdvPhs');
h2 = uicontrol('Parent',hf, ...
    'Units','points', ...
    'Position',[43.5 14.25 33.75 18.75]*PointsPerPixel, ...
    'Callback','phi_delay = phi_delay-2*pi/2000; eval(plt_txt)', ...
    'String','<<', ...
    'Tag','RedPhs');

% plot mode shape to the beam length for both lifting and hamonic transfer function
figure;
plot(xEx,-real(shps)*1000,'r--','LineWidth',2);hold on;
plot(xEx,-imag(shps)*1000,'m-.');hold on;
grid on;
xlabel('Position (m)')
ylabel('Amplitude (mm/s/N)')
title(['Mode shape at ',num2str(fn),'Hz using ', num2str(round(ScanFreq)),'Hz scan Frequency']);
legend('Real','Imaginary')

```

```

% this m-file process CSLDV measurement using harmonic power spectrum
% Channel list
    % VibVelo - Vibrometer Velocity
    % MirXout - Mirror output signal in X channel
    % Force - Forcing signal signal from the load cell (DC)

clear;clc;close all

%% CLSDV Simulator - measuring a free-free beam

% one can also put real measurement from CSLDV here

ScanFreq = 128;
wA = 2*pi*ScanFreq;
SampFreq = 10240;
dt = 1/SampFreq;
% define the driving signal as random input
N = 1e7;
Force = rand(N,1);
% Run simulation to generate simulated measurement from CSLDV
[VibVelo,MirXout,xEx] = CSLDVSimulator(ScanFreq,SampFreq,Force,'debug');

%% signal conditioning
% 1. Find the accurate scanning frequency from mirror signal -Important for high scan
% frequency in real measurement
% 2. Resample to obtain integer number of samples per scan cycle

T = dt*(0:length(VibVelo)-1);
% Find accurate scan frequency
disp('Finding scanning frequency ...');
MirXfft = fft(MirXout);
    MirXfft = MirXfft([1:(N/2+1)]);
    dw = 2*pi/(N*dt);
    MirXw = [0:dw:dw*N/2].';

[~,ScanFreqind] = max(abs(MirXfft));
f0 = MirXw(ScanFreqind)/2/pi; %integer scan freq as the initial guess

% Plot spectrum of mirror signal to check
figure(31)
subplot(3,1,1:2)
semilogy(MirXw/2/pi,abs(MirXfft)); grid on;
set(get(gca,'Children'),'LineWidth',2);
hold on; stem(f0,max(abs(MirXfft)),'ro','LineWidth',0.2);
title('FFT(x)');
xlabel('Frequency (Hz)'); ylabel('|FFT(x)|');
subplot(3,1,3)
plot(MirXw/2/pi,angle(MirXfft)*180/pi); grid on;
set(get(gca,'Children'),'LineWidth',2);
xlabel('Frequency (Hz)'); ylabel('Phase (FFT(x)) (^o)');
set(gcf,'Name','Mirror Angle X');
clear MirXfft MirXw

% use least squares to find a best estimate of the scan frequency
MirXout = MirXout(:);T = T(:);
f_obj = @(x) sum((MirXout - [cos(x*2*pi*T), sin(x*2*pi*T)]*...
    ([cos(x*2*pi*T), sin(x*2*pi*T)]\MirXout)).^2);
options = ['TolFun',1e-8,'TolX',1e-8];
ScanFreq = fminsearch(f_obj,f0,options)

% Find the delay in mirror drive signal
AB = ([cos(ScanFreq*2*pi*T), sin(ScanFreq*2*pi*T)]\MirXout);
Camp = AB(1)-sqrt(-1)*AB(2); % cosine amplitude - x(t) = real(Camp*exp(i*f0pt*2*pi*T))
th_delay = angle(Camp);

% resample and delete the initial delay in mirror signal
data = [VibVelo,Force,MirXout]; % ,SigLev
% clear VibVelo Force MirXout
% Consider the delay in fftresample. The delay is only the delay in MirX channel
[Trs, data_sync, NA] = FFTresample(T,data,ScanFreq,-th_delay,8); clear data T

```

```

    Trs = Trs-Trs(1);
    ts_cyc = Trs(1:NA);
    t_cyc = ts_cyc - ts_cyc(1);
    VibVelors=data_sync(:,1); Forcers=data_sync(:,2);
    MirXoutrs=data_sync(:,3);
    clear data_sync
%% Compute Harmonic power spectrum

% set length of sub-blocks for averaging
T = 20; % Second, equals the decay time of the first bending mode(0.1%)
Npblk = 2^nextpow2(T/dt); % Number of points in each block, FFT should be much faster if
Npblk is a power of 2
Overlapfactor = 0.85; % 85% overlap between neighbouring blocks
Noverlap = round(Overlapfactor*Npblk); % Points of overlap

% set the number of harmonics sufficiently large to include important
% harmoncis
p = 10;
py = -p:p;
py = py(:);
Ny = length(py);

% Compute only the primary column of the harmonic powr spectrum Gyys([-p:p],0);
% include zeropadding in the procedure
for ii = 1:length(py)
    yexp = VibVelors.*exp(-1i*py(ii)*wA*Trs);
    [Gyy,fs] = cpsd(yexp,VibVelors,hanning(Npblk),Noverlap,Npblk*2,1/dt,'twosided');
    if ii == 1
        Gyys = zeros(length(Gyy), Ny);
    end
    Gyys(:,ii) = Gyy;
end
% only the first half of the harmonic power spectrum
ws_est = fs(1:length(fs)/2)*2*pi;
% Harmonic correlation function
g = ifft(Gyys);
Gyys = Gyys(1:length(fs)/2,:);

% Display
figure(3);
semilogy(ws_est/2/pi,abs(Gyys),'-');
title('\bfOutput Spectrum Syy for LTP System S_{0,k}');
xlabel('\bfFrequency (Hz)');ylabel('\bfMag PSD')
legend(num2str(py));
grid on

%% Semi-auto identifcaiton to obtain Fourier coefficient
% This procedure automatically computes the best estimate of the operational
% shape from multiple harmonics - need minimum user input

% Define the natural frequency you want to look at
% This is the first bending mode of the simulated beam
fn = 92.4;

% Definie the number of sidebands included in the reconstruction
N = 3;
ns = -N:N;
ns = ns(:);

% Some frequencies may be folded from the negative axis
sign_ns = sign(fn+ns*ScanFreq);
freq = abs(fn+ns*ScanFreq);
% fold agianst SampFreq/2 (upper limit)
if any(freq>(SampFreq/2))
    sign_ns = sign_ns.*sign(freq-(SampFreq/2));
    freq(freq>(SampFreq/2)) = abs(SampFreq-freq(freq>(SampFreq/2)));
end
ns = sign_ns.*ns;

```

```

% Search around each harmoninc to find the max summation of Gyys
% This is assumed to be an accurate frequency of the harmonic.
figure(22);
semilogy(ws_est/2/pi,abs(squeeze(Gyys)));
title('\bfOutput Spectrum Syy for LTP System S_{n,0}');
xlabel('\bfFrequency (Hz)'); ylabel('\bfMag PSD')
legend(num2str(py));
grid on;
    xind = zeros(size(ns));
    vinc = 10; % search 10 points around the natural frequency
    for ii = 1:length(ns)
        xind(ii) = find(ws_est/2/pi >= freq(ii),1,'first');
        if xind(ii)<=vinc; xind(ii)= xind(ii)+vinc; end
        [~,maxind] = max(sum(abs(Gyys((xind(ii)-vinc):(xind(ii)+vinc),:))));
        xind(ii) = xind(ii)+maxind-(vinc+1);
        % mark each harmonic on the plot
        line(ws_est(xind(ii))/2/pi,abs(Gyys(xind(ii),:)), 'Marker','*','Color','k');
    end

% extract fourier coefficient vector and frequency at each harmonics via
% peak-picking
freq = ws_est(xind)/2/pi;
vs = Gyys(xind,:).';

%% Processing Fourier Coefficient vectors and reconstruct the mode shape

disp(' Harmonics vs Frequency ')
disp([' No. ', ' ns ', ' Freq '])
No = 1:length(ns);
    No = No(:);
disp([No,ns,freq])

% Shift the Fourier coefficents in each vector to the correct position
psv = py*ones(1,length(ns)) + ones(length(py),1)*ns.';
ps_all = [min(min(psv)):max(max(psv))].';
vs_all = zeros(length(ps_all),size(vs,2));
for k = 1:size(vs,2);
    for m = 1:size(vs,1);
        vs_all(find(ps_all == psv(m,k)),k) = vs(m,k);
    end
end
disp(' ');
disp('Shifted Mode Vectors:');
disp([' N ', ' py ', ' Harmonics ',])
disp([NaN,NaN,ns';NaN,fn,freq.'/1000;(1:length(ps_all)).',ps_all,abs(vs_all)])

% Delete high order terms that might be reliable
n_trunc = input('Kept terms range? (No. ex,[1,3]): ');
vs_all = vs_all(n_trunc(1):n_trunc(2),:);
ps_all = ps_all(n_trunc(1):n_trunc(2));

% Rotate all the Fourier coefficient such that they have the same phase
del_phi = zeros(1,size(vs_all,2));
for k = 1:(size(vs_all,2)-1);
    dot_ind = (vs_all(:,k) ~= 0) & (vs_all(:,k+1) ~= 0);
    del_phi(k+1) = angle(vs_all(dot_ind,k+1))*vs_all(dot_ind,k));
end
del_phi = cumsum(del_phi);
vs_all = vs_all*diag(exp(1i*del_phi));

% singular value decomposition, the best estimate is the first singular
% value
[U,S,V] = svd(vs_all);
vs_svd = U(:,1);
disp(' ');
disp('Shifted Mode Vectors:');
disp([' ', ' py ', ' vs_svd ', ' Harmonics ',])
disp([NaN,NaN,ns';NaN, fn,freq.'/ps_all, abs(vs_svd),abs(vs_all)])

% Reconstruct mode shapes from identified Fourier Coefficient vectors

```

```

shps = ltpFS2Phi(vs_svd,ps_all,wA,ts_cyc,'CSLDV');
% rotate to find the real mode shape
shps = res2real(shps.').';
% Search for best phase delay based minimizing the area enclosed by the
% first shape.
shpints = zeros(400,1);
for k = 1:400;
    x = cos(wA*ts_cyc+(k-1)*pi/400);
    shpint(k) = sum(diff([x(end); x]).*real(shps(:,1)));
end
[junk,mind] = min(abs(shpint));
phi_delay = (mind-1)*pi/400

plt_txt = 'x = cos(wA*ts_cyc+phi_delay); plot(x,real(shps), x,imag(shps),'':'');';
figure(12); clf(12);
axes('Position',[0.13 0.169048 0.775 0.755952]); eval(plt_txt);
xlabel('\bf x position'); ylabel('Shapes');
title([num2str(fn),'Hz'])
grid on; % legend(num2str(ns));

% Add buttons to adjust phi
set(gca,'tag','Main');
PointsPerPixel = 72/get(0,'ScreenPixelsPerInch');
hf = gcf;
h1 = uicontrol('Parent',hf, ...
    'Units','points', ...
    'Position',[87 14.25 33.75 18.75]*PointsPerPixel, ...
    'Callback','phi_delay = phi_delay+2*pi/400; eval(plt_txt)', ...
    'String','>>', ...
    'Tag','AdvPhs');
h2 = uicontrol('Parent',hf, ...
    'Units','points', ...
    'Position',[43.5 14.25 33.75 18.75]*PointsPerPixel, ...
    'Callback','phi_delay = phi_delay-2*pi/400; eval(plt_txt)', ...
    'String','<<', ...
    'Tag','RedPhs');

% plot real and imaginary part of the reconstructed shape
figure(9)
plot(cos(wA*ts_cyc+phi_delay),[real(shps),imag(shps)])
legend('real','imaginary')

```



```

function [VibVelo,MirXout,xEx] = CSLDVSimulator(ScanFreq,SampFreq,Force,varargin)

% [VibVelo,MirXout,xEx,NA] = CSLDVSimulator(ScanFreq,SampFreq,Force)
% [VibVelo,MirXout,xEx,NA] = CSLDVSimulator(ScanFreq,SampFreq,Force,'Debug')
%
% This function simulates the response of a free-free beam to any type of
% input. The beam is measured with CSLDV with arbitrary scan frequency and
% sampling frequency
% input: ScanFreq - Laser scan frequency
% SampFreq - Laser sampling frequency - must be an n*ScanFreq
% Force - vector of forcing signal, sampled at the sampling freq
% varargin - control handle for debug mode
% output: VibVelo - Measured velocity signal
% MirXout - Mirror output signal
% xEx - Laser position along the beam
%
% Shifei Yang 2013
% UW-Madison

% control handle
if strcmp(varargin,'debug')
    plotflag = true;
end

dt = 1/SampFreq;
N = length(Force);
T = dt*(0:N-1);
TA = 1/ScanFreq;
wA = 2*pi*ScanFreq;

%% Define beam parameters - same as a physical Aluminum beam

% ELSTIC MODULUS OF 6061-T6511 ALUMINUM IS 1E4 KSI OR 69E9 Pa
% Density of 6061-T6511 ALUMINUM is 2710 kg/m^3
rho = 2710; % kg/m^3
E = 66e9; % N/m^2

BeamLength = 38.25*0.0254; % m
Beamth = 2/16*0.0254; % m
BeamH = 1*0.0254; % m
csArea = Beamth*BeamH; % m^2
I = 1/12*BeamH*Beamth^3; % Area moment of inertia

% Continuous-Scan parameters
EdgeDistL = .125*0.0254; % m
EdgeDistR = .125*0.0254; % m
StandoffD = 205*0.0254; % m
centerdot = BeamLength/2; % perfectly centered
LeftScanLength = BeamLength/2 - EdgeDistL;
RightScanLength = BeamLength/2 - EdgeDistR;
scanlength = LeftScanLength + RightScanLength;

%% Ritzs simulation of beam subjected to any type of input
syms y real;

% This model assumes only 2 rigid body modes
NmDs = 7; % number of modes used to construct model
Nrgb = 2; % Two rigid body motion
Nbend = NmDs-Nrgb; % Number of bending modes

% Base function according Ginsberg's book
an = [zeros(1,Nrgb),4.730,(2*[4:(Nbend+2)]-3)/2*pi];
Rn = zeros(1,NmDs);
for j = 3:NmDs;
    Rn(j) = -(sin(an(j)) - sinh(an(j)))/(cos(an(j)) - cosh(an(j)));
end

% Generate Mode functions which includes the Rigid body motion
psi(1) = 1+0*y;

```

```

psi(2) = y-0.5;
for j = Nrgb+1:Nmids
    psi(j) = sin(an(j)*y) + sinh(an(j)*y) + ...
            Rn(j)*(cos(an(j)*y) + cosh(an(j)*y));
end

% Define M K C matrices
M = zeros(Nmids,Nmids); K = zeros(Nmids,Nmids); Q = zeros(Nmids,1);
for n = 1:Nmids;
    M(n,n) = double((int(psi(n)*psi(n),y,0,1))*rho*csArea*BeamLength);% % *rho*A*L % +
    ym^2*sin(j*pi*ym)*sin(n*pi*ym);
    K(n,n) = double((int((diff(psi(n),y,2)*diff(psi(n),y,2)),y,0,1))*E*I/BeamLength^3); % *EI/L^3
for nondim y
end
xi = 0.01; % apply 1% damping to each mode
C = 2*xi*sqrt(K*M);

% Compute natural frequency and mode shapes
[phiRitz, lambda] = eig(K,M);
fns = sqrt(abs(diag(lambda)))/2/pi;

% Normalize Mode Functions:
mu = diag(phiRitz.'*M*phiRitz);
PHI = zeros(size(phiRitz));
for jj = 1:1:length(phiRitz)
    PHI(:,jj) = phiRitz(:,jj)/sqrt(mu(jj));
end

% double check the mode shapes
if plotflag
    [NfreqAn,sortind] = sort(fns);
    PHI = PHI(:,sortind);
    xan = linspace(0,BeamLength,100);
    psi_vals = zeros(length(xan),length(an));
    for p = 1:Nmids
        for n = 1:length(xan)
            y = xan(n)/BeamLength;
            psi_vals(n,p) = double(eval(psi(p)));
        end
    end
    phiAn_check = psi_vals*PHI;
    figure
    plot(xan,phiAn_check)
    title('\bfcheck phiAn')
    legend(num2str(NfreqAn))
end

%% compute response to any type of input
fs = SampFreq;
% Note: The Force is a discrete force that can be applied to any point(s)
Np_F = 10; % to 10 points
xan = linspace(BeamLength*.02,BeamLength*0.98,Np_F);
psi_F = zeros(Np_F,Nmids);
psi_F(:,1) = 1+0*xan;
psi_F(:,2) = xan-0.5;
for j = Nrgb+1:Nmids
    psi_F(:,j) = sin(an(j)*xan) + sinh(an(j)*xan) + ...
            Rn(j)*(cos(an(j)*xan) + cosh(an(j)*xan));
end

% Define Force time history, can be sinusoidal/swept sine or any other
u = zeros(N,Nmids);
for ii = 1:N
    u(ii,:) = Force(ii)*ones(1,Np_F)*psi_F;
end

%% Simulate beam response to the designed input
% Define state space model
% Response in modal coordinate
A = -inv([M,zeros(size(M));zeros(size(M)),M])*[zeros(size(M)),-M;K,C];

```

```

B = inv([M,zeros(size(M));zeros(size(M)),M])*eye(2*Nmds,Nmds); %#ok<MINV>
Coutput = [zeros(Nmds,Nmds),eye(Nmds,Nmds)]; % output velocity
sys = ss(A,B,Coutput,[]);
Y = lsim(sys,u,T);
clear u

%% Simulating constinuous-scan on the beam

% use mirror signal to generate measurement point position information
NA = floor(SampFreq/ScanFreq); % Number of points per scanning cylcle
xEx = BeamLength/2*cos(wA*T(1:NA))+BeamLength/2;

% Compute the analytical mode shape at these measurement points
psi_vals = zeros(NA,Nmds);
for p = 1:Nmds
    for n = 1:NA
        y = xEx(n)/BeamLength;
        psi_vals(n,p)= double(eval(psi(p)));
    end
end
phiAn = psi_vals(1:NA,:)*PHI;

% Compute the random response at each physical location
VibVelo = zeros(N,1); % Acquired Vibration Velocity a problem here
for ii = 1:N
    n = mod(ii-1,NA)+1;
    VibVelo(ii) = psi_vals(n,:)*Y(ii,:);
end
VibVelo = VibVelo(:);
MirXout = cos(wA*dt*(0:N-1));
MirXout = MirXout(:);

if plotflag
    % Double check output signal in frequency domain
    ts_full = dt*(0:length(VibVelo)-1).';
    y_swp = VibVelo(1:length(ts_full));

    figure;
    plot(ts_full,y_swp*1000)
    xlabel('Time (s)'); ylabel('Velocity (mm/s)');
    title('CSLDV Output Signal')
    grid on;

    % Double check output signal in frequency domain
    Xfft = fft(y_swp,[],1);
    Y_swp = Xfft([1:(N/2+1)]);
    % Create Frequency vector in rad/s
    w1 = 2*pi/(N*dt);
    w_swp = [0:w1:w1*N/2].';
    figure(3)
    semilogy(w_swp/2/pi,abs(Y_swp))
    grid on;
    xlabel('Frequency (Hz)'); ylabel('Y volts');
    title('FFT')
end

```

```

function [t_sync, data_sync, f_ratio_int] = FFTresample(t, data, fopt,varargin)
% Resample a signal to be synchronous with frequency fopt (in Hz) by zero
% padding the FFT of the signal and then using linear interpolation
%
% [t_sync, data_sync, f_ratio_int] = FFTresample(t, data , fopt);
%
% t is the time vector for the system, data is matrix with each column the
% same length as t a signal that is to be resampled.  fopt is the frequency
% that the signal is to be synchronous with.  This routine resamples the
% signals such that the new sample frequency is f_ratio_int*fopt, where
% f_ratio_int is an even integer.
%
% Optional arguments:
%
% [t_sync, data_sync, f_ratio_int] = ...
%   resample(t, data , fopt, fft_exp_fact,ScanFreqMult);
%
% th_delay:
%   A phase angle.  If this argument is provided, the resampled
%   signal is shifted by theta radians relative to time zero.
% fft_exp_fact
%   The factor by which to expand the FFT of the signal before linearly
%   interpolating.  The default is to expand the signal to eight times its
%   original length.
% ScanFreqMult
%   is used for tracking data.  In that case fopt is the mirror scan
%   frequency, but this is related to f_rot by fopt = ScanFreqMult*f_rot.
%   The algorithm uses this after resampling to trim the data to assure
%   that no partial cycles of either f_rot or fopt are present.
%
% M.S. Allen, M.W. Sracic & Shifei Yang, 2007-2010
% UW-Madison

if nargin > 3;
    th_delay = varargin{1};
else
    th_delay = 0;
end
if nargin > 4
    fft_exp_fact = varargin{2};
else
    fft_exp_fact = 8;
end
if nargin > 5
    SFMult = varargin{3};
else
    SFMult = 1;
end
if size(data,2) > size(data,1);
    warning('data has more columns than rows, may not be shaped correctly.');
```

data = data.');

```

end

% Compute start time such that the phase of the mirror signal (or
% time-periodic trajectory) is zero.
np = ceil(-th_delay/2/pi);           % cycle at which mirror signal peaks.
tmm = (np+th_delay/2/pi)/fopt;
N_data = size(data,1);

dt = t(2)-t(1);
f_samp = 1/dt;
f_ratio = f_samp/fopt;

if ~isinteger(f_ratio)
    Data = fft(data);
    dw = 2*pi/(N_data*dt);
    Data = 2/N_data*Data;           % Include Scaling Factor for fft

    % Pad FFT with zeros coresp. to ideal band-limited resampling (see
    % Stearns textbook).
```

```

N_data_rs = N_data*fft_exp_fact;
data_rs = ifft(Data,N_data_rs);
data_rs = data_rs(1:(N_data_rs/2+1),:);
T = 2*pi/dw;
t_rs = T/N_data_rs*[0:size(data_rs,1)-1].';
% *N/2 - second scaling factor for resampled ifft
data_rs = data_rs*N_data_rs/2;

% Check data
if max(imag(data_rs)) > 0.0001*max(real(data_rs));
    warning('IFFT has a significant imaginary component that was discarded');
    disp('Max Imaginary Component / Max Real Component');
    max(imag(data_rs))/max(real(data_rs))
end
data_rs = real(data_rs);

% Force an even number of samples per cycle
f_ratio_int = ceil(f_ratio);
if (f_ratio_int/2)~=round(f_ratio_int/2)
    f_ratio_int = f_ratio_int+1;
end
f_samp_sync = fopt*f_ratio_int;
dt_sync = 1/f_samp_sync;
t_sync = [tmm:dt_sync:max(t)].';

% Linear interpolation
data_sync = interp1(t_rs,data_rs,t_sync,'linear',0); % use zero for extrapolated values
t_sync = t_sync - t_sync(1);

% Eliminate any extra partial cycles, so that the data contains an
% integer number of cycles.
Ncyc = length(t_sync)/f_ratio_int;
if ~isinteger(Ncyc/SFMult);
    t_sync = t_sync(1:(SFMult*floor(Ncyc/SFMult))*f_ratio_int);
    data_sync = data_sync([1:(SFMult*floor(Ncyc/SFMult))*f_ratio_int],:);
end

else % data already is synchronous, don't resample
    t_sync = t; data_sync = data;
end

```

```

function [phi] = ltpFS2Phi(B,mB,wA,ts_cyc,varargin)
%
% Conversion of Fourier Series Model to phi(t).
%
% [phi] = ltpFS2Phi(B,mB,wA,ts_cyc);
%
% B is a matrix of Fourier coefficients, mB is a matrix of integers giving
% the index for each of the Fourier coefficients. The size of each is:
%     No - number outputs
%     Nfs - number Fourier Series Coefficients
%     N - number of modes
%
% For CSLDV measurements where No = 1, B and mB are Nfs x N and call
% the function using the following syntax:
%
% [phi] = ltpFS2Phi(B,mB,wA,ts_cyc,'CSLDV');
%     the matrix phi returned is Nt x N
%
% MSA, July 2010
%

if nargin > 4 && strcmpi(varargin{1},'CSLDV');
    B = permute(B,[3,1,2]);
    mB = permute(mB,[3,1,2]);
    if size(mB,3) == 1;
        mB = mB(:,ones(1,size(B,3)));
    end
end
No = size(B,1);
Nfs = size(B,2);
N = size(B,3);
Nt = length(ts_cyc);
phi = zeros(No,Nt,N);
for k = 1:size(B,1);
    for m = 1:size(B,2); % loop over FS terms
        for n = 1:size(B,3); % loop over modes
            phi(k,:,n) = phi(k,:,n)+B(k,m,n)*exp(1i*mB(k,m,n)*wA*ts_cyc(:).');
        end
    end
end

if nargin > 4 && strcmpi(varargin{1},'CSLDV');
    phi = permute(phi,[2,3,1]);
end

```

```

function [rot_res] = res2real(cres,varargin)
% Create real mode vectors from complex ones using line-fit procedure.
% One sometimes encounters the situation where the mode vectors identified
% from experimental data are real but rotated by a complex constant [Ewins
% 2000], for example, due to phase error in the data acquisition system.
% Assuming that the mode vectors have good modal phase colinearity, one can
% fit a line through the shapes and rotate them such that they are as real
% as possible.
%
% [rot_shape] = res2real(cres)
%     Finds the best rotated shape for the mode vectors in cres,
%     considering each individually.
% [rot_shape] = res2real(cres,'plot on')
%
% real(rot_shape) is the best real approximation to the mode shape, found
% using least squares.
%
% Find best real approximation to complex residues. Residue matrix input
% in AMI's standard form:
%   cres(1i,j,k) - i corresp to mode number, j is output number, k is input
%   number
%
% Matt Allen, June, 2007
%
% update: if cres is a real matrix, the function returns the matrix with no
%         change
%   Shifei Yang, 2010.07.15

if size(cres,2) == 1 && size(cres,1) > 1;
    warning('Residue Vector has Length One - It should be input as a row vector.')
end

if imag(cres) == 0
    rot_res = cres;
    warning('Residue Vector is real');
else
    rot_res = zeros(size(cres));
    for dp_num = 1:size(cres,3);
        for k = 1:size(cres,1);
            shapel = cres(k,:,dp_num).';
            mean_angle1 = atan((real(shapel).*imag(shapel)) / ...
                               (real(shapel).*real(shapel)));
            rot_shapel = shapel.*exp(-1i*mean_angle1);
            % Note - atan is singular at 90 degrees - so this algorithm performs
            % poorly if "shape" is purely imaginary. This tries again with the
            % shape rotated 90 degrees.
            shape2 = 1i*cres(k,:,dp_num).';
            mean_angle2 = atan((real(shape2).*imag(shape2)) / ...
                               (real(shape2).*real(shape2)));
            rot_shape2 = shape2.*exp(-1i*mean_angle2);
            % Keep the shape that best minimizes the norm of the imaginary part
            if norm(imag(rot_shapel)) <= norm(imag(rot_shape2))
                rot_res(k,:,dp_num) = rot_shapel; kept_flg = 1;
                mean_angle = mean_angle1;
            else
                rot_res(k,:,dp_num) = rot_shape2; kept_flg = 2;
                mean_angle = mean_angle2;
            end
        end

        if nargin > 1
            figure;
            set(gcf,'Units', 'normalized', 'Position', [0.324,0.229,0.35,0.685]);
            subplot(2,1,1)
            line(real(shapel),imag(shapel),'Marker','.', 'LineStyle','none');
            ln_xs = real(real(shapel*exp(-1i*mean_angle1))*exp(1i*mean_angle1));
            ln_ys = imag(real(shapel*exp(-1i*mean_angle1))*exp(1i*mean_angle1));
            line(ln_xs,ln_ys,'LineStyle',':', 'Color','k', 'LineWidth',2);

            line(real(rot_shapel),imag(rot_shapel), 'Marker','o', 'LineStyle','none', 'Color','r');
            legend('Original', 'Linear Fit', 'Rotated');
        end
    end
end

```

```

        if kept_flg == 1; title('\bfKept This Result');

line(real(rot_res(k,:),dp_num)),imag(rot_res(k,:),dp_num),'Marker','d','LineStyle','none','Color',
'k');
    end
    axis equal
subplot(2,1,2)
    line(real(shape2),imag(shape2),'Marker','.', 'LineStyle','none');
    ln_xs = real(real(shape2*exp(-1i*mean_angle2))*exp(1i*mean_angle2));
    ln_ys = imag(real(shape2*exp(-1i*mean_angle2))*exp(1i*mean_angle2));
    line(ln_xs,ln_ys,'LineStyle',':', 'Color','k','LineWidth',2);

line(real(rot_shape2),imag(rot_shape2),'Marker','o','LineStyle','none','Color','r');
    legend('Original*i','Linear Fit','Rotated');
    if kept_flg == 2; title('\bfKept This Result');

line(real(rot_res(k,:),dp_num)),imag(rot_res(k,:),dp_num),'Marker','d','LineStyle','none','Color',
'k');
    end
    axis equal
    end
    end
end
end
end

```